A SEARCH FOR NEW PHYSICS IN HIGH-MASS DITAU EVENTS IN THE ATLAS DETECTOR

Ryan Reece

A DISSERTATION
in
Physics and Astronomy

Presented to the Faculties of The Univeristy of Pennsylvania
in Partial Fulfillment of the Requirements for the Degree of Doctor of Philosophy
2013

H.H. Williams, Professor, Physics
Supervisor of Dissertation

Randall Kamien, Professor, Physics
Graduate Group Chairperson

Dissertation Committee
Randall Kamien, Professor, Physics
I. Joseph Kroll, Professor, Physics
Burt Ovrut, Professor, Physics
Evelyn Thomson, Associate Professor, Physics
H.H. Williams, Professor, Physics

A SEARCH FOR NEW PHYSICS IN HIGH-MASS DITAU EVENTS IN THE ATLAS DETECTOR

Acknowledgements

Graduate school has been an incredible time and a period growth for me. Several people have been a guide, inspired my interests, taught me a concept or skill, and/or been an exceptional collaborator.

First, I would like to thank my advisor Brig Williams who is an amazing leader of a strong research group at Penn. Brig has enabled me in so many ways, often been a source of council, and had a caretaker-sense of what is important. Thanks also to Brig for all his help reviewing this thesis and helping improve the text in many ways.

I am indebted to all of the Penn faculty in the ATLAS group in some way. Thanks go to Joe Kroll for being so welcoming and often having a constructive, critical eye. Thanks to Evelyn Thomson for sharing her office at Penn and her advice, and for introducing me at the BNL Jamboree that guided me through my first steps in ATLAS software. I am grateful to Elliot Lipeles for helping me with a place to live when I first moved to CERN, and for demonstrating such an example of breadth and depth of knowledge. Burt Ovrut's lectures on quantum field theory and our discussions have been hugely influential on how I view physics, for which I will always be grateful. Thanks to Jean O'Boyle for helping keep us all organized.

Thanks to the Project Leader of the TRT during the start-up of the LHC, Christoph Rembser, for his direction and support. Many thanks go to the instrumentation group at Penn, in particular Rick Van Berg, Mitch Newcomer, and Paul Keener, who together with Ole Røhne, Franck Martin, Mike Hance, and Ben LeGeyt, pushed me up the ramp of understanding the basics of electronics and DAQ during the commissioning of the TRT. I was always playing catch-up and grateful to learn so much from the from the rest of the TRT DAQ on-call team: Mike Hance, Dominick Olivito, Jamie Saxon, Jon Stahlman, Peter Wagner, and Sarah Heim. A large part of the day-by-day success of the TRT should be accredited to the TRT Run Coordinators: Anatoli Romaniouk, Jim Degenhardt, and Andrey Loginov.

I would like to thank my collaborators that helped with the TRT straw hit efficiency study: Saša Fratina, Jared Adelman, Esben Klinkby, and Dan Guest, and the tracking experts: Andreas

Salzburger and Markus Elsing, who helped me to learn how to use track-extrapolation tools for the study.

I thank the conveners of the ATLAS tau working group that have helped us to deliver robust and performant tau identification: Elzbieta Richter-Was, Wolfgang Mader, Soshi Tsuno, Yann Coadou, Stan Lai, Stefania Xella, and Martin Flechl. Thank you to all the other collaborators that have debated the subtleties and strategies behind the ATLAS tau reconstruction and identification with me, especially Will Davey, Dugan O'Neil, Michel Trottier-McDonald, Noel Dawe, Mogens Dam, Marcus Morgenstern, Saminder Dhaliwal, Almut Pingel, and Alex Tuna.

Many thanks to the team with which I worked to observe and measure the cross section of $Z \to \tau\tau$, including: Donatella Cavalli, Elias Coniavitis, Sofia Consonni, Sinead Farrington, Felix Friedrich, Aimee Larner, Caterina Pizio, Serban Protopopescu, Trevor Vickey, Sahal Yacoob, but especially thanks for the dedication of Justin Griffiths, Anna Kaczmarska, and Susanne Kuehn. Thanks also go to the editorial board for our $Z \to \tau\tau$ result, including Attilio Andreazza, Massimiliano Bellomo, Eric Torrence, and Susana Cabrera Urban.

Thanks to those with whom I worked closely on the search for Z', including: Alex Tuna, Will Davey, Andres Florez, Gabriel Palacino, and Peter Wagner. Very special thanks goes to Alex Tuna and Will Davey, whose contributions to the fake factor methods for background estimation and the development of high-p_{T} tau systematics, respectively, have made my thesis something it would not have been otherwise. Thanks also for the attention and support of our editorial board, including: Yann Coadou, Gideon Bella, Jean-Baptiste De Vivie De Regie, and Ashutosh Kotwal.

Thanks go to collaborators Koji Nakamura and Keita Hanawa from the $H \to \tau\tau$ analysis, for comparing and discussing many issues concerning the use of fake factor methods in tau analyses.

Kyle Cranmer, Amir Farbin, and Akira Shibata helped me to first appreciate the software requirements of an analysis of ATLAS data. Attila Krasznahorkay is a careful custodian of the SFrame framework, for which I am grateful, and was so useful to me during the measurement of $Z \to \tau\tau$. Thanks to Scott Snyder organizing the ATLAS D3PDMaker to make it easy to flatten our data, and for helping Dugan, Michel, and I design a D3PDMaker for the tau working group. A huge thanks to Paul Keener, for being an observant watchman of the computing resources at Penn that enable so much of our analysis.

Thanks to Tae Min Hong for often taking the time to look out for my interests and to help to bounce and refine my ideas. Thanks to Zach Marshall for often being so generous with his time and his expertise, particularly for pointing out many of the distinctions between quark and gluon jets. Thanks to Devin Harper for working so many late nights with me, and for helping me work through the CLs method, among other adventures. Thanks to Josh Kunkle for being such an

outstanding roommate, and examining with me whatever minutiae that came up concerning ATLAS or its software. I learned so much in that apartment.

I am grateful to CERN and all the countries that fund it for being such an amazing example international scientific collaboration. I am grateful for the LHC and all the R&D efforts that bring the highest energies in reach in a laboratory. Thanks to all the members of the ATLAS Collaboration that make the functioning of the experiment possible. In the US, I would also like to acknowledge the support of the American taxpayers and the DOE and NSF agencies through which American research in particle physics is funded.

I would especially like to thank John Alison and Dominick Olivito of my incoming class, for being partners in taking apart so many problems (physics or not) in our study sessions in the Zoo and our work at CERN. More than most, you have helped shape my skills in critical thinking. Thanks also to everyone in the community of Penn dinners and all the young students at CERN that gave me a tribe to belong to. Thanks to everyone who traveled a European city or went climbing with me. You helped keep me sane and its been an incredible ride.

Thanks to Charlie Sell for helping me get serious about writing that day in January in the library in Geneva. Thanks to Jim Halverson and Austin Purves for reviewing my review of the SM in the appendix. Many, many thanks to Susan Fowler for reading and editing so many versions.

I would still like to thank Shaleena and the McGee and Rao families for their love and support throughout much of the start of this journey. My love and thanks go to the Reece and Moss families, especially my parents David and Linda, for all of your love and support throughout my life. You share in this honor too. My final thanks and love go to Susan who has been the most patient, loving, and encouraging during my months of writing.

ABSTRACT

A SEARCH FOR NEW PHYSICS IN HIGH-MASS DITAU EVENTS IN THE ATLAS DETECTOR

Ryan Reece

H.H. Williams

This thesis presents a review of work on the performance of the reconstruction and identification of hadronic tau decays and studies of events reconstructed with a $\ell\tau_{\mathrm{h}}$ final state with the ATLAS detector at the Large Hadron Collider. The first cut-based tau identification used with ATLAS data and the first observations of $W \to \tau\nu$ and $Z \to \tau\tau$ at ATLAS are described, as well as many of the issues concerning the calibration and systematic uncertainties of reconstructed taus. The first measurement of the $Z \to \tau\tau$ cross section at ATLAS with 2010 dataset is reviewed. Last, results are presented from the first search for high-mass resonances decaying to $\tau^+\tau^-$ at ATLAS with the 2011 dataset.

A preprint can be found at CDS: CERN-THESIS-2013-075.

Contents

Preface

Timeline of my experience

During my time as a graduate student at the University of Pennsylvania, working with the ATLAS experiment at the Large Hadron Collider (LHC), I have witnessed one of the world's most complex scientific undertakings during its final construction, commissioning, operation, and announcement of the discovery of a Higgs-like new particle. It has been an exciting time.

Penn helped design, assemble, and install the front-end electronics that read out, control, and power the Transition Radiation Tracker (TRT), the outermost sub-detector of the ATLAS tracker. I spent my first summers as a student with Penn (2006–08) at CERN, participating in the integration and commissioning of the TRT. I helped with diagnostic checks of the TRT front-end before the TRT was installed in ATLAS, and developed software for normalizing the analog-to-digital thresholds in the front-end electronics of the TRT. In January of 2009, I moved to the Geneva area to work at CERN full-time with the ATLAS Collaboration, and stayed there for the next four years. ATLAS began taking data from collisions at the LHC in November of 2009. Throughout most of the running of the LHC from 2010–2012, I rotated with others the on-call responsibility for the TRT DAQ.

My timing with the commissioning of the TRT and the arrival of the first collision data allowed me to contribute to a broad range of research efforts. The focus of my research with the data from ATLAS has been on the reconstruction of hadronic decays of tau leptons and their use in searches for new physics. I helped with the commissioning and validation of the ATLAS offline tau reconstruction with the first data, and the development of the cut-based identification. I contributed to the observation $Z \to \tau\tau$ and the measurement of its cross section, which lead to searching for new physics in high-mass ditau events.

About the text

The organization of the text is outlined in Section 1.2 of the introduction. There are some places where I have adapted large portions of text from other references, sometimes nearly verbatim, but only from references and sections therein, for which I was a primary author or editor, and had often drafted the original text. These include:

- Chapter 4 which follows ATLAS-CONF-2011-077, ATLAS-CONF-2011-152, and ATL-COM-PHYS-2012-394 in many places;
- Chapter 5 which follows a combination of ATL-PHYS-INT-2009-044, ATL-COM-PHYS-2011-416, and arxiv:1108.2016 [hep-ex];
- Chapter 6 which follows a combination of ATL-COM-PHYS-2012-394 and arxiv:1210.6604 [hep-ex].

Ryan Reece
Philadelphia, July 2013

Chapter 1

Introduction

1.1 Exploring at the high-energy frontier

The reductionist program and scientific method have been hugely successful in describing nature with progressively better precision. At the most fundamental level explored experimentally, we know the nuclei of atoms are bound systems of sub-atomic particles called "quarks". The quarks together with another class of particles called "leptons", to which the electron belongs, are all the known fermions which make-up stable matter. The Standard Model (SM) of particle physics is a quantum field theory where fermions interact by exchanging gauge bosons which are the quanta of the fundamental forces. Experimental research efforts world-wide in the last 100 years have probed interactions at successively higher energies, discovering the ingredients that would be pieced together into the SM in the 1960s.

The Large Hadron Collider (LHC) at the European Organization for Nuclear Research (CERN) laboratory, located on the French-Swiss border outside Geneva, is currently the world's highest energy particle collider. For three years from 2010–2012, the LHC was operational and delivered proton-proton collisions at a center-of-momentum energy of 7–8 TeV. It is currently shutdown for maintenance and upgrades, but is expected to run again in 2015 and for much of this decade.

The consistency of the SM depends on nature having certain gauge symmetries, but that the electroweak symmetry is broken via the Higgs mechanism as a way to allow gauge bosons to have masses that would otherwise ruin gauge invariance. The last few years, with the start-up of the LHC have brought the frontier of high-energy physics to a critical level of sensitivity to the Higgs boson and to many scenarios of new physics beyond the SM. The discovery of a new particle at the LHC in 2012, so far consistent with the Higgs boson, completes the cast as the last missing particle in the SM to be found. There are many ways the SM has been tested to fantastic precision, such as the g-factor of the electron, but there are others such as the Higgs-coupling and neutrino-mixing

parameters that have only recently been measured to $\sim 10\%$ or have not yet been measured.

Being a gauge theory with 12 fermions, the SM is amazingly simple for a theory that describes the fundamental interactions underlying all observable phenomena apart from gravity. However, the SM is also very ad hoc in its structure and the values of its 19 or more parameters. It is also at risk of needing to be oddly fine-tuned to be consistent without extending the model in some way with additional structure at higher energies. These and other compelling theoretical arguments give reasons to expect there to be new physics to be discovered at the TeV scale. Many theories of physics beyond the SM have revolutionary implications for the concepts of symmetry and space-time, and for our understanding of the early universe.

The ATLAS experiment is a massive multi-purpose detector, built in the Point 1 cavern of the LHC tunnel, one of four points where experiments are situated at beam crossings. The physics program of ATLAS and its 3000 collaborators includes the successful search for the Higgs boson as well as searches for other new exotic particles and evidence for physics beyond the SM.

1.2 Outline

This thesis presents a summary of much of my graduate work during the start-up of the LHC and the collection of the first years of data with ATLAS. The central topics of my research have been the reconstruction and identification of hadronic decays of tau leptons, and their use in searching for new physics. In particular, I discuss: the first cut-based tau identification used with ATLAS data, the first observations and systematic uncertainties derived for taus at ATLAS, the first measurement of the $Z \to \tau\tau$ cross section, and the first limit on high-mass resonances decaying to $\tau^+\tau^-$ with ATLAS data. Tau leptons play an important role in the physics program of ATLAS because they can have preferred couplings to new physics such as searches for the Higgs boson ($H \to \tau\tau$) and new resonances ($Z' \to \tau\tau$).

First in Chapter 2, I briefly describe the SM and introduce many of the reasons to be interested in searches for physics beyond the SM at the LHC. That chapter is suppported by Appendix A, where I give a brief review of some of the founding literature in quantum mechanics and the formation of the SM. Chapter 3 briefly describes the LHC, the ATLAS detector, and its computing and reconstruction. Chapter 4 outlines how tau reconstruction and identification work at ATLAS and reviews many of its advancements in the years 2010–2012. Chapter 5 summarizes the first ATLAS $Z \to \tau\tau$ cross section measurement, and Chapter 6 summarizes the first ATLAS search for high-mass resonances decaying to $\tau^+\tau^-$.

Chapter 2

The theoretical situation

This chapter introduces the Standard Model of particle physics, including a brief review of the discovery of a Higgs-like particle at the LHC in the summer of 2012. Then it discusses how our understanding of particle physics is incomplete and that there are several scenarios for physics beyond the Standard Model.

2.1 Introduction

The Standard Model (SM) of particle physics is our best model of fundamental physics, describing the quantum behavior of three of the fundamental forces: electromagnetic, weak, and strong, but not the weakest force: gravity. It is at the same time very simple, very rich phenomenologically, very deep, and very ad hoc. The discovery of a new particle at the LHC in 2012, so far consistent with the SM Higgs boson, brings the initial signs of a warranted confirmation of the ideas behind electroweak symmetry breaking in the SM. However, this still leaves several questions unanswered as to why the SM is the way it is. Finding answers to, or a better understanding of, these questions that concern the fundamental nature of our universe is the motivation of high-energy physics research programs world-wide.

2.2 The Standard Model

The SM is the culmination of several incremental discoveries, many of which are reviewed briefly in Appendix A; the structure of the SM is summarized here. The fundamental ingredients of the SM are a set of Dirac fermion fields in certain multiplet representations of a particular gauge group:

$$\mathrm{SU(3)_C} \times \mathrm{SU(2)_L} \times \mathrm{U(1)_Y} \,.$$

Being based on a type of quantum field theory (QFT) called a "Yang-Mills theory" [1], the interactions between the fermions are described by gauge bosons, and the structure of those interactions is determined by gauge invariance described by Lie groups of the type SU(n). For a QFT to have a local gauge invariance requires the existence of gauge boson fields to form a gauge-covariant derivative. In the case of the SM, gauge invariance implies the existence of following gauge boson fields:

$$\begin{array}{ccccc} \mathrm{SU(3)_C} & \times & \mathrm{SU(2)_L} & \times & \mathrm{U(1)_Y} \\ \Downarrow & & \Downarrow & & \Downarrow \\ G^{\alpha}_{\mu} & & W^{a}_{\mu} & & B_{\mu} \\ \alpha \in \{\,1,\,2,\,\ldots,\,8\,\} & & a \in \{\,1,\,2,\,3\,\} & & \end{array}$$

There are 8 gluon fields, G^{α}_{μ}, that describe the strong interactions, while the W^{a}_{μ} and B_{μ} fields together describe the electroweak interactions.

The Higgs mechanism demonstrates that a QFT with local gauge invariance can have massive gauge bosons if the gauge symmetry is spontaneously broken by the non-zero value of a scalar Higgs field in the ground state, and was developed independently by three groups: Robert Brout and Francois Englert [2]; Peter Higgs [3, 4]; and Gerald Guralnik, Carl R. Hagen, and Tom Kibble [5]. This explains how masses can be generated for gauge bosons and also for chiral fermions, while maintaining the gauge invariance that is fundamental to the theory but would otherwise exclude such masses.

The gauge structure of the electroweak model was proposed by Sheldon Glashow [6], Steven Weinberg [7], and Abdus Salam [8, 9, 10] in the 1960s. The $\mathrm{SU(2)_L \times U(1)_Y}$ part of the gauge group describing the electroweak interactions is spontaneously broken by the Higgs mechanism with the following breaking pattern:

$$\mathrm{SU(2)_L \times U(1)_Y} \;\rightarrow\; \mathrm{U(1)_{EM}} \;.$$

In the low-energy vacuum, the W^{a}_{μ} and B_{μ} fields mix to form the $W^{\pm}$ and Z fields of the massive gauge bosons mediating the weak force. The remaining $\mathrm{U(1)_{EM}}$ gauge invariance corresponds to an orthogonal mixing that gives a massless gauge boson, A_{μ}, which is the photon mediating the electromagnetic force.

In the 1970s, the SU(3) theory of quantum chromodynamics (QCD) was developed, describing the strong interactions that bind quarks into hadrons and bind the nuclei of atoms. Soon after, the demonstration of asymptotic freedom in the strong interactions by Politzer, Gross, and Wilczek [11, 12, 13, 14] showed that QCD has a perturbative regime because the strong interactions get weaker at higher energies. The combination of the GWS electroweak theory and QCD [15] has become known as the "Standard Model" of particle physics.

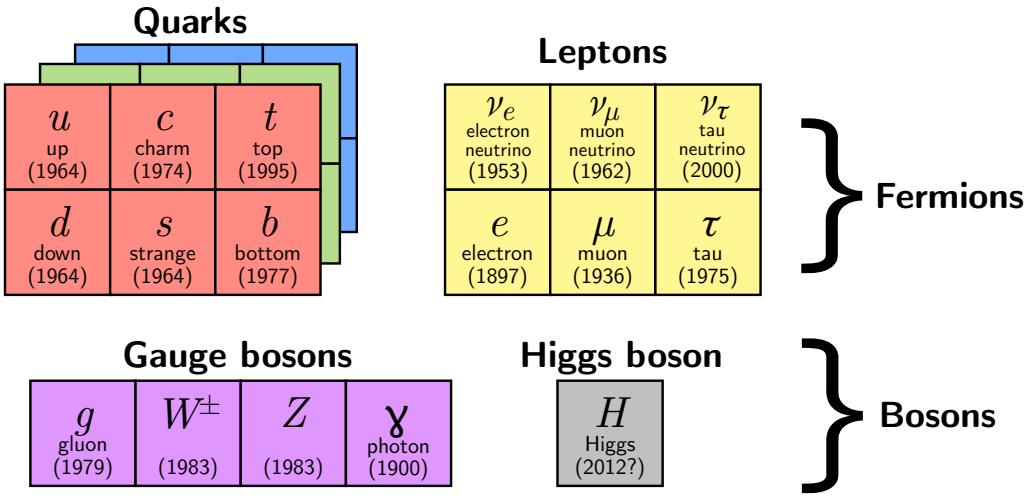

Figure 2.1: An illustration of the field content of the Standard Model. The numbers in parentheses denote the year the particle for that field was discovered. Note that the fermions are only grouped into doublets for their left-chiral parts. The right-chiral parts are $\mathrm{SU}(2)_\mathrm{L}$ singlets. The structure of the gauge group representations is shown in more detail in Figure A.3 in Appendix A.

The SM fermions come in two categories: quarks, which participate in the strong interactions as SU(3) color triplets, and the leptons, which, being color singlets, do not participate in the strong interactions. The fermion fields form chiral representations of the $\mathrm{SU}(2)_\mathrm{L}$ symmetry. The left-chiral parts of the fermions form doublet representations, and the right-chiral parts of the fermions are SU(2) singlets. The field content of the Standard Model is summarized in Figure 2.1.

2.3 The search for the Higgs boson

2.3.1 Before the start-up of the LHC

Several generations of colliders and fixed-target experiments have contributed to the experimental support for the SM and for searching for new physics, each successively climbing in energy to gain sensitivity to physics at higher energy scales. Figure 2.2 shows a plot the effective energy of collisions probed if it were a fixed-target experiment as a function of the time the experiment began taking data.

By the year 2000, LEP had reached its highest energy of $\sqrt{s} = 209$ GeV, and combined searches of the LEP experiments excluded a SM Higgs with a mass less than 114 GeV in 2003 [17]. Figure 2.3 (left) shows the upper limit on the ratio of the coupling for Higgs decays through $H \to ZZ^*$ compared to the SM as a function of the Higgs mass.

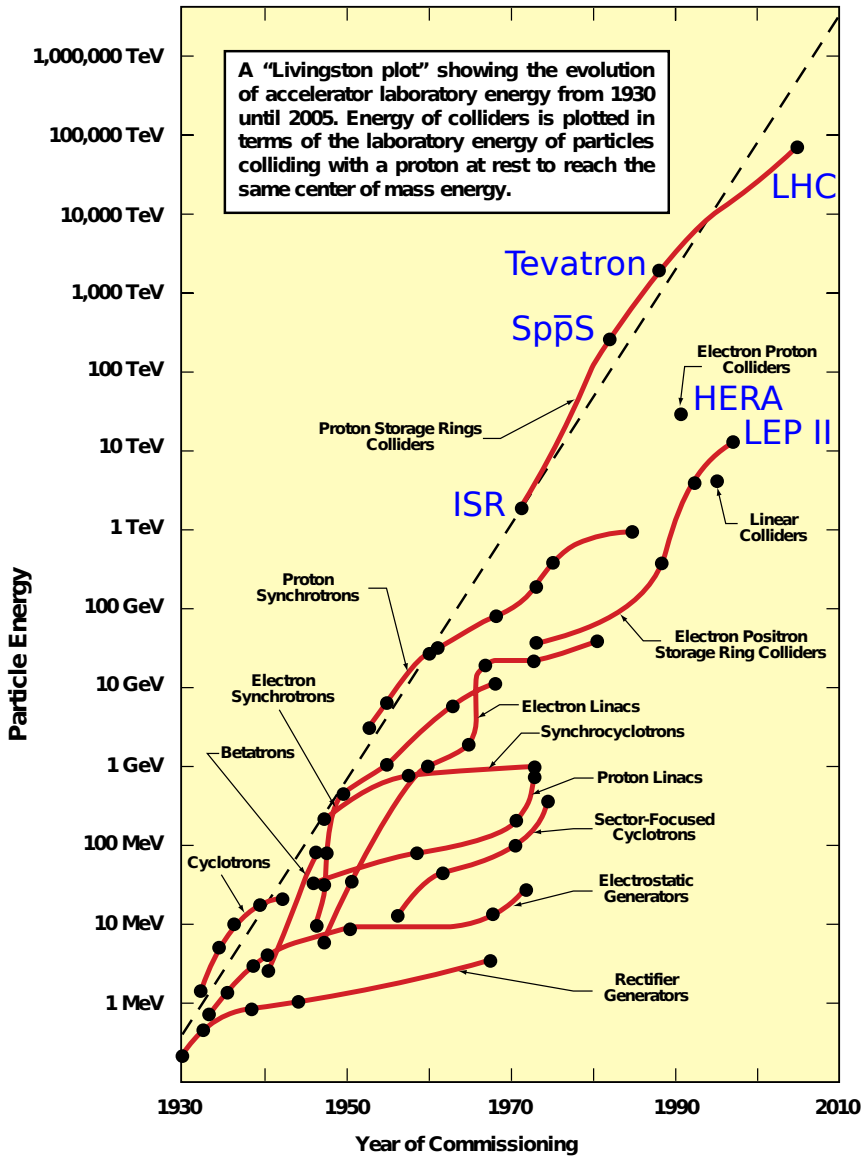

Figure 2.2: The "Livingston plot", showing the effective energy of collisions probed for various collider and fixed-target particle experiments as if they were each fixed-target experiments, as a function of the time the experiment began taking data [16].

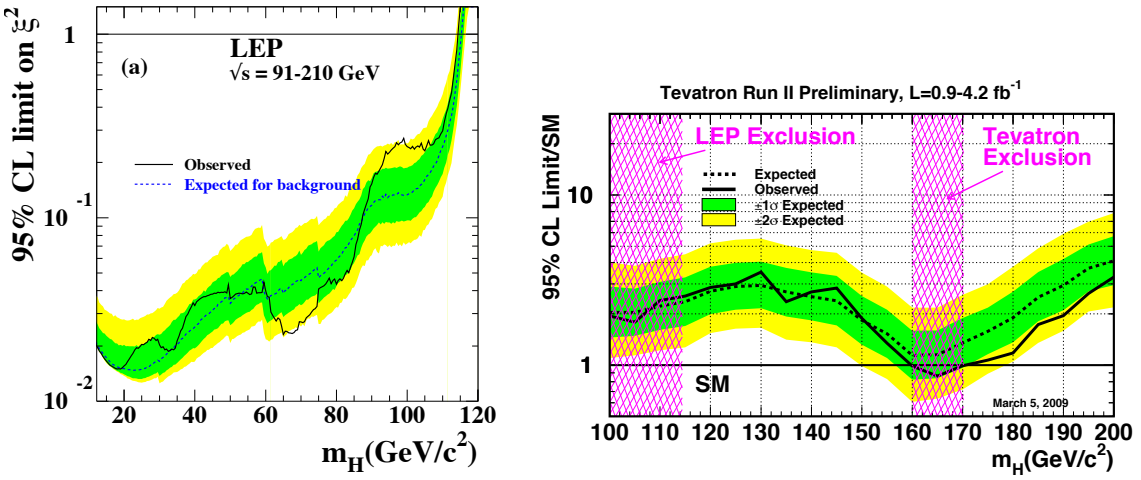

Figure 2.3: (left) The 95% CL upper limit on the coupling for Higgs production at LEP, $\xi^2 = (g_{HZZ}/g^{\mathrm{SM}}_{HZZ})^2$, as a function of the Higgs mass [17]. (right) The 95% CL upper limit on the signal strength for the SM Higgs boson as a function of its mass [19].

Then the Tevatron took the lead in searching for the Higgs boson. In 2009, before the the start-up of the LHC, the CDF and DØ experiments at the Tevatron had collected 4 fb^{-1} and excluded a SM Higgs boson in the mass range of 160–170 GeV at 95% CL. Figure 2.3 (right) shows the excluded signal strength (the ratio of the rate of Higgs production to that expected in the SM) as a function of the Higgs mass, also showing the LEP limit at low mass[1].

Indirect constraints on the Higgs mass were also made, in addition to the theoretical constraints discussed in Section 2.4.3. Assuming the SM Higgs boson exists, it contributes to virtual corrections to several EW observables, most notably through loop diagrams that contribute to the Higgs and W boson propagators that are sensitivite to the W and top quark masses. Precision measurements of the W and top quark masses, among other observables measured at LEP and the Tevatron, were combined by the LEP EW Working Group to test which Higgs mass is most preferred by the data. Figure 2.4 shows the result of the combined fit to the Tevatron and LEP results in 2009, resulting in a best fit of $m_H = 87^{+35}_{-26}$ GeV, equivalent to an upper limit of $m_H < 157$ GeV at 95% CL. Interestingly, this shows a preferrence for a low-mass Higgs with a best fit mass below that excluded by LEP, but still consistent with $m_H \approx 115$–160 GeV.

[1] Later in 2010, the Tevatron extended its analysis with the entire Tevatron dataset of 10 fb^{-1}, extending the mass range excluded to 147–180 GeV, and reporting a compeling excess in the unexcluded lower-mass region at $m_H \approx 120$–130 GeV, corresponding to a local significance of 3.0 standard deviations (σ) for the background only hypothesis [18].

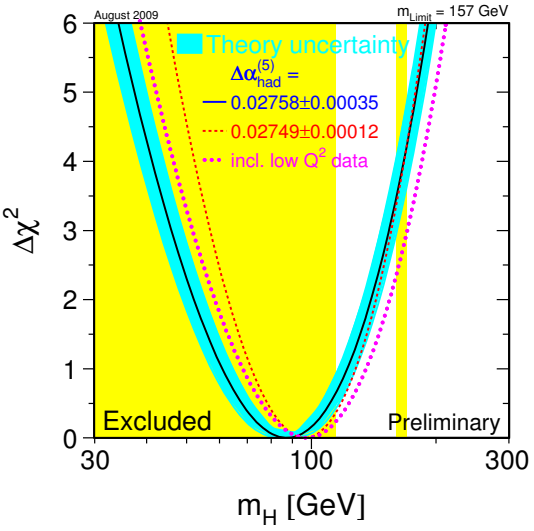

Figure 2.4: The distribution of the $\Delta\chi^2 = \chi^2 - \chi^2_{\rm min}$ as a function of the SM Higgs mass, m_H, for the combined LEP-Tevatron EW fit. The blue band illustrates the theoretical uncertainty due to missing higher order corrections. The yellow vertical bands show the m_H regions excluded by LEP-II (up 114 GeV) and the Tevatron (160–170 GeV), as of August 2009. The best-fit result is $m_H = 87^{+35}_{-26}$ GeV, equivalent to an upper limit of $m_H < 157$ GeV at 95% CL [20].

2.3.2 Observations of a Higgs-like excess at the LHC

With the 4.8 fb^{-1} of integrated luminosity at $\sqrt{s} = 7$ TeV collected in 2011, both ATLAS [21] and CMS [22] reported excesses which were compatible with SM Higgs boson production and decay in the mass range 124–126 GeV, with significances of 2.9 and 3.1 standard deviations (σ), respectively.

By the summer of 2012, the LHC had delivered about 5.8 fb^{-1} of integrated luminosity at $\sqrt{s} =$ 8 TeV. Combining results from searches for the Higgs boson with both the 2011 and 2012 datasets, on July 4, 2012, the ATLAS [23] and CMS [24] experiments independently announced discovery of a new particle consistent with a SM Higgs boson with $m_H \approx 125$ GeV, with significances of 5.9 and 5.8 σ, respectively.

Through the Yukawa couplings and the EW interactions, the SM Higgs has many ways it can decay, especially within the preferred Higgs mass range $m_H \approx 115$–160 GeV. Figure 2.5 (left) shows

Table 2.1: The approximate branching ratios for the decays of the SM Higgs boson with $m_H = 125$ GeV [27].

channel:	bb	WW^*	$\tau\tau$	ZZ^*	$\gamma\gamma$
branching ratio [%]:	58	22	6.3	2.6	0.23

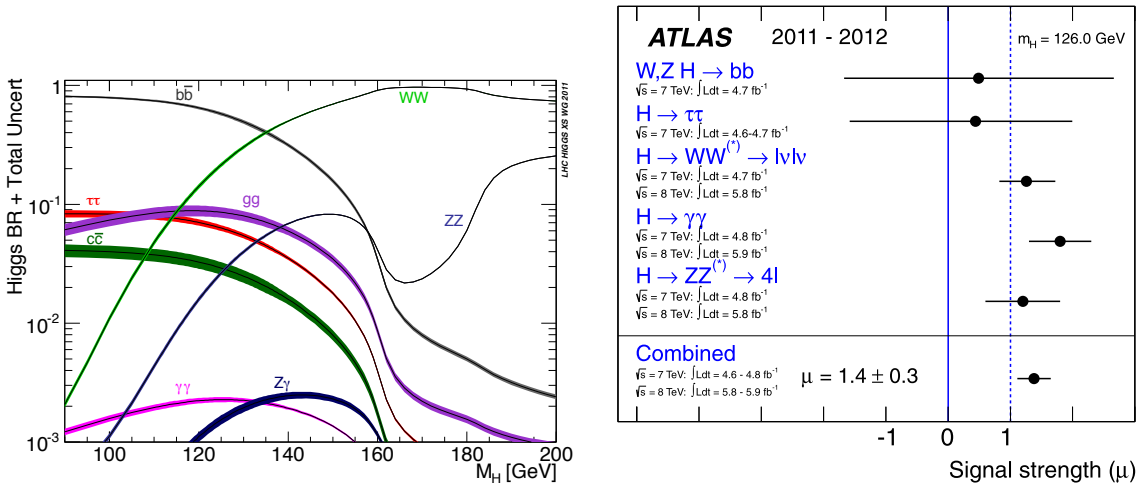

Figure 2.5: (left) The branching ratios the SM Higgs decays with estimated theoretically uncertainties shown by the bands [25, 26]. (right) Measurements of the signal strength parameter μ for $m_H = 126$ GeV for the individual channel and their combinatio [23].

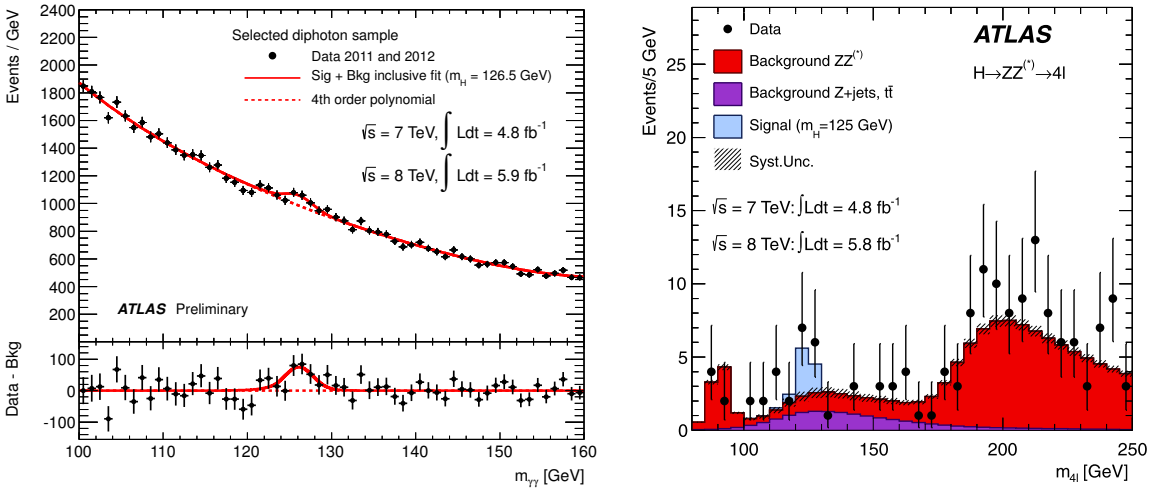

Figure 2.6: The distributions of the reconstructed m_H invariant mass of $H \to \gamma\gamma$ [28] (left) and $H \to ZZ^* \to 4\ell$ [23] (right) candidates after all selections for the combined 7 TeV (2011) and 8 TeV (2012) data sample.

a plot of the Higgs branching fractions as a function of the Higgs mass. Both the ATLAS and CMS experiments search for the Higgs boson in $H \to \gamma\gamma$, ZZ^*, WW^*, $\tau\tau$, and $b\bar{b}$ decays. Table 2.1 highlights the approximate branching fractions for a SM Higgs with $m_H = 125$ GeV.

The significance of the excesses reported in the July 2012 observation is dominated by the $H \to \gamma\gamma$, $H \to ZZ^* \to 4\ell$, and $H \to WW^* \to \ell\nu\ell\nu$ searches. The $H \to \gamma\gamma$ and $H \to ZZ^* \to 4\ell$ channels fully reconstruct the decay products of the Higgs boson and have mass resolutions better

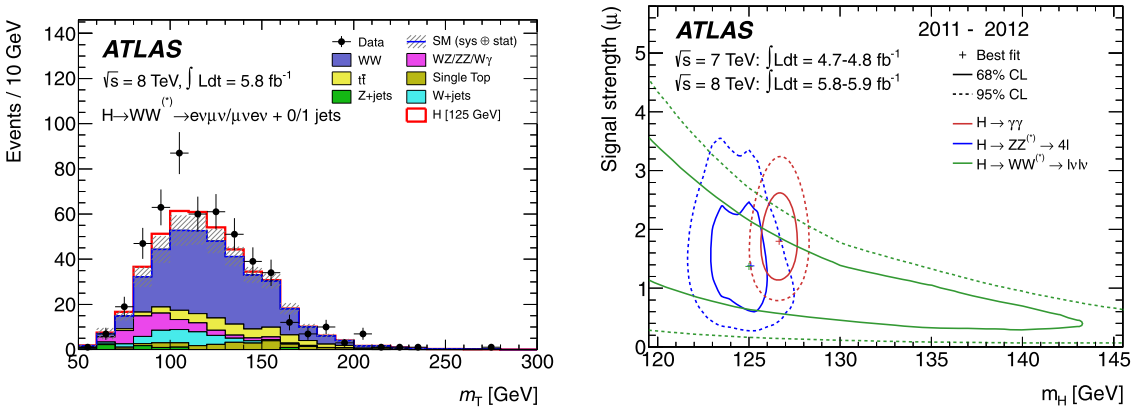

Figure 2.7: (left) The distribution of the transverse mass of the dilepton system and the missing transverse momentum, m_{T}, in the 0-jet and 1-jet channels of the $H \to WW^* \to e\mu$ search for events satisfying all selection criteria [23]. (right) Confidence intervals in the (μ, m_H) plane for the $H \to \gamma\gamma$, $H \to ZZ^* \to 4\ell$, and $H \to WW^* \to \ell\nu\ell\nu$ channels, including all systematic uncertainties. The markers indicate the maximum likelihood estimates.

than a percent. Figure 2.6 shows the reconstructed Higgs mass distributions for the $H \to \gamma\gamma$ and $H \to ZZ^* \to 4\ell$ searches. The $H \to WW^* \to \ell\nu\ell\nu$ channel has good sensitivity to the SM Higgs but a poor mass resolution because of the production of neutrinos. The distribution of the transverse mass of the dilepton system and the missing transverse momentum of the selected events in the $H \to WW^* \to e\nu\mu\nu$ channel with the 2012 data is shown in Figure 2.7 (left). Using only the 2012 data and only the $H \to \gamma\gamma$, $H \to ZZ^* \to 4\ell$, and $H \to WW^* \to e\nu\mu\nu$ channels, the combined local significance is 4.9 σ at $m_H = 126.5$ GeV [23].

The ATLAS $H \to \gamma\gamma$ and $H \to ZZ^* \to 4\ell$ channels, having precise mass resolution, are combined to measure the mass of the excess, giving a best-fit mass of $m_H = 126.0 \pm 0.4\,(\mathrm{stat}) \pm 0.4\,(\mathrm{sys})$ GeV. The best-fit signal strength for a SM Higgs with $m_H = 126$, combining all channels ($\gamma\gamma$, ZZ^*, WW^*, $\tau\tau$, and $b\bar{b}$) is $\hat{\mu} = 1.4 \pm 1.3$ [23]. Figure 2.5 (right) shows the estimated μ in each channel and the combination. Likelihood contours for 68% and 95% CL in the μ vs m_H plane are shown in Figure 2.7 (right).

The searches for $H \to \tau\tau$ [29] and $H \to b\bar{b}$ [30] at ATLAS are approaching sensitivity to the SM Higgs, having currently reported observed (expected) 95% CL upper limits on the signal strength[2], μ, of 1.9 (1.2) and 1.8 (1.9) , respectively, for $m_H = 125$ GeV. Both analyses are being updated with the total 21 fb^{-1} collected in 2012.

[2] The signal strength is the ratio of the rate of Higgs production to that expected in the SM.

2.4 Limitations of the Standard Model

2.4.1 Neutrino masses and mixing

In the SM, neutrinos are massless since there are no right-chiral parts for neutrino fields (or left-chiral parts for anti-neutrinos). Incorporating neutrino masses within the SM is theoretically possible in at least a few ways, but not currently resolved. In 1998, the Super Kamiokande experiment published the first[3] evidence of neutrino oscillations in atmospheric neutrinos [31]. In 2001, the Sudbury Neutrino Observatory provided conclusive evidence of oscillation in solar neutrinos [32]. Neutrino oscillation requires that the weak eigenstates of neutrinos be a mix of mass eigenstates with different masses. Therefore, it is now well-accepted that the neutrino mass eigenstates have small ($\lesssim 1$ eV) but non-zero masses. Recently, there has been significant progress in measuring the mass differences and mixing parameters of the neutrino sector. Its structure, however, is not completely determined, including the issue of whether neutrinos are Dirac fermions like the rest of the fermions of the SM, or whether they are Majorana fermions, which are identical to their anti-particles.

2.4.2 Ad hoc features

The SM has many features that are arguably ad hoc, and a more fundamental theory or mechanism that could explain or motivate these features would be preferred. First, the particular direct product of gauge groups, $\mathrm{SU(3)_C} \times \mathrm{SU(2)_L} \times \mathrm{U(1)_Y}$, and the corresponding structure of the fermion representations are arbitrary. Why is the SU(2) part chiral but the SU(3) part non-chiral? How are the hypercharges of quarks and leptons related, resulting in the seemingly exact balance of EM charges among hadrons and leptons? Why are there three generations of fermions for both the leptons and quarks? The SM requires the values of 19 independent parameters[4] be given, with an additional 7–9 parameters depending on the type of neutrino sector. It is also worth noting that the implementation of the Higgs mechanism in the SM is done minimally, but there could be more than one type of Higgs field in more complicated representations than the simple SM Higgs doublet [33].

2.4.3 The hierarchy problem(s)

Within the SM, there are several instances of vastly differing scales for the values of parameters in the theory that are seen as problematic or unnatural. This is often referred to as the "hierarchy

[3] Neutrino oscillation has been considered since the 1950s. The first evidence of solar neutrino oscillation dates back to the experiments of Ray Davis Jr. in the 1960s, sparking the Solar Neutrino Problem, but was not seen to be conclusive until the experiments of SNO and others around the beginning of the 21$^{\text{st}}$ century. See the discussion of neutrino oscillation in Appendix A.2.7.

[4] The 19 SM parameters are: 6 quark masses, 3 charged lepton masses, 3 gauge couplings (g_1, g_2, g_3), 2 Higgs parameters (μ^2, λ), 4 CKM parameters, and θ_{QCD}.

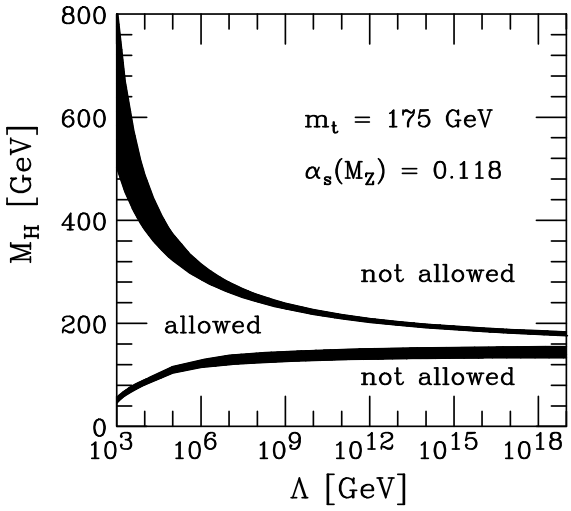

Figure 2.8: The triviality upper bound and vacuum stability lower bound on the SM Higgs boson mass vs the cut-off scale, Λ, where new physics is required to keep the theory consistent [34].

problem".

First, as the only fundamental scalar in the SM, the mass of the Higgs boson has exceptionally large quantum corrections from loop diagrams that tend to drive it much higher than the electroweak scale. For theoretical reasons, the mass of the Higgs boson cannot be too large ($\lesssim 1$ TeV) due to the *unitarity* bound to keep longitudinal WW and ZZ scattering processes from diverging at high energies, and the *triviality* bound that requires that the Higgs self-coupling, λ, not diverge when it is renormalized at higher energies. Similarly, the Higgs mass is also bounded from below by requiring that $\lambda > 0$ for the Higgs potential to have a stable minimum for vacuum stability [34]. Figure 2.8 summarizes these theoretical bounds on the Higgs mass as a function of the scale where new physics would be required to keep the theory consistent. Even within the region of Higgs masses theoretically allowed, there must be a delicate cancellation of the quantum corrections to keep the Higgs mass from being driven much higher, unless one introduces new physics at higher mass scales [35, 33].

Another way of phrasing the hierarchy problem is: why is the electroweak scale (set by the Higgs) so much smaller than the Planck mass, $m_{\rm P} \approx 1 \times 10^{19}$ GeV, the scale where gravity becomes important to quantum effects? Or, why is gravity so much weaker than the other forces?

Other forms of hierarchy problems exist in the SM, including the issue of why do the fermion masses (or equivalently the Yukawa couplings) range over so many orders of magnitude? The quark masses range over 5 orders of magnitude, while the lepton masses range over at least 9 due to the exceptionally small masses of the neutrinos[5].

[5] The range of fermion masses is illustrated in Figure A.4 of Appendix A.2.5.

2.4.4 Matter-antimatter asymmetry

One of the mysteries in particle physics concerns explaining the abundance of matter in the universe when the laws of physics seem virtually symmetric for matter and anti-matter. The Sakharov conditions [36] enumerate the requirements for an excess of matter to survive annihilation in the development of the very early universe. They require that baryon number, C-symmetry, and CP-symmetry be violated in interactions out of thermal equilibrium such that baryons are generated at a higher rate than anti-baryons during a process called *baryogenesis*. The known sources of CP violation in the SM are currently thought to be too small to account for the excess of matter, but many extensions to the SM have the potential to bring new sources of CP violation that could help explain it.

2.4.5 Dark matter and dark energy

Several astronomical observations including the rotational speeds of galaxies, instances of gravitational lensing, and detailed measurements of the Cosmic Microwave Background (CMB), suggest that there is much more matter in the universe than can be explained by the normal baryonic matter of the SM. *Dark matter* refers to this unexplained part of matter that must not interact electromagnetically or strongly, but still gathers together gravitationally with the normal matter in galaxies. The latest measurements of the CMB by the Planck satellite estimate the total energy content of the visible universe to be about 5% ordinary matter, 27% dark matter, and 68% dark energy. Therefore, dark matter is estimated to constitute about 85% of the total matter in the universe [37]. *Dark energy* is another unexplained component of the universe that hypothetically permeates empty space and drives the current accelerated expansion of the universe. It is hoped that some of this mystery could be resolved if particle experiments discover new weakly interacting stable particles that could be candidates for what constitutes the dark matter.

2.5 Scenarios beyond the Standard Model

2.5.1 Supersymmetry

Supersymmetry (SUSY) is a natural extension of the Standard Model that introduces a symmetry relating fermions and bosons. Under reasonable assumptions, it is the *unique* extension to the usual Poincaré and internal symmetries of a relativistic quantum field theory, as demonstrated by the Haag-Lopuszanski-Sohnius[6] theorem [38]. In some SUSY models, there is a Lightest Supersymmetric Particle (LSP) that must be stable to conserve the R-parity quantum number. The LSP is

[6] See the discussion in Appendix A.1.4.

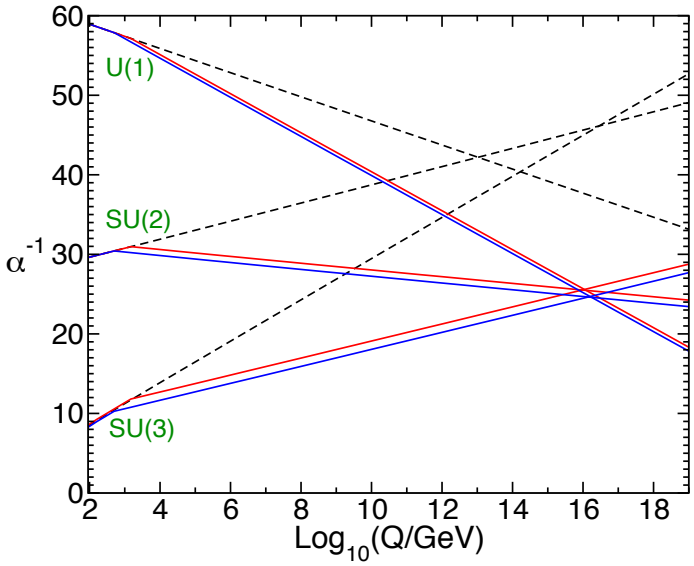

Figure 2.9: Two-loop renormalization group evolution of the inverse gauge couplings $\alpha^{-1}(Q)$ in the Standard Model (dashed lines) and the Minimal Supersymmetric Standard Model (MSSM, solid lines). In the MSSM case, the sparticle masses are treated as a common threshold varied between 500 GeV (blue) and 1.5 TeV (red) [39].

presumably only weakly interacting. It therefore would go undetected directly, but may result in events with significant missing energy in addition to the jets and/or leptons produced in the cascade of a SUSY decay. If such stable weakly interacting SUSY particles exist, they could explain the prevalence of dark matter.

2.5.2 Running of the couplings

Renormalization is a process by which the bare couplings of a QFT accumulate higher-order quantum corrections, from which relationships can be derived that describe how the effective physical couplings of the theory scale with the energy of an interaction, called the "renormalization group equations". By 1991, the experiments at the Large Electron Positron Collider (LEP) at CERN had measured the three gauge couplings of the SM with sufficient precision such that one could calculate how the couplings hypothetically scale at higher energies [40, 41] as shown in Figure 2.9. The horizontal axis shows the energy scale, Q, of an interaction and is plotted on a logarithmic scale because the couplings run slowly as logarithms of the energy. The renormalization group equations that determine the slopes of the running of the couplings depend on the particle content of the theory. The dotted lines show the strength of the couplings extrapolated to higher energies assuming only the particle content of the SM. The converging of the couplings at high energies is thought by many to possibly indicate a unification of the forces of the SM in scenarios called "grand unified theories".

With the precision of the measurements of the couplings from LEP, gauge coupling unification is actually ruled out in the SM since the dotted lines do not converge to a single coupling strength. Remarkably, if one extends the of the Standard Model with SUSY, then the renormalization group equations have to be modified to account for these additional particles, and a unification seems possible at a very high mass scale, $M_{\mathrm{GUT}} \sim 10^{16}$ GeV, as indicated by the extrapolation of the solid lines. Moreover, the unification prefers the masses of the SUSY partners to be near the TeV scale, and possibly within the reach of the experiments at the LHC [42, 43, 44, 45]. It should be noted though, that this extrapolation to the scale of M_{GUT} is many orders of magnitude above the energies that can currently be probed at collider experiments. New experimental clues are necessary to know the spectrum of particles at higher energies (with or without SUSY), which is one of the primary motivations to search for new physics at the energy frontier.

2.5.3 Grand unified theories

Grand unified theories (GUTs) refer to gauge field theories that unify the strong, weak, and electromagnetic interactions of the SM by describing them with a single simple gauge group. They combine both the quarks and leptons into larger multiplet representations of the complete symmetry group, and assume that the gauge group of the SM is the result of a larger symmetry breaking process than just electroweak symmetry breaking. Grand unified theories have the potential to explain many of the ad hoc features of the SM, including the structure of the representations and relations among the hypercharges of quarks and leptons.

The first grand unified theories developed in the 1970s are the Pati-Salam model [46] based on $\mathrm{SU}(4)_{\mathrm{C}} \times \mathrm{SU}(2)_{\mathrm{L}} \times \mathrm{SU}(2)_{\mathrm{R}}$, and the SU(5) model of Georgi and Glashow [47, 48]. Both of these models can be spontaneously broken to give the gauge group of the SM, along with direct products of additional SU(2) and/or U(1) symmetries that imply the existence of new heavy gauge bosons, often denoted W' and Z', respectively [33]. Both the Pati-Salam and Georgi-Glashow models can be further embedded in larger groups, such as Spin(10), the breaking patterns of which have been studied in detail [49, 50]. These larger gauge groups can also result from string theories and predict the existence of heavy Z' bosons [51, 52, 53]. A search for Z' bosons decaying to tau leptons at ATLAS is the topic of Chapter 6.

Clearly this is an exciting time for particle physics. The discovery of a new particle, so far consistent with the Higgs boson, is a fantastic confirmation for the Standard Model. However, ATLAS and CMS are only just beginning to constrain its parameters and measuring the properties of the Higgs will continue to be a driving topic in the future runs of the LHC. There are also

many interesting reasons to look for new physics at the TeV scale, to try to resolve the issues of whether nature has more (broken) gauge-symmetries, whether nature is supersymmetric, and what constitutes the dark matter, among others.

Chapter 3

The LHC and ATLAS

This chapter introduces the the Large Hadron Collider and the ATLAS experiment, including brief discussions of the ATLAS reconstruction, triggering, running conditions, simulation, and computing infrastructure.

3.1 The Large Hadron Collider

The Large Hadron Collider (LHC) is currently the highest-energy particle collider in the world. The LHC is a discovery machine. Its purpose is to push the frontier of experimental high-energy particle collisions in both energy and luminosity. It enables experiments observing the collision products to test the agreement of the SM at higher energies than previous probed and to search for new physics, including hypothetical particles too massive or too weakly interacting to have been produced at previous generations of colliders. Analyses of data from the LHC have unprecedented potential to measure the properties of the Higgs boson and possibly to discover evidence for physics beyond the Standard Model, such as supersymmetry or evidence for grand unified theories.

To probe the physics of the electroweak scale and beyond requires high-energy collisions. Figure 3.1 shows the production cross section for several processes of interest at hadron colliders. Note that the rate for electroweak physics processes including W, Z, and Higgs boson production, grows significantly with the center-of-momentum energy, $\sqrt{s}$. From 2010–2012 the LHC collided protons with protons at a center-of-momentum energy[7] of 7–8 TeV and with a peak luminosity of the order of 10^{32}–10^{33} cm^{-2} s^{-1}.

The LHC is located near and operated by the European Organization for Nuclear Research (CERN) laboratory, outside Geneva, Switzerland. It is situated inside a ring-shaped tunnel, ap-

[7] The Superconducting Super Collider (SSC) that was to be built near Dallas, TX in the 1990s would have created even more energetic proton-proton collisions, designed with $\sqrt{s} = 40$ TeV, but it was cancelled by the US Congress in 1993 because its budget was not supported [56, 57].

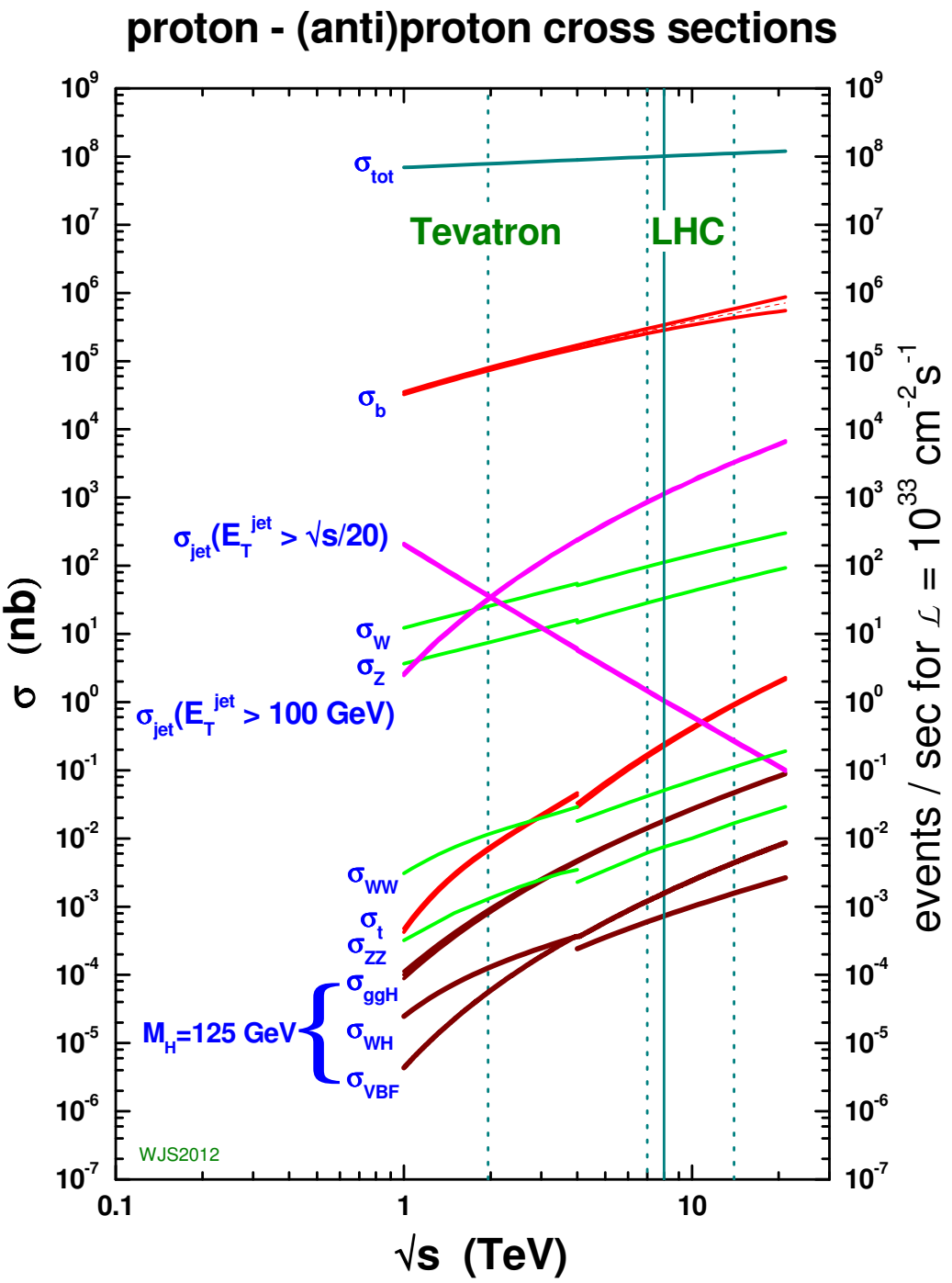

Figure 3.1: Production cross sections from proton-(anti)proton collisions for several processes of interest as a function of center-of-momentum energy, $\sqrt{s}$. The discontinuity at ≈ 4 TeV is from the difference in $p\bar{p}$ cross sections on the left for the Tevatron, and pp cross sections on the right for the LHC. The vertical lines indicate the center-of-momentum energy for the Tevatron at 1.96 TeV (2001-2011), for the LHC at 7 TeV (2010-2011) and 8 TeV (2012) and 13 TeV (target for future 2015 run) [54, 55].

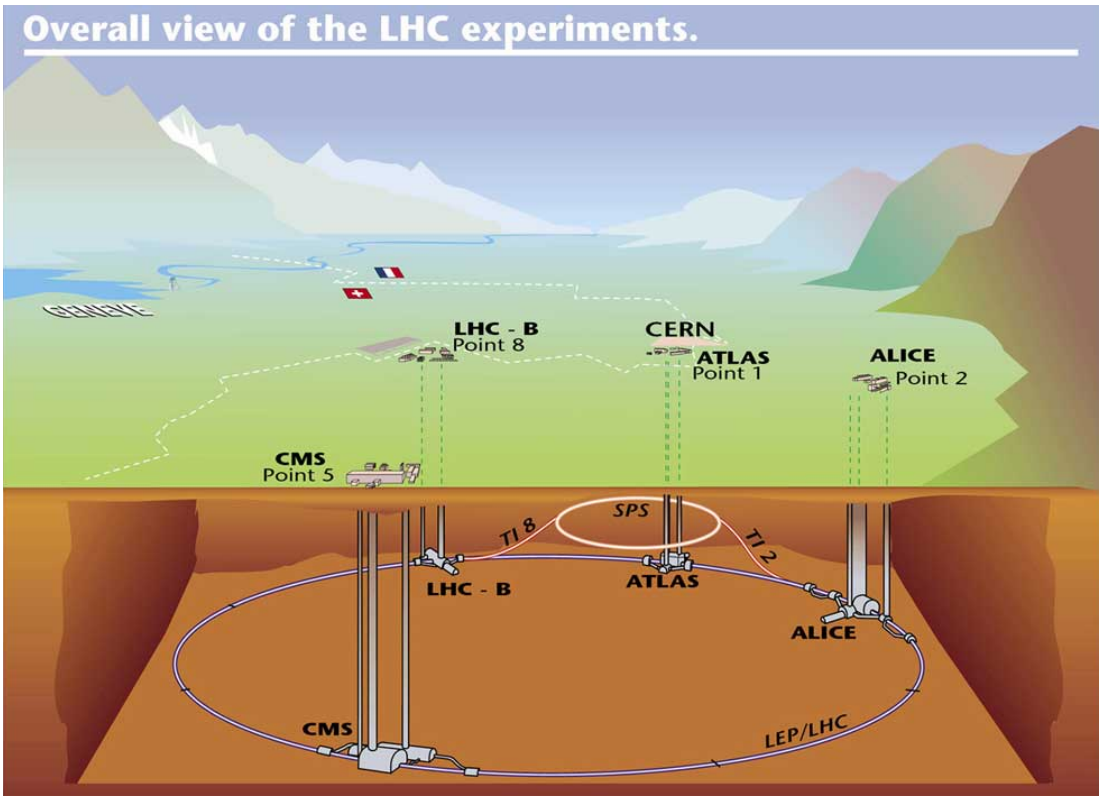

Figure 3.2: An illustration of the location of the LHC, facing south between the Alps and Jura mountain chains on the left and right respectively. The vertical dimension is exaggerated since the LHC is about 100 m underground and 27 km in circumference or 9 km in diameter [58].

proximately 100 m underground and 27 km (17 miles) in circumference, crossing the French-Swiss border four times. The same tunnel was used by the Large Electron-Positron Collider (LEP) from the years 1989 to 2000 (see Figure 3.2).

The LHC and its experiments are technologically exceptional, pushing the boundaries of engineering complexity and scale in many ways. For example, approximately 100 metric tons of liquid helium are needed to cool the superconducting magnets in LHC to 1.9 K (-271.3°C), making the LHC the largest cryogenic facility in the world at liquid helium temperature [59]. To process the data produced from the experiments at the LHC requires one of the largest world-wide distributed computing grids[8] ever assembled, storing over 100 petabytes (1 PB = 10^{15} bytes = 10^{6} GB). Finally, the experiments at the LHC are each massive technological undertakings, some with collaborations of scientists and engineers numbering in the thousands.

There are four primary experiments at the LHC, each at a different point around the ring where

[8] The LHC computing grid is discussed more in Section 3.7.1. The same pressures to organize and share information previously led CERN to develop the World Wide Web in the early 1990s [60, 61].

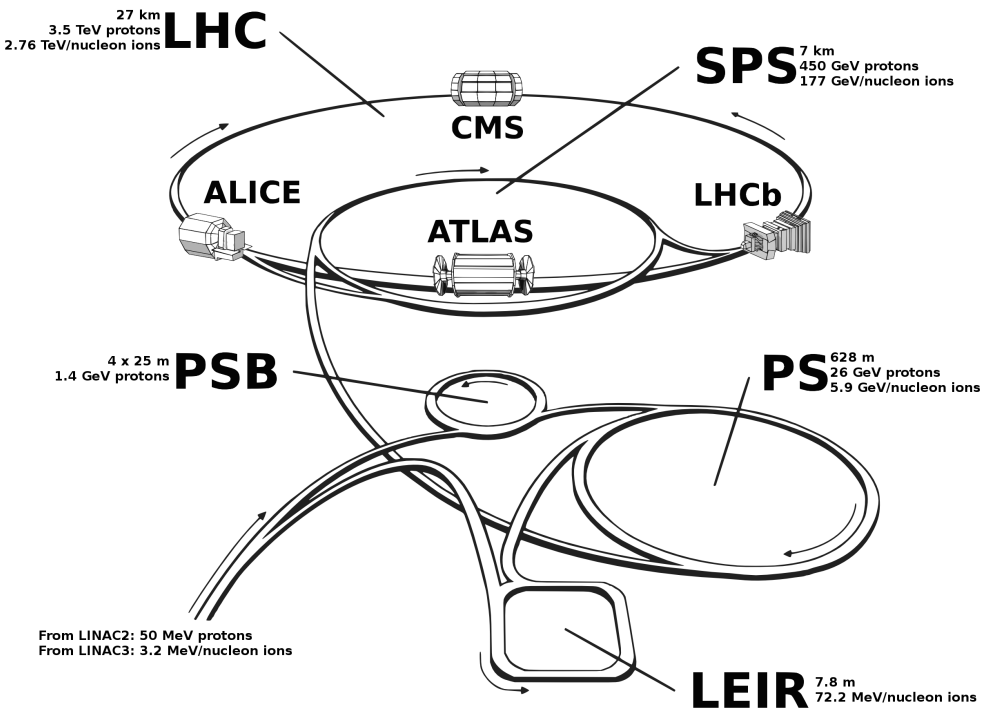

Figure 3.3: The CERN accelerator complex for the LHC [62, 63].

the proton beams collide: ATLAS, CMS, ALICE, and LHCb. All four are designed to explore high-energy phenomena in the SM and to look for new physics. ATLAS and CMS are general purpose high-energy physics experiments. ALICE specializes in heavy-ion collision runs that happen for about a month per year of LHC operation. LHCb is optimized to study the physics of B meson decays. Each of these experiments have predecessors from previous generations of colliders, like the Tevatron, but they are now the flagship experiments in their sub-fields.

The LHC is supported by the CERN accelerator complex to supply it with high-energy proton beams (see Figure 3.3). First, proton beams with an energy of 50 MeV per proton are provided by a linear accelerator, LINAC2, and passed through the Proton Synchrotron Booster (PSB) which raises the energy to 1.4 GeV. The beams are collected in the Proton Synchrotron (PS) where they are split into bunches of $\sim 10^{11}$ protons and accelerated to 25 GeV per proton. Then, the PS feeds the bunches to the Super Proton Synchrotron (SPS), in 3–4 batches of 72 bunches each. The SPS accelerates the beam to 450 GeV per proton and injects the beam into the LHC. The entire process can be repeated to fill the total number of bunches in the two independent, oppositely circulating, proton beams in the LHC. There were over a thousand bunches per beam in typical runs[9] in the years 2011 and 2012.

[9] The running conditions of the LHC will be discussed in more detail in Section 3.5.

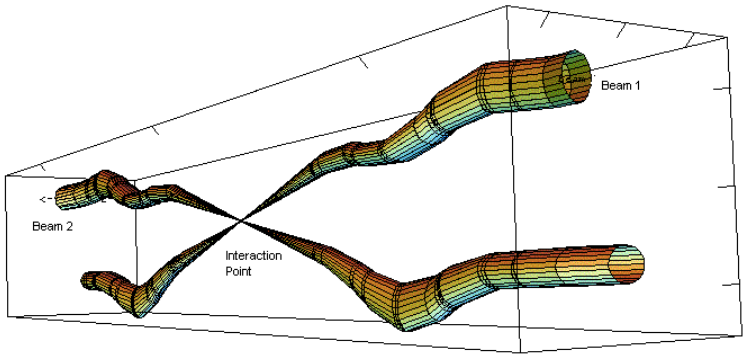

Figure 3.4: An illustration of the relative sizes of the region enveloping the beam at the interaction point in ATLAS [64]. At the point of collisions the beams are squeezed in the transverse plane to be confined in an area of about 0.1 mm × 0.1 mm.

After a complete fill, which usually takes less than 20 minutes, the LHC ramps the beam energy to its maximum of 3.5–4 TeV per proton in the timespan of about another 20 minutes. Then the beams are focused and brought into collision with $\sqrt{s}$ = 7–8 TeV. A run can last 12 hours or more before the beams have dissipated significantly and are safely dumped so that a new fill can be initiated.

In the luminous region where the protons collide, or *beamspot*, the beams are squeezed in the transverse plane to be confined in an area of about 0.1 mm × 0.1 mm (see Figure 3.4). The primary vertices from collisions are distributed[10] in z within about 10 cm, reflecting the approximate length of a bunch along the *beamline*.

Most of the circumference of the LHC consists of the 1232 dipole magnets, each 15 m long with a 8.3 T magnetic field that provides the bending power to keep the beams in the ring. Unlike LEP, which produced e^+e^- collisions with a maximum energy of $\sqrt{s} = 209$ GeV limited by the loss of beam energy due to synchrotron radiation, the LHC is limited by the bending power of the magnets. Table 3.1 summarizes some notable facts about the design of the LHC [62, 66].

[10] During the 2011 run, the typical beamspot where primary vertices were distributed had a width in the transverse plane of about 0.1 mm ($2\,\sigma_x = 2\,\sigma_y$) and about 10 cm long in $\hat{z}$ ($2\,\sigma_z$) [65].

Table 3.1: Some notable facts about the LHC. The LHC beam parameters are shown in more detail in Table 3.4.

27 km circumference	≈ 1000 bunches per beam
1232 dipoles: 15 m, 8.3 T	≈ 10^{11} protons per bunch
100 metric tons liquid He (1.9 K)	bunch spacing: 50 ns
pp collisions at $\sqrt{s}$ = 7–8 TeV	bunch-crossing rate: 20 MHz
instantaneous luminosity: 10^{32}–10^{34}	mean interactions per crossing: 1–40
revolution rate: 11.2 kHz	∼ 0.5 × 10^9 interactions/second

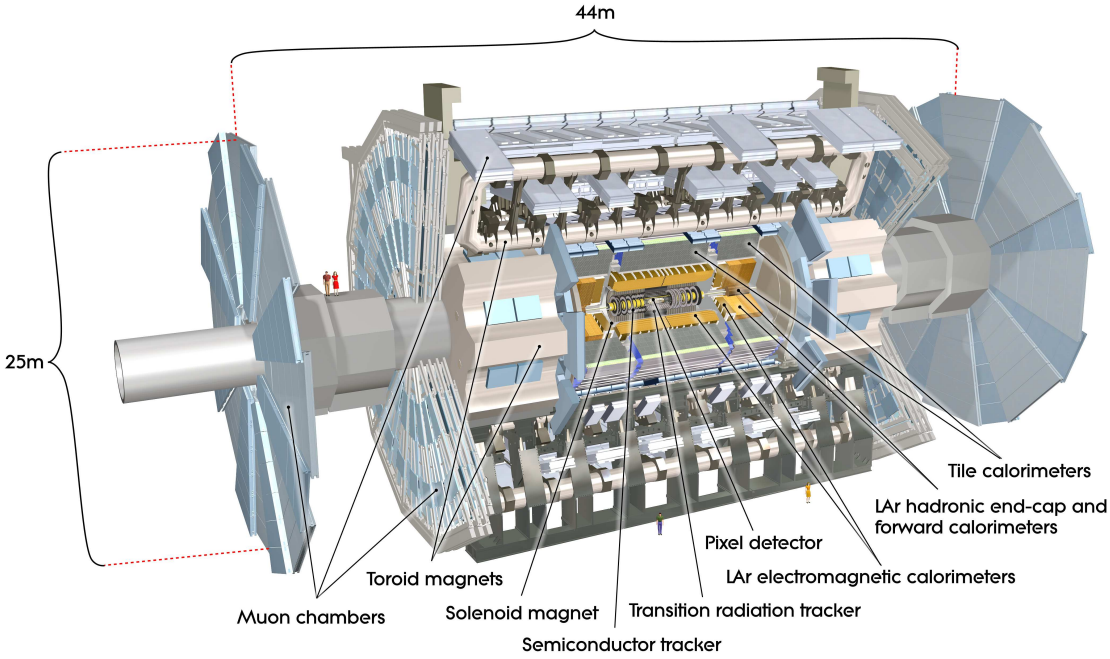

Figure 3.5: An illustration giving an overview of the ATLAS experiment [68].

3.2 The ATLAS experiment

3.2.1 Overview

ATLAS [67, 68, 69] is a multi-purpose experiment inside the Point 1 cavern of the LHC tunnel designed to study a wide range of high-energy physics processes. ATLAS consists of several layers of sub-detectors. Starting from the interaction point and moving outwards[11], there is the inner detector, the electromagnetic and hadronic calorimeters, and finally the muon spectrometer (see Figure 3.5). The collaboration supporting ATLAS has over 2900 members, coming from 177 different universities and laboratories in 38 different countries [70].

3.2.2 Magnet systems

Three types of superconducting magnet systems in ATLAS provide Tesla-level magnetic fields to bend the path of tracks inversely proportional to their momentum to enable tracking reconstruction

[11] The ATLAS coordinate system [68] is a right-handed system with the x-axis pointing to the center of the LHC ring, the y-axis pointing upwards, and the z-axis following the beam line. The spherical coordinates ϕ and θ are defined in the usual way, with the azimuthal angle, ϕ, measuring the angle in the xy-plane from the positive x-axis, increasing towards positive y. The polar angle, θ, measures the angle from the positive z-axis, but this coordinate is often specified by the pseudorapidity, η, defined as $\eta = -\ln(\tan\frac{\theta}{2})$. The transverse momentum p_{T}, the transverse energy E_{T}, and the missing transverse momentum $E_{\mathrm{T}}^{\mathrm{miss}}$; are defined in the x-y plane. The distance ΔR in the η-ϕ space is defined as $\Delta R = \sqrt{\Delta\eta^2 + \Delta\phi^2}$.

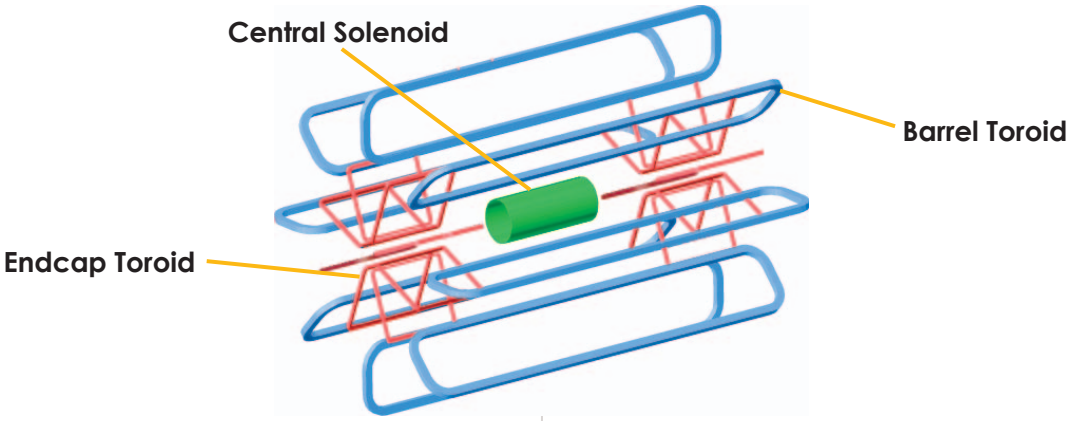

Figure 3.6: An illustration of the ATLAS magnet systems [70]

to resolve the momentum of charged particles (see Figure 3.6). The multi-part magnet system is one of the most notable differences in the designs of ATLAS and CMS [71], which has a single 3.8 T solenoid surrounding its entire inner detector and calorimetry sub-systems. A summary of some of the key differences between the designs of the ATLAS and CMS experiments is given in Table 3.2.

A central solenoid, 5.8 m long and 2.5 m in diameter, surrounds the ATLAS inner detector, and immerses it in a 2 T magnetic field along the beam axis ($\hat{z}$). The design of the central solenoid has been optimized to provide a high magnetic field while minimizing the material thickness to approximately 0.66 radiation lengths, since the central solenoid is inside the calorimeters. The flux is returned by the steel of the ATLAS hadronic calorimeter and its girder structure.

Outside the calorimeters, a barrel toroid consisting of 8 independent coils, each 25.3 m long, provides a peak magnetic field of 4 T for bending tracks in the muon spectrometer. Two end-cap toroids provide a peak magnetic field of 4 T for bending tracks in the forward muon detectors. Both toroids produce magnetic fields circling along $\hat{\phi}$, bending muons in η [68].

3.2.3 Inner detector

The inner detector is designed to provide high precision tracking information for measuring the momentum and track parameters of charged particles. It consists of three sub-systems: the Pixel

Table 3.2: Some of the key differences in the designs of the ATLAS and CMS experiments [68, 71].

	ATLAS	CMS
length × diameter:	44 m × 25 m	25 m × 15 m
magnet systems:	2 T solenoid (inside the calo.) 4 T air-core toroid	3.8 T solenoid (outside the calo.)
EM calorimeter:	3-layer Pb-LAr sampling	$PbWO_4$ crystal

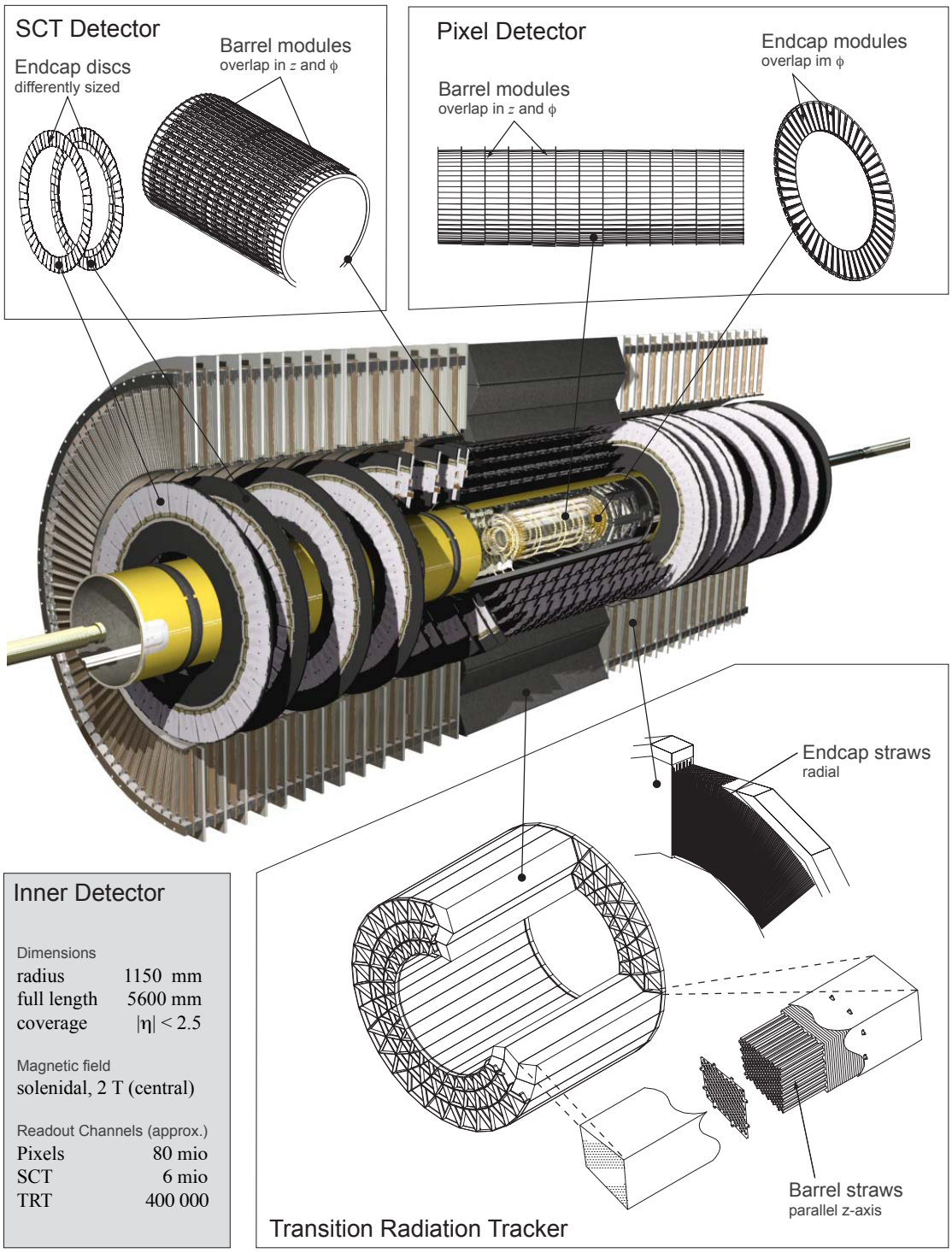

Figure 3.7: An illustration of the ATLAS inner detector and its sub-systems [68, 72].

detector, the Semi-Conductor Tracker (SCT) and the Transition Radiation Tracker (TRT).

The Pixel detector consists of three finely-granulated layers of silicon detectors with approximately 80 M channels (about 90% of the total readout channels in ATLAS, see Table 3.3) to provide precise measurements of the tracking parameters near the interaction point. The first layer, the so-called B-layer, is essential for good secondary vertexing. The intrinsic accuracies in the barrel of the Pixels are 10 μm in R-ϕ and 115 μm in z. The Pixel detector has a very high hit efficiency of about 99%.

The SCT surrounds the Pixel detector and is in turn enveloped by the TRT. Similar to the Pixel detector, the SCT uses silicon detector elements in small strips with intrinsic accuracies of 17 μm in R-ϕ and 580 μm in z, and with a very high hit efficiency of about 99% [68].

The TRT is a gaseous straw-tube tracker with straws of 4 mm diameter that serve as the active elements. Each conducting straw body is held at a high negative voltage of typically -1.4 kV with an anode wire held at ground potential running down the center of the straw. A charged particle passing through a straw ionizes some of the Xe-CO_2-O_2 gas mixture in the straws, forming an avalanche onto the wire with a gain of a few times 10^4. The front-end electronics of the TRT amplify and digitize the ionization current read from the wire with two thresholds for discrimination. The low threshold[12] provides the discriminant for tracking hits, and the high-threshold is sensitive to transition radiation [76, 77, 78, 79]. The width of the pulse in time, a result of the drift time of the avalanche, is sensitive to the distance from the wire to the track of a charged particle. Precise reading of the timing allows for a hit resolution of approximately 130 μm. The measurement from a

[12] The author designed the algorithm for calibrating the the low thresholds channel-by-channel to give a uniform noise occupancy, as described in Ref. [73]. He also contributed to studies of the TRT straw hit efficiency, as described in Refs. [74, 75].

Table 3.3: Number of readout channels per sub-detector in ATLAS for the primary sub-detectors (ignoring the minbias trigger system, luminosity monitors, and DCS sensors) [68].

inner detector	Pixels	80 M
	SCT	6.3 M
	TRT	350 k
EM calorimeter	LAr barrel	110 k
	LAr end-cap	64 k
hadronic calorimeter	tile barrel	9.8 k
	LAr end-cap	5.6 k
	LAr forward calo.	3.5 k
muon spectrometer	MDTs	350 k
	CSCs	31 k
	RPCs	370 k
	TGCs	320 k
total		88 M

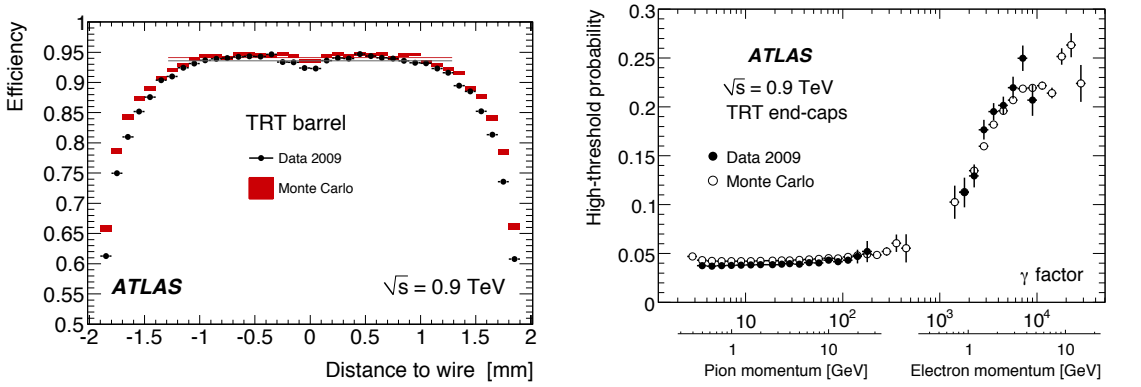

Figure 3.8: (left) A plot of the TRT hit efficiency as a function of the distance of the track from the wire in the centre of the straw, for straws in the barrel of the TRT [75]. (right) A plot of the probability for a hit on a track to trigger the TRT high-threshold as a function of γ factor, for samples of pions and electrons in the TRT end-caps [68]. Both of these plots use the first collision data taken in 2009 at $\sqrt{s} = 0.9$ TeV and compare the corresponding distributions from Monte Carlo simulation.

straw hit and its associated error are referred to as a "*drift circle*", being a measured distance from a track to a wire. The TRT straw hit efficiency is approximately 94% for tracks that are within the plateau of the efficiency, within about 1.3 mm of the wire (see Figure 3.8 (left)) [74, 75].

The Pixel detector and SCT cover a region of $|\eta| < 2.5$ in pseudo-rapidity, while the TRT reaches up to $|\eta| = 2.0$. A track typically crosses three layers of the Pixel detector. For the SCT barrel region the typical number of hits per track are eight, and the TRT typically provides about 36 hits per track.

The TRT provides electron identification information through the detection of transition radiation in the xenon-based gas mixture of its straw tubes. Transition radiation photons are emitted when charged particles cross a boundary between media with different dielectric constants. In the TRT barrel, radiator mats of fine polypropylene/polyethylene fibers are situated perpendicular to the barrel straws, with punched holes that the straws pass through. Thin polypropylene foils are layered between wheels of radial straws in the TRT end-caps. When a charged particle with energy E and mass m crosses a transition of two materials with different dielectric constants, it has a probability proportional to $\gamma = E/m$ to emit photons in the keV range (soft X-rays). These high-energy photons convert in the Xenon gas via the photoelectric effect and cause a large avalanche that triggers the high-threshold for a straw. This effect is more pronounced for electrons than pions because the small electron mass gives it a high γ-factor and correspondingly higher probability to fire the high threshold, as shown in Figure 3.8 (right). This provides electron identification[13] [80] information that is completely uncorrelated with the shower-shape information used from the calorimeters.

[13] Electron reconstruction and identification are introduced in Section 3.3.4.

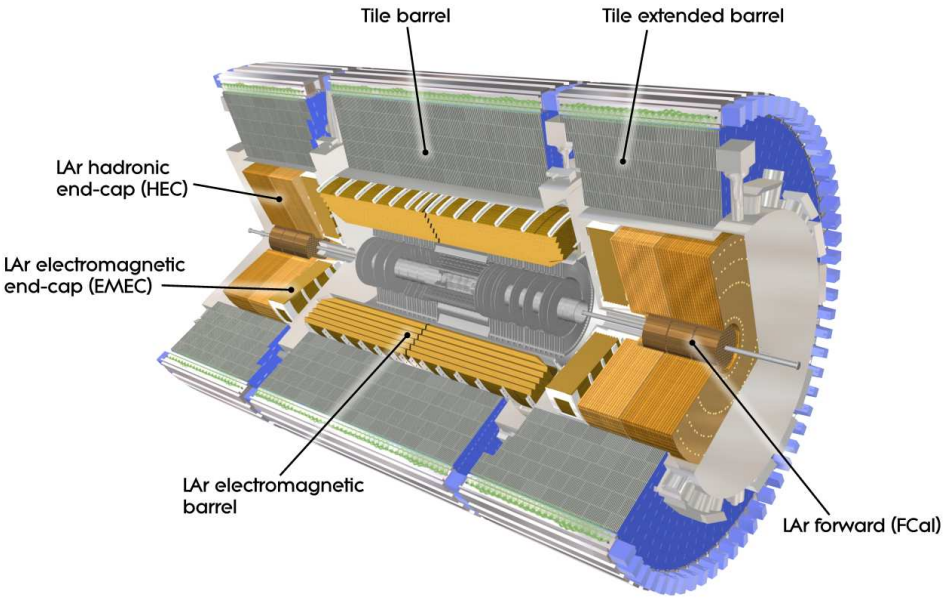

Figure 3.9: An illustration of the ATLAS calorimeter and its sub-systems [68].

The transverse momentum resolution of the inner detector was measured with $Z \to \mu\mu$ events in the 2010 collision data, and parametrized [81] as approximately

$$\frac{\sigma_{p_{\mathrm{T}}}}{p_{\mathrm{T}}} = 1.6\text{–}3.4\% \quad \oplus \quad 50\text{–}140\% \left(\frac{p_{\mathrm{T}}}{\mathrm{TeV}}\right) ,$$

with better p_{T}-resolution in the barrel than in the end-caps.

3.2.4 Calorimeters

The ATLAS electromagnetic and hadronic calorimeters are designed to absorb and measure the energy of high-energy electrons, photons, and hadrons up to $|\eta| < 4.9$, and consist of the sub-systems shown in Figure 3.9. Each sub-system is a type of sampling calorimeter, with alternating layers of a dense absorber material to help initiate an electromagnetic or hadronic shower, and layers of an active material for detecting the shower.

The EM calorimeter consists of a barrel part ($|\eta| < 1.475$), two end-caps ($1.375 < |\eta| < 3.2$), and a presampler ($|\eta| < 1.8$) used to correct for the energy that electrons and photons lose upstream of the calorimeters. It is constructed with lead absorber plates layered between electrodes bathed in liquid argon (LAr), in an accordion-like geometry to maximize coverage. The EM calorimeter is finely segmented, with nearly 170k total readout channels. The region with $|\eta| < 2.5$ has significantly finer granularity, since it is within the acceptance of the ATLAS tracking system and needed for precise measurements of electrons and photons. Figure 3.10 shows the granularity of the readout

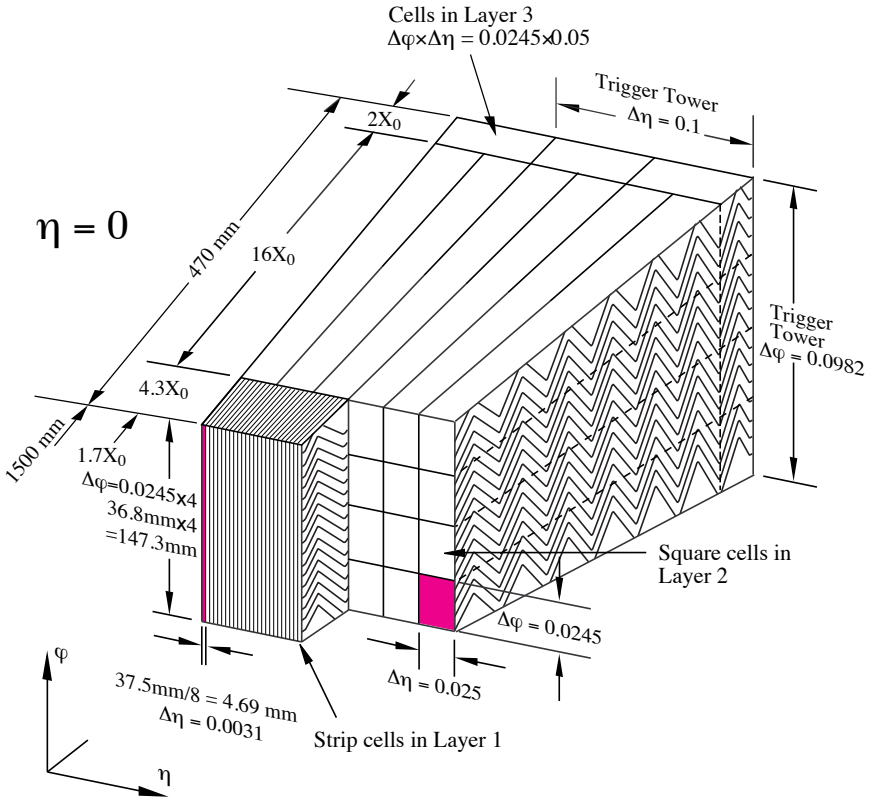

Figure 3.10: An illustration of the ATLAS barrel EM calorimeter and the granularity of its readout cells [68].

cells in the various layers of the barrel EM calorimeter. The first layer of the barrel EM calorimeter is a presampler layer (not shown), divided into readout cells with $\Delta\eta \times \Delta\phi = 0.025 \times 0.1$. The next layer, Layer 1, is even more finely segmented in η. It has thin strip-shaped cells with $\Delta\eta \times \Delta\phi = 0.025/8 \times 0.1$ to provide a good position measurement for the shower and good separation of prompt photons from the double-peaks of $\pi^0 \to \gamma\gamma$ decays. Layer 2 is the thickest layer, having about 16 radiation lengths and cells in a grid with $\Delta\eta \times \Delta\phi = 0.025 \times 0.025$. Layer 3 is doubly coarse in η, with $\Delta\eta \times \Delta\phi = 0.050 \times 0.025$, and measures the tail of an electromagnetic shower.

The hadronic tile calorimeter is a sampling calorimeter covering $|\eta| < 1.7$, using steel as the absorber and scintillating tiles as the active material. There are three layers of readout cells, with the finest layer having a granularity of $\Delta\eta \times \Delta\phi = 0.1 \times 0.1$. The region with $1.7 < |\eta| < 3.2$ is covered by the Hadronic End-cap Calorimeter (HEC), placed directly behind the end-cap EM calorimeter. It uses copper as the absorber and LAr as the active material, with the granularity of finest layer of readout cells being $\Delta\eta \times \Delta\phi = 0.1 \times 0.1$. Finally, the Forward Calorimeter (FCal) covers the most forward region up to approximately $3.1 < |\eta| < 4.9$ and consists of three modules

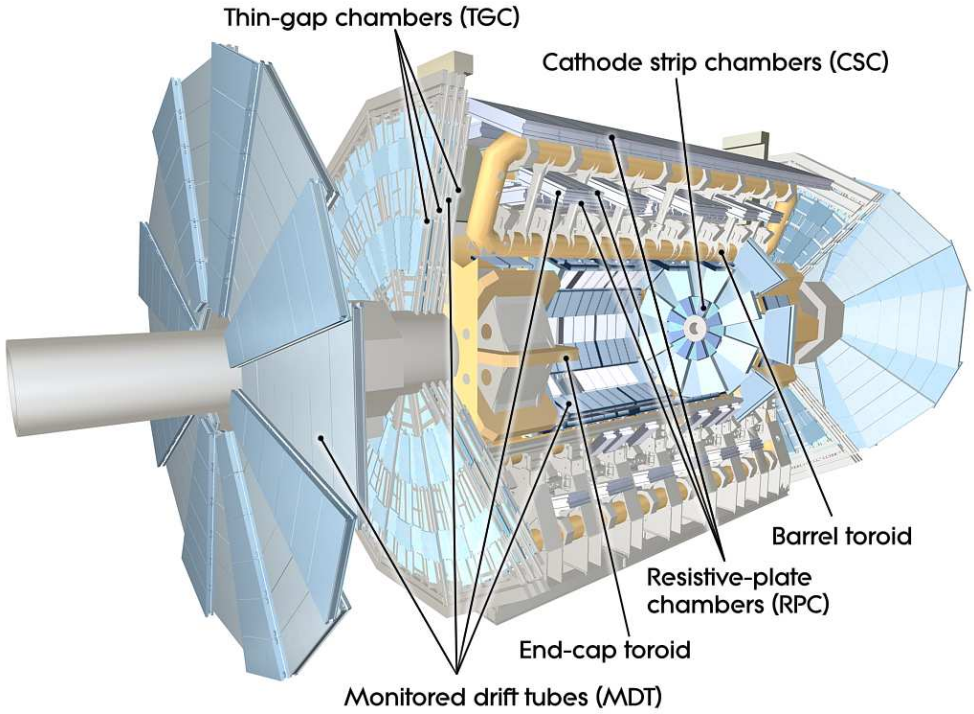

Figure 3.11: An illustration of the ATLAS muon spectrometer and its sub-systems [68].

in each end-cap, the first made of copper and the other two of tungsten, with LAr as the active material.

The energy resolutions of sub-sections of the ATLAS calorimeter were measured in studies using $\pi^{\pm}$ and electron test-beams in an independent setup at CERN before the start-up of the LHC, and were parametrized [68] as approximately

$$\begin{aligned}
\frac{\sigma_E}{E} &= \frac{10\%}{\sqrt{E/\mathrm{GeV}}} && && \text{EM calorimeter,}\\
\frac{\sigma_E}{E} &= \frac{56\%}{\sqrt{E/\mathrm{GeV}}} && \oplus\ 6\% && \text{hadronic barrel,}\\
\frac{\sigma_E}{E} &= \frac{70\%}{\sqrt{E/\mathrm{GeV}}} && \oplus\ 6\% && \text{hadronic end-cap,}\\
\frac{\sigma_E}{E} &= \frac{94\%}{\sqrt{E/\mathrm{GeV}}} && \oplus\ 8\% && \text{forward calorimeter.}
\end{aligned}$$

3.2.5 Muon spectrometer

Muons with $p_{\mathrm{T}} \gtrsim 4$ GeV have enough energy to not curl back before reaching the ATLAS muon spectrometer, which provides measurements of muon track parameters. In the central barrel part of the muon spectrometer, the large barrel toroid provides the magnetic field for muons with $|\eta| < 1.4$.

For $1.6 < |\eta| < 2.7$, the magnetic field is provided by two end-cap toroid magnets, while for the transition region $1.4 < |\eta| < 1.6$ it is provided by a combination of the barrel and end-cap fields. Three layers of Monitored Drift Tubes (MDTs) are used over most of the η-range for the precision measurement of muon tracks in the bending direction of the magnetic field in η. Cathode Strip Chambers (CSCs) are used in the innermost plane for $2 < |\eta| < 2.7$. Finally, to obtain the muon ϕ-coordinate in the direction orthogonal to the precision-tracking chambers, as well as for triggering, Resistive Plate Chambers (RPCs) are used in the barrel and Thin Gap Chambers (TGCs) in the end-caps. Combined, there are approximately 1.2 M readout channels in the muon spectrometer (see Figure 3.11).

The transverse momentum resolution of the muon spectrometer was measured with $Z \to \mu\mu$ events in the 2010 collision data, and parametrized [81] as approximately

$$\frac{\sigma_{p_{\mathrm{T}}}}{p_{\mathrm{T}}} = 0\text{–}6\% \left(\frac{4\ \mathrm{GeV}}{p_{\mathrm{T}}}\right) \oplus 4\text{–}9\% \oplus 23\text{–}30\% \left(\frac{p_{\mathrm{T}}}{\mathrm{TeV}}\right),$$

with better performance in the barrel and end-caps than in the transition region. The inner detector provides the best measurement at low to intermediate momenta, whereas the muon spectrometer takes over above ≈ 30 GeV.

3.3 Reconstruction

3.3.1 Introduction

Offline *reconstruction* software processes the raw data from ATLAS to find the signatures of high-p_{T} particles streaking through the detector. The primary reconstructed objects are tracks in the inner detector and muon spectrometer, and clustered energy deposits in the calorimeter. Dedicated reconstruction algorithms search for electrons, photons, muons, jets, b-jets, hadronic tau decays, and reconstruct the missing transverse momentum. ATLAS developed the Athena framework [82], which divides the reconstruction problem into several algorithms, tools, and detailed representations of the detector geometry and conditions.

The output of reconstruction[14] is generally a set of collections of candidates for electrons, muons, etc. Athena reconstruction produces two types of output files: ESDs and AODs (see Figure 3.12). Event Summary Data (ESD) files contain the outputs of basic calibration and pattern recognition algorithms, including hits and drift circles in the tracking systems and detailed cell-based information from the calorimeters, as well as the full derived objects from object-level reconstruction like electrons, muons, jets, etc. The ESD includes sufficient information to re-run basic-level reconstruction, including tracking and clustering. Analyses Object Data (AOD) files contain a smaller subset

[14] The ATLAS computing infrastructure for reconstruction, analysis, production of MC is discussed in Section 3.7.

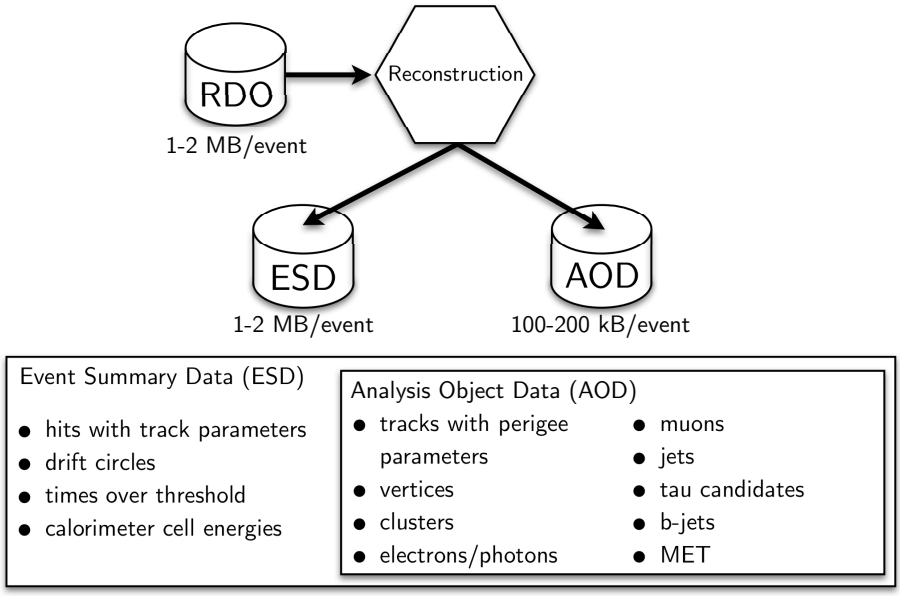

Figure 3.12: An illustration of the inputs and outputs of ATLAS reconstruction. Raw Data Object (RDO) files are typically the input to reconstruction (event size: 1–2 MB/event). Event Summary Data (ESD) files are produced, containing the hit- and cell-level information as well as the reconstructed objects (1–2 MB/event). The reconstruction also produced Analysis Object Data (AOD) files, containing a sub-set of the information in the ESD intended for use in analyses (100–200 kB/event).

of the data in an ESD, giving the derived objects intended for use by analyses, including tracks, vertices, and all derived objects, but not the full hit- and cell-based information.

An analysis will typically define a *preselection* of objects with a loose selection and basic quality requirements. Pre-selected electrons and muons are then used to remove overlapping candidates for hadronic tau decays or jets in a selection process called *overlap removal*. Then, an analysis typically defines an *object selection*, resulting in the accepted objects later used in the event selection[15].

3.3.2 Tracking

Tracks are reconstructed from the hits produced by charged particles passing through the inner detector. First, the primary track-finding forms space-points in the Pixel and SCT detectors and builds track-segments that later seed inside-out track-finding that extrapolates a track outward and associates hits in the TRT. The track parameters on the surface of each active detector element (pixel, strip, or straw) are determined from a combined fit of the hits on a track using track extrapolation

[15] Since reconstructed candidates for electrons, jets, taus, etc. can all arise from the same track or clustered energy deposit, the reconstruction is not unique and has overlapping candidates. Typically analyses select objects in the order: muons, electrons, taus, and then jets, as needed, removing overlapping candidates if they are selected. More details about overlap-removal and the object selection used in analyses is discussed in Sections 5.4.3 and 6.3.

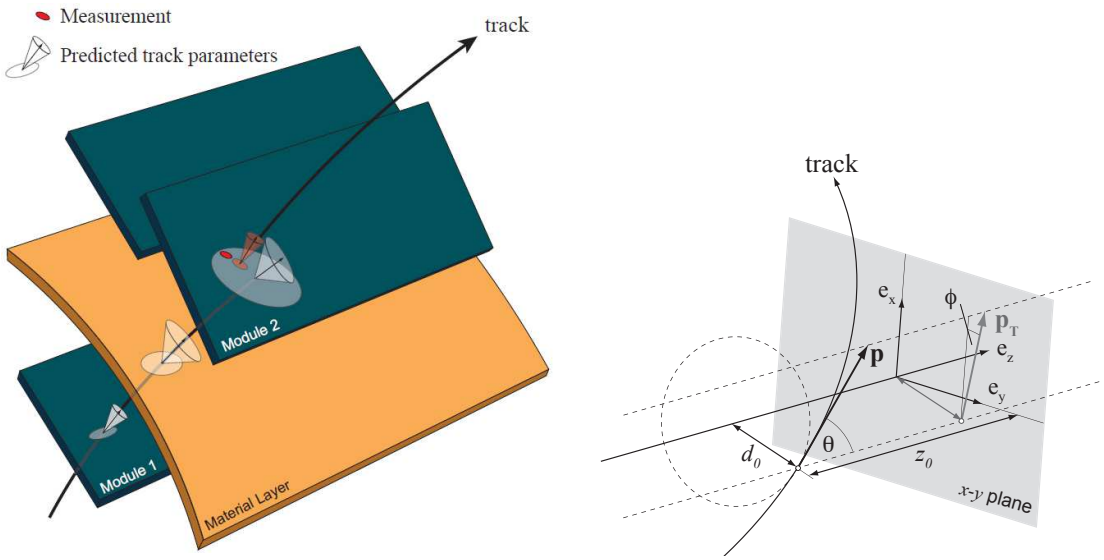

Figure 3.13: (left) An illustration of a typical extrapolation process within a Kalman filter step. The track parameters on an active layer of the detector, Module 1, are propagated onto the next measurement surface, resulting in the track prediction on Module 2. The traversing of the material layer between the two modules is accounted for by inflating the uncertainties on the track parameters. The final resulting measurement of the track parameters (shown in red) is improved by combination of all the hits on track. (right) An illustration of the perigee parameters for a track: the longitudinal coordinate along the beamline, z_0, and the impact parameter, d_0, being the distance-of-closest-approach of a track to the beamline in the transverse plane [83].

tools and the Kalman filtering method, which takes into account the smearing of a track from multiple scattering when going through material in the detector and a detailed map of the magnetic field (see Figure 3.13 (left)). A second outside-in tracking reconstruction builds track segments from the remaining hits and in the TRT, and extrapolates backwards to combine hits in the silicon detectors [83, 84].

The most important track parameters are reconstructed at the *perigee* point, the point along the track that is closest to the beamline. Figure 3.13 (right) illustrates the z_0 parameter, giving the the longitudinal position of a track along the beamline, and the d_0 parameter, giving the distance of the perigee point from the beamline in the transverse plane. The z_0 parameter has a resolution of approximately $100\,\mu$m, and is often used to select tracks near a particular vertex. The d_0 parameter has a resolution of approximately $10\,\mu$m, and is important for selecting or suppressing in-flight decays such as muons from B meson decays, and is used in tagging b-jets and hadronic tau decays [68].

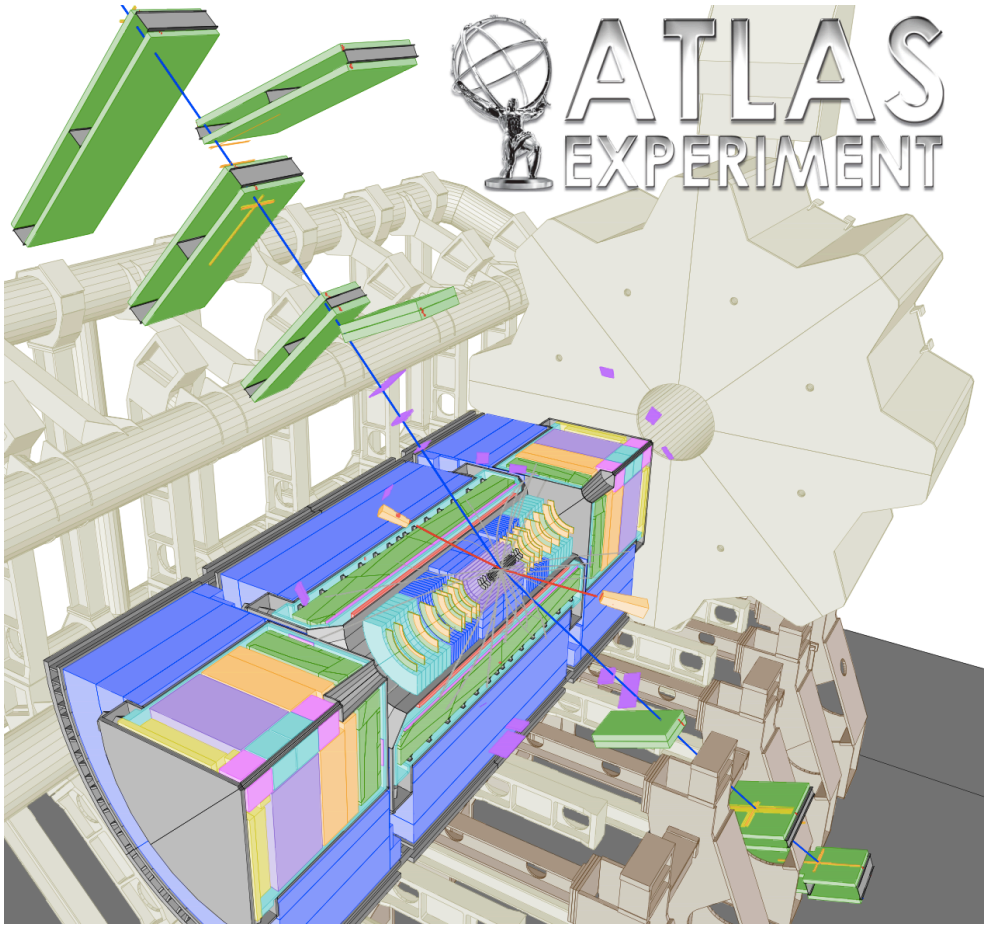

Figure 3.14: An event display of a $ee\mu\mu$ candidate event from a search for $H \to ZZ^* \to 4\ell$ with the 2011 dataset [85]. The masses of the lepton pairs are 76.8 GeV and 45.7 GeV, and the event has $m_{4l} = 124.3$ GeV. The tracks from the muon candidates are traced in blue. The electron candidates are absorbed in the calorimeter and traced in red [86].

3.3.3 Muons

Muon candidates are primarily seeded by track segments found in the muon spectrometer as *stand-alone* muon candidates and matched to tracks in the inner detector, forming *combined* muon candidates. More inclusive selections can use *segment-tagged* muons, which did not successfully form a stand-alone muon candidate, but have a muon segment matching an inner-detector track [69, 68]. As an example of muon candidates in the ATLAS detector, Figure 3.14 shows an event display of a $ZZ^* \to ee\mu\mu$ candidate event.

Analyses discussed in this document preselect muon candidates with $|\eta| < 2.5$, $p_{\mathrm{T}} > 10$ GeV, and passing various quality cuts discussed in Chapters 5 and 6. These quality requirements correspond to a muon reconstruction and identification efficiency of approximately 95% for combined muons in

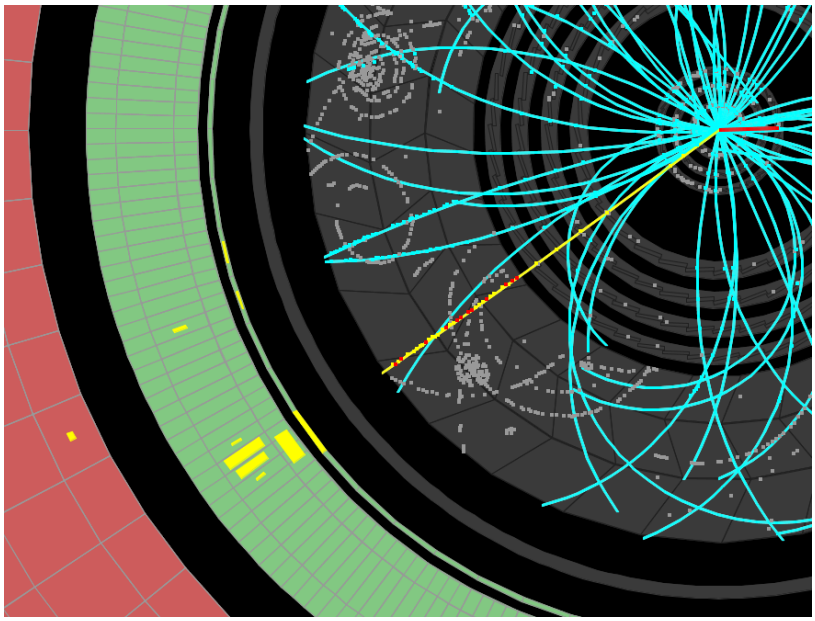

Figure 3.15: An event display of an e^+ candidate in a $W^+ \to e^+\nu$ candidate event in the ATLAS 2010 run. The positron track is traced in yellow and the energy deposit in the EM calorimeter is indicated in yellow as well. High-threshold hits in the TRT are indicated by the red dots. The positron has $p_{\mathrm{T}} = 23$ GeV and $\eta = 0.6$. The missing transverse momentum, $E_{\mathrm{T}}^{\mathrm{miss}}$, was measured to be 31 GeV and its direction is indicated by the red line from the beam axis. The transverse mass of the combination of the positron and the $E_{\mathrm{T}}^{\mathrm{miss}}$ is 55 GeV [86].

the majority of the combined acceptance of the muon spectrometer and inner detector ($|\eta| < 2.5$), dipping to 80% in the most central ($\eta \sim 0$) and crack regions between the barrel and end-caps [87].

3.3.4 Electrons and photons

Electron candidates are reconstructed by matching clustered energy deposits in the EM calorimeter to tracks found in the inner detector. Electron reconstruction is seeded by clusters found in the EM calorimeter with a sliding-window algorithm [69], independent of the topological clusters used to build jets. Then, tracks are matched with the EM clusters, resulting in electron candidates if they have a track and photon candidates if they are without a track. Special attention is payed to tagging electrons that are actually from converted photons by finding the secondary vertex, since about half of the high-p_{T} photons in ATLAS will have a conversion before reaching the EM calorimeter [68]. Figure 3.15 shows an event display of a selected electron candidate in ATLAS in a $W \to e\nu$ candidate event.

Analyses discussed here typically preselect electron candidates if they have $p_{\mathrm{T}} > 15$ GeV, $|\eta| < 2.47$, are not in the barrel—end-cap transition region where $1.37 < |\eta| < 1.52$ (also called the "crack" re-

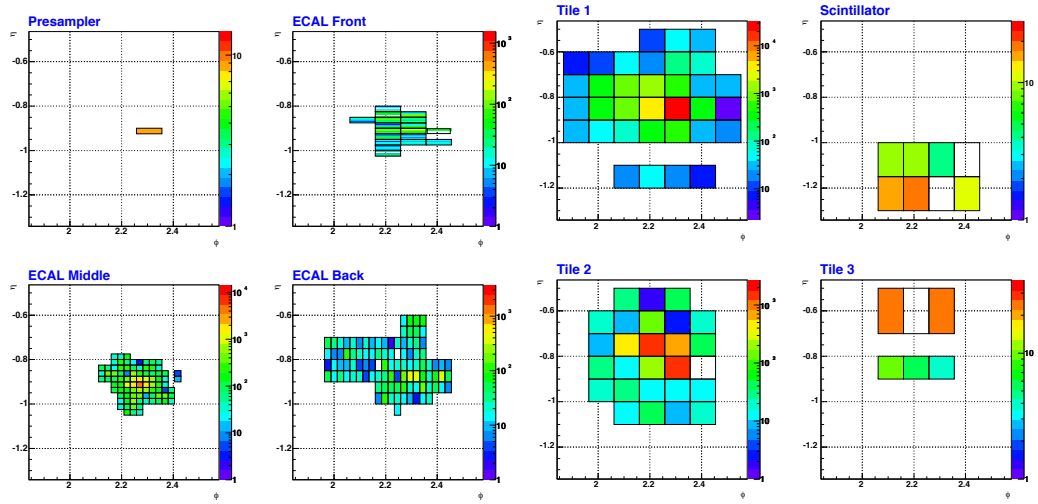

Figure 3.16: Plots of the energy in MeV distributed in $\eta \times \phi$ cells in each layer of the barrel calorimeter for a single topological cluster from a simulated charged pion. Each pane shows a different layer of the calorimeter but within the same $\eta \times \phi$ range [92].

gion), and pass ATLAS cut-based identification [88, 89]. The identification thins the list of electron candidates considered, rejecting fakes from charged and neutral pions by requiring track quality criteria, strict track-cluster matching, cuts on EM calorimeter shower shapes, and by requiring high-threshold hits in the TRT. The cut-based identification has tight, medium, and loose working points. The medium working point is the most commonly used, and has a high-p_{T} electron efficiency of near 90% for a few percent fake rate for charged pions [90].

3.3.5 Clustering

Energy deposits in the calorimeter are grouped into three-dimensional clusters using a topological clustering technique [91], incorporating both the EM and hadronic layers of the calorimeter. The standard topological clustering algorithm in ATLAS uses the `4-2-0` method, where clusters are seeded by cells that are 4 times the noise level for that cell, ranging from approximately 30 MeV to 3 GeV, increasing in $|\eta|$ [68]. Then, adjacent cells are added to the cluster if they are over 2 times the noise level, and then any cells adjacent to those are added as well.

Figure 3.16 shows an illustration of a topological cluster from a simulated charged pion in the ATLAS barrel calorimeter, showing the variety of cell granularities between layers of the calorimeter that are all combined 3.16. Topological clusters are used to assemble reconstructed jets and hadronic tau decays as described in the following sub-sections.

3.3.6 Jets

As a consequence of the strength of the strong interaction and its confining properties discussed briefly in Appendix A.2.5, out-going scattered quarks or gluons produce additional quarks and gluons almost immediately to nullify any free color charge. An out-going quark or gluon, struck out of a proton in the colliding beams, goes through a hadronization process where multiple (meta)stable hadrons are produced, resulting in a spray of nearby energy deposits in the calorimeters called a "jet".

An industry of algorithms has grown for finding jets by appropriately associating clustered energy deposits. The process of jet reconstruction uses such a jet-finding algorithm to identify jets, and produces a collection of reconstructed four-momenta for the initial scattered out-going partons. Sophisticated techniques are used to calibrate the energy of jets depending on things such as the geometry of the jet with respect to the detector and the primary vertex, parametrizations for the amount of expected additional energy deposited due to in-time and out-of-time pile-up[16], the number reconstructed primary vertices, and the bunch position in time within the trains of adjacent proton bunches in the LHC [93].

For the analyses discussed here, jets are reconstructed with the anti-k_t algorithm [94] with distance parameter $R = 0.4$, taking as input three-dimensional topological clusters [91] of the cells in both the EM and hadronic calorimeters. The clusters are corrected for dead material and out-of-cluster energy losses, and the energy scale is calibrated with the local hadron calibration scheme (LC) [95], where the energy is split and corrected for each cluster in a jet [93]. Jets with $p_T > 25$ GeV, $|\eta| < 4.5$, and passing some recommended cleaning criteria[17], are preselected.

Especially for the highest luminosity runs ($L \sim 10^{33}$ cm^{-2} s^{-1}) in the later part of 2011 and throughout 2012, it is not rare for secondary pile-up interactions to produce jets. For jets within the tracking acceptance, one can select jets with energy deposits consistent with coming from the primary reconstructed vertex with a quantity called "jet-vertex fraction" (JVF) [98, 99].

JVF is in general a function of any pairing of a jet and a primary vertex within an event. First, tracks are matched to the jet in question (fundamentally a calorimeter-based object) if the ΔR between the tangent vector of a track extrapolated to the beamline and the jet axis is less the size of the R-parameter used for the jet (typically 0.4 in this work). Then, JVF is defined as the fraction of the scalar sum of the transverse momentum of those matching tracks that are associated with the

[16] See the discussion of pile-up in Section 3.5.2.

[17] Jet cleaning cuts are described in more detail on `JetEtMiss` twiki internal documentation pages [96] and in Appendix B of Ref. [97].

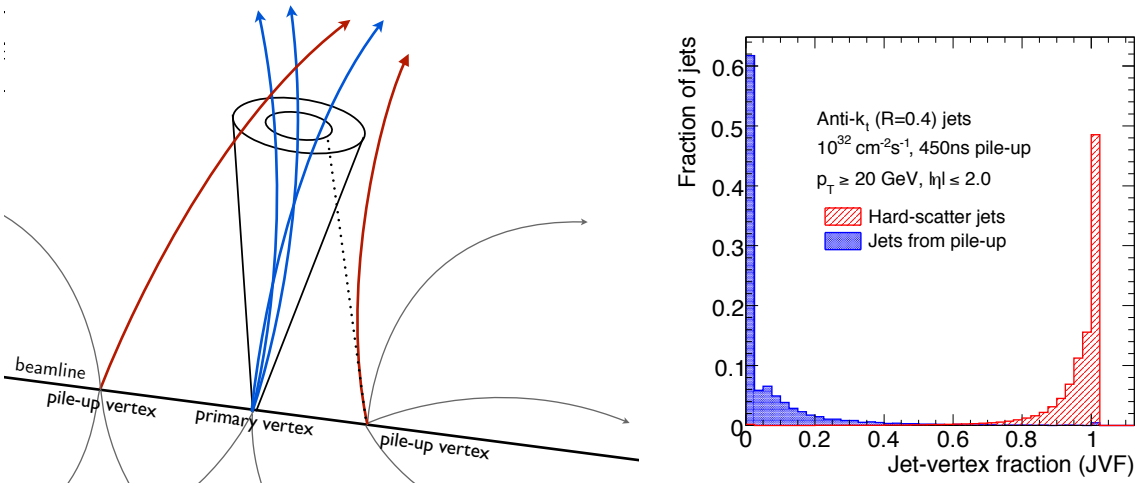

Figure 3.17: (left) A diagram illustrating tracks from pile-up vertices (in red) falling on a tau candidate (in blue). Conceptually, JVF is the fraction of the scalar sum of the p_{T} of the tracks pointing to the jet seeding the tau candidate that are associated with the chosen primary vertex (*i.e.* the fraction of the scalar some of the blue and red tracks that is blue). (right) The distribution of JVF from ATLAS simulation for jets truth-matched to the hard-scatter (in red) and jets from pile-up interactions (in blue) for events with $L \approx 10^{32}$ cm^{-2} s^{-1}, corresponding to $\langle N_{\mathrm{vertex}} \rangle \approx 5$ [99].

vertex in question. That is,

$$\mathrm{JVF}(\mathrm{jet}_i, \mathrm{vertex}_j) \equiv \frac{\sum_k p_{\mathrm{T}}(\mathrm{track}_k)|\mathrm{vertex}_j}{\sum_n \sum_\ell p_{\mathrm{T}}(\mathrm{track}_\ell)|\mathrm{vertex}_n} ,$$

$$k \in \{\text{tracks matching jet}_i \text{ from vertex}_j\} ,$$

$$\ell \in \{\text{tracks matching jet}_i \text{ from vertex}_n\} ,$$

$$n \in \{\text{vertices}\} ,$$

where k runs over over all tracks matched to jet$_i$ from vertex$_j$, where ℓ runs over over all tracks matched to jet$_i$ from vertex$_n$, and n runs over all the reconstructed primary vertices in the event. Figure 3.17 (left) shows an illustration of a jet with nearby tracks from additional pile-up vertices, in which case JVF would be calculated as the ratio of the sum of the p_{T} of the blue tracks (which are associated to the denoted "primary vertex" in question) to that of the combination of the blue and red tracks (which includes pile-up tracks from other vertices). In the language of the ATLAS Collaboration, *the* "JVF of a jet" often denotes the JVF of that jet and the primary vertex with the highest $\sum p_{\mathrm{T}}^2$ of tracks, which is often the vertex of interest for most selections.

JVF gives a natural way to quantify how associated a jet is to the hard-scatter interaction. For jets with a substantial fraction of matching tracks coming from the hard-scatter vertex, JVF will be nearly 1, while for jets consistent with coming from pile-up activity, JVF will be closer to 0 (see

Figure 3.17 (right)). For jets without matching tracks, most likely due to being too forward to be accepted by the tracker, JVF is set to -1.

Analyses discussed here require $|\text{JVF}| > 0.75$ for jets within $|\eta| < 2.4$. Finally, jet candidates that overlap with *preselected* electron or *selected*[18] hadronic tau candidates within $\Delta R < 0.2$ are removed from consideration.

3.3.7 Hadronic tau decays

Tau leptons are the only known leptons massive enough to have hadronic decays, which makes them somewhat similar to B mesons in that they have hadronic signatures that can be tagged with about a 50% efficiency for a few percent or sub-percent fake rate. They decay hadronically approximately 65% of the time, to predominantly either one or three charged pions, with possibly a few additional neutral pions. The ATLAS reconstruction of hadronic tau candidates is seeded by each reconstructed calorimeter jet with $p_{\text{T}} > 10$ GeV and $|\eta| < 2.5$. Tracks are associated to the jets, and variables are calculated from the combined tracking and calorimeter information to discriminate hadronic tau decays from fakes and from other hadrons and electrons [100, 101, 102, 103].

Hadronic tau decays can be distinguished in the large multijet background by the close association of one or three tracks with a narrow clustering of EM and hadronic calorimeter activity that is characteristic of hadronic tau decays. Figure 3.18 is an event display of a $\mu\tau_{\text{h}}$ event with two jets, typical of the type of events studied in this thesis. It illustrates that a hadronic decay has a low track multiplicity and is much more isolated than the deposits associated with the jets in the event from QCD production. The most sophisticated methods of tau identification also make use of the significance of a reconstructed secondary vertex if there is one for 3-track candidates.

Multivariate discriminants based on Boosted Decision Trees (BDTs) have been developed to discriminate hadronic tau decays from fakes. One BDT-based discriminant has been developed to discriminate hadronic tau decays from jets produced in strong interactions, and a separate BDT-based discriminant has been developed to reject electrons. Fakes from muons with tracks that happen to overlap with calorimeter clusters are more easily suppressed by removing candidates overlapping with preselected muons, and with a cut-based muon veto. The reconstruction and identification of hadronic tau decays is discussed in more detail in Chapter 4.

For the analyses discussed here, tau candidates are preselected if they have $p_{\text{T}} > 25$ GeV, $|\eta| < 2.47$ and not in the crack region where $1.37 < |\eta| < 1.52$, and have 1 or 3 core tracks. Core tracks are the tracks associated to a tau candidate, selected to be consistant with the primary vertex associated with the tau candidate, and within $\Delta R < 0.2$ of the tau axis, defined with respect to the η, ϕ of the

[18] See the discussion of selection and preselection in Section 3.3.1.

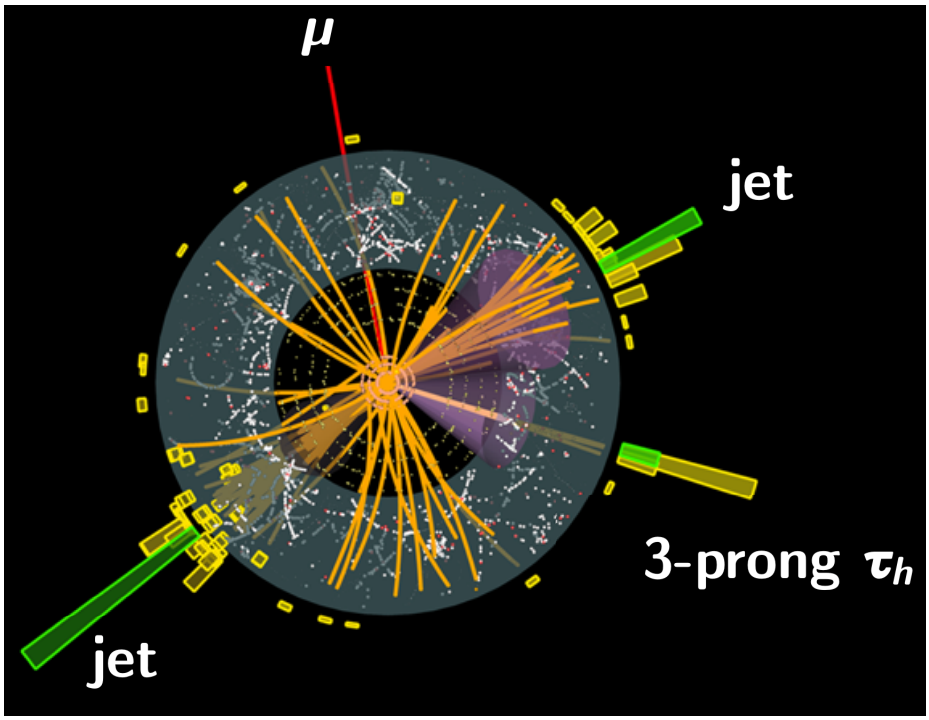

Figure 3.18: An event display of a $\mu\tau_{\mathrm{h}}$ + 2 jet candidate event from a search for $t\bar{t}$ events with hadronic tau decays in the 2011 dataset [104]. The muon track is shown in red, has positive reconstructed electric charge, and $p_{\mathrm{T}} = 20$ GeV. The 3-track tau candidate is shown at the lower right, has negative charge, and $p_{\mathrm{T}} = 53$ GeV [86].

calorimeter jet that seeded the tau candidate [101]. Tau candidates are removed from consideration if they overlap with preselected electron or muon candidates within $\Delta R < 0.2$.

3.3.8 Missing transverse momentum

The production of neutrinos or any hypothetical new weakly-interacting particle with some significant p_{T} will result in a imbalance in the vector sum of transverse momentum of all particles produced in the hard scatter. Conceptually, the missing transverse momentum, $E_{\mathrm{T}}^{\mathrm{miss}}$ (or MET), is reconstructed from the negative vector sum of the transverse momentum of everything reconstructed in the event:

$$\vec{E}_{\mathrm{T}}^{\mathrm{miss}} = -\sum \vec{p}_{\mathrm{T}}\,.$$

ATLAS has a so-called *refined* method of calculating the $E_{\mathrm{T}}^{\mathrm{miss}}$, where the terms in the vector sum are calibrated independently for each type of high-p_{T} object (electons, muons, jets, etc.). Additional terms account for the soft jets and remaining calorimeter cells not associated with an identified object [105].

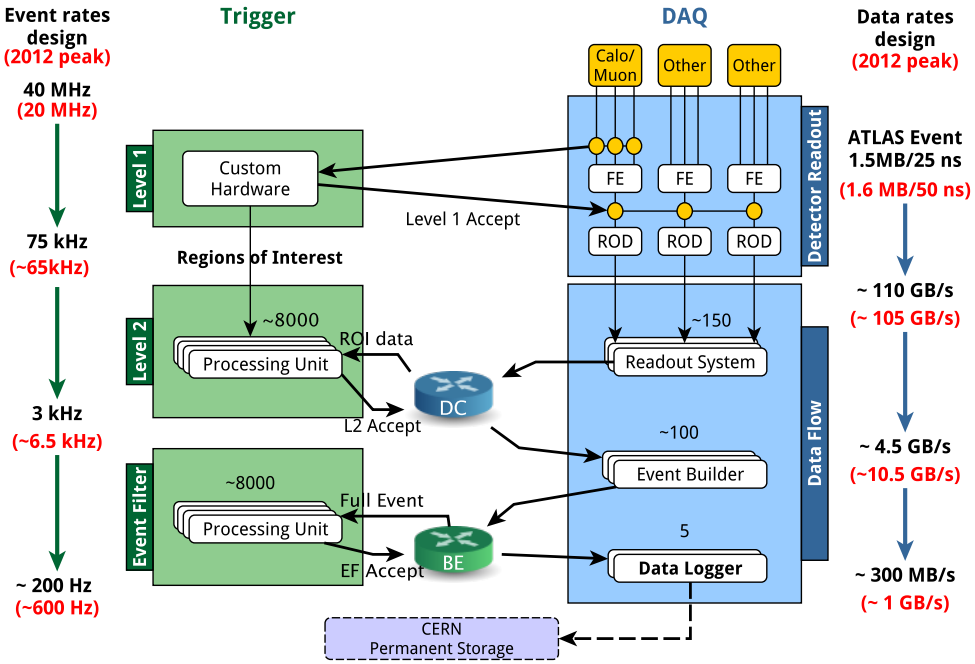

Figure 3.19: The design of the ATLAS trigger and DAQ architecture, indicating the event rate passing the trigger levels on the left, and showing the flow of the data volume on the right. The numbers in black indicate the design specifications and the numbers in red indicate the peak running conditions in 2012 [106].

3.4 Triggering

ATLAS has a three-level trigger architecture for reducing the data rate from collisions. The first level (L1) uses custom hardware based on ASICs and FPGAs, while level 2 (L2) and third level Event Filter (EF) uses software algorithms running on farms of commercial CPUs [68]. Figure 3.19 illustrates the design of the ATLAS trigger and data acquisition system (DAQ).

3.4.1 Level 1

The L1 trigger uses coarse information from calorimeters and muon systems, but no information from the inner detector. It reduces the bunch-crossing rate of 20 MHz by approximately a factor of 300 to about 65 kHz for events accepted by L1. It quickly identifies Regions of Interests (RoIs) in $\Delta\eta \times \Delta\phi$ that are passed to the L2 algorithms for further investigation. Data streaming from the detector are buffered in custom front-end hardware waiting for a L1 accept within a latency of less than 2.5 μs. Events passing L1 are sent to detector-specific Read Out Drivers (ROD) to be assembled and pushed to the dedicated memories on Read Out System (ROS) PCs.

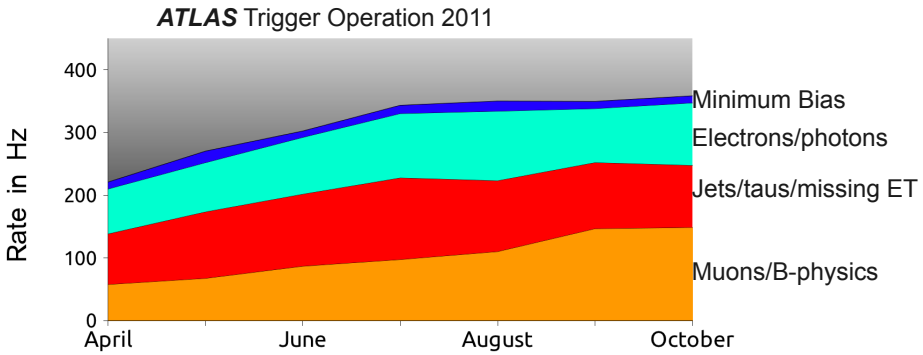

Figure 3.20: The Event Filter (EF) bandwidth used by each trigger stream as function of time in the year 2011 [107].

3.4.2 Level 2

The L2 trigger receives RoI-based information from L1 and fetches only the data in these regions from respective ROSes, where the full event data is buffering. The L2 trigger applies a set of fast and coarse selection algorithms on RoI data to reduce the event rate by approximately a factor of ten, from 65 kHz to 6.5 kHz with an average latency of 40 ms. A L2 accept initiates the Event Builder (EB) which retrieves all of the event data from the ROSes, together with L2 results. The EB assembles the full event data and assigns it to Event Filter (EF) process.

3.4.3 Event filter

The EF has access to full event data and the same functionalities as the offline reconstruction. It applies detailed object- and event-level selection algorithms to reduce the event rates by about a factor of ten, from 6.5 kHz to about 500 Hz. Each EF process uses about four seconds on average to reach a decision. Accepted events are recorded in permanent storage at CERN [106].

The data are accepted in different streams[19] depending on the type of trigger that fired, leading to different files. The main physics streams are called `Muons`, `Egamma`, and `JetTauEtMiss` for events triggered by muons, electrons/photons, and jet/tau/$E_{\mathrm{T}}^{\mathrm{miss}}$-based signatures, respectively. Figure 3.20 shows the EF bandwidth used by each trigger stream as function of time in the year 2011.

[19] The ATLAS trigger streams are inclusive in that an event with both signatures can end up in both the muon and egamma streams.

3.5 Running conditions and dataset

3.5.1 Overview

After many months in 2008 of ATLAS doing commissioning runs triggering on cosmic ray muons, the LHC delivered the first proton-proton collisions in the LHC at $\sqrt{s} = 900$ GeV on November 23, 2009. A few μb^{-1} of integrated luminosity of minbias events were collected in the following weeks that were used for further commissioning studies of the performance of ATLAS [75].

The first substantial dataset for physics analysis came in 2010 with approximately 36 pb^{-1} of integrated luminosity at the record-breaking energy of $\sqrt{s} = 7$ TeV. This dataset allowed ATLAS to make many of its first electroweak SM measurements, including measurements of the W and Z boson production cross sections [108, 109], p_T distributions of W and Z bosons [110, 111], and the $t\bar{t}$ cross section [112]. The measurement of the cross section of $Z \to \tau\tau$ at ATLAS [113] is the topic of Chapter 5.

Improvements in the number of bunches per beam and the other beam parameters allowed the luminosity of LHC to continue to climb throughout 2009–2012. Figure 3.21 shows distributions of the number of bunches per beam, the peak instantaneous luminosity, and the peak number of interactions per bunch crossing as a function of time. Table 3.4 summarizes typical ranges for some of the important beam parameters of the LHC in different years of running 3.4.

The reach of searches for the Higgs boson and new physics at ATLAS were significantly extended with the higher-luminosity runs ($\sim 10^{33} cm^{-2} s^{-1}$) in 2011, with approximately 5 fb^{-1} of integrated luminosity at $\sqrt{s} = 7$ TeV, and in 2012, with 21 fb^{-1} of integrated luminosity at $\sqrt{s} = 8$ TeV. Figure 3.22 (left) shows the integrated luminosity vs time for the years 2010, 2011, and 2012.

3.5.2 Pile-up

The increase in luminosity of the LHC has led to an increase of *pile-up*, the overlapping of the detector response from multiple proton-proton interactions within the same event. Pile-up can be *in-time*, due to the presence of additional proton-proton interactions in the same bunch crossing as

Table 3.4: Milestones of some of important beam parameters of the LHC for 2009 to 2012 [66, 115].

	design	2009	2010	2011	2012
center-of-momentum energy, $\sqrt{s}$ [TeV]	14	0.9–2.4	0.9–7	7	8
peak luminosity $[cm^{-2} s^{-1}]$	10^{34}	10^{26}	10^{27}–10^{33}	10^{22}–10^{33}	10^{33}
max bunches per beam	2808	9	348	1331	1380
protons per bunch	10^{11}	10^{10}	10^{11}	10^{11}	10^{11}
mean interactions per crossing	23	0	0–2.2	2–20	10–35

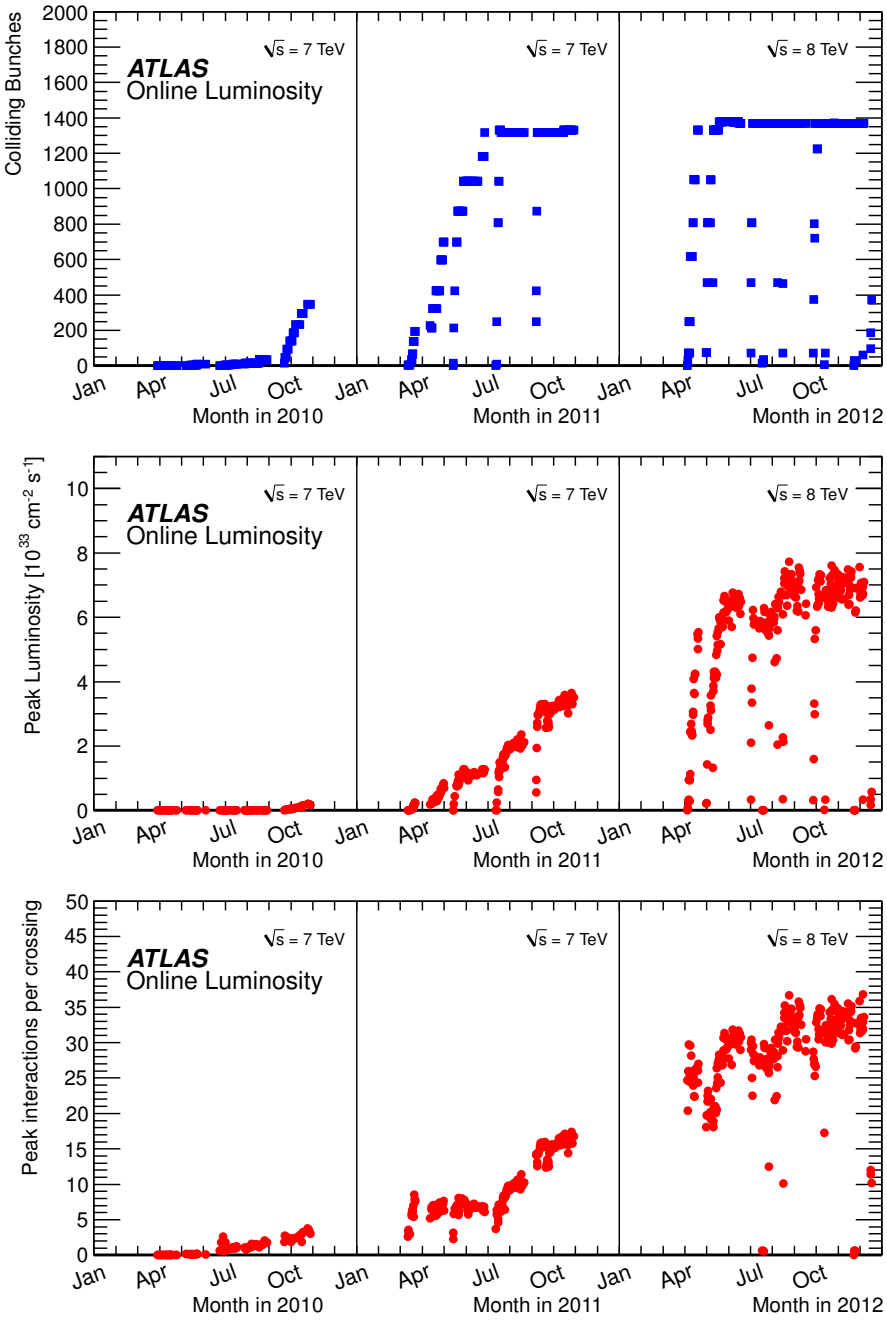

Figure 3.21: Distributions of the number of colliding bunches per beam, the peak instantaneous luminosity, and the peak mean number of interactions per bunch crossing, as a function of time for the years 2010–2012 [114].

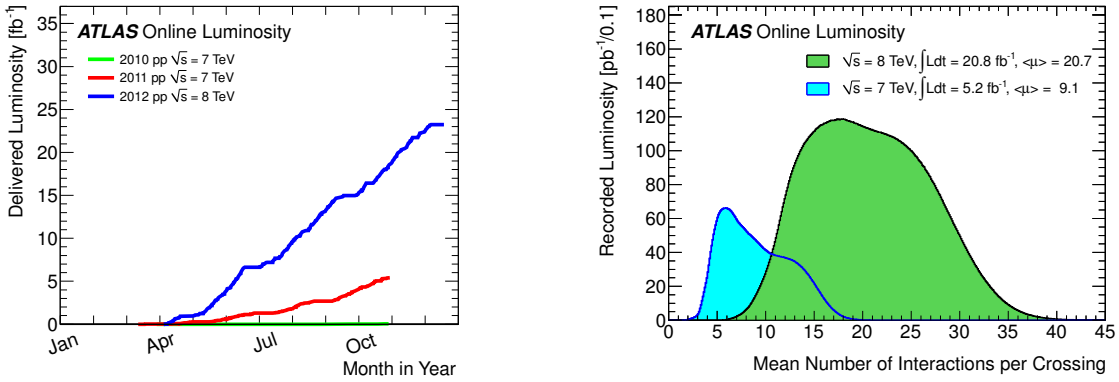

Figure 3.22: (left) The integrated luminosity delivered by the LHC as a function of time for the years 2010–2012. (right) The distribution of the mean number of interactions per bunch crossing, μ, for the $\sqrt{s} = 7$ TeV run in 2011 and the $\sqrt{s} = 8$ TeV run in 2012 [114].

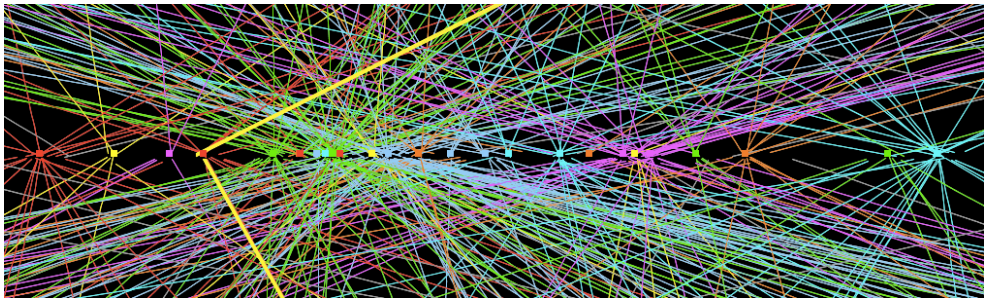

Figure 3.23: A close-up event display of the reconstructed primary vertices in a $Z \to \mu\mu$ event in the 2012 dataset with 25 vertices. The tracks from the muons are highlighted with thick yellow lines [86].

the primary interaction, or *out-of-time*, due to the remaining detector response from previous bunch crossings.

In the year 2010 (the dataset used for the $Z \to \tau\tau$ cross section measurement discussed in Chapter 5), the instantaneous luminosity of the LHC climbed from 1×10^{27} to 10^{33} cm^{-2} s^{-1}, with the average number of interactions per bunch crossing (μ) typically ranging from 0 to 2.2. In the year 2011 (the dataset used for the Z' search discussed in Chapter 6), the instantaneous luminosity was typically 1–4 $\times 10^{33}$ cm^{-2} s^{-1}, with $\mu = 2$–20. In 2012, the luminosity stayed of the order of 10^{33} cm^{-2} s^{-1} with the mean number of interactions per bunch crossing ranging up to 40. Figure 3.22 (right) compares distributions of the mean number of interactions per bunch crossing for the 2011 and 2012 datasets.

Tracking-related quantities can often be defined in a pile-up robust way by only considering tracks associated with a chosen vertex [102, 116]. Figure 3.23 shows a close-up event display of reconstructed primary vertices in a $Z \to \mu\mu$ event in the 2012 dataset with 25 reconstructed vertices. The precision

tracking capabilities of the inner detector allow the vertices to be reliably distinguished, and for one to usually associate muon candidates to the correct primary vertex.

The proper timing of the detector, fast restoration of the readout electronics, noise suppression, clustering, etc. are expected to sufficiently suppress the effects of out-of-time pile-up such that in-time pile-up is the leading contributor of additional clusters in the calorimeter [117]. The effects of pile-up on the reconstruction of hadronic decays of tau leptons will be discussed in some detail in Section 4.4.9.

3.6 Simulation

As a very important comparison for understanding the composition of the events and distributions in the data, ATLAS generates fully simulated Monte Carlo samples that behave like the raw data from the detector. Monte Carlo samples used in this analysis were produced as part of the ATLAS `mc08`, `mc09`, `mc10`, `mc11c`, and `mc12a` production campaigns.

3.6.1 Generation

In the ATLAS simulation infrastructure [118], first Monte Carlo matrix element generators produce the primary kinematics from simulated proton-proton scattering events. Final-state quarks and gluons go through a simulated *hadronization* step producing the out-going hadrons.

Unless otherwise noted, background processes from W and Z + jets events were generated with Alpgen [119]. Samples of $t\bar{t}$, Wt, and diboson events (WW, WZ, and ZZ) were generated with MC@NLO [120]. For all of these Monte Carlo samples, the simulated parton shower and hadronization was done with Herwig [121] interfaced with Jimmy [122], specially tuned for the underlying event at ATLAS [123]. Samples of s-channel and t-channel single top events were generated with AcerMC [124], with the parton shower and hadronization done with PYTHIA [125]. Signal samples representing hypothetical Z' decays consistent with the SSM were generated with PYTHIA. The effects of QED radiation were generated with PHOTOS [126], and hadronic tau decays were generated with TAUOLA [127].

3.6.2 Detector simulation

After generation, the detector response for each Monte Carlo sample was fully simulated with a GEANT4 [128] model of the ATLAS detector, with a detailed description of the geometry and amount of material. Activity from multiple pile-up interactions per bunch crossing was modeled by overlaying simulated minimum bias events, generated with PYTHIA and specially tuned for

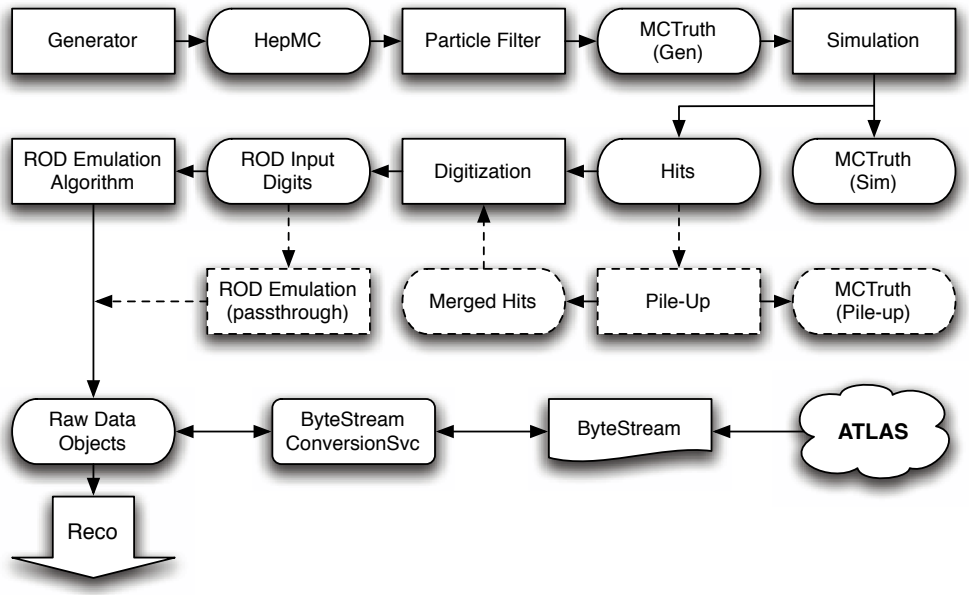

Figure 3.24: The flow of the ATLAS simulation software, from event generators (top-left) through to the reconstruction (bottom-left). Additional minimum bias pile-up events are generated and overlaid. Monte Carlo truth is saved in addition to energy depositions in the detector (hits). Digitization simulates the read-out electronics and RODs to give simulated raw data that is processed with the Athena reconstruction like the data from ATLAS [82].

minimum-bias interactions at the LHC [129], over the original hard-scattering event. Then the Monte Carlo was processed by sub-detector-specific *digitization* algorithms, which translate the particle signatures in the detectors into raw byte-stream data of the form that comes from the ATLAS detector. Finally, the fully simulated RDOs are reconstructed with an appropriate release of the ATLAS Athena reconstruction software just like the processing of the real data. Figure 3.24 illustrates the process of producing ATLAS Monte Carlo simulation, beginning at the generator in the top-left, going through the GEANT4 simulation, generating and merging pile-up events, through digitization, and pushed through the ATLAS reconstruction.

3.6.3 Corrections and scale factors

The accuracy in modeling several effects by the ATLAS simulation is corrected and validated in control samples of the data, including effects like trigger and identification efficiencies and the distribution of the number of primary vertices[20]. Generally, *scale factors* are used as parametrized corrections, derived in control samples to bring the Monte Carlo into agreement with the data. This can significantly improve the accuracy of the yields predicted by the simulation. The systematic

[20] See the discussion of primary vertex re-weighting in Section 5.3.2.

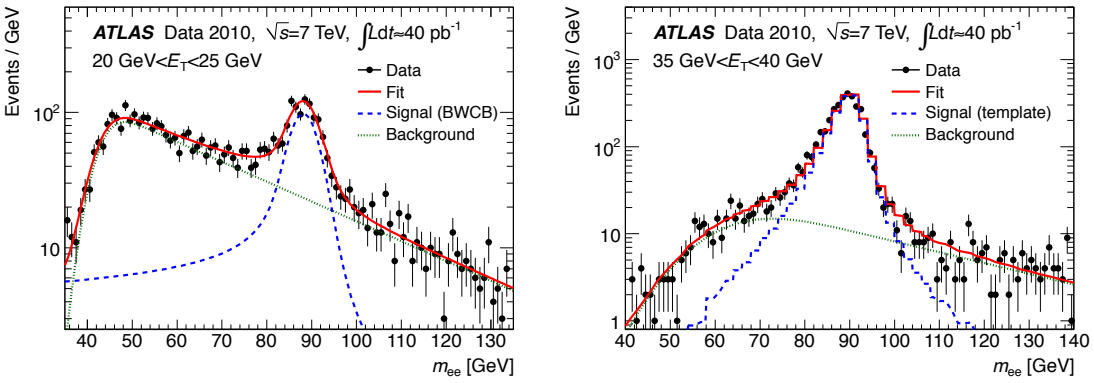

Figure 3.25: The distributions of the dielectron invariant mass of $Z \to ee$ candidate events, before applying electron identification cuts on the probe electron, in the E_{T}-range 20–25 GeV (left) and 35–40 GeV (right) [90].

uncertainties on the scale factors estimated in these performance studies are primary sources of systematic uncertainties for analyses of ATLAS data.

A common method for deriving a scale factor is the *tag-and-probe* method. Essentially it involves selecting a control sample for which the purity can be estimated, without requiring the identification requirement in question. As an example[21], consider the $Z \to ee$ tag-and-probe study of the electron identification efficiency. $Z \to ee$ events are tagged by selecting events with a single tight electron and another "probe" candidate, without the full identification requirements. Then the efficiency of requiring that identification is compared with data and Monte Carlo simulation. The ratio of data to Monte Carlo is parametrized (as a function of p_{T}, η, ...) to be used as a scale factor to weight Monte Carlo events. It is important that the fake electron background is estimated and subtracted in the calculation of the efficiency. Figure 3.25 shows distributions of the dielectron invariant mass in the $Z \to ee$ tag-and-probe sample, before requiring electron identification on the probe electron.

3.7 Computing

3.7.1 Infrastructure

The demands of the ATLAS computing infrastructure include the real-time processing and reconstruction of the data accepted by the Event Filter at 500 MB/s, large-scale production of Monte Carlo simulation, large-scale re-reconstruction and derived-data production for both ATLAS data and simulation, and analysis jobs from ATLAS collaborators world-wide.

[21] Also see the discussion of the tau identification efficiency measurement using a $Z \to \tau\tau$ tag-and-probe sample in Section 4.4.6.

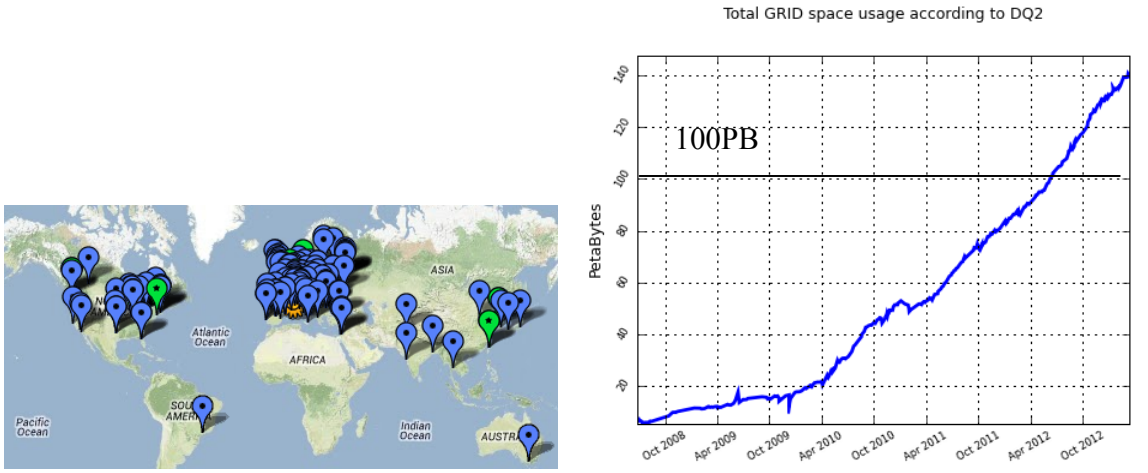

Figure 3.26: (left) Locations of the sites of WLCG computing centers with an orange spot indicating tier-0 at CERN, green spots indicating the 10 tier-1 centers, and blues spots indicating tier-2 centers [130]. (right) The amount of data available to ATLAS users on the WLCG grid, including replicas, as a function of time. By the end of 2012, the data volume exceeded 140 PB = 140 million GB [131].

To satisfy these demands the LHC collaborations have formed the largest existing scientific computing grid, the Worldwide LHC Computing Grid (WLCG). The WLCG utilizes over 100,000 CPUs in more than 170 computing centers located within 36 countries. In the US, this includes the resources of the Open Science Grid (OSG). Figure 3.26 (left) indicates the locations of WLCG sites around the world. Combining data and Monte Carlo production, the four large experiments at the LHC produce about 25 PB of data per year [130]. By the end of 2012, the combined distributed data volume from ATLAS data and Monte Carlo, including replicas, exceeded 140 PB (see Figure 3.26 (right)).

The WLCG has a tiered architecture, with tier-0 being a $\sim$ 1000 CPU computer farm at CERN doing the real-time first-pass reconstruction of the data from ATLAS (see Figure 3.27). The output ESDs and AODs are archived at tier-0. The AODs and a fraction of the ESDs are copied to the 10 tier-1 centers around the world and a few additional replicas are distributed among the tier-2 sites, numbering over a hundred. The data are flattened in large scale productions of ROOT [133] compatible ntuples, denoted "D3PDs", which are also distributed among tier-1 and tier-2 sites. Users doing analysis often produce more derived ntuples on the grid, and then download them to a private computing cluster or tier-3 where further analysis is done.

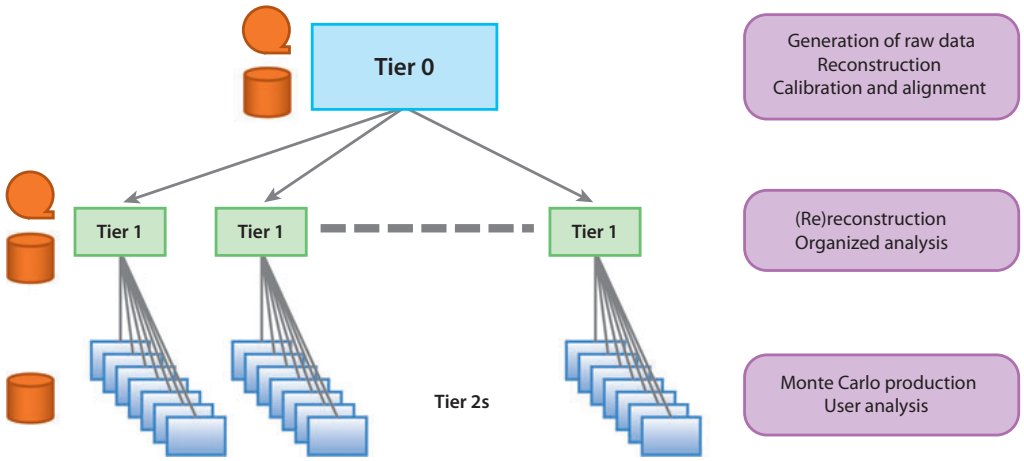

Figure 3.27: An illustration of the tiered structure of the ATLAS computing infrastructure [132].

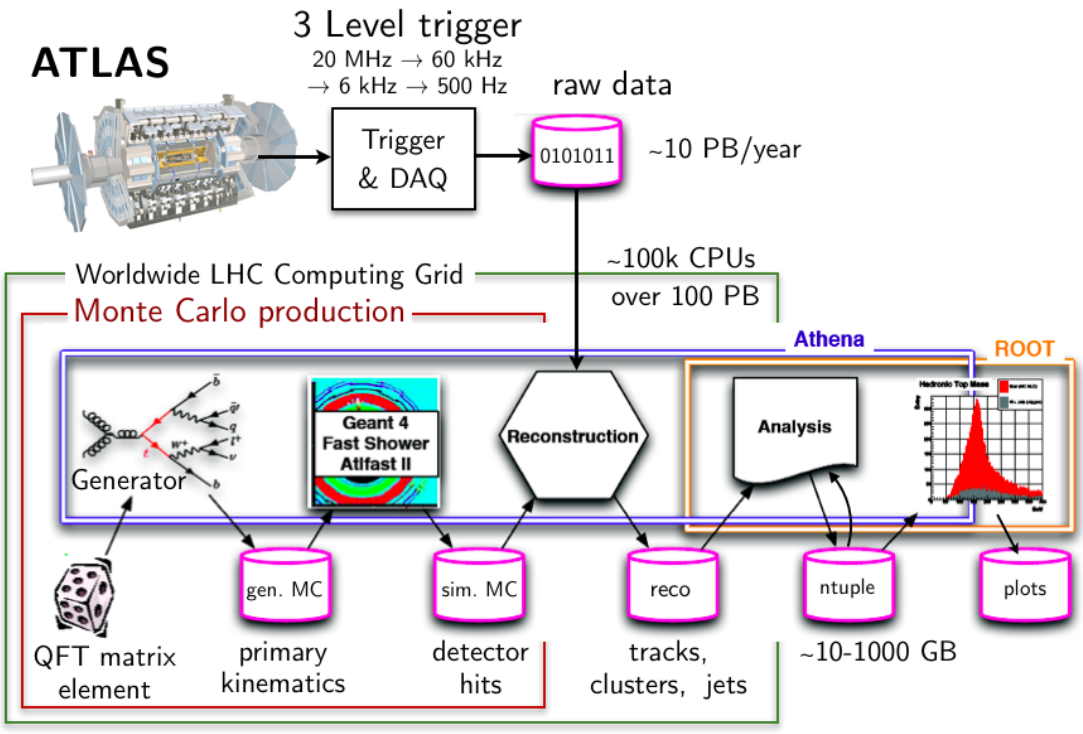

Figure 3.28: An illustration of the flow of ATLAS data as it is reconstructed and analyzed on the WLCG computing grid. The process of producing Monte Carlo simulation and pushing it through the same reconstruction and user analysis is also shown [134].

3.7.2 Data reduction

The data from ATLAS are reduced significantly by reconstruction and selection. Figure 3.28 re-caps the flow of ATLAS data and Monte Carlo. Starting at the top-left, the ATLAS data that pass the 3-level trigger system are recorded and reconstructed, producing the AODs, ESDs, and later D3PDs (collectly denoted "reco" in Figure 3.28). Note that Monte Carlo production involves processing the simulation through the same reconstruction and analysis procedures as the data from the ATLAS detector.

In analysis steps, a user may produce and iterate on one or more cycles of derived ntuples, and usually produce several plots to visualize the data. The sequence of progressively reduced data formats used can be summarized as

$$\text{RAW} \rightarrow \text{RDO} \rightarrow \text{AOD/ESD} \rightarrow \text{D3PD} \left(\rightarrow \text{skimmed D3PD} \rightarrow \text{personalized ntuple} \right).$$

Table 3.5 summarizes the typical sizes per event of the various data formats.

Table 3.5: A summary of the size per event for various ATLAS data formats [135].

data format	size per event
raw data	1–2 MB
ESD	1–2 MB
AOD	100–200 kB
D3PD	100–200 kB
personalized ntuple (TNT)	2–3 kB

Chapter 4

Tau reconstruction and identification

In this chapter, I describe the ATLAS reconstruction of hadronic tau decays and many of the advancements in tau identification and calibration during 2010–2012. In particular, I focus on topics to which I personally contributed including: the first comparisons of ATLAS data and Monte Carlo for tau identification variables in minimum-bias events in 2009, the development of the first cut-based tau identification used with ATLAS data in 2010, the p_{T}-parameterized tau identification, and studies of fake rates and pile-up robustness, but I also try to pedagogically review other major developments, which helps to introduce many of the technical issues and systematic uncertainties involving reconstructed taus, used by the analysis discussed in the following chapters.

4.1 Introduction

Having a mean lifetime of 2.9×10^{-13} seconds ($c\tau \approx 87$ μm), tau leptons decay before leaving the ATLAS beam pipe. Tau leptons can decay leptonically, either to $e\nu_e\nu_\tau$ (branching ratio, BR $\approx$ 17.9%) or to $\mu\nu_\mu\nu_\tau$ (BR $\approx$ 17.4%). In the remaining majority of cases (BR $\approx$ 64.7%), tau leptons decay hadronically, being the only leptons massive enough to do so ($m_\tau \approx 1.8$ GeV). These hadronic final states predominantly consist of one or three charged pions, along with a neutrino, and possibly with a few additional neutral pions. There are also rarer decays involving kaons, with a branching fraction of 2.9%. The hadronic decays of tau leptons are generally categorized by the number of charged decay products, that is, the number of tracks or "prongs" observable in the detector. Hadronic 1-prong decays are the most common (BR $\approx$ 49.5%), followed by 3-prong decays (BR $\approx$ 15.2%). Figure 4.1 illustrates the approximate branching ratios of the tau lepton. Throughout this thesis, "1-prong" refers to the hadronic decay modes with a single track, excluding the leptonic decays of the tau lepton.

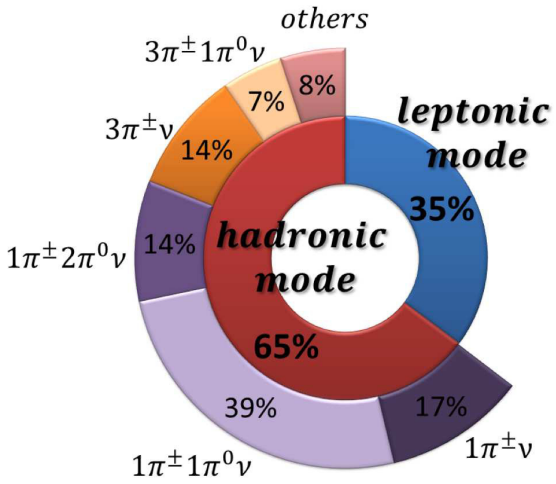

Figure 4.1: The approximate branching ratios of the dominate decay modes of the tau lepton. For the decays within the hadronic mode, the branching ratios are shown as the fraction of the total hadronic mode and not the fraction of all decays.

A majority of hadronic decays of the tau lepton go through the intermediate mesons:

$$\rho^{\pm}(770\,\mathrm{MeV}) \qquad \mathrm{I^G(J^{PC})} = 1^{+}(1^{--})$$

$$\tau \to \nu\,\rho^{\pm} \to \pi^{\pm}\,\pi^{0}\,\nu \qquad 26\%\ \text{of BR}(\tau)\,,$$

corresponding to 39% of the hadronic mode, and

$$a_1^{\pm}(1260\,\mathrm{MeV}) \qquad 1^{-}(1^{++})$$

$$\tau \to \nu\,a_1^{\pm} \to \pi^{\pm}\,2\pi^{0}\,\nu \quad 9\%\ \text{of BR}(\tau)$$

$$\tau \to \nu\,a_1^{\pm} \to 3\pi^{0}\,\nu \qquad 9\%\ \text{of BR}(\tau)\,,$$

each corresponding to 14% of the hadronic mode [136].

The challenge when identifying hadronic tau decays at high-energy hadron colliders is that the cross section for QCD production of quark or gluon initiated jets, which can be falsely identified as tau decays, is many orders of magnitude above the cross sections for weak interaction processes involving tau leptons[22]. Indeed, most of the tracks reconstructed in the ATLAS inner dectector are from charged pions from inclusive QCD processes. Reconstructing and identifying hadronic tau decays involves distinguishing tau-like groupings of pions from other generic pions. The most discriminating features for identifying taus among the multijet background are the characteristic 1- or 3-prong signature of a hadronic tau decay, consequently low track multiplicity, relatively narrow

[22] For example, the jet production cross section is approximately 4×10^3 nb for inclusive jets with $p_{\mathrm{T}} > 60$ GeV and $|\eta| < 2.8$ [137], while the cross section for $W \to \tau_{\mathrm{h}}\nu$ production is 6.8 nb at $\sqrt{s} = 7$ TeV [138].

clustering of tracks and depositions in the calorimeters, and the existence of a possible displaced secondary vertex.

4.2 Tau reconstruction

4.2.1 Overview

The reconstruction of candidates for hadronically decaying tau leptons occurs late in the ATLAS reconstruction chain. Tracks and clusters have already been reconstructed, and clusters have been grouped with jet-finding algorithms (see Section 3.3). Tau reconstruction can be split into the following steps. First, tau reconstruction is seeded by each reconstructed jet. Then, the list of calorimeter clusters associated to each tau candidate[23] is refined and calibrated to calculate the four-momentum. Tracks are then associated to the candidate, and a list of identification variables is calculated for each candidate from the combined tracking and calorimeter information. Last, these variables are combined into multivariate discriminants to reject fake candidates from QCD jets and electrons [100, 101, 102, 103].

4.2.2 Seeding

Tau reconstruction is seeded by calorimeter jets, reconstructed with the anti-k_t algorithm [94], using distance parameter $R = 0.4$, from three-dimensional topological clusters [91] of the cells in both the EM and hadronic calorimeters. Each such jet with $p_{\mathrm{T}} > 10$ GeV (at the EM-scale) and within $|\eta| < 2.5$, (the η-range of the ATLAS tracking system) is considered as a tau candidate.

The reconstruction efficiency for true hadronic tau decays is nearly 100% for tau candidates with $p_{\mathrm{T}} \gtrsim 15$ GeV and $|\eta| \lesssim 2.3$, however, this efficiency is only to get a reconstructed candidate in the calorimeter, irrespective of the track association. After associating reconstructed tracks to the candidate, the efficiency to correctly identify 1- and 3-prong suffers some track-finding inefficiency[24] for each track, degrading the efficiency to correctly reconstruct 3-prong with 3-tracks more than that of 1-prong (see Figure 4.2).

[23] There's been perhaps too much debate about notation in ATLAS [139], although I agree that one should be clear. My conventions in this thesis are "1-prong" tau decays are *hadronic* only. The symbol "τ_{h}" denotes the visible sum of a hadronic tau decay, but not the neutrinos. So I would write "$Z \to \tau\tau \to \mu\tau_{\mathrm{h}}3\nu$". And "$p_{\mathrm{T}}(\tau_{\mathrm{h}})$" makes sense, as the visible, reconstructible transverse momentum of a hadronic tau decay, not including the neutrinos. I also often write and say "tau candidate", intending it to be short for a "reconstructed candidate for a tau lepton that decayed hadronically". But I am generally careful to reserve a lone "tau" to refer to the lepton, or to emphasize "tau lepton".

[24] Within the ATLAS Tau Performance Group, to incorrectly reconstruct the number of tracks for a hadronic tau decay is often called"track migration", referring to the migration from one bin to another in the distribution of the number of reconstructed tracks (see Figure 4.5). Some effort to mitigate the track association inefficiency with respect to pile-up will be discussed in Section 4.2.5. Issues with tracking inefficiency at high-p_{T} will be discussed in Section 4.4.7.

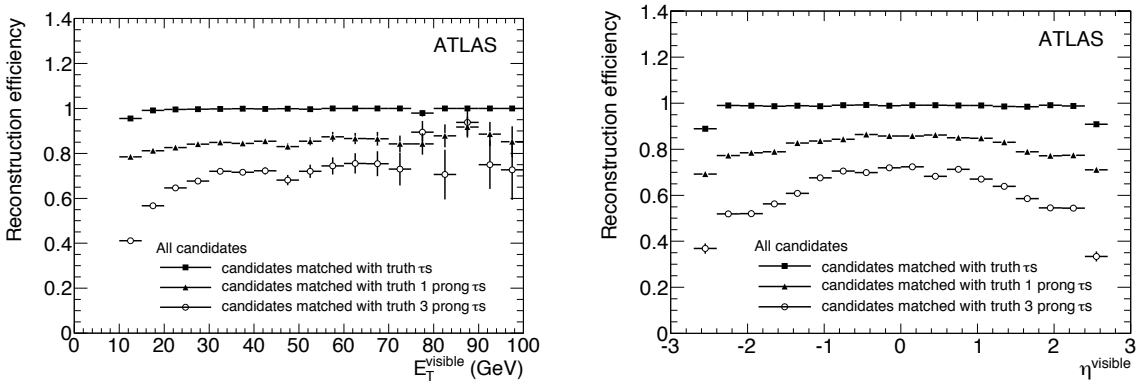

Figure 4.2: The reconstruction efficiency of true hadronic decays of tau leptons as a function of $E_{\mathrm{T}}^{\mathrm{visible}}$ and η^{visible} from a sample of MC $W \to \tau\nu$ events (`mc08`) [140].

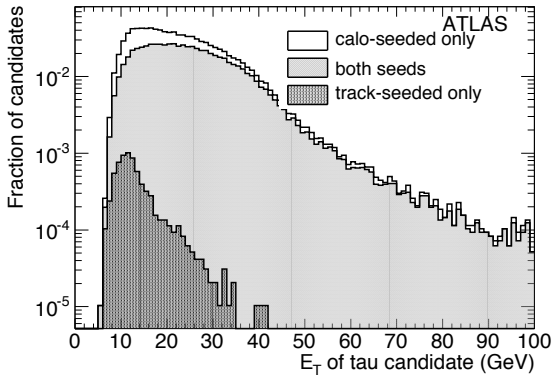

Figure 4.3: The overlap between track and calorimeter seeds as a function of E_{T} in a Monte Carlo sample of true $W \to \tau_{\mathrm{h}}\nu$ decays (`mc08`) [140].

Historically, ATLAS developed two independent reconstruction algorithms for hadronic tau decays: the calorimeter-seeded `tauRec`, which used the jet seeding described above, and the track-seeded `tau1p3p`, which was seeded by inner-detector tracks with $p_{\mathrm{T}} > 6$ GeV. Figure 4.3 shows the overlap between track and calorimeter seeds as a function of E_{T} in a Monte Carlo sample of true $W \to \tau_{\mathrm{h}}\nu$ decays. In 2009, since the track seeds were effectively a subset of the calorimeter seeds, the `tauRec` algorithm became the preferred reconstruction seed, and the identification variables calculated by the two algorithms were merged [140].

4.2.3 Four-momentum definition

The reconstructed four-momentum of a tau candidate is defined in terms of three degrees of freedom: p_{T}, η, and ϕ. The η and ϕ are taken from the seed jet, and are determined by calculating the sum of the four-vectors of the constituent topological clusters, assuming zero mass for each of

the constituents [93]. The mass of tau candidates is defined to be identically zero, and therefore transverse momentum, p_{T}, and transverse energy, $E_{\mathrm{T}} = E \sin\theta$, are identical. Because hadronic tau decays consist of a specific mix of charged and neutral pions, the energy scale of hadronic tau candidates is calibrated independent of the jet energy scale with a Monte Carlo based calibration procedure using the clusters within $\Delta R < 0.2$ of the seed jet barycenter axis. The tau energy calibration is described later, in Section 4.4.5.

4.2.4 Track counting

Tracks are associated to each tau candidate if they are within the *core cone*, defined as the region within $\Delta R < 0.2$ of the axis of the seed jet, and pass the following quality criteria:

- $p_{\mathrm{T}} > 1$ GeV,
- number of pixel hits ≥ 2,
- number of pixel hits + number of SCT hits ≥ 7,
- $|d_0| < 1.0$ mm,
- $|z_0 \sin\theta| < 1.5$ mm,

where d_0 is the distance of closest approach, in the plane transverse to the beamline, of the track to the selected primary vertex (discussed in the next section), while z_0 is the distance of closet approach along the beamline.

Tau candidates are classified as single- or multi-prong, depending on the number of tracks counted in the core cone. The charge of a tau candidate is reconstructed as the sum of the charges of the associated tracks in the core cone. Tracks within the *isolation annulus*, defined by $0.2 < \Delta R < 0.4$ of the axis of the seed jet, are also counted for variable calculations, and are required to satisfy the same track quality criteria.

4.2.5 Vertex selection

In order to select the vertex representing the interaction of hardest-scatter in an event, typically analyses select the vertex with the highest $\sum p_{\mathrm{T}}^2$ of the tracks associated to it. As discussed in the previous section, it is important to define a vertex with which to calculate z_0 and d_0 for selecting the tracks to associate to a tau candidate. As the instantaneous luminosity, and consequently the number of reconstructed vertices per event grew at the LHC, the probability also grew for a tau candidate to originate from a vertex without the highest $\sum p_{\mathrm{T}}^2$, and therefore fail to have its track

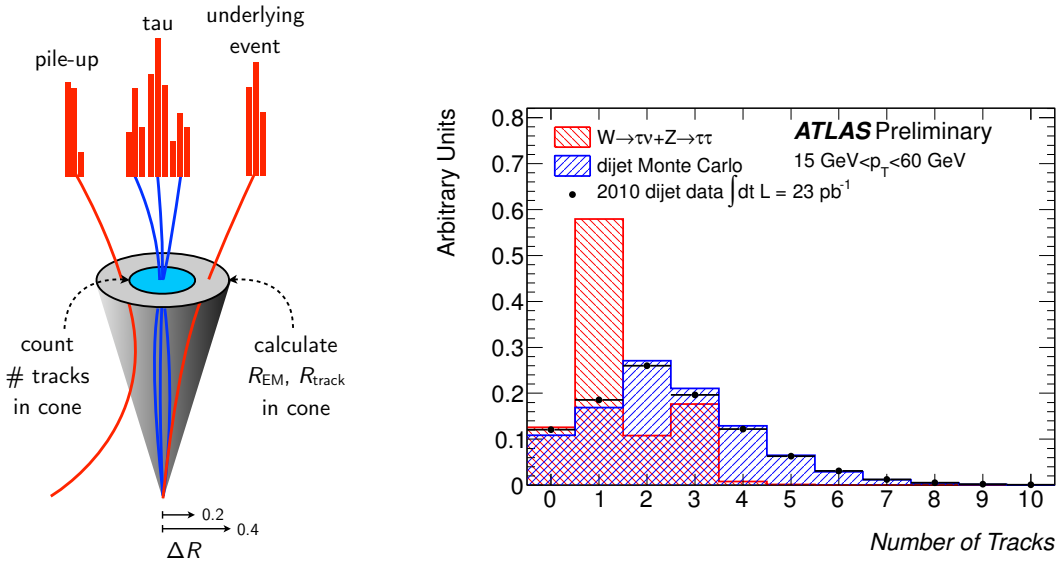

Figure 4.4: (left) A sketch illustrating things that can affect tau identification, and that the core tracks are counted in $\Delta R < 0.2$, while many ID variables are calculated in $\Delta R < 0.4$. (right) The N_{track} distribution for simulated hadronic decays of taus in MC $W \to \tau\nu$ and $Z \to \tau\tau$ events, and the distribution for a selection of dijet background events from both the 2010 data and compared with PYTHIA dijet MC (`mc09`) [100].

selected (see Figure 4.5). While initially the ATLAS tau reconstruction chose the vertex with the highest $\sum p_{\text{T}}^2$, it was improved beginning in 2012 to choose the vertex with the highest JVF[25] for that tau candidate. This method selects the vertex to which a significant fraction of the tracks pointing at that tau candidate are associated, improving the efficiency to select the correct vertex and core tracks, even in the high pile-up scenario with $\mu \approx 40$ [102].

4.3 Tau identification

4.3.1 Identification variables

As every seed jet forms a tau candidate, the reconstruction of tau candidates provides virtually no rejection against the multijet background to hadronically decaying tau leptons. This rejection is achieved in a separate identification (ID) step, using discriminating variables that are calculated during the reconstruction. In this section, the distributions of some of the most important variables are shown, and the use of those variables in tau identification is discussed.

As discussed previously, hadronic tau decays can be distinguished from generic QCD jets because they are generally narrow and well isolated, with one or three tracks. Three of the most important

[25] JVF is discussed in some detail in Section 3.3.6.

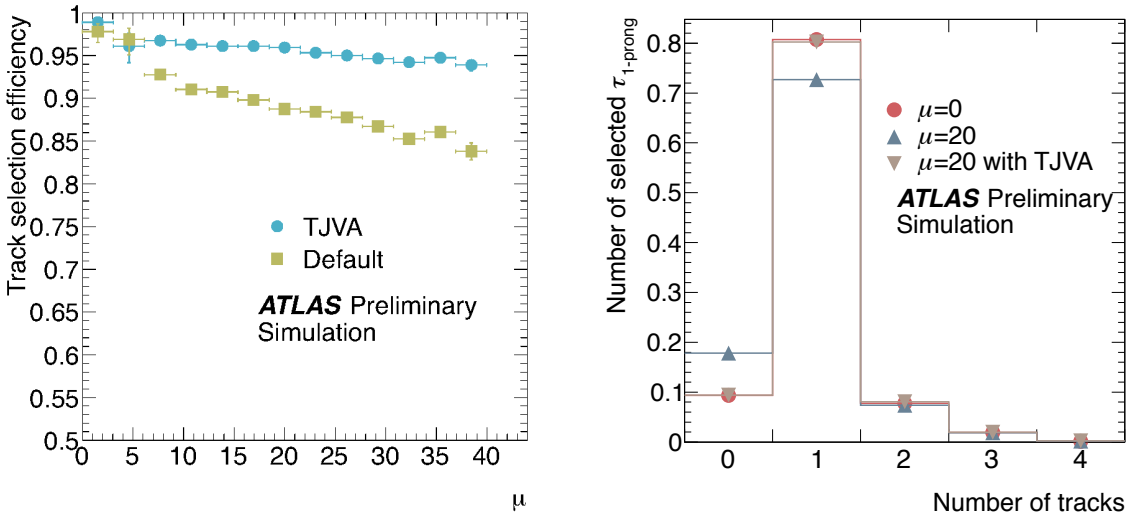

Figure 4.5: (left) The reconstruction efficiency to correctly select the track from a 1-prong hadronic decay as a function of μ in MC $Z \to \tau\tau$ events from `mc11`, using track selection with respect to the "Default" vertex with the highest $\sum p_{\mathrm{T}}^2$, or with respect to the vertex with the highest JVF, called "Tau Jet Vertex Association (TJVA)" in this figure. (right) The N_{track} distribution in ideal MC with no additional pile-up ($\mu = 0$), compared to the distribution with significant pile-up ($\mu = 20$), showing both the Default and TJVA vertex selection (`mc11`) [102].

tau identification variables used by the cut-based identification quantify the narrowness of a tau candidate in the calorimeter, the close association of the calorimeter activity with one or three tracks, and the momentum fraction carried by the leading track. They are:

Electromagnetic radius (R_{EM}): the transverse energy weighted shower width in the electromagnetic (EM) calorimeter:

$$R_{\mathrm{EM}} = \frac{\sum_{i\in\{\mathrm{EM\ 0-2}\}}^{\Delta R_i<0.4} E_{\mathrm{T},i}\,\Delta R_i}{\sum_{i\in\{\mathrm{EM\ 0-2}\}}^{\Delta R_i<0.4} E_{\mathrm{T},i}},$$

where i runs over cells in the first three layers of the EM calorimeter (pre-sampler, layer 1, and layer 2), associated to the tau candidate.

Track radius (R_{track}): the p_{T} weighted track width:

$$R_{\mathrm{track}} = \frac{\sum_{i}^{\Delta R_i<0.4} p_{\mathrm{T},i}\,\Delta R_i}{\sum_{i}^{\Delta R_i<0.4} p_{\mathrm{T},i}},$$

where i runs over all core and isolation tracks of the tau candidate, and $p_{\mathrm{T},i}$ is the track transverse momentum. Note that for candidates with only one track, R_{track} simplifies to the ΔR between the track and the tau candidate axis.

Leading track momentum fraction (f_{track}):

$$f_{\text{track}} = \frac{p_{\text{T},1}^{\text{track}}}{p_{\text{T}}^{\tau}},$$

where $p_{\text{T},1}^{\text{track}}$ is the transverse momentum of the leading p_{T} core track and p_{T}^{τ} is the transverse momentum of the tau candidate, calibrated at the EM energy scale. Note that for candidates with one track, f_{track} is the fraction of the candidate's momentum attributed to the track, compared to the total momentum of the candidate, which can have contributions from the calorimeter deposits from π^0s and other neutrals.

A more complete list of the definitions of the various tau identification variables is given in Appendix B. Distributions of these and other tau identification variables are shown in Figures 4.6 and 4.12-4.14, showing ATLAS simulation of $Z \to \tau\tau$ and $W \to \tau\nu$ for signal, and comparing simulation of dijet events with a sample of dijet events in the 2010 data for background. Table 4.3 shows which identification variables were used by the ATLAS jet-tau discriminants to analyze the 2010 dataset [100].

4.3.2 Cut-based jet-tau discrimination

After the preliminary first collisions at the LHC at $\sqrt{s} = 900$ GeV in 2009, efforts in ATLAS began converging to deliver tau discriminants for the first record-energy collisions at $\sqrt{s} = 7$ TeV in 2010, the year ATLAS would collect its first significant sample of W and Z boson decays. The simple cut-based identification was optimized with only three of the well-studied variables, and binned in the number of reconstructed core tracks, being one or many. The three variables used are those discussed in the previous section and quantify: the narrowness of the tau candidate in the calorimeter, the close association of the seed jet and the selected tracks, and the fraction of the reconstructed momentum carried by the leading track [141].

The cuts were optimized in three separate *working points*, called "*loose*", "*medium*", and "*tight*", which are approximately 60%, 50%, and 30% efficient to reconstruct and identify hadronic tau decays with the correct number of tracks. The optimization used a cross-section-weighted sample of fully simulated $W \to \tau\nu$ and $Z \to \tau\tau$ decays to model the signal. A fully simulated sample of dijet events was used to model the background. Figure 4.6 shows distributions of the variables used by the cut-based tau identification, for both signal and background samples, as well as the critical values of the cuts for the identification working points.

The working points were optimized by exhaustively constructing each possible combination of cuts on the three variables in reasonably spaced steps, and evaluating their signal and background efficiencies. The combinations that gave efficiencies near the loose/medium/tight targets were then

selected and sorted by background efficiency. The final working points were then chosen among the combinations of cuts giving the target signal efficiencies, by selecting those which minimize the background efficiency, under the constraint that the candidates that pass the medium identification are a subset of those that pass loose, and tight a subset of medium. Table 4.1 shows the critical values of the cuts for the working points, as well as their signal and background efficiencies as estimated with simulation [142].

With the 2010 collision data collected by ATLAS, this simple cut-based approach was used for the first data-MC comparisons of tau candidates [144] (discussed in Section 4.4.1), the first observation of $W \to \tau\nu$ [145] (discussed in Section 4.4.2), and the first observation of $Z \to \tau\tau$ [146] (discussed in Section 5.5),

4.3.3 p_{T}-parametrized cuts

Following the initial use of the cut-based tau identification in 2010, the cuts were updated to have a more uniform efficiency as a function of the candidate p_{T}. Like the previous version, the method still uses cuts on only three variables: R_{EM}, R_{track}, and f_{track}, binned in candidates that have one or multiple tracks. The method has been improved by parameterizing the cuts on R_{EM} and R_{track} by the p_{T} of the tau candidate, since the optimal cuts are very p_{T}-dependent because of the Lorentz collimation of the decay products in hadronic tau decays. Figure 4.7 shows *profile plots*[26] of the p_{T}-dependence of several of the tau ID variables for both signal and background distributions.

Two of the three variables (R_{EM}, R_{track}) used by the cut-based identification rely on the narrowness of the width of the hadronic shower in tau decays compared to QCD jets. While the tau can

[26] The plots in Figure 4.8 are examples of *profile plots* which refer to 2-dimensional histograms that has been averaged along one of its dimensions, resulting in a 2-d plot of the mean of some variable $\langle y \rangle$ in bins of some other variable x, often also with the standard deviation of y visualzed as a band in the same bins.

Table 4.1: The values of the loose/medium/tight cuts for the working points of the 2010 simple cut-based ID [142].

R_{EM} <	R_{track} <	$f_{\mathrm{trk,1}}$ >	sig eff	bkg eff
1-prong				
0.08	0.09	0.06	0.599	0.137
0.07	0.08	0.12	0.497	0.0825
0.05	0.08	0.12	0.274	0.0262
3-prong				
0.15	0.12	0.12	0.57	0.468
0.12	0.08	0.24	0.499	0.161
0.09	0.05	0.32	0.296	0.0282

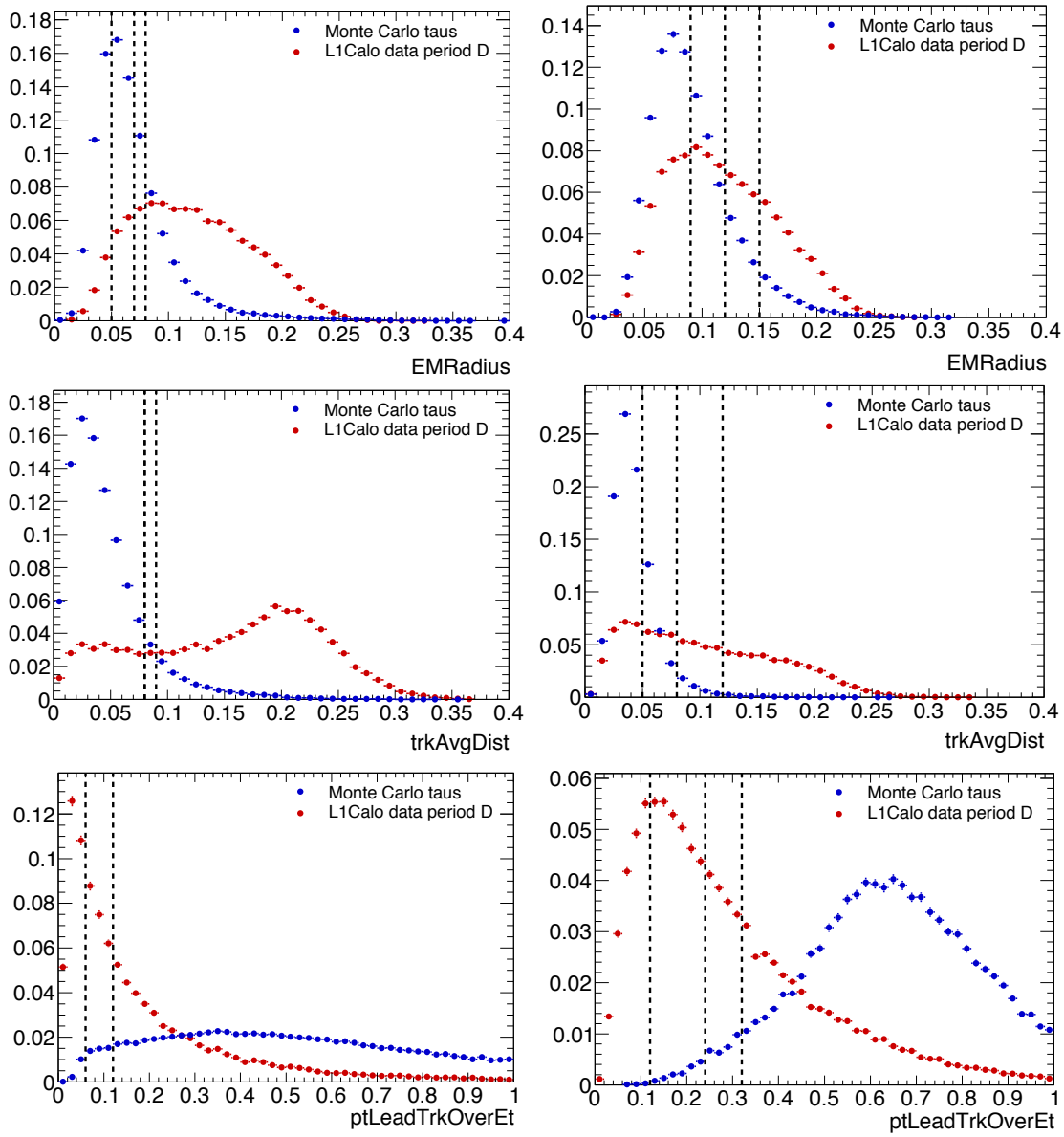

Figure 4.6: The distributions for the three tau identification variables used by the cut-based ID for 1-prong (left) and 3-prong (right) candidates. The signal sample is MC $Z \to \tau\tau$ events (blue) and the background is dijet events from 2010 (red). The cuts for the working points are indicated by the dashed lines. The values of these cuts are shown in Table 4.1 (`mc09`) [143].

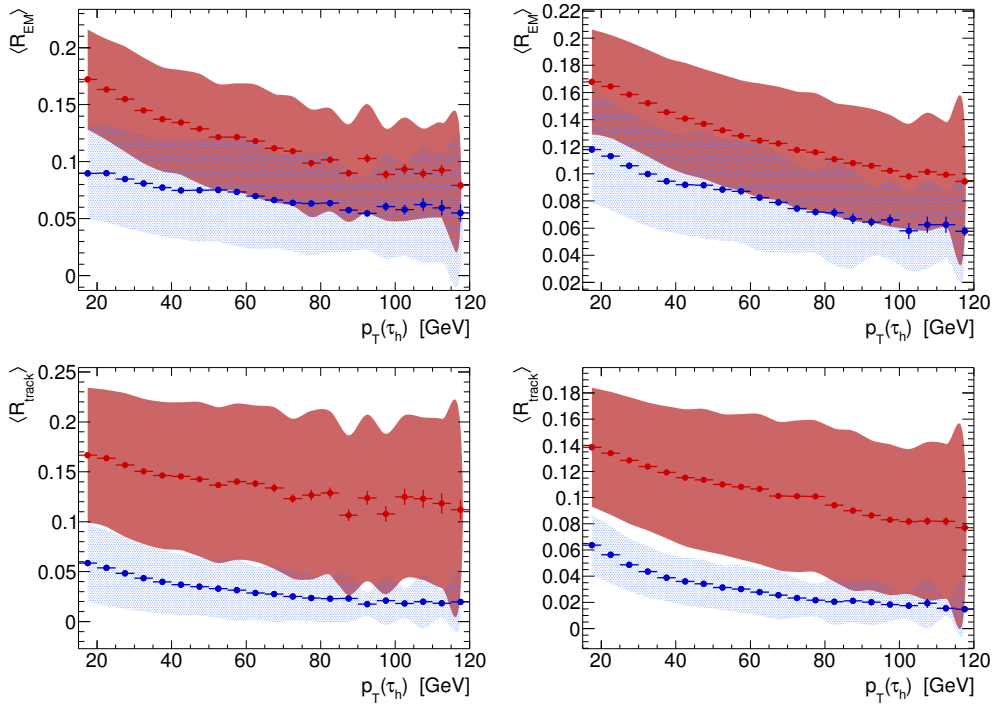

Figure 4.7: The dependence of key tau identification variables as a function of the candidate p_{T}, separately for 1-prong (left) and 3-prong (right) tau candidates. The points indicate the means in each bin. The colored bands indicate the standard deviation. The blue points correspond to tau candidates matched to hadronically decaying taus in simulated $W \to \tau\nu$ and $Z \to \tau\tau$ events. The red points are for the dijet sample from data (`mc10`) [117].

send its decay products in any direction in the rest frame of the tau lepton, taus are not produced at rest in the ATLAS detector. In the laboratory frame, the decay products will be collimated along the momentum of the tau lepton. The Lorentz boost to the laboratory frame implies that width-like variables, R, should collimate as

$$R(p_{\mathrm{T}}) \propto 1/p_{\mathrm{T}}.$$

This can be seen by noting that width-like variables, R, depend linearly on an average among the angles, $\Delta\phi$, between axis of the jet seed and the momentum vector of constituent pions in the tau decay. For small angles, this is approximately $\tan\Delta\phi$, which is the ratio of a constituent's momentum transverse to the jet axis, k_{T}, and the total reconstructed momentum of the tau candidate transverse to the beam line, p_{T}. Therefore,

$$R \propto \Delta\phi \approx \tan\Delta\phi = k_{\mathrm{T}}/p_{\mathrm{T}}.$$

The collimation of hadronic tau decays makes the optimal cut on variables like R_{EM} and R_{track} very p_{T}-dependent. Multiplying R by p_{T} should flatten the p_{T}-dependence, and it largely does (see

Figure 4.8). The remaining p_{T}-dependence is parametrized by fitting a second-order polynomial to the means of $R \times p_{\mathrm{T}}$, binned in p_{T}, separately for both signal and background distributions.

$$g(p_{\mathrm{T}}) = a_0 + a_1\, p_{\mathrm{T}} + a_2\, p_{\mathrm{T}}^2$$

Then, possible cut curves between the signal and background distributions were constructed as

$$R^{\mathrm{cut}}(p_{\mathrm{T}}; x)\, p_{\mathrm{T}} = (1 - x)\, g_{\mathrm{sig}}(p_{\mathrm{T}}) + x\, g_{\mathrm{bkg}}(p_{\mathrm{T}})$$

for different values of the parameter x, where $x = 0$ is completely along the mean of the signal distribution, and $x = 1$ is completely along the mean of the background [100].

Figure 4.8 shows that while multiplying R by p_{T} does flatten out the p_{T}-dependence for true hadronic tau decays, QCD jets tend to grow wider with p_{T} at a higher (non-linear) rate, presumably because competing with the effects of Lorentz collimation is the fact that higher-p_{T} jets have more energy to hardonize more particles, producing more tracks and clusters, and thus wider jets [143].

The p_{T}-parametrized cuts were optimized with a method similar to that used for the simple cuts discussed in Section 4.3.2. Possible combinations of critical values for f_{track}, and the x variables for R_{EM} and R_{track}, were exhaustively evaluated in reasonable steps to achieve approximately 60%/50%/30% signal efficiency for the loose/medium/tight working points (respectively), minimizing the background efficiency under the constraint that the candidates that pass medium are a subset of loose, and tight a subset of medium. Unlike the simple cuts that were optimized against simulated dijet events, the p_{T}-parametrized cuts were the first tau discriminant optimized with a background sample from ATLAS data, using a sample of dijet events collected in period G of the 2010 run.

In order to limit the p_{T}-parametrized cuts from indefinitely becoming more strict with p_{T}, the shape of the cut curves are defined piecewise in p_{T}, becoming constant cuts for $p_{\mathrm{T}} \geq 80$ GeV. Figure 4.9 shows the final optimized cut curves for each working point. It shows that while R_{EM} is the most effective discriminating variable for 1-prong decays, R_{track} radius becomes more important for 3-prong. Table 4.2 shows the parametrizations of the cuts for each working point.

Figures 4.10 and 4.11 show the signal and background efficiencies of both the simple cut-based tau identification and the p_{T}-parametrized cuts, estimated using a cross-section-weighted sample of fully simulated $W \to \tau\nu$ and $Z \to \tau\tau$ decays for signal, and a sample of dijet events from ATLAS data for background. They show that the p_{T}-parametrization achieves efficiencies that are more flat in p_{T} for both signal and background, correcting the rising fake rates that were problematic for the simple cut-based identification.

The medium working point of the p_{T}-parametrized cuts was used to identify tau candidates for $Z \to \tau\tau$ cross section measurement with the 2010 ATLAS dataset [113] (as discussed in Chapter 5).

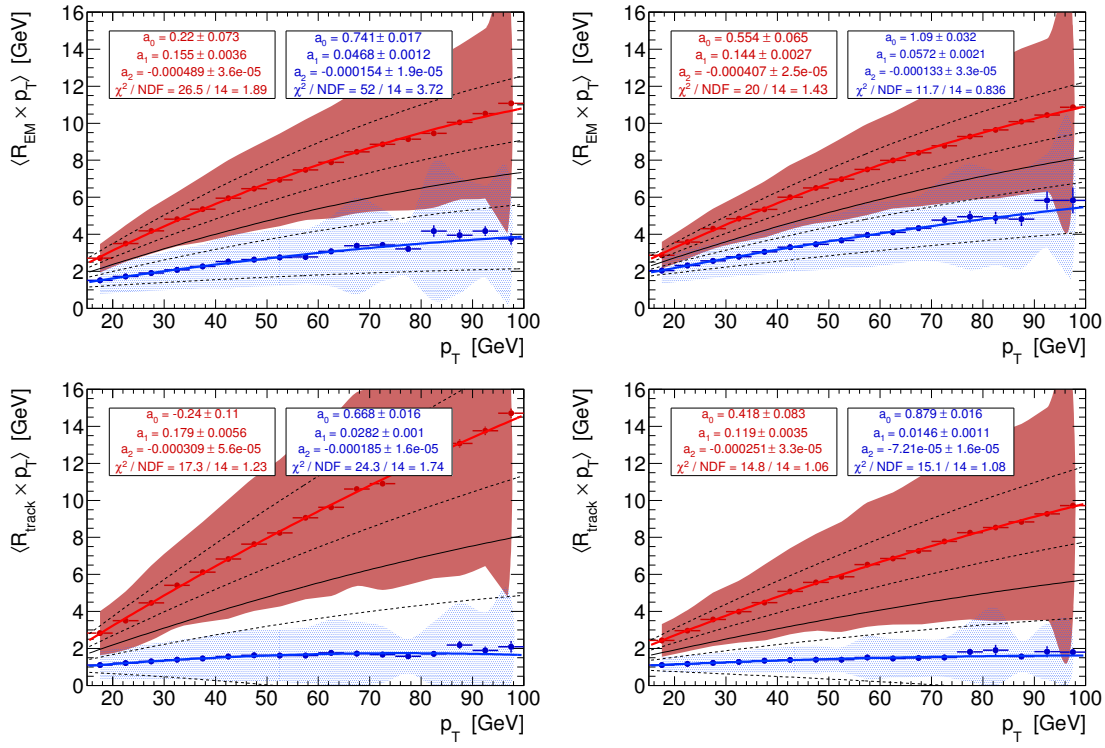

Figure 4.8: Profile plots of $\langle R \times p_{\mathrm{T}} \rangle$ vs the candidate p_{T}, separately for 1-prong (left) and 3-prong (right) tau candidates, for R_{EM} (top) and R_{track} (bottom). The points indicate the means in each bin. The colored bands indicate the standard deviation. The blue points correspond to tau candidates matched to hadronically decaying taus in simulated $W \rightarrow \tau\nu$ and $Z \rightarrow \tau\tau$ events. The red points are for the dijet sample from data (`mc09`) [147].

4.3.4 Multivariate techniques

There have been many efforts to use more sophisticated techniques to identify hadronic tau decays than a cut-based approach, taking advantage of more calorimeter- and tracking-related variables, especially the significance of the transverse displacement of secondary vertex that can be found in multi-prong decays. The two main competing approaches involve using a likelihood ratio based on the combined distributions of the tau identification variables, and the use of boosted decision trees, and are described briefly in this section. Distributions of all of the identification variables used by the discriminants for the 2010 dataset are shown in Figures 4.12-4.14. Table 4.3 compares which variables were used by each discriminant. In 2011, as experience with ATLAS tau identification grew, identification based on likelihoods and boosted decision trees became the preferred techniques.

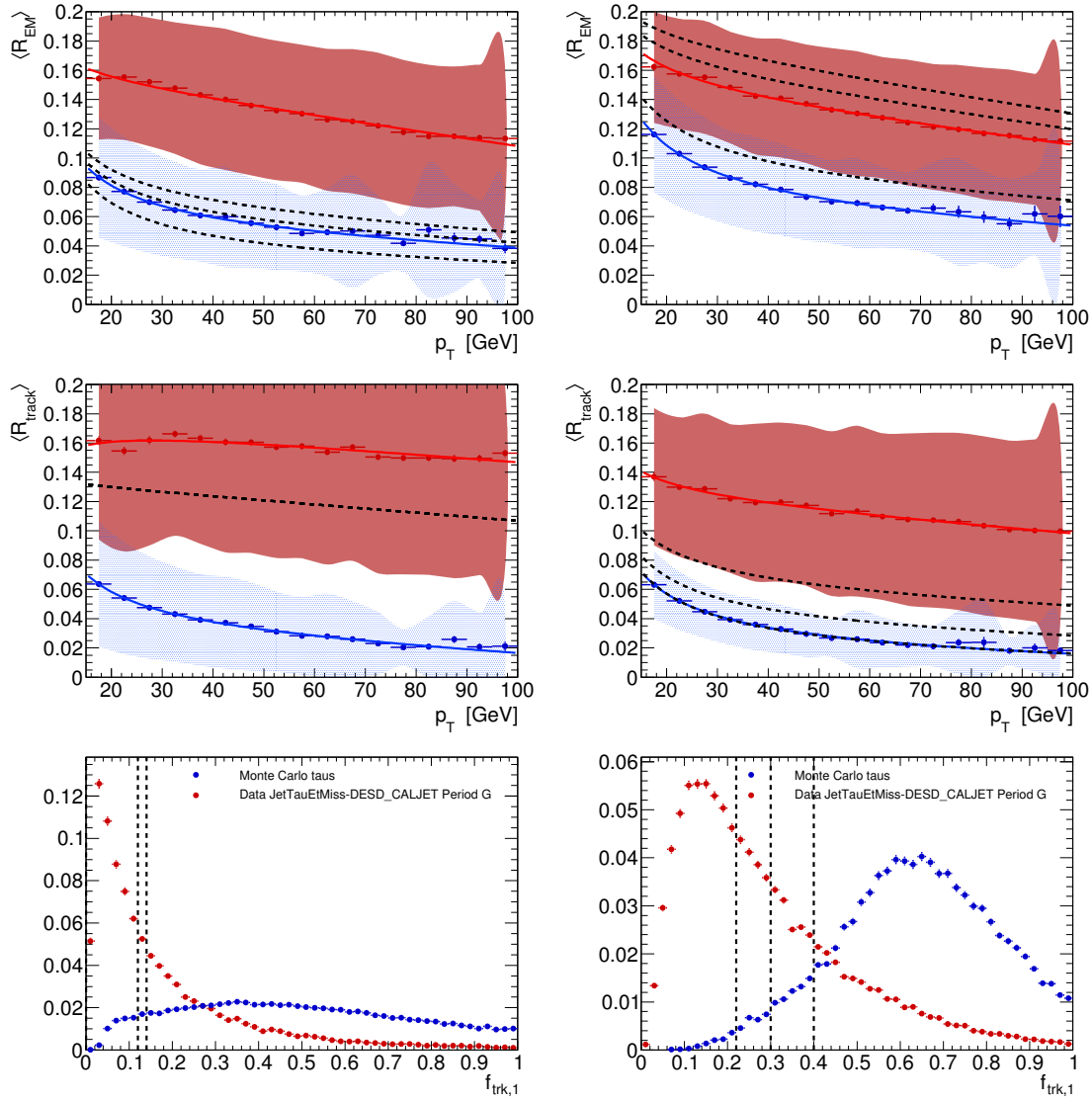

Figure 4.9: The cut values for the working points for the updated p_{T}-parametrized cut-based ID with the 2010 dataset are shown by the dashed lines. Note that the piecewise parts with constant cut values for $p_{\mathrm{T}} \geq 80$ GeV are not shown, but would simply be a flat continuation of the curves shown, beginning at 80 GeV. The same cut values are given in Table 4.2 (`mc09`) [147].

Table 4.2: Parametrized cut values for the updated 2010 working points. The formulas for the parametrized cuts use p_{T} in units of GeV. Currently, $1/f_{\mathrm{track}}$, and not its inverse, is the variable stored in the tau Event Data Model (EDM) [147].

			$p_{\mathrm{T}} < 80$ GeV	$p_{\mathrm{T}} \geq 80$ GeV
1-prong	loose	$R_{\mathrm{EM}} <$	$0.663/p_{\mathrm{T}} + 0.063 - 2.04 \times 10^{-4} p_{\mathrm{T}}$	0.055
		$R_{\mathrm{track}} <$	$0.0328/p_{\mathrm{T}} + 0.134 - 2.72 \times 10^{-4} p_{\mathrm{T}}$	0.113
		$1/f_{\mathrm{track}}$	no cut	no cut
	medium	$R_{\mathrm{EM}} <$	$0.715/p_{\mathrm{T}} + 0.0522 - 1.71 \times 10^{-4} p_{\mathrm{T}}$	0.0475
		$R_{\mathrm{track}} <$	$0.0328/p_{\mathrm{T}} + 0.134 - 2.72 \times 10^{-4} p_{\mathrm{T}}$	0.113
		$1/f_{\mathrm{track}} <$	8.33	8.33
	tight	$R_{\mathrm{EM}} <$	$0.819/p_{\mathrm{T}} + 0.0306 - 1.03 \times 10^{-4} p_{\mathrm{T}}$	0.0325
		$R_{\mathrm{track}} <$	$0.0328/p_{\mathrm{T}} + 0.134 - 2.72 \times 10^{-4} p_{\mathrm{T}}$	0.113
		$1/f_{\mathrm{track}} <$	7.14	7.14
3-prong	loose	$R_{\mathrm{EM}} <$	$0.339/p_{\mathrm{T}} + 0.179 - 5.17 \times 10^{-4} p_{\mathrm{T}}$	0.142
		$R_{\mathrm{track}} <$	$0.695/p_{\mathrm{T}} + 0.0565 - 1.44 \times 10^{-4} p_{\mathrm{T}}$	0.0536
		$1/f_{\mathrm{track}} <$	4.55	4.55
	medium	$R_{\mathrm{EM}} <$	$0.447/p_{\mathrm{T}} + 0.162 - 4.62 \times 10^{-4} p_{\mathrm{T}}$	0.13
		$R_{\mathrm{track}} <$	$0.810/p_{\mathrm{T}} + 0.0303 - 9.90 \times 10^{-5} p_{\mathrm{T}}$	0.0325
		$1/f_{\mathrm{track}} <$	3.33	3.33
	tight	$R_{\mathrm{EM}} <$	$0.930/p_{\mathrm{T}} + 0.0833 - 2.15 \times 10^{-4} p_{\mathrm{T}}$	0.0777
		$R_{\mathrm{track}} <$	$0.879/p_{\mathrm{T}} + 0.0146 - 7.21 \times 10^{-5} p_{\mathrm{T}}$	0.0198
		$1/f_{\mathrm{track}} <$	2.5	2.5

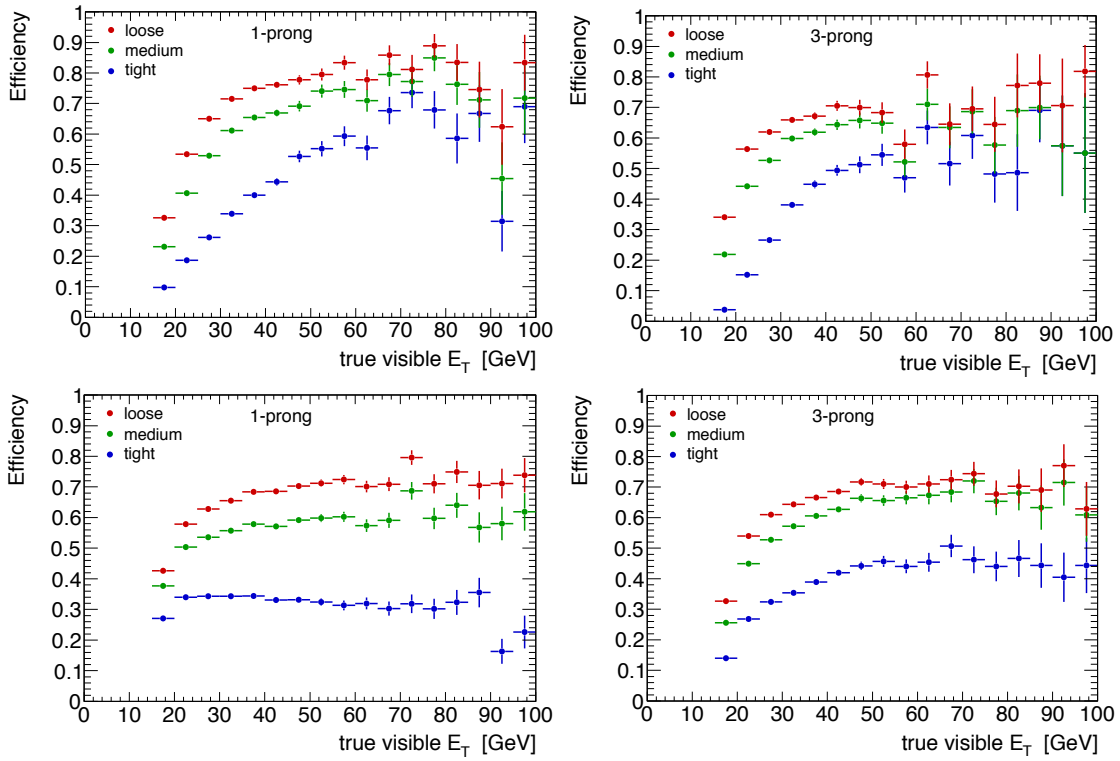

Figure 4.10: The efficiency of the 2010 simple cut-based ID (top) and the p_{T}-parametrized cuts (bottom), for both 1-prong (left) and 3-prong (right) true hadronic tau decays (`mc09`) [143].

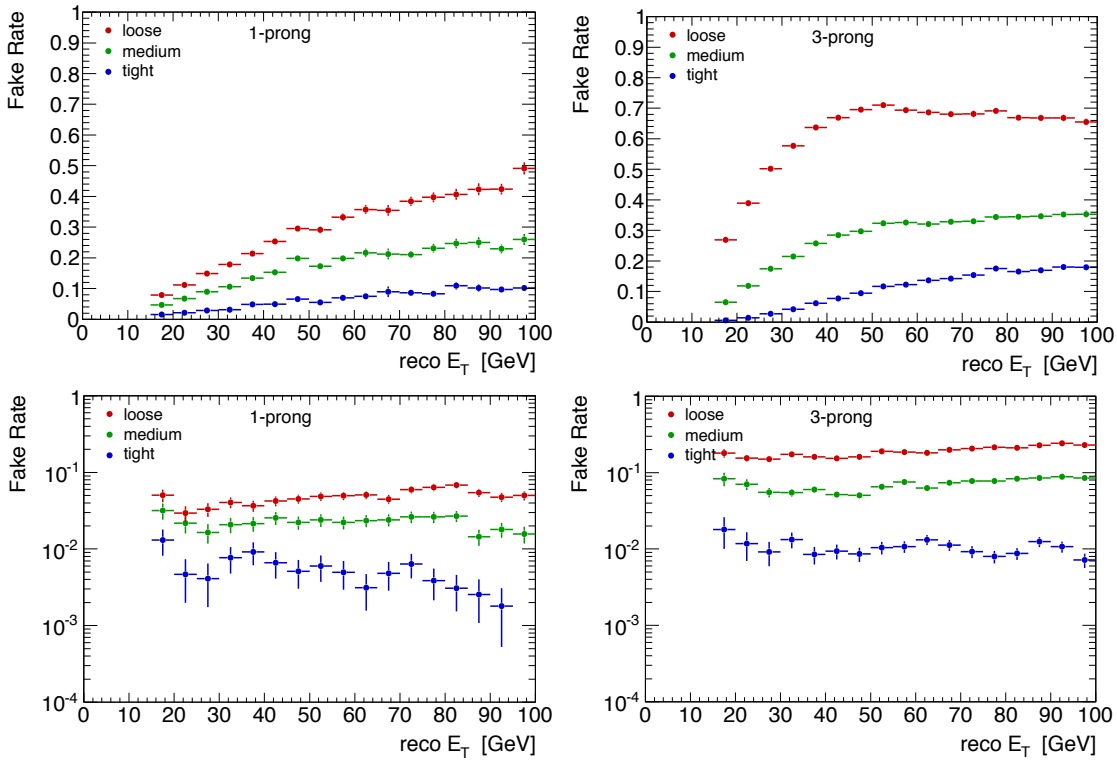

Figure 4.11: The fake rate of the 2010 simple cut-based ID (top) and the p_{T}-parametrized cuts (bottom), for both 1-prong (left) and 3-prong (right) tau candidates in a dijet sample from the 2010 dataset.

Table 4.3: Comparison of variables used by each discriminant for the 2010 dataset [100].

	R_{EM}	R_{track}	f_{track}	f_{core}	f_{EM}	m_{clusters}	m_{tracks}	$S_{\mathrm{T}}^{\mathrm{flight}}$	f_{HT}
Cuts	•	•	•						
Llh single-prong	•	•				•			
Llh multi-prong	•		•		•		•	•	
BDT single-prong	•	•	•	•	•	•			
BDT multi-prong	•	•	•	•	•	•	•	•	
e-BDT single-prong	•	•	•	•	•	•			•

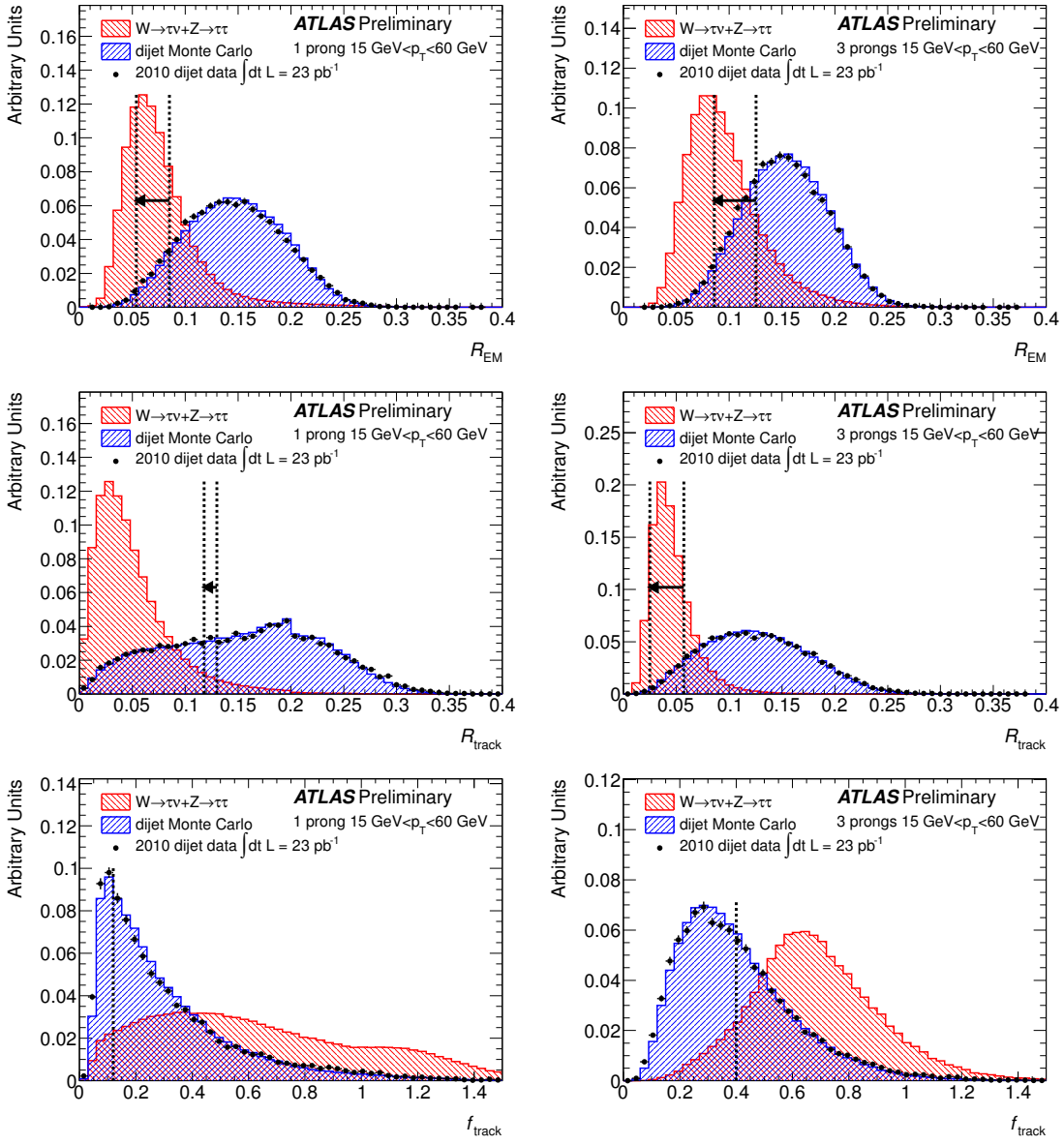

Figure 4.12: Distributions for R_{EM}, R_{track}, and f_{track}, for 1-prong (left) and 3-prong (right) candidates. Note that the discontinuity in R_{track} for 1-prong candidates is due to the fact that they can optionally have additional tracks in the isolation annulus (see the definition of R_{track} in Section 4.3.1). The dashed lines indicate the cut boundaries for the tight p_{T}-parameterized cut-based ID, discussed later in Section 4.3.3. Since the cuts on R_{EM} and R_{track} are parameterized in p_{T}, the characteristic range of the cut values is demonstrated by showing lines for the cuts for candidates with $p_{\mathrm{T}} = 20$ GeV, and then an arrow pointing to the cut for candidates with $p_{\mathrm{T}} = 60$ GeV (`mc09`) [100].

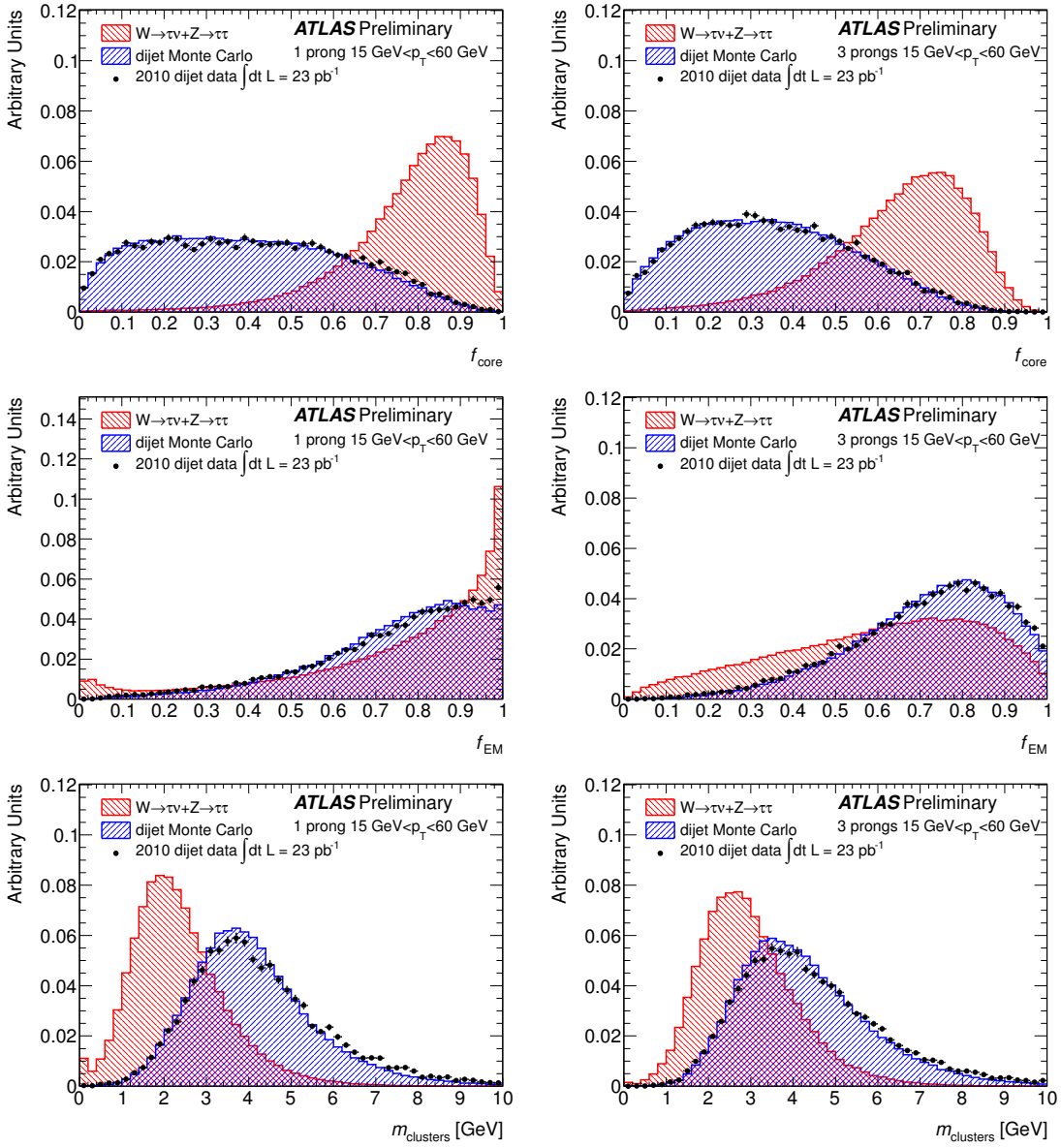

Figure 4.13: Distributions for f_{core}, f_{EM}, and m_{clusters}, for 1-prong (left) and 3-prong (right) candidates (mc09) [100].

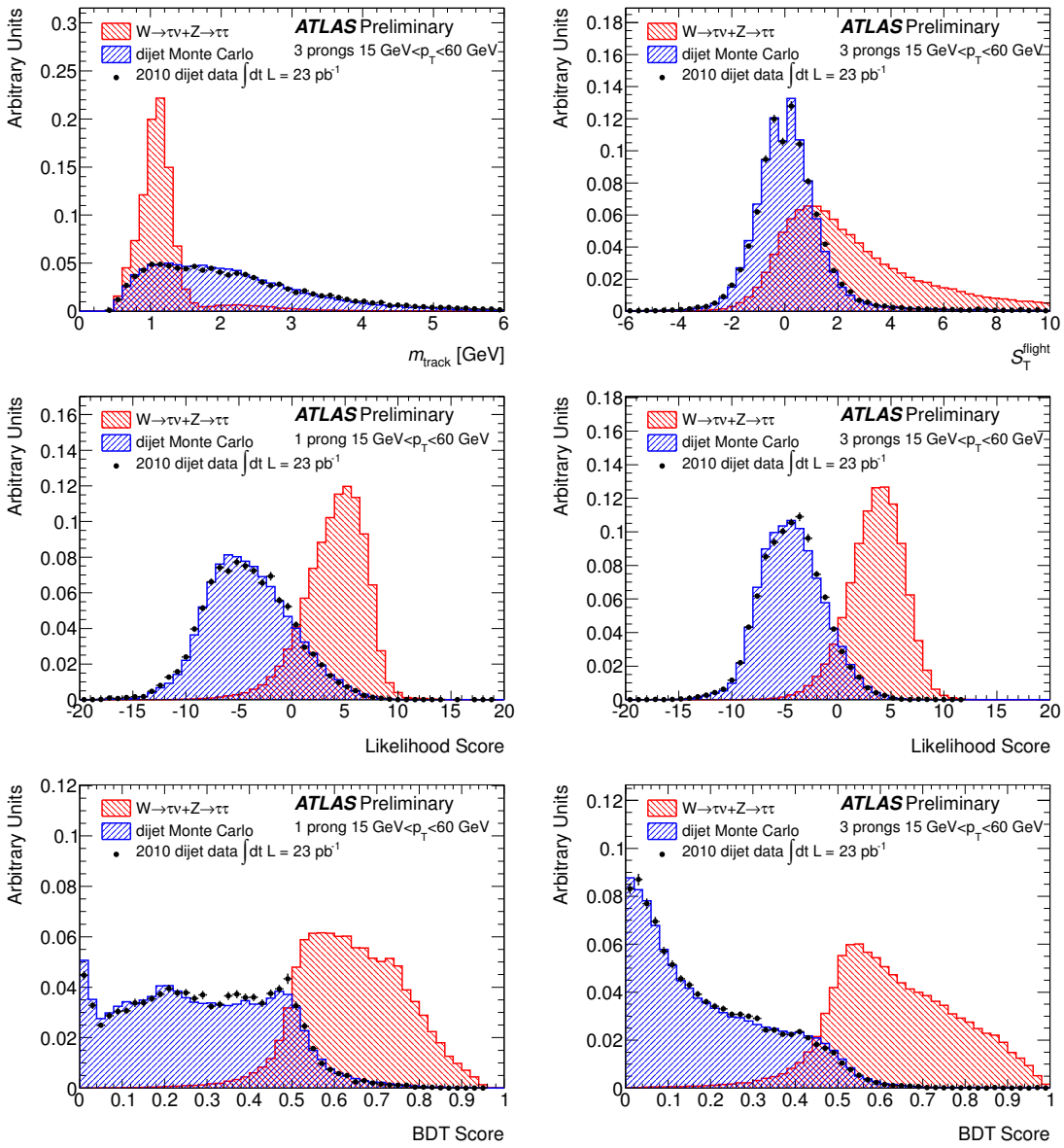

Figure 4.14: Distributions of m_{tracks} (top-left) and $S_{\text{T}}^{\text{flight}}$ (top-right) for 3-prong candidates, the log-likelihood-ratio for 1-prong (center-left) and 3-prong (center-right) tau candidates, and the jet BDT score for 1-prong (bottom-left) and 3-prong (bottom-right) tau candidates (`mc09`) [100].

Likelihood-based identification

Likelihood-based tau identification has been explored by the ATLAS Collaboration for several years, well before first collision data [148]. The method relies on having well-modeled distributions for each of the identification variables, for both signal and background, and constructing a likelihood function based on the product of those distributions.

The likelihood function, $L_{S(B)}$, for signal(background) is defined as the product of the distributions of the identification variables:

$$L_{S(B)} = \prod_{i=1}^{N} p_i^{S(B)}(x_i),$$

where $p_i^{S(B)}(x_i)$ is the signal (background) probability density function of identification variable x_i of N variables. The likelihood function represents the joint probability distribution for the identification variables, neglecting correlations between the variables. The discriminant used by the likelihood method is defined as the log-likelihood-ratio between signal and background:

$$d = \ln\left(\frac{L_S}{L_B}\right) = \sum_{i=1}^{N} \ln\left(\frac{p_i^S(x_i)}{p_i^B(x_i)}\right).$$

The likelihood has been constructed in separate categories based on the tau candidate's transverse momentum ($p_{\mathrm{T}} < 45$, $45{-}100$, > 100 GeV), track multiplicity (single-prong or multi-prong), track quality criteria (presence of a track with $p_{\mathrm{T}} > 6$ GeV or not) and the pile-up activity in the event (1-2, or more than 2 reconstructed primary vertices). A linear interpolation of the log-likelihood-ratio between neighbouring p_{T} bins is applied if the distance to the bin border is less than 10 GeV [100]. The variables used to construct the likelihood are listed in Table 4.3. Distributions of the log-likelihood-ratio for signal and background are shown in Figure 4.14.

Identification with boosted decision trees

Decision trees [149] perform a sequence of cuts on multiple variables to classify objects as signal or background. The exact sequence of cuts, or path through a tree, can depend on which previous cuts are passed, such that the decision can have many branches like a tree. A tree is constructed from multiple nodes, where each node represents a specific cut on a variable.

A sample of signal and background objects are required to train a set of trees. The algorithm begins with the entire training sample at the root node. The optimal cut, separating signal from background, is then determined separately for each variable. The best of these optimal cuts is chosen and two child nodes are constructed. All objects which fall below the cut are passed to the left node, and all objects which fall above the cut are passed to the right node. This cut improves the signal purity in one of the child nodes. The same algorithm is then applied recursively on each child node

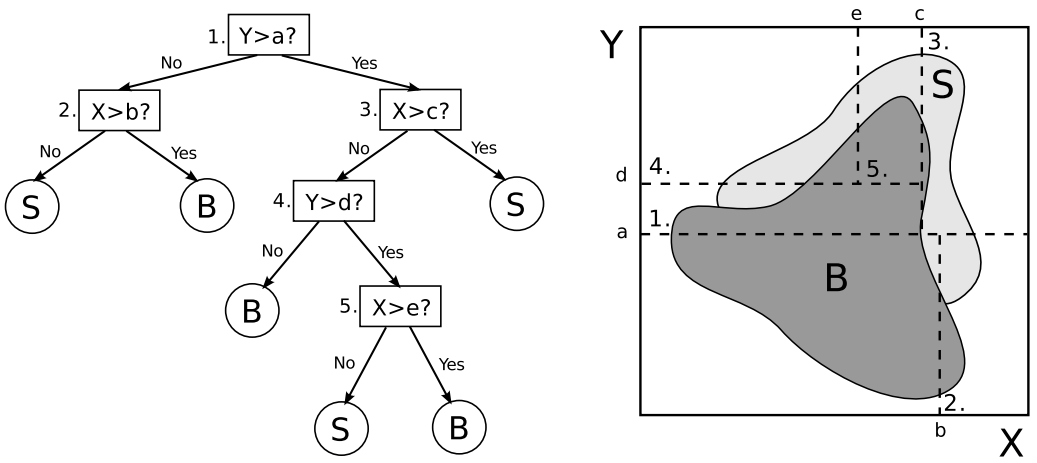

Figure 4.15: A simple example of a decision tree training process where there are two distributions labeled signal (S) and background (B) over two variables X and Y. The process begins at point 1, by determining the best value of the best variable to cut on, which in this case is Y at a. All objects with $Y > a$ are passed to the right node and all objects with $Y \leq a$ are passed to the left. This process continues recursively until a stopping condition is satisfied, such as a minimum number of objects contained by a node [147].

until a stopping condition is satisfied (in this case, a minimum number of tau candidates contained within a node). This leads to a binary tree structure, like the example shown in Figure 4.15. TMVA [150], a package for multivariate analysis that is part of the ROOT analysis toolkit [133], is used for training [147].

During classification, an object begins at the root node and is passed down the tree according to the cut made by each node until a final leaf node is reached. The response of the decision tree is then the signal purity of the leaf node. A Boosted Decision Tree (BDT) [151] takes advantage of multiple decision trees and forms a normalized weighted sum of their outputs, resulting in a final score that is between 0 (background-like) and 1 (signal-like) [152].

BDTs for jet rejection are trained separately for candidates with one track and candidates with three tracks. The BDT trained on candidates with three tracks is then used for classifying any candidate with two or more tracks. Distributions of the BDT score for discriminating taus from jets are shown in Figure 4.14, for both signal and background.

Loose, medium, and tight working points, similar to the cut-based identification, are defined for both the likelihood- and BDT-based identification. A cut is made on the final log-likelihood-ratio or BDT score to discriminate signal from background. The working points have been tuned with p_{T}-dependent selections to compensate for the p_{T}-dependence of the log-likelihood-ratio and BDT scores, yielding roughly flat[27] signal and background efficiencies as a function of p_{T} [100]. The

[27] See Figures 4.20 and 4.21, which show the p_{T}-dependence of the performance of the discriminants used with the

performance of the ATLAS tau identification is discussed in more detail in Section 4.4.3.

4.3.5 Electron-tau discrimination

Providing both a track and a well-matched cluster, electrons readily produce tau candidates. Much of this background can be suppressed by overlap-removing tau candidates which pass some electron identification. Figure 4.16 (top-left) shows the efficiency for true hadronic decays of tau leptons in 2010 $Z \to \tau\tau$ MC events to be identified as loose/medium/tight electrons. It demonstrates that one can safely remove tau candidates which pass medium ID with only removing $\sim 1\%$ of true tau decays. Since electron ID improved, in 2011 and 2012 it is reasonable to remove loose^{++} candidates.

To further suppress electrons faking tau candidates after overlap-removing identified electrons, electron-tau discriminants have been developed, first a simple cut-based method [153], which was later superseded by a BDT-based electron-veto (e-veto) [102]. The e-vetoes use a list of variables similar to those used by the jet-tau discriminants, but with additional variables like the TRT high-threshold-hit fraction (see Figure 4.16 (top-right)) targeted at discriminating electrons from charged pions. The distribution of the BDT score for the e-veto for 2011 is shown in Figure 4.16 (bottom-left). Loose/medium/tight working points with signal efficiencies of approximately 95%/85%/75% are defined, the efficiency and rejection of which are shown in Figure 4.16 (bottom-right). The measurement of the performance and its uncertainty for the BDT e-veto is discussed in Section 4.4.4.

4.4 Performance and systematic uncertainties

4.4.1 First data-MC comparisons

While considerable progress was made in developing the core of the ATLAS tau reconstruction algorithm and preliminary versions of the identification before the LHC circulated any beam, first collisions brought the first concrete evaluations of that software with real data, and the first tests of the modeling of tau-related variables in the ATLAS simulation.

In November and December of 2009, following the single-beam commissioning of the LHC, ATLAS collected data from the first proton-proton collisions at the LHC at $\sqrt{s} = 900$ GeV. The peak luminosity ranged between 10^{25} and 10^{27} cm^{-2} s^{-1}, resulting in a few μb^{-1} of integrated luminosity. The following year, the LHC produced the first record-energy proton-proton collisions at $\sqrt{s} = 7$ TeV. Between March and May 2010, the peak luminosity ranged from 10^{27} to 10^{29} cm^{-2}s^{-1}, and 15.6 nb^{-1} of integrated luminosity were collected.

2010 dataset.

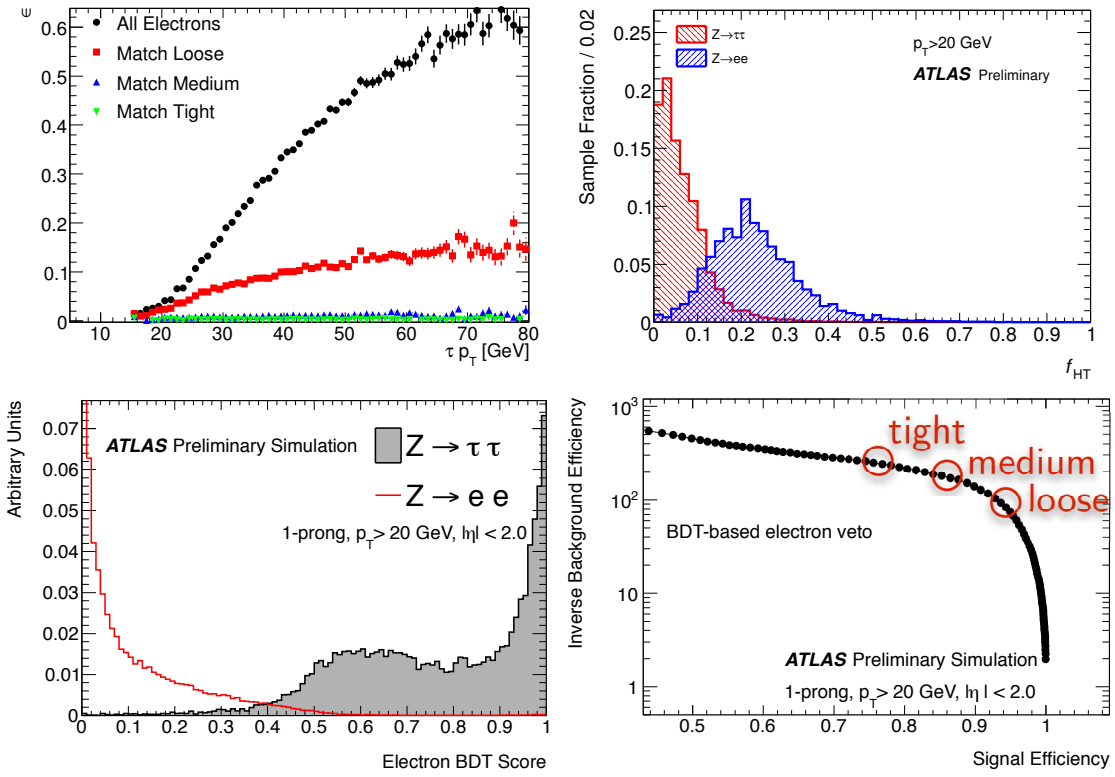

Figure 4.16: (top-left) The efficiency for true hadronic tau decays to the identified with by an overlapping electron candidates with the 2010 ID. (top-right) The distributions of the TRT high-threshold-fraction for tau candidates in MC $Z \to \tau\tau$ and $Z \to ee$ events, a variables used to discriminant electrons from hadronic decays of taus [101]. (bottom-left) The distribution of the BDT score for the e-veto used to veto real electrons faking tau candidates. (bottom-right) The inverse background efficiency vs signal efficiency for various cuts on the BDT score for the e-veto [102].

The events in the 2009 sample were collected according to a minimum-bias trigger, and are dominated by soft, non-diffractive interactions. In the 2010 dataset, the higher luminosity and collision energy allowed for the production of a more substantial sample of high-p_{T} jets for seeding tau candidates. While the number of real tau leptons produced in the momentum range relevant to the ATLAS physics program is expected to be negligible in both samples, the data have been used to commission the operation of the tau reconstruction algorithm and to validate the modeling of several identification variables for background candidates. Figure 4.17 shows data-MC comparisons of some of the tau-related variables with both of these datasets [154, 144].

In the plot of R_{EM}, Figure 4.17 (bottom-right), note that one could already see signs of the mis-modeling of the jet width in the ATLAS simulation. PYTHIA [125], specially tuned for minimum-bias events at ATLAS [129], was used to generate the simulated background events, producing jets

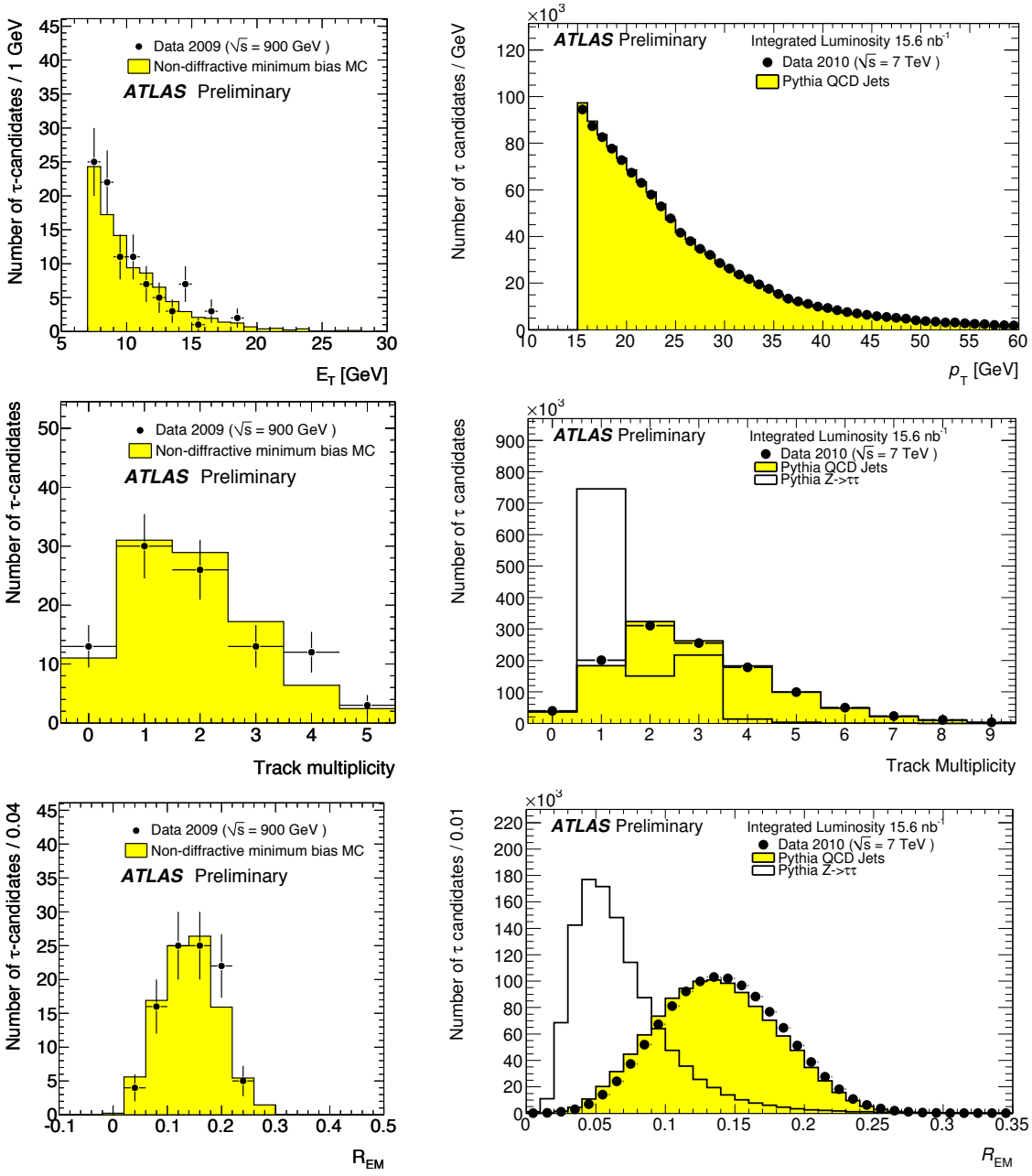

Figure 4.17: First data-MC comparison of tau candidates in soft, non-diffractive events from 2009 collisions at $\sqrt{s} = 900$ GeV (left), and from dijet events from 2010 collisions at $\sqrt{s} = 7$ TeV (right) [154, 144].

that are systematically more narrow than jets of the same p_{T} in the data. Since tau ID prefers candidates with narrow distributions of clusters and tracks, the jet fake rate is mis-modeled for tau ID. As noted later in Section 5.7 concerning the background estimation for the observation of $Z \to \tau\tau$, this mis-modeling results in a factor ~ 2 disagreement between data and MC for the $W+$jets background to events with a selected lepton and a hadronic tau candidate which is faked by a jet. The ATLAS Jet Performance Group also noted the mis-modeling of the jet width [155], and made detailed data-MC comparisons of measures of jet width with different MC generators [156, 157].

As a result of the sensitivity of the fake rate of tau ID on measures of jet width and the mis-modeling of such measures in ATLAS MC, analyses using hadronic decays of taus generally require data-driven methods to model the rate of fake backgrounds[28]. The rate of identifying true hadronic tau decays, on the other hand, is modeled reasonably well with the ATLAS MC, as demonstrated in samples like selections of $W \to \tau_{\mathrm{h}}\nu$ or $Z \to \tau\tau$ events, such as discussed in the following section on the observation of $W \to \tau_{\mathrm{h}}\nu$ at ATLAS. Indeed, scale factors have been measured for the rates of true hadronic decays of tau leptons, both in samples of $W \to \tau_{\mathrm{h}}\nu$ and $Z \to \tau\tau$ events, which are generally consistent with 1 within their uncertainties [101, 102].

4.4.2 Observation of $W \to \tau\nu$

The initial data-MC comparisons, discussed in the previous section, offered the first tests of the tau reconstruction and modeling of background candidates from QCD jets. The inaugural appearance of real hadronic decays of tau leptons at ATLAS came when sufficient data were collected in 2010 to observe the production W bosons decaying to tau leptons. With 546 nb^{-1} of integrated luminosity, ATLAS claimed observation of $W \to \tau_{\mathrm{h}}\nu$ decays [145].

Events were triggered which have a L2 tau candidate, which consists of a loosely-isolated calorimeter cluster with at least one matching track with $p_{\mathrm{T}} > 6$ GeV. The EF trigger that was used, required $E_{\mathrm{T}}^{\mathrm{miss}} > 15$ GeV. Events were selected if they have a hadronic tau decay with p_{T} between 20 and 60 GeV, selected according to the tight cut-based selection described in Section 4.3.2; $E_{\mathrm{T}}^{\mathrm{miss}} > 30$ GeV; estimated significance[29] of the $E_{\mathrm{T}}^{\mathrm{miss}}$, $S_{E_{\mathrm{T}}^{\mathrm{miss}}} > 6$; and no electrons or muons with $p_{\mathrm{T}} > 15$ GeV. The background is dominated by QCD multijet events. The $E_{\mathrm{T}}^{\mathrm{miss}}$ significance requirement substantially purifies the $W \to \tau_{\mathrm{h}}\nu$ sample, and a clear peak can be seen in the distribution of the transverse mass between the tau candidate and the $E_{\mathrm{T}}^{\mathrm{miss}}$ near the W mass as expected (see Figure 4.18).

[28] Modeling backgrounds that fake tau ID is a theme that will be returned to many times in this thesis. For example, the use of the k_W scale factor for the $Z \to \tau\tau$ cross section measurement discussed in Section 5.7.2, and the fake factor method used to predict the $W+$jets background for the search for Z' discussed in Section 6.4.4.

[29] $S_{E_{\mathrm{T}}^{\mathrm{miss}}} = \frac{E_{\mathrm{T}}^{\mathrm{miss}}}{0.5\ \sqrt{\mathrm{GeV}}\ \sqrt{\sum E_{\mathrm{T}}}}$

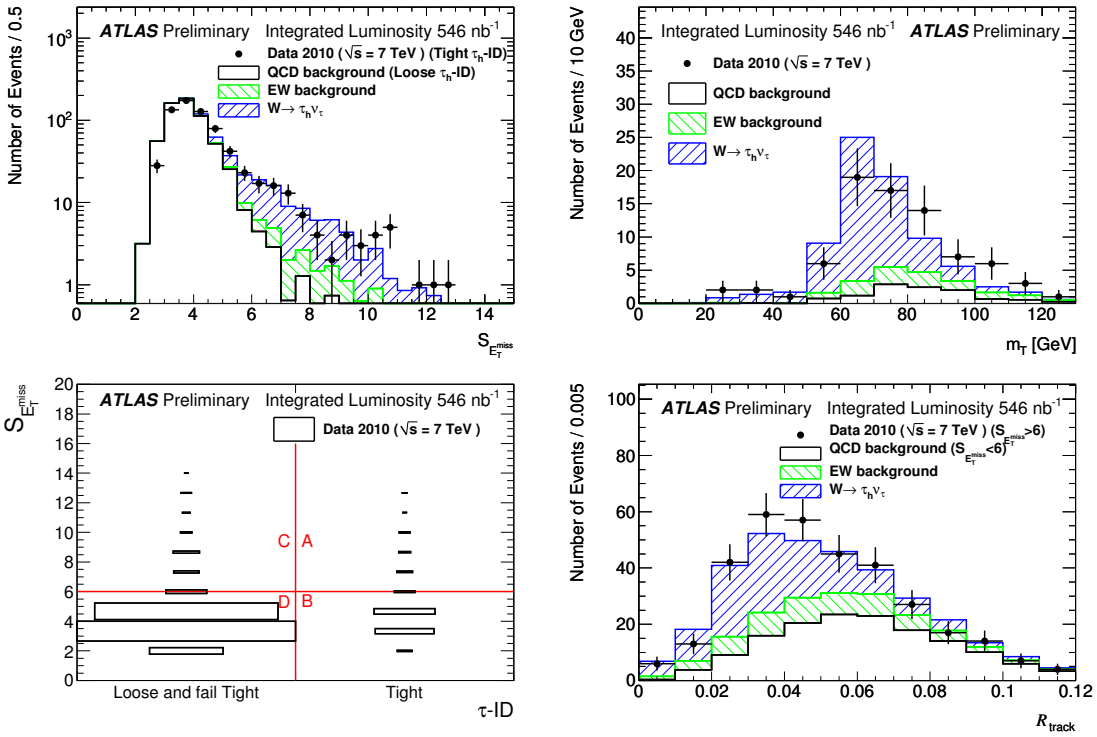

Figure 4.18: From the $W \to \tau_{\mathrm{h}}\nu$ observation, distributions of the the $S_{E_{\mathrm{T}}^{\mathrm{miss}}}$ with the full event selection except for the $S_{E_{\mathrm{T}}^{\mathrm{miss}}}$ cut (top-left), the m_{T} distribution in the full event selection (top-right), the R_{track} distribution in the full event selection except with tau ID relaxed to loose (bottom-right), and an illustration of the ABCD control regions (bottom-left) [145].

The multijet background is estimated with a data-driven technique using the so-called "*ABCD method*". Four regions of the sample are selected, depending on if the events have a tau candidate that passes the tight tau identification or fails tight and passes loose, and if the events fail or pass the $E_{\mathrm{T}}^{\mathrm{miss}}$ significance requirement as shown in Figure 4.18 (bottom-left). The shapes of the QCD background distributions in the signal region, A, are modeled with the data in region CD, scaled by the ratio of numbers of events in region B to D, corrected with Monte-Carlo-based estimates of the electroweak contamination.

The sample contains an estimated 55.3 $W \to \tau_{\mathrm{h}}\nu$ events with a 70% purity. Figure 4.18 (bottom-right) shows the distribution of one of the tau identification variables, R_{track}, in events with the tau identification requirement relaxed to passing loose, showing an excess of events above the backgrounds at low values of R_{track}, consistent with real hadronic decays of tau leptons.

The next process producing tau leptons to emerge in the ATLAS data was $Z \to \tau\tau$, the observation and cross section measurement of which are discussed in Chapter 5. It includes a more

throughly explained example of using the ABCD method to the estimate the multijet background to $Z \to \tau\tau \to \ell\tau_{\mathrm{h}}$. After the completion of the 2010 run, the cross sections for the production of $W \to \tau\nu$ [138] and $Z \to \tau\tau$ [113] were measured with approximately 35 pb^{-1} of integrated luminosity.

4.4.3 Jet discrimination performance

As an illustration of the kind of performance one can expect for the jet-tau discriminants, Figure 4.19 shows plots of the tau signal and jet background efficiencies for each of the identification methods used with the 2010 dataset. The background sample is taken from a selection of dijet events in the ATLAS data taken in late 2010 (period G). The signal is a combination of $W \to \tau\nu$ and $Z \to \tau\tau$ simulation [147].

One should note that in practice, the background efficiency will depend on the event selection, as it depends on the p_{T} distribution of the candidates considered and the type of partons that initiated the jets (*i.e.* the gluon/light-quark/b-quark fractions). Background efficiencies can differ by as much as a factor of five, depending on whether the jet is quark or gluon initiated [158]. The variation of the jet fake rate with composition is discussed in more detail in Section 4.4.8.

The evaluation shown in Figure 4.19 gives an estimate of the performance[30] for discriminating hadronic decays of tau leptons from QCD jets, independent of the optional requirements for discriminating taus from electrons, the performance of which is discussed in Section 4.4.4. Typically one can expect a medium working point to have a signal efficiency of $\approx 50\%$, with background efficiencies being less than 10% for the cut-based identification and a few percent for the likelihood- or BDT-based ID. Figures 4.20 and 4.21 show the p_{T}-dependence of the performance of the discriminants. The upper bound on the signal efficiency is limited by the tracking reconstruction efficiency and therefore, is worse for 3-prong candidates.

Note that being binned in the number of reconstructed tracks, these background efficiencies reported are with respect to tau candidates that have already been reconstructed with either 1 or 3 tracks, a small subset of reconstructed jets which generally have a broader distribution of number of tracks, as shown previously in Figure 4.4. The signal and background efficiencies are defined as the following.

[30] There was a bug in `TauDiscriminant` at the time of release of this conference note [100]. The tight working point of the 1-prong cuts was not $\sim 15\%$ efficient for 1-prong tau decays. As one can see in the plot of efficiency vs p_{T} in Figure 4.21, the efficiency is consistently between 30 and 40%. `TauDiscriminant` was patched for physics use with the 2010 dataset and the working point decisions could be re-calculated real-time.

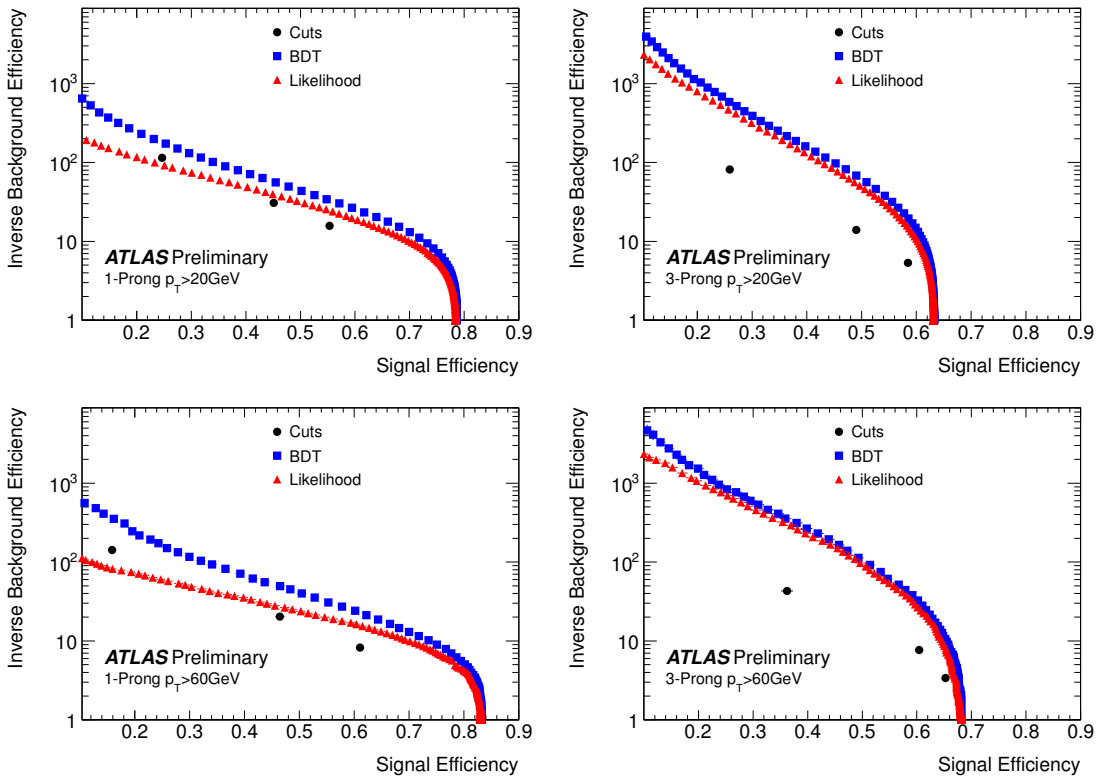

Figure 4.19: The inverse background efficiency versus signal efficiency for the jet-tau discriminants for 1-prong (left) and 3-prong (right) candidates, with $p_{\mathrm{T}} > 20$ GeV (top) and $p_{\mathrm{T}} > 60$ GeV (bottom), used with the 2010 dataset [100].

Signal efficiency:

$$\varepsilon_{\mathrm{sig}}^{1/3\text{-prong}} = \frac{\left(\begin{array}{l}\#\text{ of tau candidates with 1/3 reconstructed track(s),}\\ \text{passing ID, and truth-matched to a simulated 1/3-prong}\\ \text{decay}\end{array}\right)}{(\#\text{ of simulated visible hadronic taus with 1/3 prong(s)})}$$

Background efficiency:

$$\varepsilon_{\mathrm{bkg}}^{1/3\text{-prong}} = \frac{(\#\text{ of tau candidates with 1/3 reconstructed track(s), passing ID})}{(\#\text{ of tau candidates with 1/3 reconstructed track(s)})}$$

4.4.4 Electron discrimination performance

Figure 4.16 showed the signal and background efficiencies of the BDT e-veto, previously introduced in Section 4.3.5. To constrain an uncertainty on the background efficiency, a modified tag-and-probe[31] method with $Z \to ee$ events was used to measure the efficiency for real electrons to pass the e-veto.

[31] See the discussion of the tag-and-probe method in Section 3.6.3.

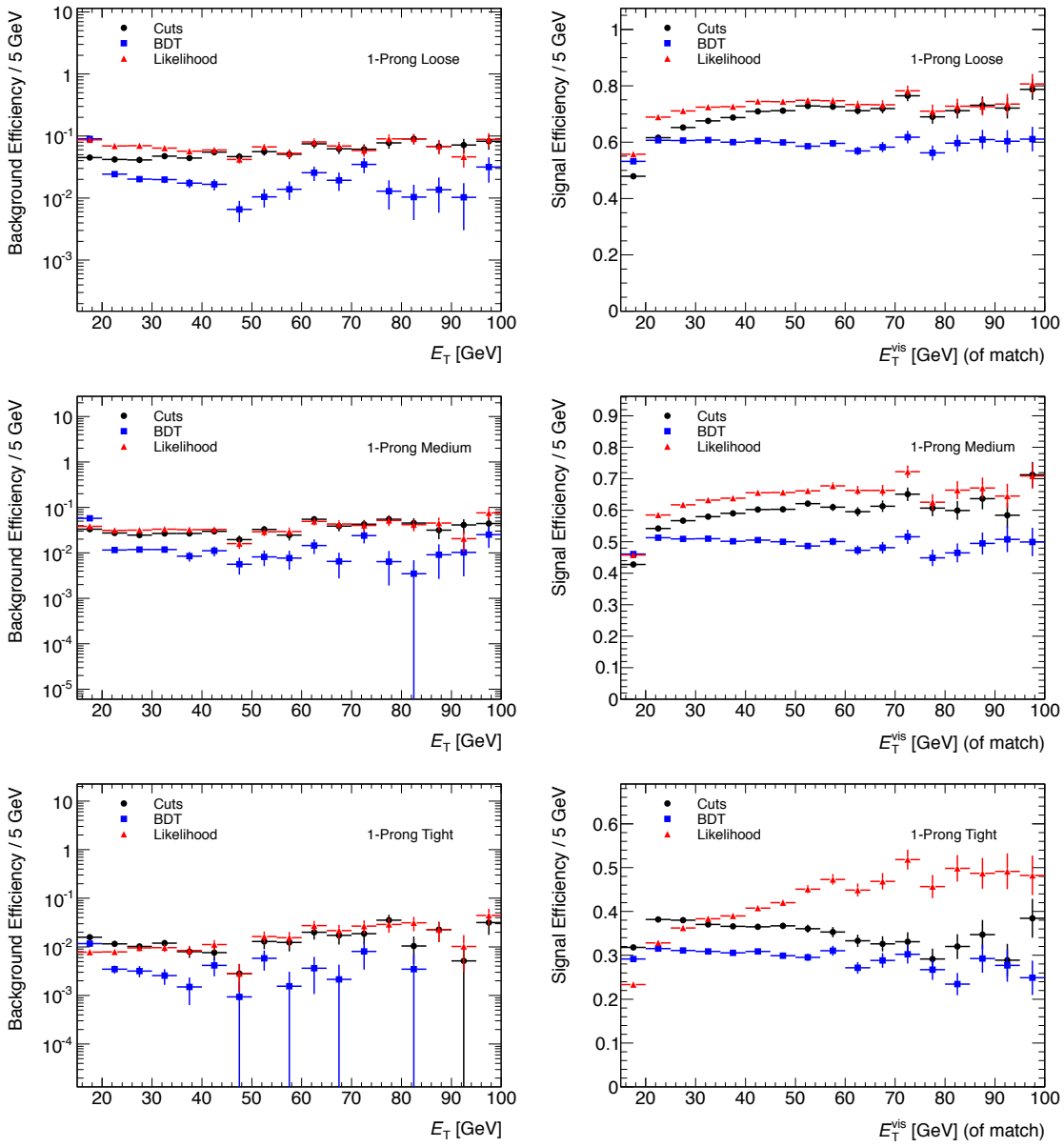

Figure 4.20: The background efficiency (left) and signal efficiency (right) vs p_T for the loose/medium/tight working points (top/center/bottom) of the jet-tau discriminants for 1-prong candidates, used with the 2010 dataset [147].

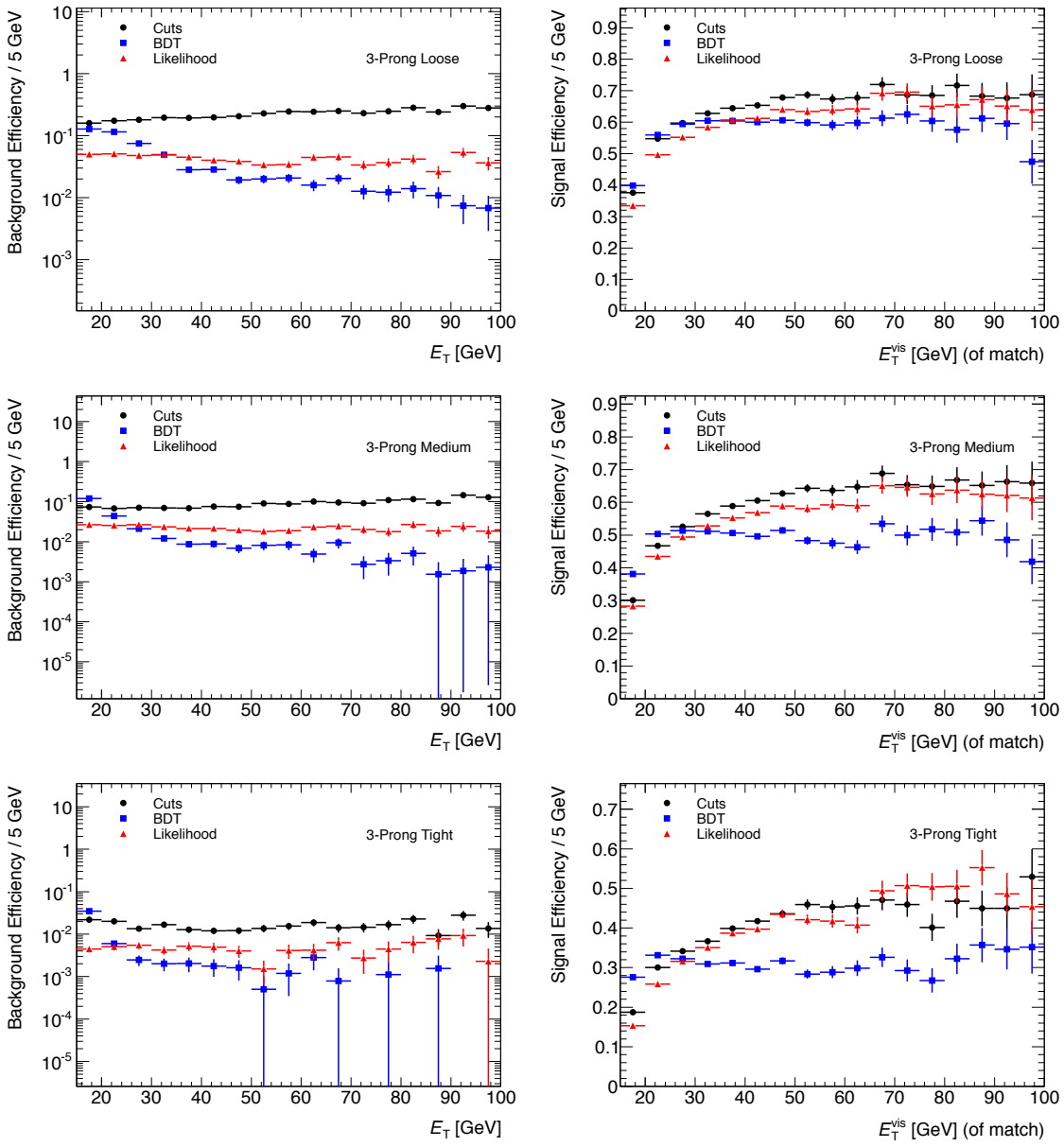

Figure 4.21: The background efficiency (left) and signal efficiency (right) vs p_T for the loose/medium/tight working points (top/center/bottom) of the jet-tau discriminants for 3-prong candidates, used with the 2010 dataset [147].

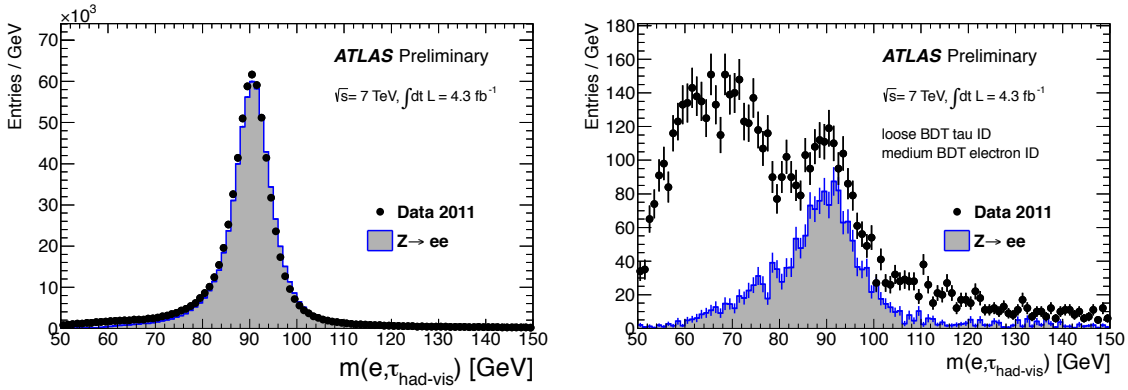

Figure 4.22: Visible mass distributions of $e\tau_{\mathrm{h}}$ candidates from the $Z \to ee$ tag-and-probe measurement of e-veto efficiency, for the selection without (left) and with (right) the medium BDT e-veto applied, using the 2011 dataset [102].

Figure 4.22 shows the visible mass of $e\tau_{\mathrm{h}}$ pairs in the tag-and-probe selection, with and without the e-veto applied to the probe. In the selection without the veto, the $Z \to ee$ contribution is very pure. In the selection with the veto applied, the background contamination that is subtracted in the efficiency measurement becomes significant. The estimation of that background is the largest contribution to the systematic error on the e-veto scale factor. The multijet background is estimated from the statistically limited same-sign (SS) sample of $\ell\tau_{\mathrm{h}}$ events in data, assuming the multijet background to be OS/SS symmetric. The remaining backgrounds from $W \to e\nu$ and $t\bar{t}$ events are estimated with MC [102].

Table 4.4 summarizes the results of the e-veto scale factor measurement with the 2011 dataset. Note that for the medium working point used by many analyses, the scale factors range from 0.5–2.3 in η-bins, with uncertainties ranging from 40–80%.

4.4.5 Energy calibration

The clusters associated with a tau candidate are calibrated using the local hadron calibration (LC) [95], which should correctly bring the energy scale of the charged pions to the hadronic scale from the EM energy scale. The transverse energy of a tau candidate is calculated as the sum of the

Table 4.4: The 2011 e-veto scale factors derived from the $Z \to ee$ tag-and-probe measurement [102].

electron BDT veto	$\lvert\eta_{\mathrm{trk}}\rvert < 1.37$	$1.37 < \lvert\eta_{\mathrm{trk}}\rvert < 1.52$	$1.52 < \lvert\eta_{\mathrm{trk}}\rvert < 2.00$	$\lvert\eta_{\mathrm{trk}}\rvert > 2.00$
loose	0.96±0.22	0.8±0.3	0.47±0.14	1.7 ±0.4
medium	1.3 ±0.5	-	0.5 ±0.4	2.8 ±1.3

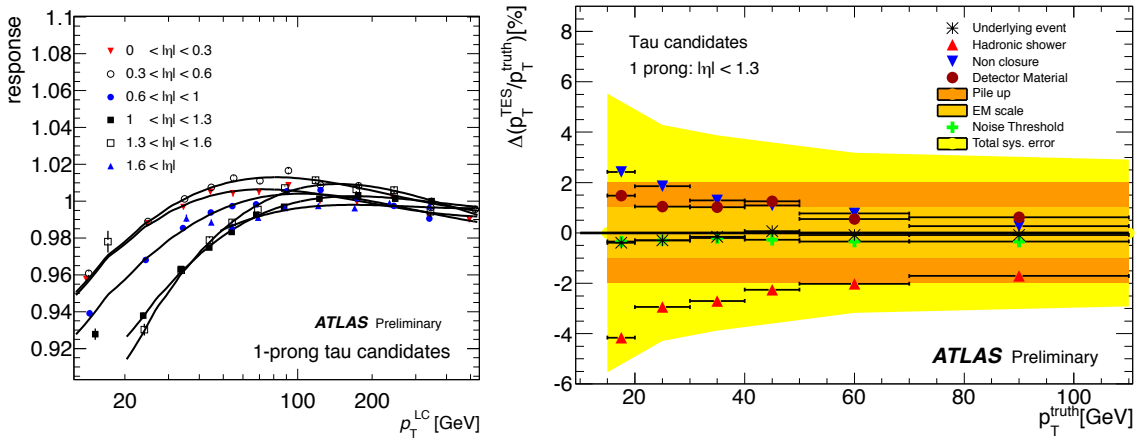

Figure 4.23: (left) Response functions for the 2011 TES. (right) The uncertainty on the 2011 TES as a function of p_{T} derived with systematically shifted MC [101].

E_{T} of each cluster associated to the tau in the core cone ($\Delta R < 0.2$). As a final correction to this energy, response functions are constructed based on Monte Carlo simulation of hadronic tau decays:

$$\mathrm{response}(p_{\mathrm{T}}^{\mathrm{LC}}) = \frac{p_{\mathrm{T}}^{\mathrm{LC}}}{p_{\mathrm{T}}^{\mathrm{truth}}} \,.$$

Then the reconstructed energy of a tau candidate is calculated by dividing the energy from the LC calibration by the response to bring it to the tau energy scale (TES). For example, Figure 4.23 (left) shows the response curves derived for tau candidates with the 2011 simulation and calibration. The corrections are generally small ($\sim 1\%$) but drop from 1 more significantly at low-p_{T}.

Since the method of calibration relies on Monte Carlo, errors in the modeling need to be accounted for in the systematic uncertainties on the tau energy scale. Monte Carlo samples dedicated to evaluating systematics were generated and fully simulated with systematic shifts or changes of: the event generator, underlying event model, hadronic shower model, amount of detector material, and the topological clustering noise thresholds [100]. The uncertainty due to the changes in pile-up in 2011 dataset (with μ typically in the range of 3–20) is taken as the largest deviation in response in bins of μ resulting in 2% (1-prong) and 1.5% (3-prong). The uncertainty on the EM energy scale is 3% for all candidates, taken from test-beam measurements [90]. Finally an uncertainty is accounted for the non-closure of the nominal MC sample evaluated as the deviation in the mean of the response from unity in bins of p_{T}. The largest uncertainties come from the hadronic shower model which range from 2–4% (1-prong) and 2–6% (3-prong) as a function of p_{T}, and from non-closure which range from 1–5% as a function of p_{T}, with largest total uncertainty being for low-p_{T} 3-prong candidates (see Figure 4.23) [101].

Later in 2012, the TES was updated for the 2011 dataset with studies propagating single-particle-

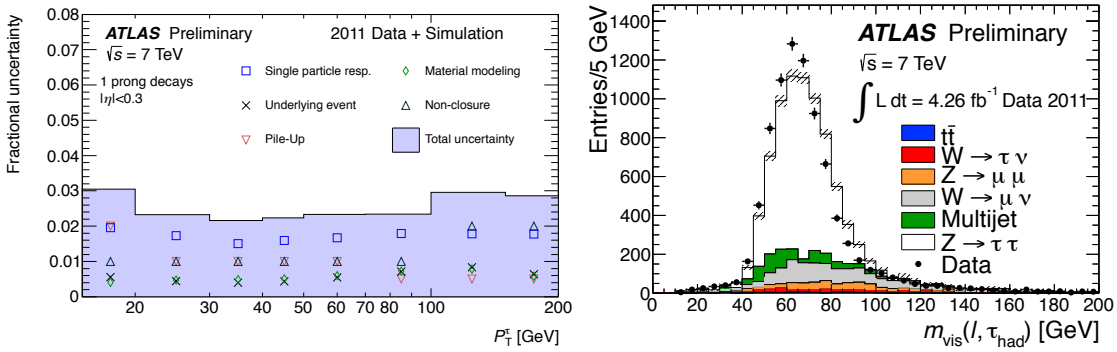

Figure 4.24: (left) The uncertainty on the updated 2011 TES as a function of p_{T} derived with single-particle-response uncertainties. (right) The visible mass of $\mu\tau_{\mathrm{h}}$ candidates in a $Z \to \tau\tau$ selection with the TES shifted by +10%, for example, which can be constrained by the poor agreement between data and MC in the $Z \to \tau\tau$ peak [159].

response uncertainties constrained separately for low-p_{T} hadrons (from *in situ* $\langle E/p \rangle$ measurements), high-p_{T} hadrons (from test-beam measurements), and neutral pions (EM scale from $Z \to ee$ measurements), directly to simulated hadronic decays of tau leptons, constraining the TES to 2–3% (see Figure 4.24 (left)).

A data-driven method has also been tested, directly measuring the shift of the visible mass peak of a sample of $Z \to \tau\tau \to \mu\tau_{\mathrm{h}}$ events, which resulted in an uncertainty of $\approx 3\%$ with the 2011 dataset of 4.26 fb^{-1} (see Figure 4.24 (right)). This data-driven method is expected to improve in precision as it is updated with the 2012 dataset [159, 160].

4.4.6 Tau identification efficiency

Like the first systematic uncertainty on the tau energy scale described in the previous section, the first recommended systematic on the tau identification efficiency was derived with dedicated Monte Carlo samples with systematic shifts or changes of: the event generator, underlying event model, hadronic shower model, amount of detector material, and the topological clustering noise thresholds. This constrains the efficiency scale factor to $\approx 10\%$, consistent with 1 [100]. Figure 4.25 shows the efficiency turn-on vs p_{T} for true hadronic taus passing the 2010 medium cut-based identification, illustrating the change in efficiency for each systematic shift.

Later, the tau identification efficiency was measured with a tag-and-probe sample of $W \to \tau\nu$ events in the 2010 data [161], and tag-and-probe samples of $W \to \tau\nu$ and $Z \to \tau\tau \to \mu\tau_{\mathrm{h}}$ events in the 2011 data [101]. Figure 4.26 shows the 2011 $Z \to \tau\tau \to \mu\tau_{\mathrm{h}}$ tag-and-probe events before and after the medium BDT identification is applied. In 2012, the $Z \to \tau\tau$ tag-and-probe study has constrained the efficiency to 2–3% for true 1-prong hadronic tau decays and 5–6% for 3-prong [103].

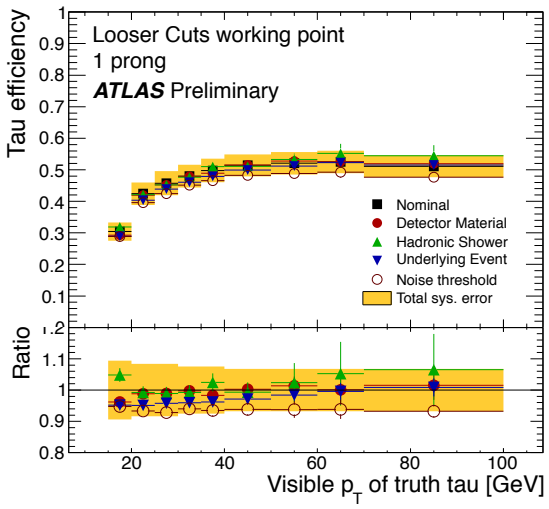

Figure 4.25: The tau identification efficiency uncertainty for the 2010 cut-based ID, using dedicated Monte Carlo samples with systematic shifts or changes of: the event generator, underlying event model, hadronic shower model, amount of detector material, and the topological clustering noise thresholds, [100].

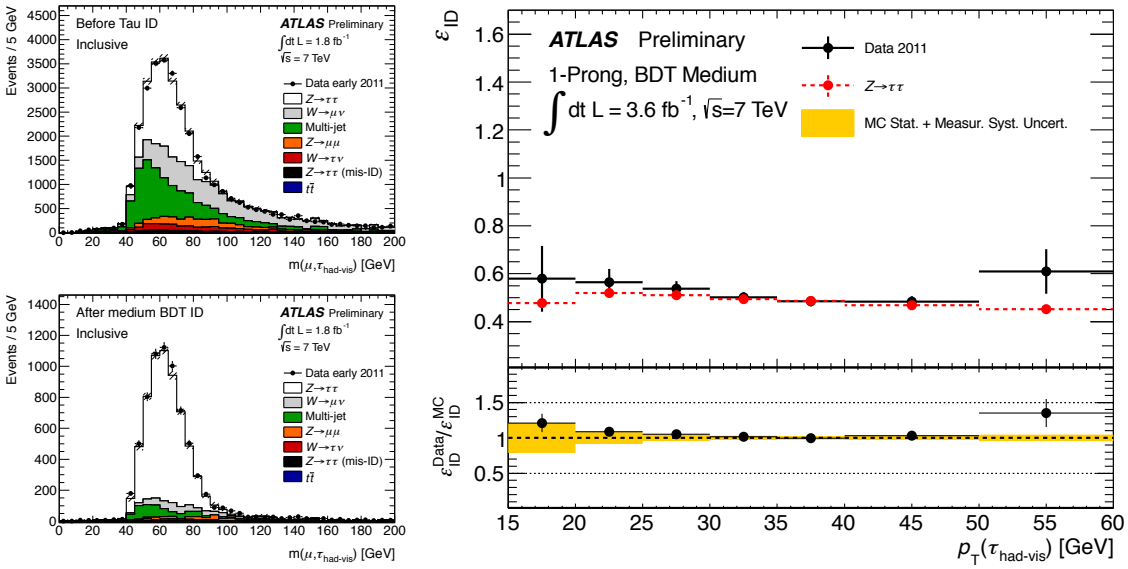

Figure 4.26: The visible mass of $\mu\tau_{\mathrm{h}}$ candidates in the $Z \to \tau\tau$ tag-and-probe selection without tau ID required (left-top), and after medium BDT ID (left-bottom). (right) The scale factors derived after subtracting background and dividing those selections [102].

4.4.7 Performance at high-p_{T}

Primarily in the course of the analysis of the 2011 dataset for the $Z' \to \tau\tau$ search reported in Chapter 6, several issues arose concerning the high-p_{T} behavior of reconstructed hadronic decays of taus. These include specific degradations in the performance of parts of the reconstruction and identification, and uncertainties on the modeling of the high-p_{T}behavior. The issues discussed here are documented in more detail in the 2011 $Z' \to \tau\tau$ search support note [97].

High-p_{T} tau ID performance with Z' Monte Carlo

Figure 4.27 shows the tau identification efficiency measured with a sample of high-p_{T} tau decays from Monte Carlo simulation of a Sequential Standard Model (SSM) Z' boson with a mass of 1000 GeV. It shows that the tau reconstruction and identification efficiency is flat vs p_{T} for the 1-prong identification, but falls gradually for the 3-prong identification.

Figure 4.28 shows the reconstruction efficiency for true 3-prong hadronic tau decays to be reconstructed with 2, 3, or 4 tracks. It demonstrates that the falling 3-prong efficiency is due to miscounting the number of tracks at high p_{T}, and not due to the tau discriminants themselves [162]. The effect is most likely due to highly collimated tracks having overlapping hits and not being resolvable, but this hypothesis needs additional study.

Figures 4.29 and 4.30 show the efficiencies for the tau discriminants for 1-prong hadronic tau decays for the 2011 dataset, measured with Monte Carlo simulation of a SSM Z' with a mass of 1000 GeV. They show that the jet and muon discrimination is flat vs p_{T}, while the electron vetoes are more harsh on the signal at high p_{T}.

Table 4.5: Data/MC tau ID efficiency ratio (SF) measured in bin of tau-p_{T} in the $Z \to \tau\tau$ tag and probe analysis. The individual contributions to the uncertainty are: the statistical uncertainty, $\Delta\mathrm{SF}_{stat}$; the normalisation uncertainties on the W+jets and multijet backgrounds, $\Delta\mathrm{SF}_{\mathrm{W}+jets}$ and $\Delta\mathrm{SF}_{QCD}$; and the experimental uncertainties on the muon, tau and the integrated luminosity, $\Delta\mathrm{SF}_{exp}$ [97].

		Data/MC Scale factor uncertainty contributions (%)				
p_{T} [GeV]	SF	$\Delta\mathrm{SF}_{stat}$	$\Delta\mathrm{SF}_{\mathrm{W}+jets}$	$\Delta\mathrm{SF}_{QCD}$	$\Delta\mathrm{SF}_{exp}$	$\Delta\mathrm{SF}_{\mathrm{T}otal}$
20–25	1.112±0.107	5.3	1.2	7.4	1.8	9.6
25–30	1.054±0.060	3.7	0.7	3.5	1.9	5.7
30–35	1.000±0.045	3.3	0.6	1.9	2.0	4.5
35–40	1.018±0.045	3.5	0.6	1.3	2.0	4.4
40–50	1.022±0.047	3.8	0.5	1.2	2.0	4.6
50–60	1.301±0.190	13.8	2.1	2.6	1.5	14.6

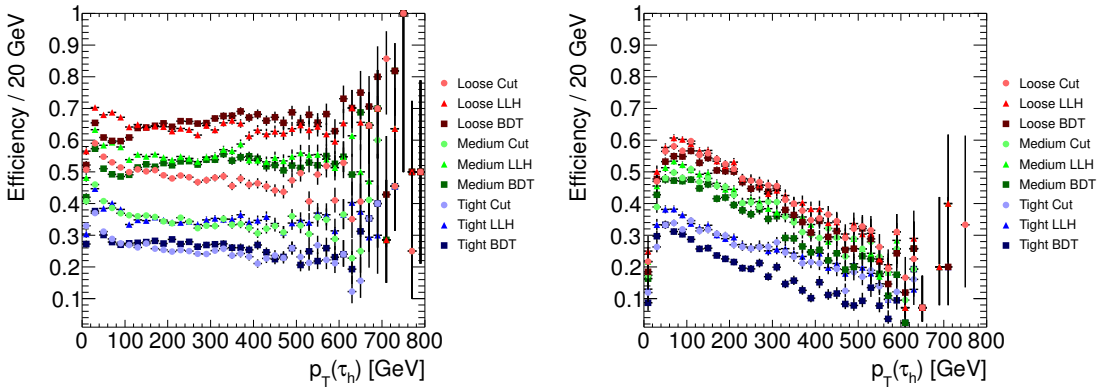

Figure 4.27: The efficiency for true 1-prong (left) and 3-prong (right) hadronic tau decays to be reconstructed with the correct number of tracks and pass the tau discriminants for rejecting jets, measured with Monte Carlo simulation for a SSM Z' with a mass of 1000 GeV [97].

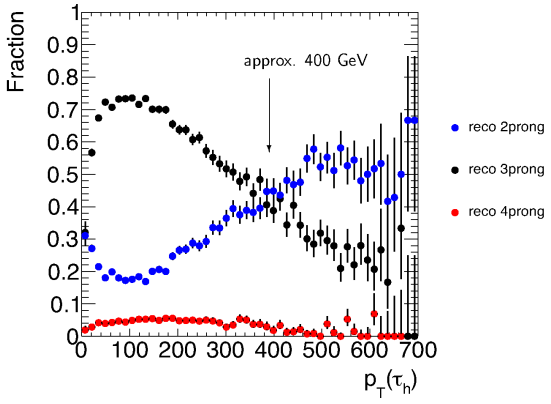

Figure 4.28: The efficiency for true 3-prong hadronic tau decays to be reconstructed with 2, 3, or 4 tracks, measured with Monte Carlo simulation for a SSM Z' with a mass of 1000 GeV [97].

High-p_T tau ID efficiency uncertainty

In support of the $Z' \to \tau\tau$ analysis, studies were done to quantify the fidelity of the simulation in modelling the tau identification at high-p_T. The conclusion of these studies is that while no degradation of the modeling at high-p_T is observed (within the uncertainty of the measurements), the uncertainty on the tau ID efficiency should be inflated linearly with p_T, up to a maximum uncertainty, to account for the increased uncertainty from the extrapolation technique used in the studies.

The tau ID efficiency is constrained to within about 4% with a tag-and-probe[32] measurement selecting $Z \to \tau\tau$ events [101], but that quantifies the performance only with candidates $p_T \lesssim 60$ GeV.

[32] See the discussion of the tag-and-probe method in Section 3.6.3.

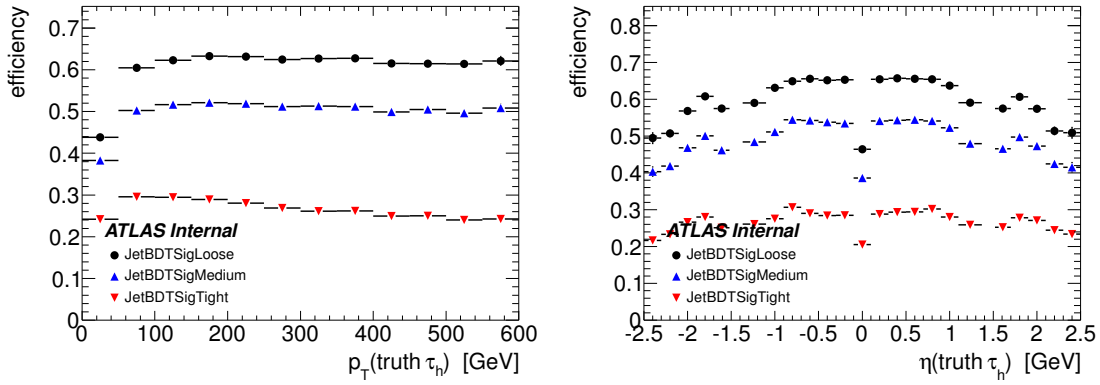

Figure 4.29: The efficiency true for 1-prong hadronic tau decays to be reconstructed and pass the tau discriminants for rejecting jets, in Monte Carlo simulation for a SSM Z' with a mass of 1000 GeV, as a function of the true visible p_{T} (left) and η of hadronic tau decays [97].

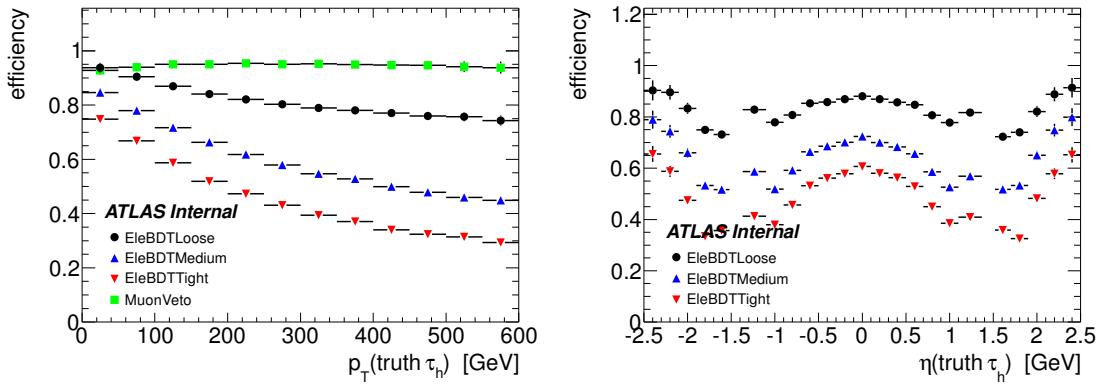

Figure 4.30: The efficiency true for 1-prong hadronic tau decays to be reconstructed with the corrected number of tracks and pass the tau discriminants for rejecting leptons, in Monte Carlo simulation for a SSM Z' with a mass of 1000 GeV, as a function of the true visible p_{T} (left) and η of hadronic tau decays [97].

The difficulty in quantifying the fidelity of tau ID at high-p_{T} is that there are no abundant sources of hadronic tau decays with $p_{\mathrm{T}} \gtrsim 80$ GeV in the data. This disqualifies the possibility of a direct measurement, however, one can ask whether the modeling of tau ID in simulation at high-p_{T} is any poorer than at low-p_{T}.

To answer this question, the assumption is made that data-MC mis-modelling can be attributed to incorrect modelling of either 1) the tau decay, or 2) the detector response. Since the simulation of tau decay branching-fractions and kinematics done by TAUOLA [127] has been well constrained for low-p_{T} candidates, boosting taus to higher p_{T} should not introduce mis-modelings. Therefore, the most important aspect of the study is to show that the detector response is modelled accurately

at high-p_{T}.

To establish an estimate of the uncertainty of the high-p_{T} tau ID efficiency, first the tag-and-probe efficiency measurement using $Z \to \tau\tau$ was performed in a number of p_{T}-bins to investigate the behaviour of the data-MC efficiency scale factors as a function of p_{T}. Figure 4.26 and Table 4.5 show the results of the scale factor measurements, giving no suggestion of a trend [97].

Second, a comparison was made of the tau ID variables for high-p_{T} candidates between simulated dijet events and dijet events selected from data, since a sample of fake taus still provides plenty of pions to test detector modeling. The scale factor for the fake rate was evaluated as a function of p_{T} and found not to have a significant trend. The scale factor vs p_{T} was fit to a line, with the slope constrained to 0.016% per 100 GeV. Given these observations, the uncertainty on the tau identification efficiency with 2011 dataset is suggested to be:

- $p_{\mathrm{T}} \leq 100$ GeV: $\Delta\varepsilon = 4\%$ (taken from the $Z \to \tau\tau$ measurement)
- $100 < p_{\mathrm{T}} < 350$ GeV: $\Delta\varepsilon = 4 + 0.016 \cdot (p_{\mathrm{T}} - 100)\%$, with p_{T} in GeV (taken from the linear fit in the dijets measurement).
- $p_{\mathrm{T}} \geq 350$ GeV: $\Delta\varepsilon = 8\%$, (taken from the largest deviation in the dijets measurement).

This prescription details a low uncertainty at low-p_{T} (coming from the tag and probe measurements), followed by a linear inflation in the uncertainty as a function of p_{T} (quantifying the limitation of our knowledge from the dijets measurement), with a maximum uncertainty of 8% reached at $p_{\mathrm{T}} = 350$ GeV (which is the maximum deviation in the dijets measurement) [97].

High-p_{T} 3-prong reconstruction efficiency uncertainty

As shown in Figure 4.28, the reconstruction efficiency for 3-prong taus decreases at high-p_{T}. The effect is due to track merging, which becomes more probable as the tracks in the tau decay become more collimated, hence a large number of 3-prong taus are reconstructed with only two tracks. Track merging in hadronic jets has been studied [163, 164]. In general, the modelling of shared and merged hits in MC simulation is observed to be in very good agreement with data. However, a conservative uncertainty of 50% on the tracking efficiency loss due to shared hits in MC simulation is assumed, as a direct measurement of the data/MC efficiency ratio was not possible. The same prescription is used to derive an uncertainty on the 3-prong reconstruction efficiency in this analysis. Firstly, it is observed from Figure 4.28 that above ≈ 150 GeV, the 3-prong reconstruction efficiency in MC drops by $\approx 12\%$ every 100 GeV. Taking 50% of this efficiency drop as the uncertainty on the 3-prong reconstruction efficiency leads to the following prescription:

- $p_{\mathrm{T}} \leq 150$ GeV: no additional uncertainty

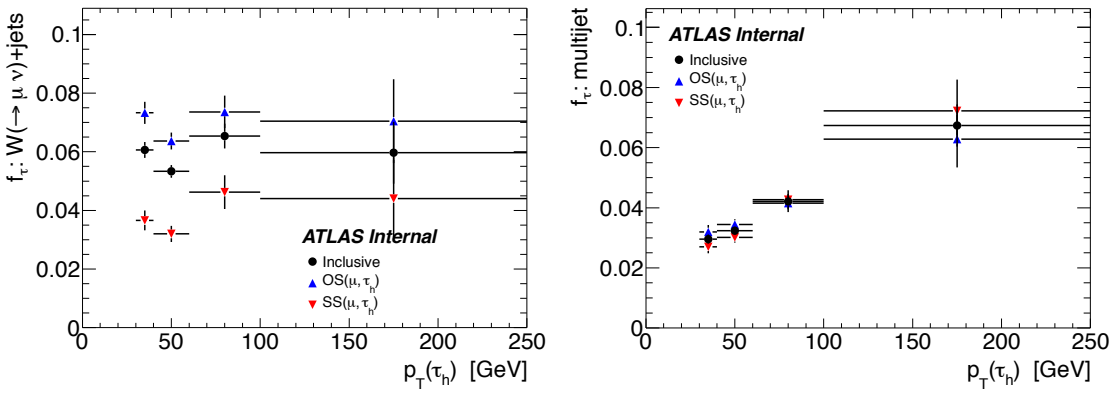

Figure 4.31: Fake factors derived for the medium BDT tau ID in a sample of events from the 2011 dataset rich in $W \to \mu\nu$+jets events (left) and dijet events (right) with the 2011 data [97].

- $p_{\mathrm{T}} > 150$ GeV: $\Delta\varepsilon_{\text{3-prong}} = 0.06 \cdot (p_{\mathrm{T}} - 150)\%$ with p_{T} in GeV.

4.4.8 Variation of jet fake rates with composition

As previously noted in Section 4.4.1, fake rates for jet-tau discrimination are strongly correlated with measures of the width the tau candidate, in both the calorimeter and among its associated tracks. Mis-modeling of the width of jets and the distribution of tracks in the ATLAS MC motivates the use of data-driven estimates of fake backgrounds to hadronic tau decays.

An additional challenge when modeling fake backgrounds is that the width of jets can vary among samples in the data, depending on the kinematics and composition of the jets that are selected. Figure 4.31 shows distributions of fake factors[33] measured samples enriched in W + jets and dijet events. Note that the fake factor can be significantly higher in a sample of W + jets events than in dijet events.

An explanation for the variance in these fake rates, even within a given p_{T}-bin, is that the composition of the hard partons that initiated the jets (the fraction outgoing of quarks or gluons) are different among the samples, and moreover, quark- and gluon-initiated jets have different distributions of tracks and jet width for jets of the same p_{T}. This suggests one to ask how quark-gluon-composition can effect tau ID fake rates.

Why do quarks and gluons have different fake rates?

Studies of the properties of quark- and gluon-initiated jets within the ATLAS Jet Performance Group show that, while measures of jet width are not perfectly modeled in MC, the salient features that

[33] Fake factors are discussed in more detail in Section 6.4.4 on their use in the $Z' \to \tau\tau$ search.

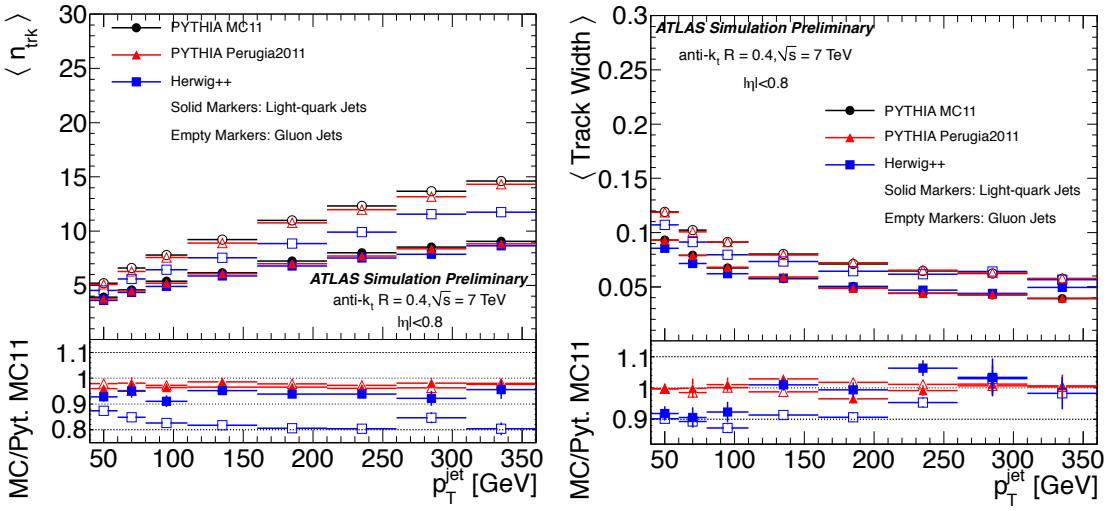

Figure 4.32: Profile plots of the number of tracks associated to a jet (left) and the track width (defined the same as R_{track}) (right) vs p_{T} of jets in ATLAS simulation. Note that gluon-initiated jets are systematically wider and have a higher track multiplicity than quark-initiated jets (`mc11`) [166].

distinguish quark jets from gluon jets can be seen [165, 166, 167]. Figure 4.32 shows profile plots[34] of the average number of tracks associated to a jet within $\Delta R < 0.4$ and track width vs p_{T} of the jet. Track width is identical to what is called R_{track} in ATLAS tau identification (see Section 4.3.1). Quark-initiated jets are also more narrow in calorimeter-based measures of width. Figure 4.33 shows distributions of the *integrated jet shape*, $\Psi(r)$, defined as the fraction of the jet constituent p_{T} that lies inside a cone of radius r concentric with the jet cone:

$$\Psi(r) \equiv \frac{\sum_i p_{\text{T}}^i \big| \Delta R_i < r}{\sum_j p_{\text{T}}^j},$$

where the indexes i and j run over the constituents of the jet (either clusters in the case of a reconstructed jet, or the generator-level truth particles in simulation). Figure 4.33 (left) shows that jets get more narrow with p_{T}, and that quark-initiated jets are significantly more narrow than gluon-initiated. The figure on the right shows a similar generator-level study by Gallicchio and Schwartz, who discuss the phenomenological differences among quark- and gluon-initiated jets [168] and suggest how to select control samples in the data enriching either quarks or gluons [169].

In general, gluon-initiated jets tend to have higher track and cluster multiplicities, and wider angles among their constituents than quark-initiated jets. This results in lower tau ID fake rates in samples enriched with gluon-initiated jets, and higher for quarks.

[34] Profile plots were first discussed in Section 4.3.3.

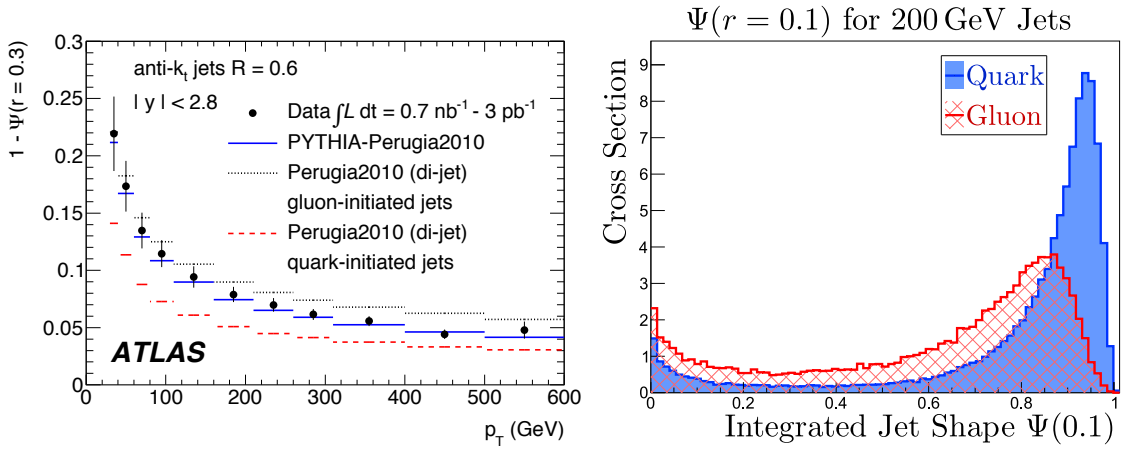

Figure 4.33: (left) A profile plot of $1 - \Psi(0.3)$ vs p_{T} using 2010 ATLAS data. Such a quantity is a measure of the jet width, quantifying the fraction of the jet energy not within $\Delta R < 0.3$ [157]. (right) The generator-level distribution for $\Psi(0.1)$ separately for quark- and gluon-initiated jets with $p_{\mathrm{T}} = 200$ GeV [168]. Note that while both have significant tails with Ψ approaching 0, quark-initiated jets have Ψ peaked much closer to 1, meaning that quark-initiated jets are more likely to be tightly collimated.

How does the quark/gluon fraction vary among samples?

It being clear that the quark/gluon fraction can have a large effect on tau ID fake rates, next one is lead to question how the quark/gluon fraction can vary among selections. Figure 4.34 shows the leading order diagrams for W + jet production at hadron-hadron colliders. Note that the first two diagrams have a quark-initiated jet in the final state, while the third diagram has a gluon-initiated jet. The exact details behind the hadronization of these jets are complicated, but studies with MC truth have shown [167] that the sign of the charge of a reconstructed tau candidate, counted from the sum of the charges of the associated tracks, is anti-correlated with the sign of the W boson emitted, presumably because the sign of the charge of the out-going quark is correlated with the final reconstructed charge of the resulting tau candidate. Therefore the W + jets processes with quark-initiated jets are more likely to counted with the tau candidate and lepton having opposite-sign charges (OS). Gluon-initiated jets, on the other hand, show no bias towards a reconstructed charge.

This results in a more quark-enriched W + jet sample in OS than in same-sign (SS), explaining why the fake factor is highest for OS W + jet in Figure 4.31, and why the dijet sample, which is more gluon dominated, is more OS/SS symmetric.

Figure 4.35 shows the estimated quark/gluon fraction for samples of W/Z + jets and dijet events as a function of the jet p_{T} at the generator-level from Gallicchio and Schwartz [169], demonstrating that W/Z + jets events are dominated by quark-initiated jets, while dijet events are more gluon-

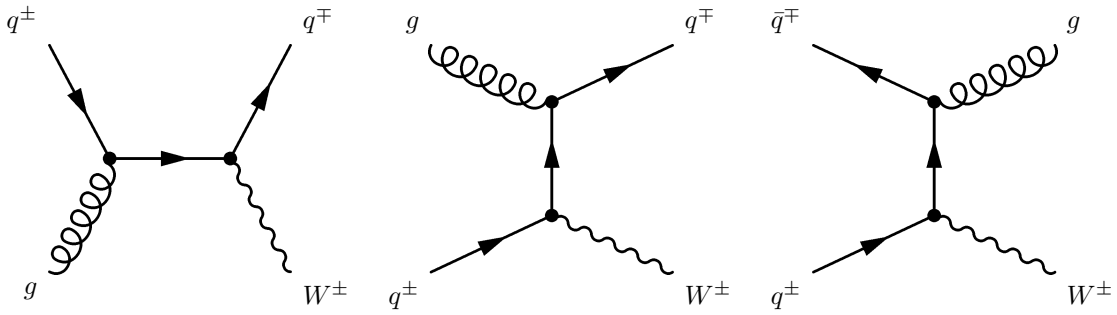

Figure 4.34: Leading order Feynman diagrams for production of W + jets at hadron-hadron colliders. Note that the $\pm$ simply denotes the sign of the electric charge, and that quarks have fractional magnitudes of charge. The diagrams with the quark current flipped also contribute, but diagrams with a $\bar{q}$ in the initial state will be suppressed by the proton PDFs.

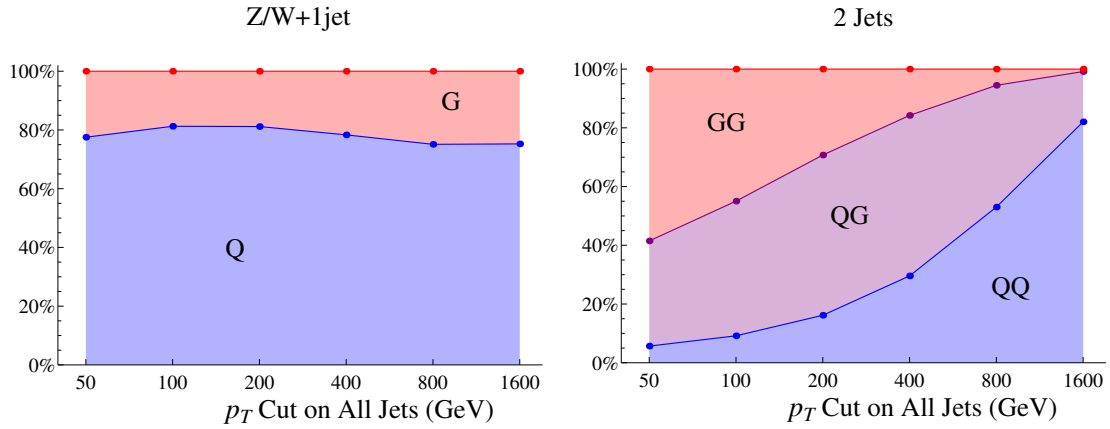

Figure 4.35: Distributions of the predicted quark/gluon fraction of jets in W/Z + jets events (left) and dijet events (right) [169].

dominated but with quarks contributing more significantly for jets with $p_{\mathrm{T}} \gtrsim 100$ GeV. Figure 4.36 plots the generator-level quark-gluon fraction for the true outgoing parton matched to a tau candidate in Alpgen W + jets Monte Carlo, showing that the fake tau candidates get more quark-rich at high-p_{T}.

4.4.9 Pile-up robustness

Motivation for pile-up concerns

Following the initial success of the tau identification for the 2010 dataset, tau performance efforts in 2011 quickly shifted to focus on evaluating the pile-up robustness of the reconstruction and identification, in anticipation of the coming climb in instantaneous luminosity that year. In the later runs of the 2010 dataset in October and November, the peak average number of hard interactions

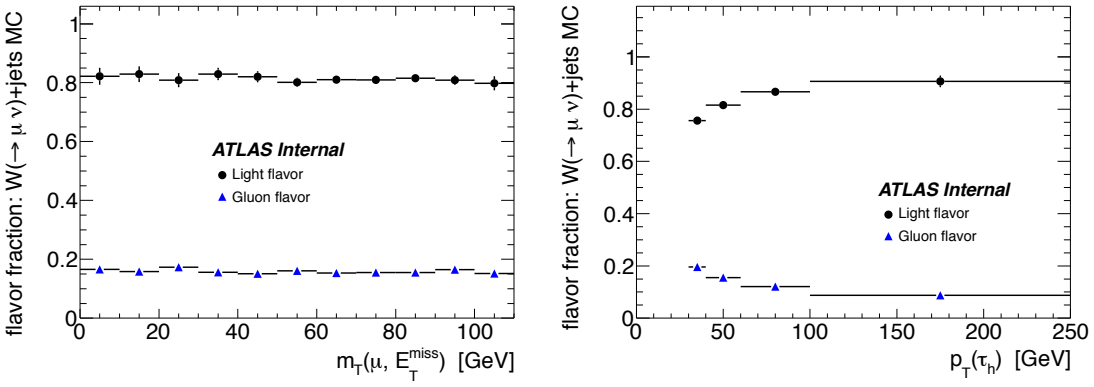

Figure 4.36: The true leading quark/gluon fraction of a jet in Alpgen W + jets Monte Carlo events plotted as a function of the transverse mass, m_{T}, of the selected muon and $E_{\mathrm{T}}^{\mathrm{miss}}$ (left), and as a function of the p_{T} of the tau candidate seeded by the jet (right) [97].

per bunch-crossing exceeded 3, providing significant samples of events with up to 5 reconstructed vertices per bunch-crossing for evaluating the effects of pile-up. In 2011, the peak average number of hard interactions would climb to nearly nearly 20, and surpass 30 in 2012[35].

With the first samples of events with many vertices per bunch-crossing taken in later 2010, one could already see significant degradation in the efficiency to select true tau signal with the cut-based ID. As shown in Figure 4.37, the tight cut-based ID for 1-prong candidates, for example, falls from being $\approx 40\%$ efficient for tau candidates with $p_{\mathrm{T}} \approx 30$ GeV in events with 1 reconstructed vertex, to $\approx 25\%$ in events with 4 vertices, an alarming sensitivity to pile-up that would soon increase.

The main improvement to the tau reconstruction in 2011 to mitigate the effects of pile-up concern the procedure for associating a vertex to a tau candidate, discussed previously in Section 4.2.5. Instead of selecting tracks with d_0 and z_0 selection requirements with respect to the primary vertex with the highest $\sum p_{\mathrm{T}}^2$ of tracks, the vertex with the highest JVF for a tau candidate is associated to that candidate, which improves the efficiency to select the correct tracks in high-pile-up events. Selecting the proper vertex for a tau candidate with the highest JVF, which selects the vertex with tracks that are most correlated with the jet seeding that candidate, and then only selecting tracks consistent with that vertex, stabilized the tracking-related variables used with tau identification, with respect to pile-up.

The other improvements to the reconstruction concerned correcting calorimeter-related variables to dampen the effects of pile-up. First, explorations to mitigate pile-up in the cut-based ID are discussed. Then, the current corrections to the multivariate-based ID for the 2012 dataset will be reviewed.

[35] See the discussion of pile-up in Section 3.5.2.

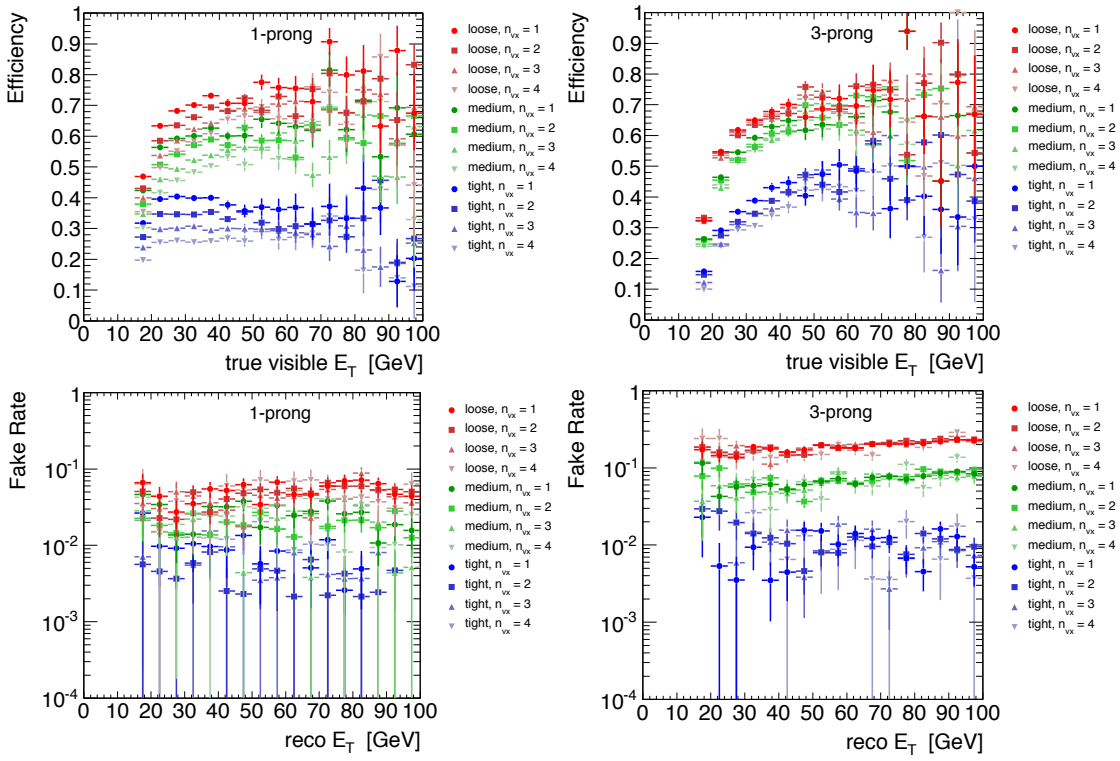

Figure 4.37: Distributions showing the pile-up dependence of the signal efficiency (top) and fake rate (bottom) of the 2010 p_{T}-parametrized cut-based tau ID, using ATLAS simulation. There is a distribution for each loose/medium/tight working point, and binned in the number of reconstructed vertices, showing a dramatic drop in efficiency as the number of vertices increases (mc09) [147].

Calorimeter-related variables are susceptible to pile-up, because unlike tracking-related variables which can be constructed to consider only the tracks consistent with a certain vertex, the calorimeter experiences the sum of activity from all interactions in an event[36]. Figure 4.38 illustrates that calorimeter-related variables, such as the number of clusters or R_{EM}, will be affected by pile-up activity that happens to fall near a tau candidate.

Exploring pile-up corrections with the cut-based ID

The cut-based tau identification was updated in 2011 from its previous version [100], with the main goal of reducing pile-up dependence [101]. The previous version used cuts on only three variables: R_{EM}, R_{track}, and f_{track}, binned in 1-prong and multi-prong candidates. The cuts on R_{EM} and R_{track} were parameterized by the p_{T} of the tau candidate to remove the p_{T} dependence from the identification efficiency. In addition to the p_{T}-dependence, the pile-up-dependence of the tau ID

[36] And in some ways, is effected by events in the recent past, called out-of-time pile-up, discussed in Section 3.5.2.

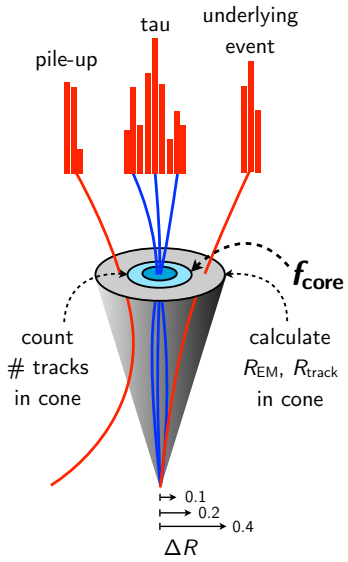

Figure 4.38: A sketch illustrating that f_{core} is calculated as the ratio of energies in $\Delta R < 0.1$ to $\Delta R < 0.2$, smaller than the R_{EM} size of 0.4, to be more pile-up robust.

variables was investigated. These dependences are summarized for some of the key ID variables in Table 4.6. A new pile-up-corrected calorimeter isolation variable was developed to replace R_{EM}, and additional cuts on tracking isolation and transverse flight path significance were added.

Two of the three variables (R_{EM} and R_{track}) used by the previous cut-based ID quantify the width of the hadronic shower, which tends to be larger for QCD jets than for taus of the same energy. The track-based variable R_{track} is robust against pile-up because the tracks are required to be consistent

Table 4.6: An accounting of the p_{T} and pile-up dependence of some of the key tau ID variables. A '+' indicates a positive correlation of that variable with p_{T} or N_{vertex}. A '-' indicates a negative correlation. Tau^{++} refers to the experimental version of the cut-based ID discuss in Section 4.4.9 [170].

	dependence		variable used in Tau^{++}	
	p_{T}	pile-up	1-prong	3-prong
R_{EM}	-	+		
R_{track}	-	0	•	•
f_{track}	weak-	0	•	•
$\sum E_{\text{T}}^{\text{iso}}$(cluster)	weak-	+	•	•
$\sum p_{\text{T}}^{\text{iso}}$(track)	0	0	•	•
N_{eff}(clusters)	-	+		
m_{clusters}	+	+		
m(core clusters)	+	+		
m_{tracks}	bkg weak+	0		
$S_{\text{T}}^{\text{flight}}$	0	0		•

with the primary vertex by demanding ($|z_0 \sin\theta| < 1.5$ mm). By contrast, the calorimeter-based quantity R_{EM} is more sensitive to pile-up since by using calorimeter information alone one cannot measure z_0 at the precision required to distinguish different proton-proton collisions. Additional contributions from pile-up bias the R_{EM} distribution for real hadronic tau decays, making them wider, and more like QCD jets. This can be seen in Figure 4.40, which shows R_{EM} as a function of the number of reconstructed vertices.

One might consider that discriminating hadronic tau decays from QCD jets by requiring a small R_{EM} within the arbitrary cone of $\Delta R < 0.4$ is not the most natural use of the calorimeter information. One can accurately predict the transverse width of true hadronic tau decays with Monte Carlo as a function of p_{T}. Figure 4.7 shows that the spread of calorimeter deposits and tracks for true hadronic tau decays is well within $\Delta R < 0.2$. Having tracks or clusters at wider ΔR is more consistent with a tau candidate being a QCD jet, and hence the discriminating power of R_{EM}. But tracks or clusters at wider ΔR can also be due to activity from pile-up or the underlying event falling on a true hadronic tau decay (see Figure 4.38). The challenge is to distinguish true hadronic tau decays covered in the noise of pile-up from QCD jets. Requiring a narrow R_{EM} is indirectly requiring a tau candidate to be isolated in the calorimeter, that is, without much energy deposited in the annulus of $0.2 < \Delta R < 0.4$. By directly cutting on the energy deposited in this isolation annulus one can exploit the same discriminating information as R_{EM}, but with a quantity that can be more readily corrected by subtracting an estimate of the isolation energy due to pile-up, than could done to correct the pile-up effects on a width variable like R_{EM}.

A new calorimeter isolation variable ($E^{\mathrm{iso}}_{\mathrm{T,corr}}$) is defined as the sum of the E_{T} of the clusters in the isolation annulus and a pile-up correction term:

$$E^{\mathrm{iso}}_{\mathrm{T,corr}} = \sum_{0.2<\Delta R<0.4} E_{\mathrm{T}}(\mathrm{cluster}) - E^{\mathrm{pile\text{-}up}}_{\mathrm{T}} ,$$

with a pile-up correction term to be defined. In order to mitigate pile-up dependence, the newest version of the cut based identification drops cuts on R_{EM}, in favor of making cuts on the $E^{\mathrm{iso}}_{\mathrm{T,corr}}$.

The jet-vertex fraction (JVF) reconstructed for each tau candidate, is calculated as the fraction of the summed p_{T} of tracks associated to the seed jet that are consistent with the selected vertex[37]. Not only can JVF be used to tell if a vertex is consistent with the jet activity, it can indicate the degree of pile-up activity on a candidate. Figure 4.39 shows the distribution of JVF in a 2011 data sample with $\mu \approx 5$. A JVF-based correction to suppress the effects of pile-up on the calorimeter isolation is calculated as follows [170]. When JVF = 1, all tracks falling in a jet are consistent with the primary vertex and not pile-up. If JVF is 95%, then 5% of the sum of the p_{T} of tracks that fall

[37] JVF is discussed in some detail in Section 3.3.6.

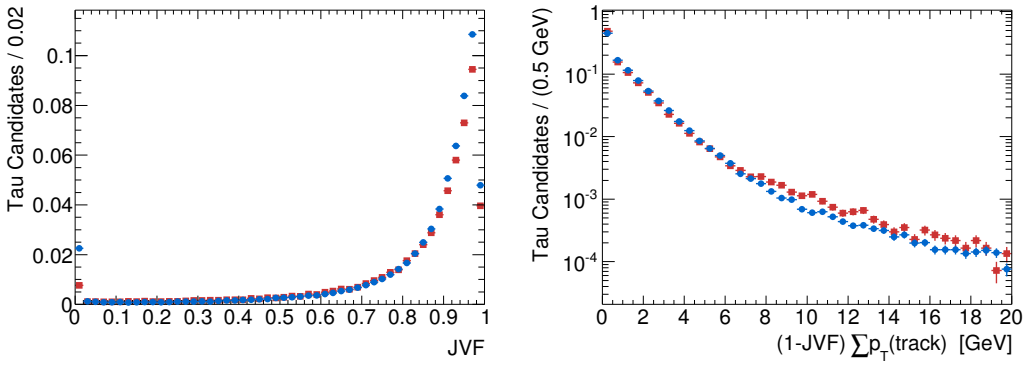

Figure 4.39: Distributions of JVF (left) and $p_{\mathrm{T}}^{\text{pile-up}} = (1 - \mathrm{JVF}) \sum p_{\mathrm{T}}(\text{track})$ (right), for true Monte Carlo hadronic tau decays (blue) and jets from a dijet sample of 2011 ATLAS data (red).

in a jet are from pile-up vertices. Therefore, $1 - \mathrm{JVF}$, estimates the fraction of p_{T} of tracks in a jet that is from pile-up. Multiplying this by the denominator of JVF gives an estimate of the p_{T} of tracks in a jet from pile-up:

$$p_{\mathrm{T}}^{\text{pile-up}} = (1 - \mathrm{JVF}) \sum p_{\mathrm{T}}(\text{track}) \,.$$

This quantity gives a *local* measure of the *charged* pile-up contribution to a jet, in contrast to other measures of pile-up like N_{vertex}, which only quantify the pile-up activity globally in the event.

Note that $p_{\mathrm{T}}^{\text{pile-up}}$, as defined above, does not account for pile-up energy deposits from neutral particles. To the degree that charged and neutral pile-up are correlated, the neutral pile-up can still be estimated from the charged. Ideally one should only correct $E_{\mathrm{T}}^{\text{iso}}$ for the pile-up energy deposited in the isolation annulus, which takes up 3/4 of the area of a cone of $\Delta R < 0.4$. To calibrate the isolation correction, parameterizing to correct for neutrals and for the mismatch in areas for calculating JVF and $E_{\mathrm{T}}^{\text{iso}}$, we introduce a dimensionless parameter α:

$$E_{\mathrm{T}}^{\text{pile-up}} = \min\Big(\alpha \, (1 - \mathrm{JVF}) \sum p_{\mathrm{T}}(\text{track}),\ 4 \ \ \mathrm{GeV}\Big) \,.$$

Several values of α are considered, and a value of $\alpha = 1$ is chosen based on considerations of efficiency and pile-up insensitivity. To keep the correction conservative, the pile-up correction is limited to a maximum of 4 GeV. Only ≈1% of the jets in the training sample with $\mu \approx 5$ would otherwise have exceeded this limit. Figure 4.41 shows that the uncorrected $\langle E_{\mathrm{T}}^{\text{iso}} \rangle$ clearly depends linearly on $p_{\mathrm{T}}^{\text{pile-up}}$, while the dependence is reduced for $\langle E_{\mathrm{T,corr}}^{\text{iso}} \rangle$. Figure 4.40 shows that the correction term largely succeeds in removing the bias in $\langle E_{\mathrm{T}}^{\text{iso}} \rangle$ as a function of N_{vertex} and $p_{\mathrm{T}}^{\text{pile-up}}$. Figure 4.42 shows the cut-based identification efficiency as a function of p_{T} in bins of the number of pile-up vertices.

In addition to introducing pile-up-corrected calorimeter isolation, the cuts have been improved by adding cuts on $N_{\text{track}}^{\text{iso}}$ and $S_{\mathrm{T}}^{\text{flight}}$. Tight and medium levels of the cut-based identification require

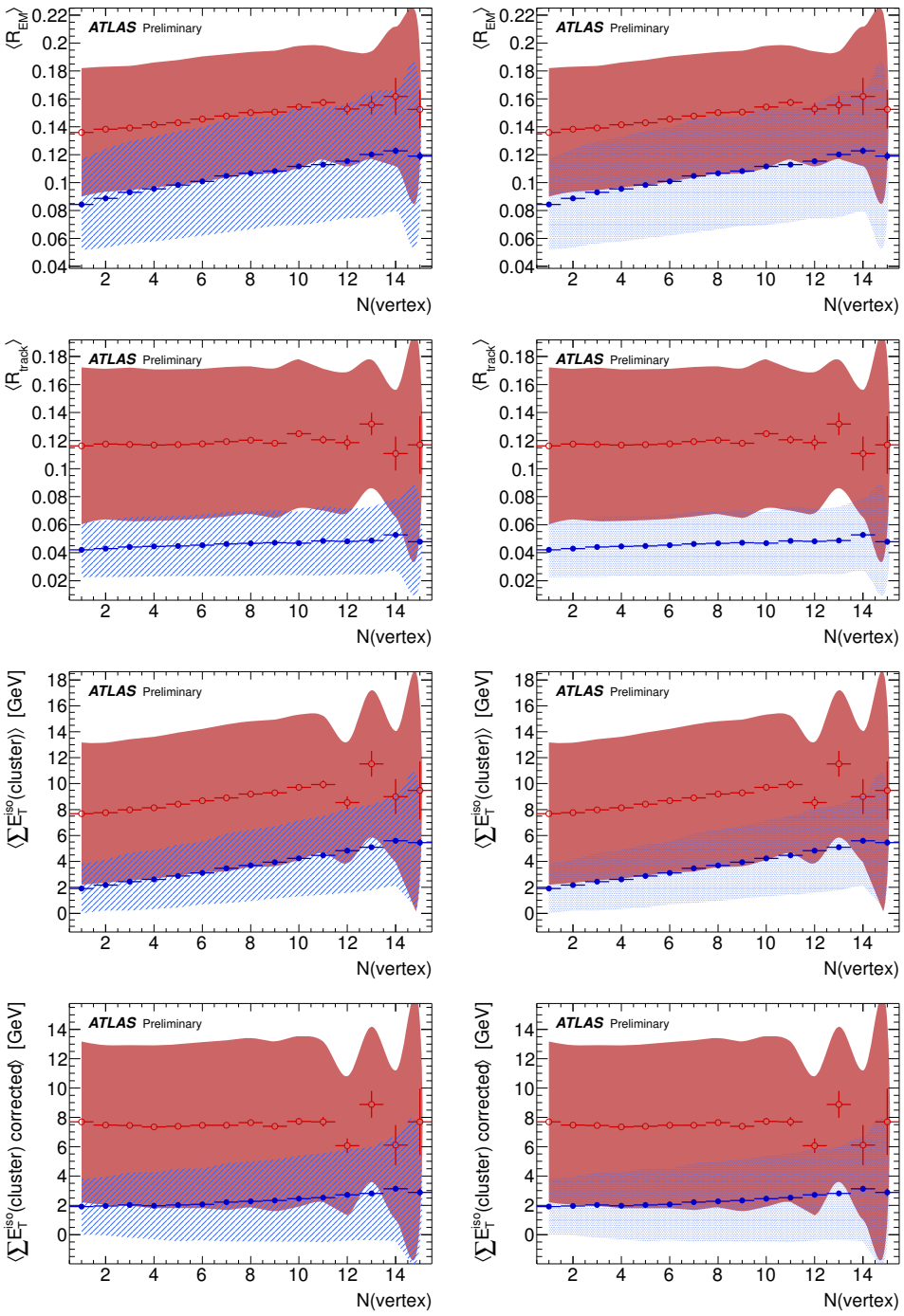

Figure 4.40: The dependence of key tau identification variables as a function of the number of reconstructed vertices, separately for 1-prong (left) and 3-prong (right) tau candidates. The points indicate the means in each bin. The coloured bands indicate the standard deviation. The blue (filled) points correspond to tau candidates matched to hadronically decaying taus in simulated $W \to \tau\nu$ and $Z \to \tau\tau$ events. The red (open) points are for the dijet sample from data [101].

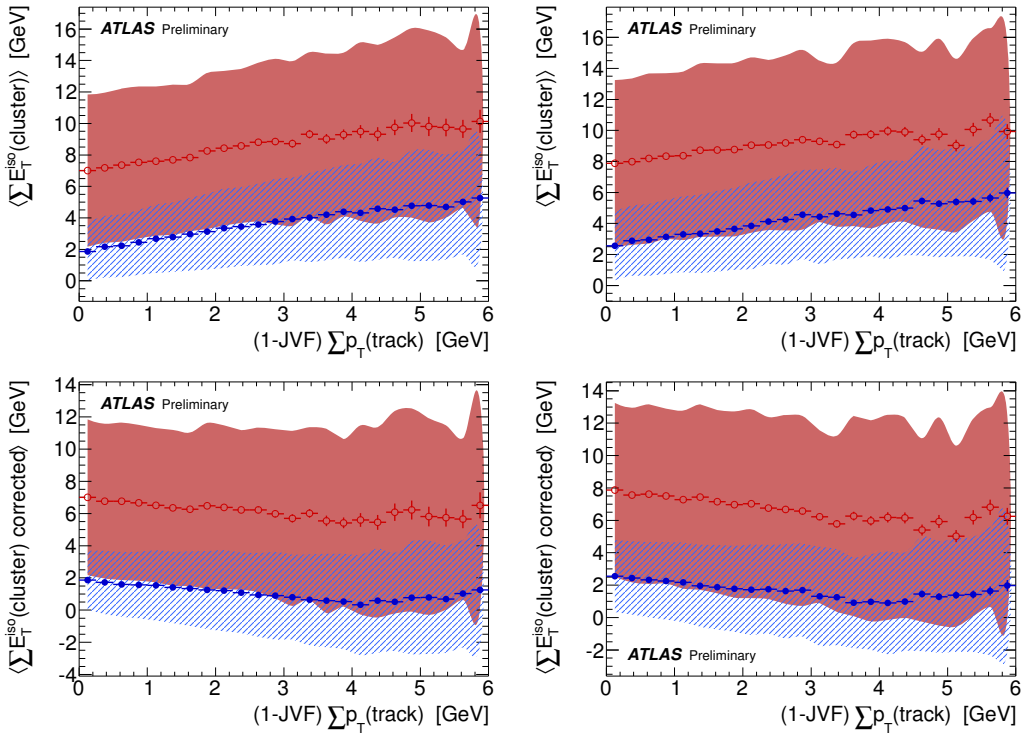

Figure 4.41: The dependence of key tau identification variables as a function of $(1 - \mathrm{JVF}) \sum p_{\mathrm{T}}(\mathrm{track})$, a local measure of the summed p_{T} from pile-up tracks that contribute to the tau candidate, separately for 1-prong (left) and 3-prong (right) tau candidates. The points indicate the means in each bin. The coloured bands indicate the standard deviation. The blue (filled) points correspond to tau candidates matched to hadronically decaying taus in simulated $W \to \tau\nu$ and $Z \to \tau\tau$ events. The red (open) points are for the dijet sample from data [101].

$N_{\mathrm{track}}^{\mathrm{iso}} = 0$. This selection performs better than applying selection based on the sum of track p_{T} in the isolation annulus. For 3-prong candidates, a minimum $S_{\mathrm{T}}^{\mathrm{flight}}$ of 0 and 0.5 is required for the medium and tight-level cuts, respectively. Table 4.7 shows the re-tuned cuts using the pile-up corrected calorimeter isolation.

Figure 4.43 shows the performance of the jet-tau discriminants re-optimzed in 2011. The likelihood- and BDT-based ID methods did not yet use any directly pile-up corrected ID variables, but binned the working points in the number of reconstructed vertices for stability. One can see that for $p_{\mathrm{T}} \gtrsim 40$ GeV the candidates are sufficiently Lorentz collimated that the experimental new cuts suffer from not using any calorimeter information in $\Delta R < 0.2$, and have lower discriminating power.

Instead of using JVF to measure the amount of pile-up on a candidate, a more direct approach would be make a correction for each individual pile-up track that falls near a candidate. Further

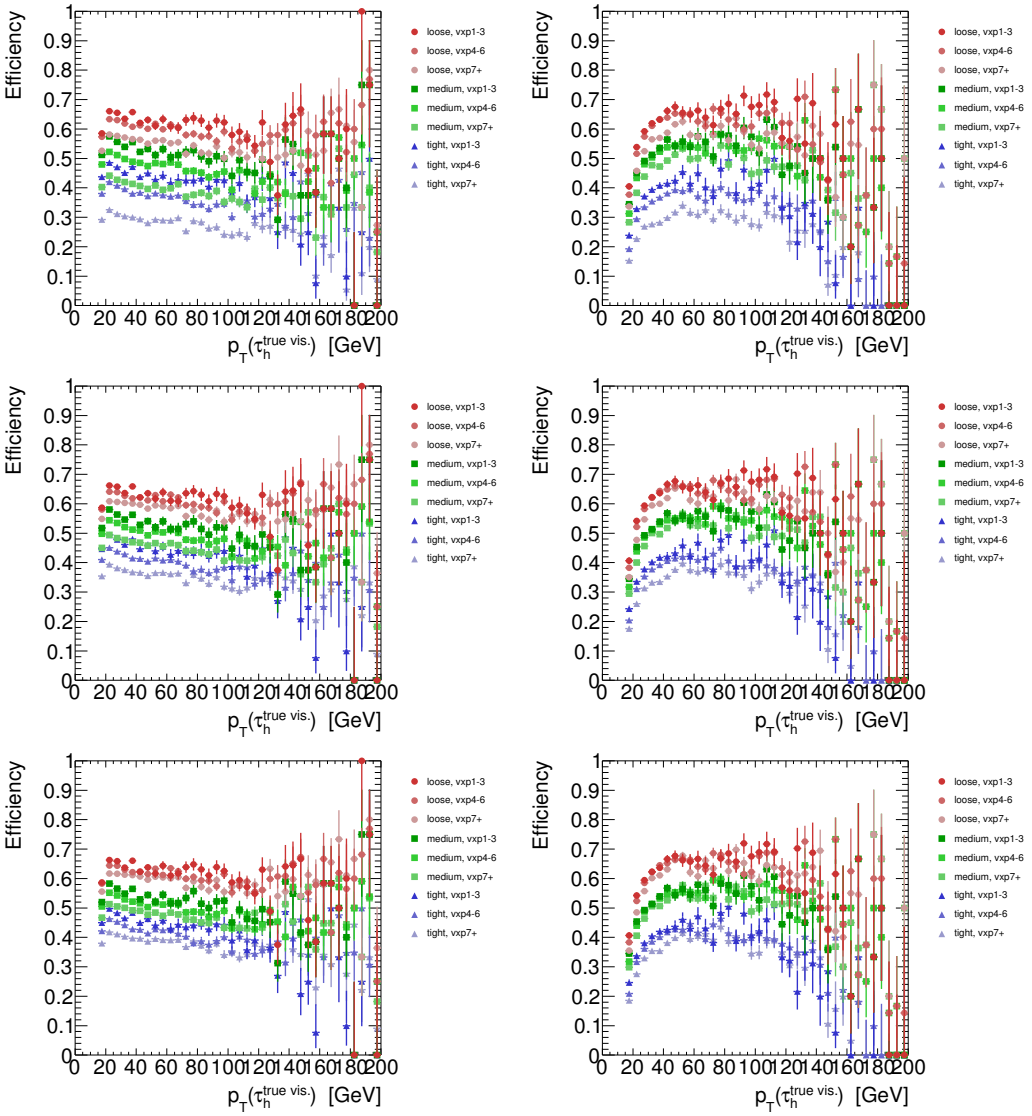

Figure 4.42: Signal efficiency of the experimental Tau^{++} cut-based identification for 1-prong (left) and 3-prong (right) candidates using the chosen value of the parameter, $\alpha = 0.0/0.6/1.0$ for (top/center/bottom) [117].

investigation was done using track extrapolation tools to find each pile-up track falling near a tau candidate, and to use each one to make a correction to the isolation. Although the principle is attractive, manpower and time constraints left the study with only preliminary results [171].

Pile-up tracks that are not consistent with the selected vertex of the tau candidate are extrapolated to layer-2 of the EM calorimeter and the sum of their p_{T} is counted if the tracks fall within the isolation annulus ($0.2 < \Delta R < 0.4$). This sum is used to make a correction term to the isolation with a second correction depending on the number of reconstructed vertices:

$$E_{\mathrm{T}}^{\mathrm{iso}\prime} = \sum_{0.2<\Delta R<0.4} E_{\mathrm{T}}(\text{cluster}) - a \sum_{0.2<\Delta R<0.4} p_{\mathrm{T}}(\text{track extrap.}) - b\, N_{\mathrm{vertex}}\,,$$

where a and b are parameters that can be tuned to slope of the dependence of $E_{\mathrm{T}}^{\mathrm{iso}}$ on the respective terms.

Figure 4.44 shows that the uncorrected calorimeter isolation shows a strong dependence on the number of reconstructed vertices, adding approximately 320 MeV per vertex. The first correction using the extrapolated pile-up tracks succeeds in suppressing the dependence on N_{vertex} to approximately 190 MeV per vertex. Part of the remaining dependence is because only approximately 50% of the candidates in the $Z \to \tau\tau$ MC used with $\mu \approx 5$ do not have any pile-up tracks matched to them. The remaining dependence is removed with the second term. The performance of the experimental cut-based tau ID with this correction was comparable to the cuts using the JVF-based correction.

Table 4.7: Cut values for the working points for the experimental Tau^{++} ID, using the JVF-corrected $E_{\mathrm{T,corr}}^{\mathrm{iso}}$ [117].

1-prong				
R_{track}	$<$	$417/p_{\mathrm{T}} + 0.0824 - 2.61\times10^{-7} p_{\mathrm{T}}$	for $p_{\mathrm{T}} < 80$ GeV	loose or medium
		0.0667	for $p_{\mathrm{T}} \geq 80$ GeV	
		$417/p_{\mathrm{T}} + 0.0724 - 2.61\times10^{-7} p_{\mathrm{T}}$	for $p_{\mathrm{T}} < 80$ GeV	tight
		0.0567	for $p_{\mathrm{T}} \geq 80$ GeV	
$1\ /\ f_{\mathrm{track}}$	$<$	4.0, 3.33, 2.5		loose, medium, tight
$E_{\mathrm{T,corr}}^{\mathrm{iso}}$	$<$	6, 4, 3 GeV		
$N_{\mathrm{track}}^{\mathrm{iso}}$	$=$	no cut, 0, 0		
3-prong				
R_{track}	$<$	$375/p_{\mathrm{T}} + 0.0696 - 3.28\times10^{-7} p_{\mathrm{T}}$	for $p_{\mathrm{T}} < 80$ GeV	loose or medium
		0.048	for $p_{\mathrm{T}} \geq 80$ GeV	
		$375/p_{\mathrm{T}} + 0.0596 - 3.28\times10^{-7} p_{\mathrm{T}}$	for $p_{\mathrm{T}} < 80$ GeV	tight
		0.038	for $p_{\mathrm{T}} \geq 80$ GeV	
$1\ /\ f_{\mathrm{track}}$	$<$	3.33, 3.33, 2.5		loose, medium, tight
$E_{\mathrm{T,corr}}^{\mathrm{iso}}$	$<$	7, 7, 4 GeV		
$N_{\mathrm{track}}^{\mathrm{iso}}$	$=$	no cut, 0, 0		
$S_{\mathrm{T}}^{\mathrm{flight}}$	$>$	no cut, 0, 0.5		

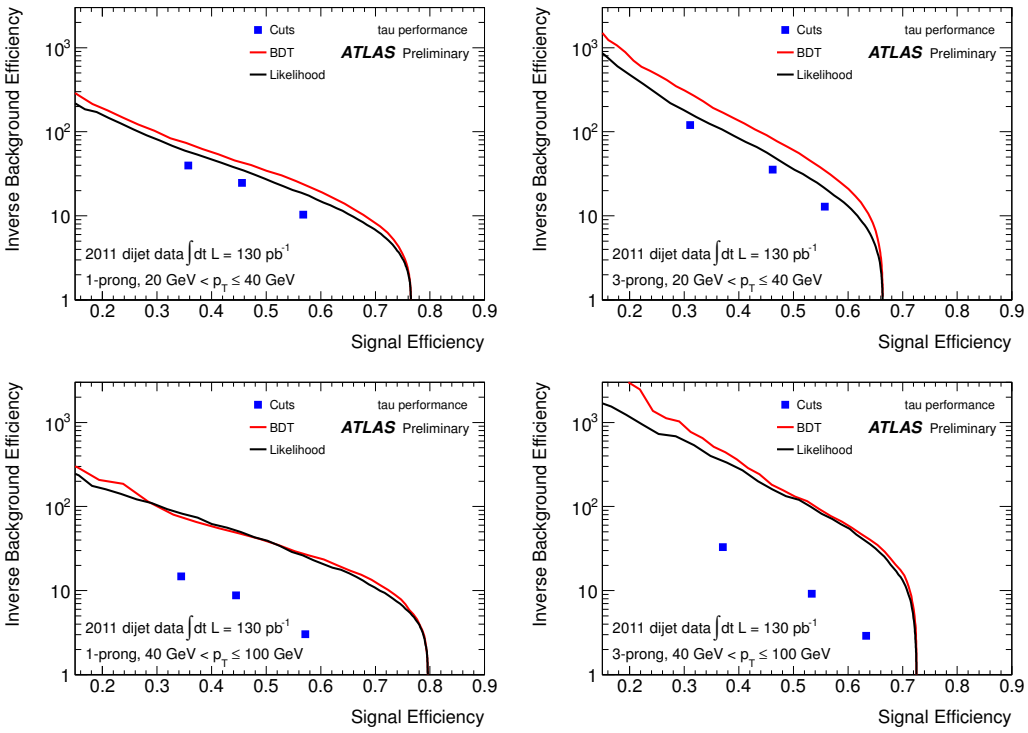

Figure 4.43: Inverse background efficiency as a function of signal efficiency for 1-prong (left) and 3-prong (right) candidates, in low (top) and high (bottom) p_{T} ranges, for the jet-tau discriminants re-optimized in the summer of 2011 [101].

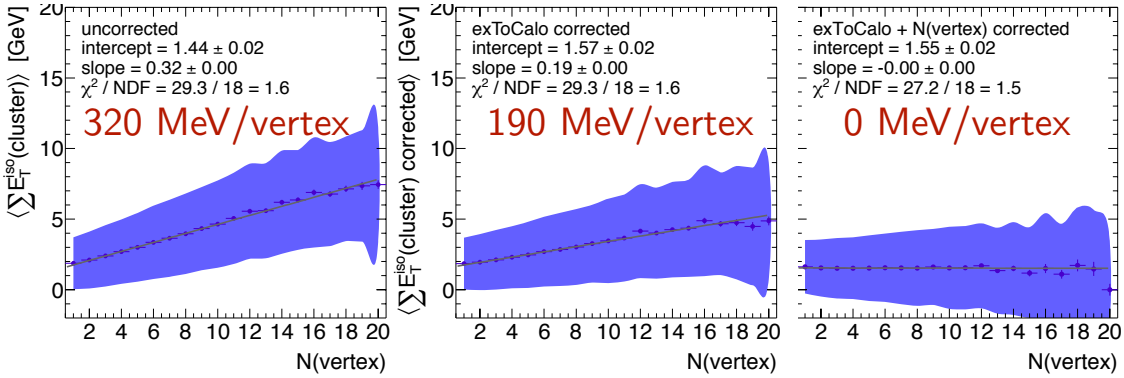

Figure 4.44: Profile plots of the cluster isolation, $E_{\mathrm{T}}^{\mathrm{iso}}$, without a pile-up correction (left), corrected with extrapolated pile-up tracks (center), and corrected with extrapolated pile-up tracks and a term linear in N_{vertex} (right) [171].

Pile-up corrections in the 2012 ID

It became clear that the experimental versions of the cuts, while aggressively attempting to make a pile-up correction using information local to the tau candidate, had lost performance by not using calorimeter information in the core cone of $\Delta R < 0.2$. For use with the 2012 dataset, a method of reducing the pile-up dependence of the tau identification was developed by using the *core energy fraction*, f_{core}, calculated as the ratio of the sum of the calorimeter cells associated to the candidate within $\Delta R < 0.1$ to that of $\Delta R < 0.2$ (see the definition in Appendix B). This variable would replace R_{EM} in the multivariate ID methods, having less pile-up dependence because it uses a cones smaller than 0.4 (see Figure 4.38), and the ratio of energies naturally cancels some of the dependence.

The remaining pile-up dependence was corrected with a simple global correction depending on the number of reconstructed vertices. Such a linear correction is defined for f_{core} and f_{track}:

$$f_{\text{core}}^{\text{corr}} = f_{\text{core}} + 0.003 \times N_{\text{vertex}}\,, \text{ for } p_{\text{T}} < 80 \text{ GeV},$$

$$f_{\text{track}}^{\text{corr}} = f_{\text{track}} + 0.003 \times N_{\text{vertex}}\,.$$

Figure 4.45 (left) shows the dependence of f_{core} and its corrected version on N_{vertex}, as well as the efficiency of the 2012 BDT-based jet-tau discriminant. Putting the pile-up corrected variables into the training of the BDT and the construction of the likelihood resulted in a much more flat efficiency as a function of the number of reconstructed vertices for both methods. For example, the signal efficiencies for the BDT working points for 1-prong candidates vs N_{vertex} are shown in Figure 4.45 (right)[38].

[38] The primary references discussing the topics of this chapter in more detail are

- *Commissioning of the ATLAS tau lepton reconstruction using 900 GeV minimum bias data* `ATLAS-CONF-2010-012` [154] – the first note to document the commissioning of the ATLAS tau reconstruction with the first minimum-bias data,
- *Reconstruction of hadronic tau candidates in QCD events at ATLAS with 7 TeV proton-proton collisions* `ATLAS-CONF-2010-059` [144] – commissioning note,
- *Reconstruction, energy calibration, and identification of hadronically decaying tau leptons* `ATLAS-CONF-2011-077` [100] – the first report of the ATLAS tau performance with the 2010 data,
- *Performance of the reconstruction and identification of hadronic tau decays with ATLAS* `ATLAS-CONF-2011-152` [101] – the report of the ATLAS tau performance with the 2011 data,
- *A search for high-mass resonances decaying to $\tau^+\tau^-$ in pp collisions at $\sqrt{s} = 7$ TeV with the ATLAS detector* `ATL-COM-PHYS-2012-394` [97] – support note for the $Z' \to \tau\tau$ search, including some of the first recommendations for high-p_{T} taus,
- *Performance of the reconstruction and identification of hadronic tau decays in ATLAS with 2011 data* `ATLAS-CONF-2012-142` [102] – an updated report of the ATLAS tau performance with the 2011 data,
- *Identification of the hadronic decays of tau leptons in 2012 data* `ATL-COM-PHYS-2012-1821` [103] – the support note for the upcoming report of the ATLAS tau performance with the 2012 data.

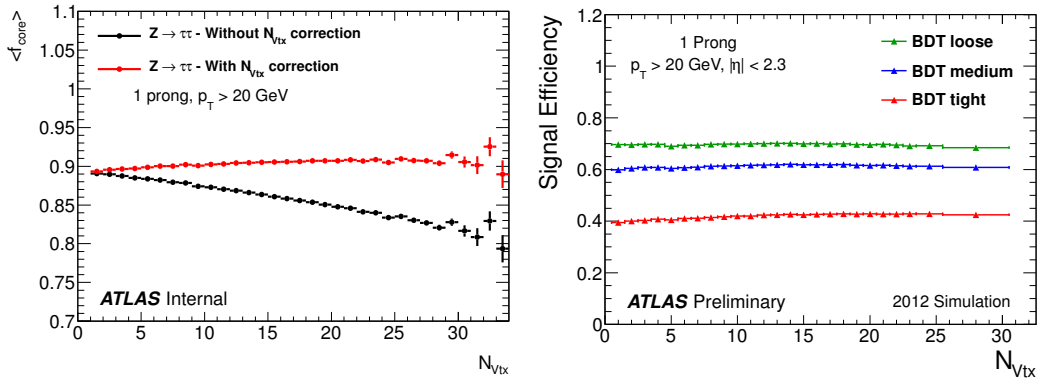

Figure 4.45: (left) Profile plot of f_{core} vs N_{vertex} for the uncorrected (black) and pile-up corrected (red) versions. (right) The signal efficiency of the BDT working points vs N_{vertex}, using the pile-up corrected versions of f_{core} and f_{track}, from 2012 ATLAS simulation [103].

Chapter 5

Measurement of the $Z \to \tau\tau$ cross section

This chapter describes studies of the event kinematics of $\ell\tau_{\rm h}$ events with Monte Carlo before the start-up of the LHC, the observation of $Z \to \tau\tau$ with the first 8.5 pb^{-1} of ATLAS data in 2010, and the $Z \to \tau\tau$ cross section measurement with the 36 pb^{-1} dataset collected in 2010. The discussion is focused on the $\ell\tau_{\rm h}$ channel because of its interest as a $\tau_{\rm h}$ control sample, its use in new physics searches, and because it was the focus of my graduate research.

5.1 Introduction

5.1.1 Motivation

The production of $W \to \tau\nu$ and $Z \to \tau\tau$ events at the LHC provides the critical control samples for evaluating the performance of the triggering, reconstruction, and identification of hadronically decaying tau leptons. Such events provide true tau leptons with relatively low visible transverse momenta and with genuine missing transverse momentum. The $\ell\tau_{\rm h}$ final state is especially interesting because one can trigger on the lepton, leaving an unbiased sample of tau candidates for studying tau performance[39]. In addition, because the visible mass distribution of the $\ell\tau_{\rm h}$ system is sensitive to the energy scale of the reconstructed tau candidates, a measurement of the tau energy scale can be made with this sample. Additionally, the $\tau\tau$ invariant mass distribution, using the collinear approximation[40], is sensitive to the $E_{\rm T}^{\rm miss}$ scale. Therefore, $Z \to \tau\tau$ events can be used as a control sample for the $E_{\rm T}^{\rm miss}$ reconstruction in events with genuine $E_{\rm T}^{\rm miss}$ [172, 173, 159].

[39] For example, the $Z \to \tau\tau$ tag-and-probe study, discussed briefly in Section 4.4.7, takes advantage of this sample of tau decays.

[40] The *collinear approximation* is a mass-reconstruction technique for ditau systems where the components of the $E_{\rm T}^{\rm miss}$ are projected along the visible decay products. The fractions of the momenta carried by neutrinos for each tau decay can be solved for analytically if the decays are not back-to-back. The method is described in more detail in Refs. [69, 172].

Moreover, $Z \to \tau\tau$ will often dominate control regions and/or the signal region in searches for new physics with the $\tau\tau$ final state like $H \to \tau\tau$ and $Z' \to \tau\tau$. The $Z \to \tau\tau$ process forms the main irreducible background that must be understood in order to search for new physics in this channel [69].

5.1.2 Backgrounds

When trying to select the $Z \to \tau\tau$ process itself, in the $\ell\tau_{\text{h}}$ channel, there is a complicated background composition dominated by processes that produce a real lepton and a real or fake hadronic tau decay. They include:

- **$W(\to \ell\nu)$ + jets** Decays of W bosons produce a real lepton and missing transverse momentum, and jets produced in association with the W are mis-identified as hadronic tau decays at a rate of a few percent. The relatively large cross section for these events make W+jets events the largest background in the signal region. The process $W \to \tau\nu \to \ell\nu\nu\nu$, where the electron or muon comes from the tau decay, also contributes a few percent to the total $W \to \ell\nu$ background.

- **$Z/\gamma^*(\to \ell\ell)$ + jets** If one of the electrons or muons from $Z/\gamma^*(\to \ell\ell)$ does not pass the object preselection, this process will pass the dilepton veto, and jets produced in association with the Z are mis-identified as hadronic tau decays at a rate of a few percent. One of the leptons can also be mis-identified as a tau candidate. $Z \to ee$ is a more challenging background in the $e\tau_{\text{h}}$ channel than $Z \to \mu\mu$ is for the $\mu\tau_{\text{h}}$ channel because it is much more rare for a muon to deposit significant energy in the calorimeter, while electrons readily make a track and an isolated cluster.

- **Multijet** Multijet events are a challenge at hadron colliders because the cross section for multijet events produced in strong interactions is many orders of magnitude above the electroweak processes that produce tau leptons[41]. This background is dominated by B-meson and kaon in-flight decays within a jet, which provide sources of real leptons, but there is also a contribution from mis-identified leptons that is more significant in the $e\tau_{\text{h}}$ channel. The multijet background can be suppressed with lepton isolation, and a pure control sample of the multijet background can be selected by requiring a non-isolated lepton candidate.

- **$t\bar{t}$ and single top** The decay of top quarks provides sources of leptons, real and fake hadronic taus, and often significant $E_{\text{T}}^{\text{miss}}$.

[41] Recall the introductory discussion of hadronic tau decays and fakes in Section 3.3.7 and the review of tau reconstruction in Chapter 4.

- **Diboson** The production of vector boson pairs (WW, WZ, ZZ) provides sources of leptons, real and fake hadronic taus, and often significant $E_{\mathrm{T}}^{\mathrm{miss}}$.

5.2 MC studies of $\ell\tau_{\mathrm{h}}$ event kinematics

In order to better understand the background composition and optimal selection criteria, studies of $Z \to \tau\tau$ were performed prior to the start-up of the LHC[42], the results of which are reviewed in this section.

5.2.1 Multijet background

Without data to employ a data-driven technique, it was a challenge to model the estimated multijet background. Independent of the issues of Monte Carlo modeling of QCD hadronization, the resulting distributions of jet-shapes, and their consequences on the modeling of the efficiency for jets to pass tau identification[43], the multijet background is especially difficult to estimate with Monte Carlo because it has the worst combination of having a high event-rate and low selection-rate. Therefore, the multijet background of a selection of events at the LHC often has limited Monte Carlo statistics passing object identification and event selection, but is not always clearly negligible.

Figure 5.1 concerns the sources of reconstructed muon candidates in a Monte Carlo dijet sample. Figure 5.1 (a) shows that approximately 2/3 of the muons in dijets come from prompt sources, and therefore can be matched to a true generator-level muon. Most of the other third come from the decay of pions or kaons in flight, which happen after generation in the GEANT detector simulation. Since one cannot select events which will have a pion or kaon decay with a generator-level filter, it is not practical to efficiently sample this background with Monte Carlo. Figure 5.1 (b) shows that of the generator-level muons, most of them come from B hadron decays. Therefore it is relevant to focus on the $b\bar{b}$ background, for which ATLAS produced Monte Carlo samples with a generator-level filter for a muon with $p_{\mathrm{T}} > 15$ GeV.

The lepton-p_{T} distribution of the multijet background is steeply falling, and therefore the background may be effectively cut away with a high-p_{T} requirement, but at the cost of much of the $Z \to \tau\tau$ sample, which also prefers low-p_{T} leptons (see Figure 5.2).

Analyses that require significant $E_{\mathrm{T}}^{\mathrm{miss}}$ can effectively suppress the multijet background, as shown in Figure 5.3, but $Z \to \tau\tau$ events generally have soft $E_{\mathrm{T}}^{\mathrm{miss}}$ because most often the tau decays are back-to-back and the vector-sum of the neutrino momenta largely cancel.

[42] This section uses Monte Carlo from the `mc08` ATLAS Monte Carlo before the start-up of the LHC, around the time of ATLAS Full Dress Rehearsal (FDR) in 2008 when large scale Monte Carlo production was being done to exercise the entire ATLAS computing chain [174, 175].

[43] See the discussion of jet-shapes and tau identification in Section 4.4.1 and Section 4.4.8.

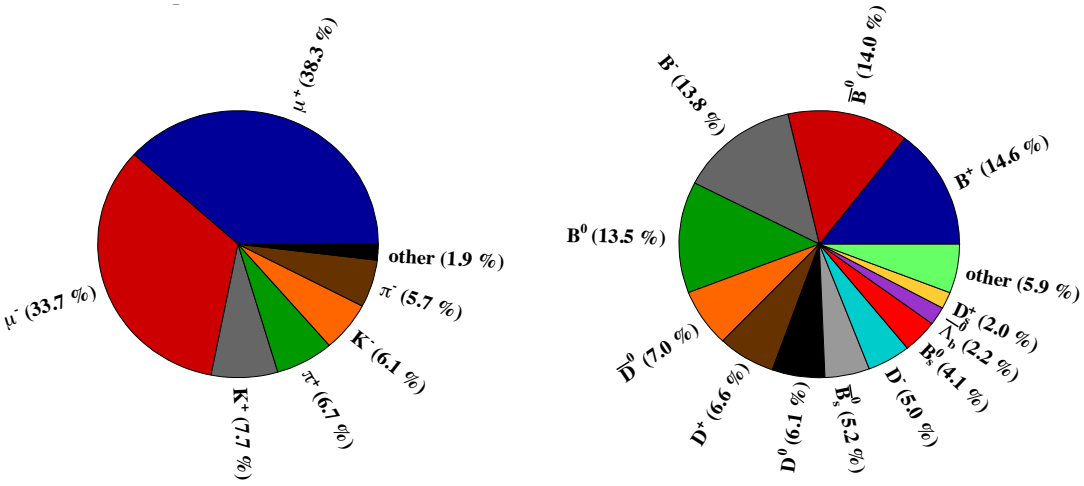

(a) Nearest generator truth particle to a reconstructed muon

(b) Parent particle of true generator muons

Figure 5.1: Generator-level truth information for muons in the `mc08` PYTHIA J2 dijet sample [176].

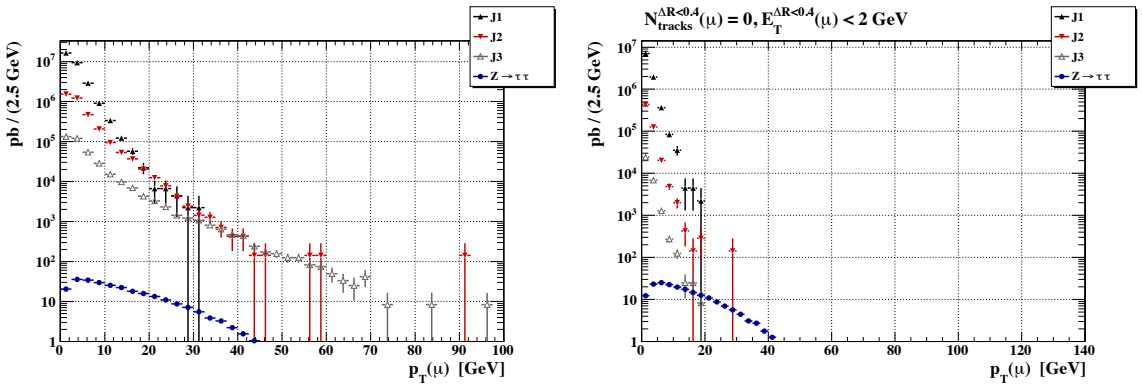

(a) Without isolation

(b) With isolation

Figure 5.2: The p_{T} of reconstructed muon candidates, comparing dijet and $Z \to \tau\tau$ MC (`mc08`, $\sqrt{s} = 10$ TeV) [176] J1, J2, and J3 denote simulated dijet samples with an out-going parton in the p_{T} ranges 17–35, 35–70, and 70–140 GeV respectively.

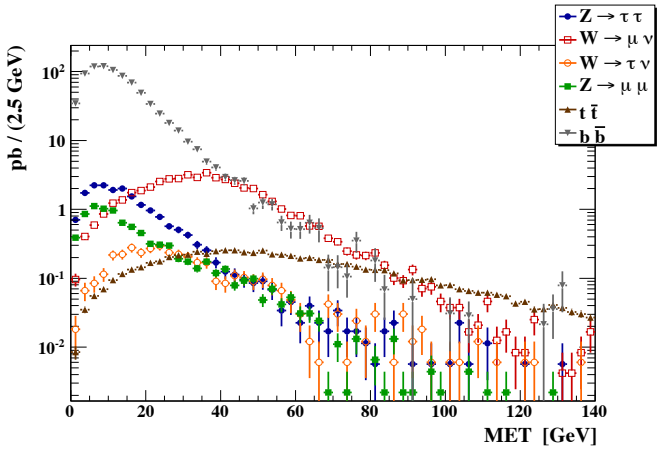

Figure 5.3: The distribution of the reconstructed missing transverse momentum for the relevant MC samples with preselected $\mu\tau_{\mathrm{h}}$ events [176].

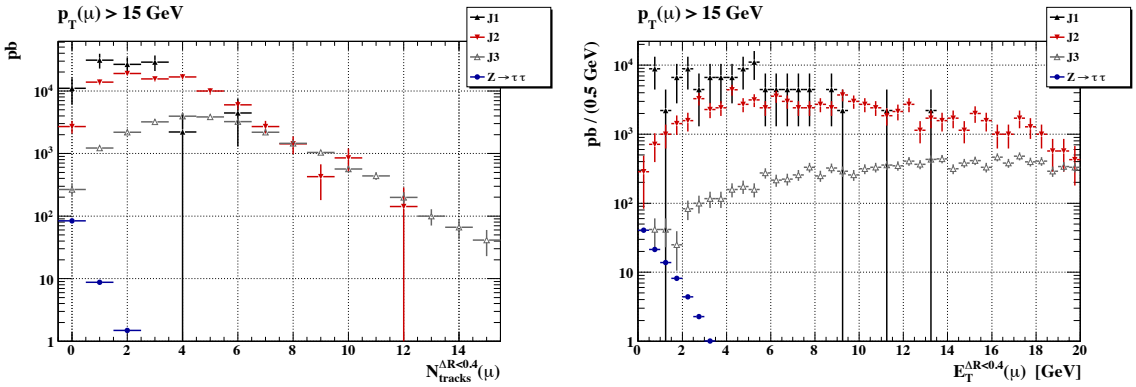

Figure 5.4: Distributions of tracking- and calorimeter-based muon isolation variables for $Z \to \tau\tau$ and dijet samples [176].

The most effective way to suppress the multijet background in events with a selected lepton is to require that the lepton be isolated. Leptons produced in jets will tend to be collimated with the other particles in the jet. Requiring that a lepton not be near other tracks or significant energy deposits in the calorimeter will exclude these background events. Figure 5.4 shows examples of two muon isolation variables, one using tracking information and the other being calorimeter-based.

- $N_{\mathrm{tracks}}^{\Delta R<0.4}(\mu)$ (`nucone40` in Athena)

  The number of tracks with $p_{\mathrm{T}} > 1$ GeV within $\Delta R < 0.4$ around the trajectory of the muon (not including the track of the reconstructed muon).

- $E_{\mathrm{T}}^{\Delta R<0.4}(\mu)$ (`etcone40` in Athena[44])

[44] Also referred to as $I_{E_{\mathrm{T}}}^{0.4}$ in Section 5.4.4.

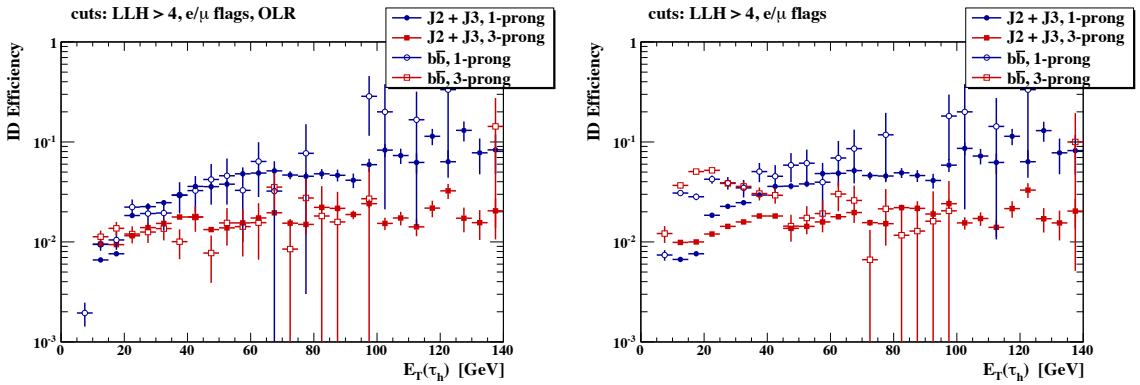

(a) With overlap removal (b) Without overlap removal

Figure 5.5: Tau identification fake rates derived with dijet and $b\bar{b}$ Monte Carlo samples (mc08, $\sqrt{s} = 10$ TeV) [176]. The identification used is a preliminary version of the likelihood method [148]. The fake rate in the $b\bar{b}$ sample is enhanced compared to the inclusive sample of dijets, mainly due to the presence of real leptons from B decays, but the effect is not significant after removing pre-selected leptons.

The E_{T} deposited in calorimeters within $\Delta R < 0.4$ around the trajectory of the muon.

Requiring that an event pass lepton isolation cuts and tau identification each suppress the multijet background by a factor of 10–100, resulting in poor Monte Carlo statistics for modeling the multijet background. In order to improve the statistics of the multijet model, the rate for jets to fake tau identification was parameterized and used to weight MC events instead of directly applying the tau identification requirements. This method is valid, assuming that the rate to pass tau identification depends on the local properties of the jet forming the tau candidate, and is largely uncorrelated[45] with the global event kinematics (invariant masses, $\Delta\phi$, etc.) [176]. This method is similar to the fake factor methods developed later for the search for $Z' \to \tau\tau$, discussed in Section 6.4.4.

First, the fake rate for jets to pass the tau identification cuts, as measured with the dijet Monte Carlo, was parametrized in bins of the reconstructed visible E_{T} and the number of tracks (prongs) associated to a tau candidate. Figure 5.5 shows the fake rate measured with an inclusive dijet sample and a $b\bar{b}$ sample. These fake-rates are defined[46] as

$$\varepsilon = \frac{\text{number of } n\text{-prong candidates in the } E_{\mathrm{T}}\text{-bin that pass selection}}{\text{number of n-prong candidates in the } E_{\mathrm{T}}\text{-bin}},$$

After parametrizing the fake rate[47], when analyzing the $b\bar{b}$ Monte Carlo sample, the tau identification

[45] There *is* actually some sample dependence in the fake rates for tau identification, mainly due to variations in the quark-gluon fraction of the out-going parton initiating a jet as discussed in Section 4.4.8.

[46] Here, "selection" denotes identification and overlap-removal requirements that will be discussed in more detail in Section 5.4.4.

[47] The fake rates of the inclusive dijet and $b\bar{b}$ sample were in statistical agreement after overlap removing preselected leptons, and therefore the fake rates from the large inclusive dijet sample where used. Pre-selection and overlap removal are discussed later in Section 5.4.3.

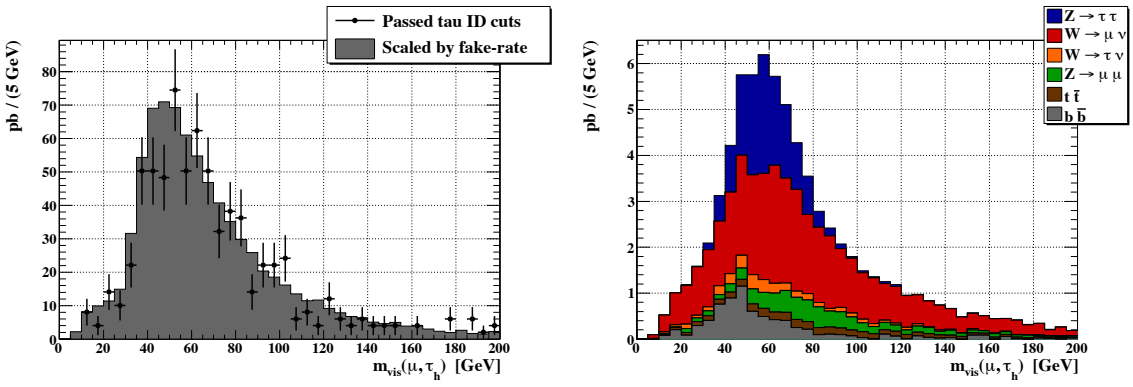

Figure 5.6: Distributions of the visible mass of the combination of a muon and a selected tau candidate. (left) A comparison of Monte Carlo $b\bar{b}$ events that pass tau identification with a distribution from scaling candidates by a fake rate (with no lepton isolation). (right) The combined SM background model for selected $\mu\tau_{\mathrm{h}}$ events with tau identification and muon isolation requirements. A preliminary likelihood-based tau identification [148] was used by requiring that the likelihood score was greater than 4. The isolation requirements used were: $N_{\mathrm{tracks}}^{\Delta R<0.4}(\mu) = 0$ and $E_{\mathrm{T}}^{\Delta R<0.4}(\mu) < 2$ GeV [176].

requirements were not applied and instead the events were weighted by the fake rate, tau candidate-by-candidate.

Figure 5.6 shows the predicted distribution of the visible mass of the combination of a muon and a tau candidate passing identification. Figure 5.6 (a) compares the $b\bar{b}$ estimates when requiring the tau identification and when weighting by the fake rate, showing that the shape looks generally well-modeled. Figure 5.6 (b) shows the visible mass after requiring muon isolation, which suppresses the $b\bar{b}$ background by a factor of ≈ 100. Without parametrizing and weighting by the fake rate, the $b\bar{b}$ model would not have a statistically significant shape. Requiring both tau identification and lepton isolation bring the multijet background rate to the order of the other electroweak backgrounds.

5.2.2 W+jets background

After the multijet background has been suppressed by lepton isolation and tau identification, the leading background to tackle is W + jets. There are contributions from both $W \to \ell\nu$ and $W \to \tau\nu \to \ell\nu\nu\nu$ where a jet in the event is falsely identified as the tau candidate.

Opposite-sign vs same-sign

An important property of W + jets events to note is that they are biased towards having a lepton and tau candidate with opposite-sign (OS) reconstructed charges (see Figure 5.7). One can explain this feature by noting that the leading order W + jet diagrams are biased towards having an out-going lepton and quark with opposite-sign charges, and quark-initiated jets are biased towards hadronizing

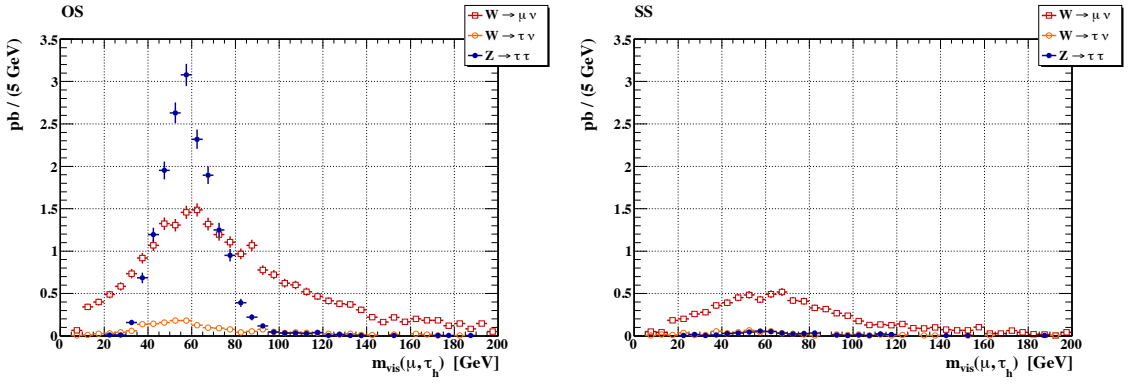

Figure 5.7: The visible mass of $\mu\tau_{\mathrm{h}}$ events with opposite-sign (left) and same-sign (right) reconstructed charges. Note that the W + jets background is OS-biased [176].

and being reconstructed as tau candidates with charge the same sign as the initial out-going quark[48]. Moreover, the quark-gluon fraction is different among the OS and same-sign (SS) W + jets samples[49].

$\boldsymbol{E}_{\mathrm{T}}^{\mathrm{miss}}$ angular correlations

The leptons from W + jets events and other electroweak processes tend to be well isolated. To reject the W + jets background, angular correlations of the direction of the $E_{\mathrm{T}}^{\mathrm{miss}}$ and the directions of the lepton and tau candidate can be exploited. Because the mass of the Z boson is much larger than the mass of the τ lepton, the τ leptons in $Z \to \tau\tau$ will be boosted such that their decay products will be collimated along the trajectory of the parent τ lepton. Ignoring underlying interactions in the event and mis-measurements of $E_{\mathrm{T}}^{\mathrm{miss}}$, the $E_{\mathrm{T}}^{\mathrm{miss}}$ will be the vector sum of the p_{T} of the neutrinos, as depicted in Figure 5.8. The majority of Z bosons produced will have low p_{T}, and therefore the taus will be back-to-back, but in the case that the Z has significant nonzero boost in the transverse plane, the $E_{\mathrm{T}}^{\mathrm{miss}}$ vector will fall in the angle (less than π) between the decay products of the Z.

In contrast, in events from the W + jets background, the neutrino, jet, and muon will all tend to point in different directions, balancing p_{T} in the transverse plane. Ignoring underlying interactions in the event and $E_{\mathrm{T}}^{\mathrm{miss}}$ mis-measurement, the $E_{\mathrm{T}}^{\mathrm{miss}}$ vector should point along the neutrino which is *not* in the angle between the fake tau candidate and the muon. In $W \to \tau\nu \to \mu\nu\nu\nu$ events, there are two additional neutrinos, but the $E_{\mathrm{T}}^{\mathrm{miss}}$ will still point outside of the angle between the muon and the fake tau candidate.

The traditional[50] variable for suppressing W + jets is the transverse mass of the lepton and $E_{\mathrm{T}}^{\mathrm{miss}}$, m_{T}, usually by requiring $m_{\mathrm{T}} \lesssim 30$ GeV. Figure 5.9 shows the distribution of m_{T} for $Z \to \tau\tau$ and

[48] Refer back to Figure 4.34 and the discussion of W + jets fake rates in Section 4.4.8.
[49] Therefore the SS sample cannot simply be used to model the background from W + jets events like the method for estimating the multijet background that will be discussed in Section 5.7.3.
[50] Previous MC $Z \to \tau\tau$ studies in Refs. [172, 177] used $m_{\mathrm{T}} < 30$ and 35 GeV, respectively.

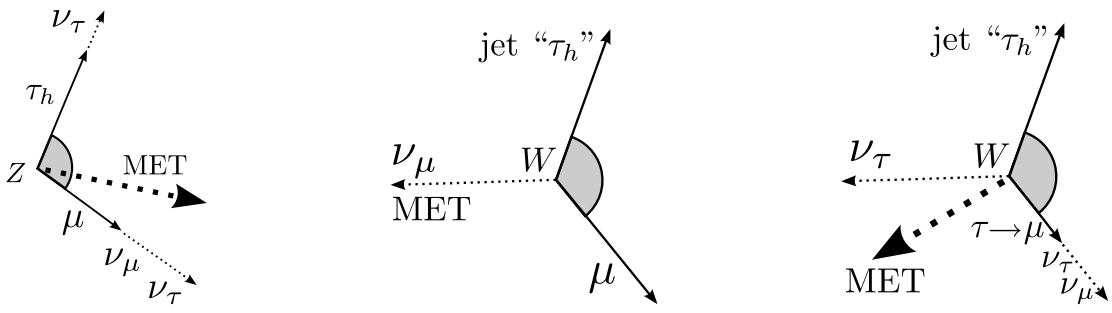

(a) $Z \to \tau\tau \to \mu\tau_{\mathrm{h}}$ (b) $W \to \mu\nu$ (c) $W \to \tau\nu \to \mu\nu\nu\nu$

Figure 5.8: Diagrams illustrating representative transverse plane orientations of W and Z decay products and the $E_{\mathrm{T}}^{\mathrm{miss}}$. The shaded angles indicate the angle less than π between the lepton and the (fake) tau-jet. τ_{h} denotes the visible sum of the decay products of a hadronic decay of a tau lepton. In (a), the Z is depicted to have nonzero p_{T}, which must be balanced on the left by some other activity omitted for clarity [176].

W + jets events. In $Z \to \tau\tau \to \ell\tau_{\mathrm{h}}$ events, since there are two neutrinos on the side of the leptonic decay, the $E_{\mathrm{T}}^{\mathrm{miss}}$ tends to point along the lepton in the transverse plane. Ignoring the masses of the leptons, the transverse mass can be calculated as

$$m_{\mathrm{T}} \equiv \sqrt{2\, p_{\mathrm{T}}(\ell)\, E_{\mathrm{T}}^{\mathrm{miss}}\, (1 - \cos\Delta\phi(\ell, E_{\mathrm{T}}^{\mathrm{miss}}))}\,,$$

which illustrates that the m_{T} goes to zero when the $E_{\mathrm{T}}^{\mathrm{miss}}$ is along the lepton, explaining the spike in the m_{T} distribution at low m_{T} for $Z \to \tau\tau$. However, there is also some phase-space where the neutrino from the hadronic tau decay has an exceptionally high share of the p_{T}, and the $E_{\mathrm{T}}^{\mathrm{miss}}$ points along the τ_{h}, giving the higher-m_{T} tail for $Z \to \tau\tau$ that is lost if requiring low m_{T}. For $W \to \ell\nu$ events, m_{T} is maximal when the momentum vectors of the neutrino and lepton have zero z-components, in which case m_{T} is a measurement of the W mass.

Using m_{T} to reject W + jets does not take into account the information of the direction of the tau candidate. One way to see that the $E_{\mathrm{T}}^{\mathrm{miss}}$ tends to point between the decay products in $Z \to \tau\tau$ events, rather than away as in W + jets events, is to consider the scatter plot in Figure 5.10(left), which shows $\cos\Delta\phi(\tau_{\mathrm{h}}, E_{\mathrm{T}}^{\mathrm{miss}})$ versus $\cos\Delta\phi(\ell, E_{\mathrm{T}}^{\mathrm{miss}})$. The up/down dimension of this plot corresponds to the $E_{\mathrm{T}}^{\mathrm{miss}}$ pointing towards/away from the hadronic tau decay, while the right/left dimension of this plot corresponds to the $E_{\mathrm{T}}^{\mathrm{miss}}$ pointing towards/away from the muon. The upper-right triangle corresponds to the $E_{\mathrm{T}}^{\mathrm{miss}}$ being within the angle between the muon and hadronic tau, while the bottom-left corresponds to the $E_{\mathrm{T}}^{\mathrm{miss}}$ being outside of it. The diagonal going from the top-left to the bottom-right corner corresponds to cases where the muon and hadronic tau are back-to-back. A cut passing up to a maximum m_{T} will tend to exclude events on the left side of this plot, ignoring the vertical dimension. This cut will favor the $Z \to \tau\tau$ events in the bottom-right corner,

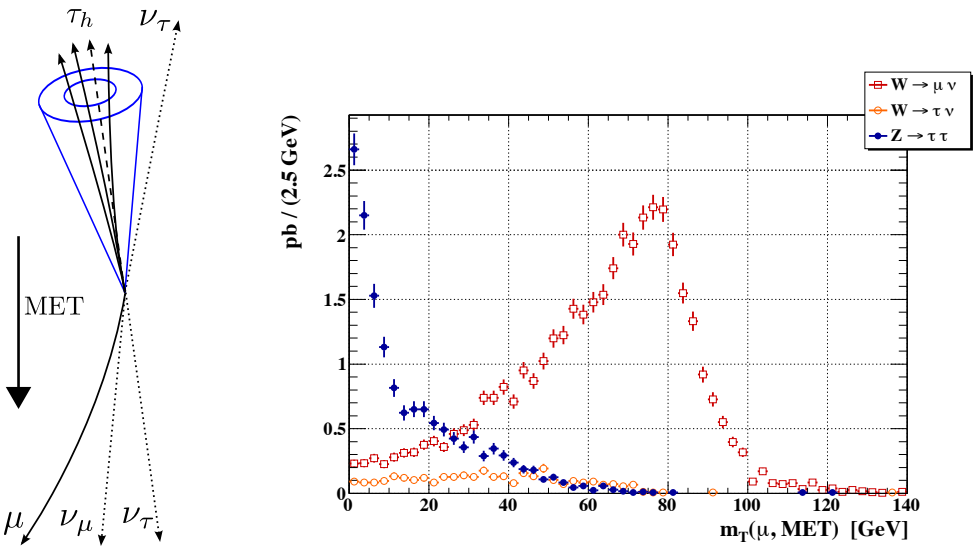

Figure 5.9: (left) In $Z \to \tau\tau \to \ell\tau_{\mathrm{h}}$ events, since there are two neutrinos on the side of the leptonic decay, the $E_{\mathrm{T}}^{\mathrm{miss}}$ tends to point along the lepton in the transverse plane. (right) The transverse mass of the lepton and the $E_{\mathrm{T}}^{\mathrm{miss}}$ in reconstructed $\mu\tau_{\mathrm{h}}$ events for $Z \to \tau\tau$ and W + jets Monte Carlo samples (`mc08`, $\sqrt{s} = 10$ TeV) [176].

but will tend to lose the top-left corner, corresponding to the case when the neutrino on the side of the τ_{h} has large p_{T}.

A variable for suppressing W + jets using the direction of both decay products and the $E_{\mathrm{T}}^{\mathrm{miss}}$ was introduced [176]. Rotating Figure 5.10 (left) by clockwise by $\pi/4$ and projecting down gives the sum of the cosines of the $\Delta\phi$ between each decay product and the $E_{\mathrm{T}}^{\mathrm{miss}}$:

$$\sum \cos\Delta\phi = \cos\Delta\phi(\tau_{\mathrm{h}}, E_{\mathrm{T}}^{\mathrm{miss}}) + \cos\Delta\phi(\ell, E_{\mathrm{T}}^{\mathrm{miss}}) \,,$$

This variable separates the $Z \to \tau\tau$ events with high $\sum\cos\Delta\phi$ and the $E_{\mathrm{T}}^{\mathrm{miss}}$ between the decay products, from the W + jets events with low $\sum\cos\Delta\phi$ and the $E_{\mathrm{T}}^{\mathrm{miss}}$ outside the angle between the decay products, as shown in Figure 5.10(right). The peak at zero corresponds to events with lepton and tau candidates that are back-to-back in the transverse plane.

Requiring $\sum\cos\Delta\phi > -0.15$ accepts the back-to-back events and the upper-right triangle of Figure 5.10(left). Figure 5.11 shows the same scatter plot and the distribution of m_{T} after requiring $\sum\cos\Delta\phi > -0.15$. Combining this $\sum\cos\Delta\phi$ cut with a looser cut on the transverse mass, $m_{\mathrm{T}} < 50$ GeV, gave 9% more signal acceptance and a 15% increase in the signal-to-background ratio compared to just a $m_{\mathrm{T}} < 30$ GeV cut in MC studies [176].

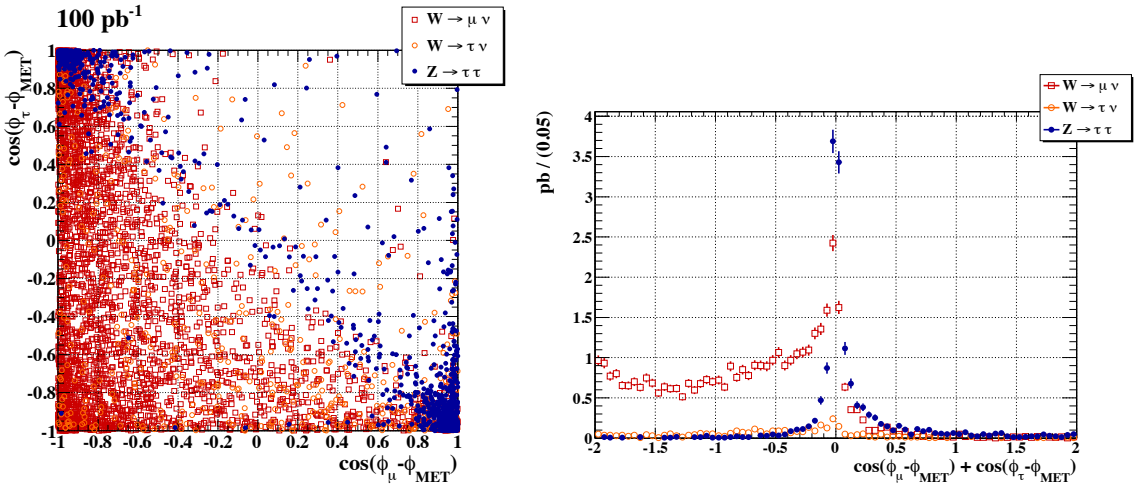

Figure 5.10: (left) A scatter plot of the $\cos\Delta\phi$ for the angles between each decay product and the $E_{\mathrm{T}}^{\mathrm{miss}}$ for $\mu\tau_{\mathrm{h}}$ events with Monte Carlo. (right) The distribution of $\sum\cos\Delta\phi$ for the same events [176].

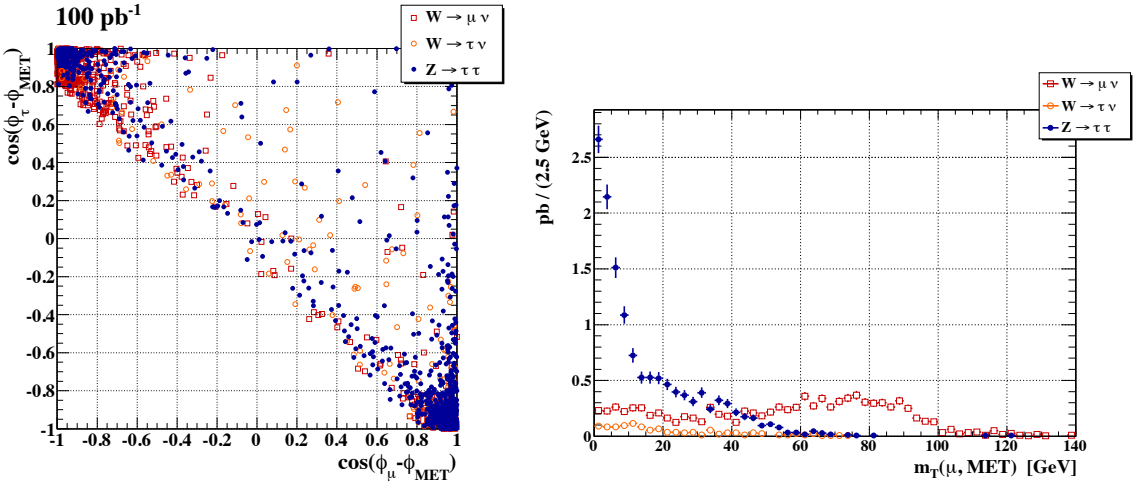

Figure 5.11: (left) A scatter plot of the $\cos\Delta\phi$ for the angles between each decay product and the $E_{\mathrm{T}}^{\mathrm{miss}}$ for $\mu\tau_{\mathrm{h}}$ events from Monte Carlo. (right) The distribution of the transverse mass of the combination of the muon and the $E_{\mathrm{T}}^{\mathrm{miss}}$. Both of these plots are after requiring $\sum\cos\Delta\phi > -0.15$ [176].

5.2.3 Preliminary event selection

Figure 5.12 illustrates the effective cross section selected for $Z \to \tau\tau$ and background processes, stepping through a preliminary event selection, which is described in detail in Ref. [176]. A detailed discussion of the event selection used for the $Z \to \tau\tau$ cross section measurement will be given in Section 5.4.5, but can be briefly summarized as

- opposite-sign isolated lepton and selected tau candidate
- no other leptons
- W + jets suppression cuts on m_{T} and $\sum \cos\Delta\phi$
- a visible mass window.

Figure 5.13 (left) shows the visible mass of the muon and selected tau candidate after all selections except a mass window. Figure 5.13 (right) shows the distribution of the number of tracks associated to the selected tau candidate in events passing all event selection except a cut on this number of tracks. In both figures, to help visualize the expected statistics in 100 pb^{-1} of data with $\sqrt{s}$ = 10 TeV, toy data are shown, drawn from Poisson distributions for the expected number of events in each bin.

The efforts from other ATLAS preliminary MC investigations of selecting $Z \to \tau\tau$ [172, 177] converged in 2009 to define the ATLAS "benchmark analysis" for $Z \to \tau\tau$ [173]. These studies demonstrate that with an integrated luminosity of 100 pb^{-1} at $\sqrt{s} = 10$ TeV and using conservative cut-based tau identification and event selection, approximately 1000 $Z \to \tau\tau$ events could be selected with about 80% purity, which could be improved with tighter tau identification. The tau identification is the one requirement where the selection efficiency of $Z \to \tau\tau$ could be most improved, as it is the step that results in the largest loss of $Z \to \tau\tau$ ($\approx 30\%$ efficient for tight cuts) after requiring a high-p_{T} lepton and tau candidate.

For the benchmark analysis, studies were also done to estimate the multijet background with ATLFAST-II [178] fast Monte Carlo simulation. Since the trigger decisions were not simulated in the fast simulation, the efficiency to pass the single lepton triggers was parametrized as a function of p_{T}, as measured in the full simulation Monte Carlo, and used to weight the fast simulation events (see Figure 5.14). The visible mass distributions are compared for estimates of the multijet background using full simulation weighted by the tau identification fake rate as in Section 5.2.1, and using ATLFAST-II in Figure 5.15.

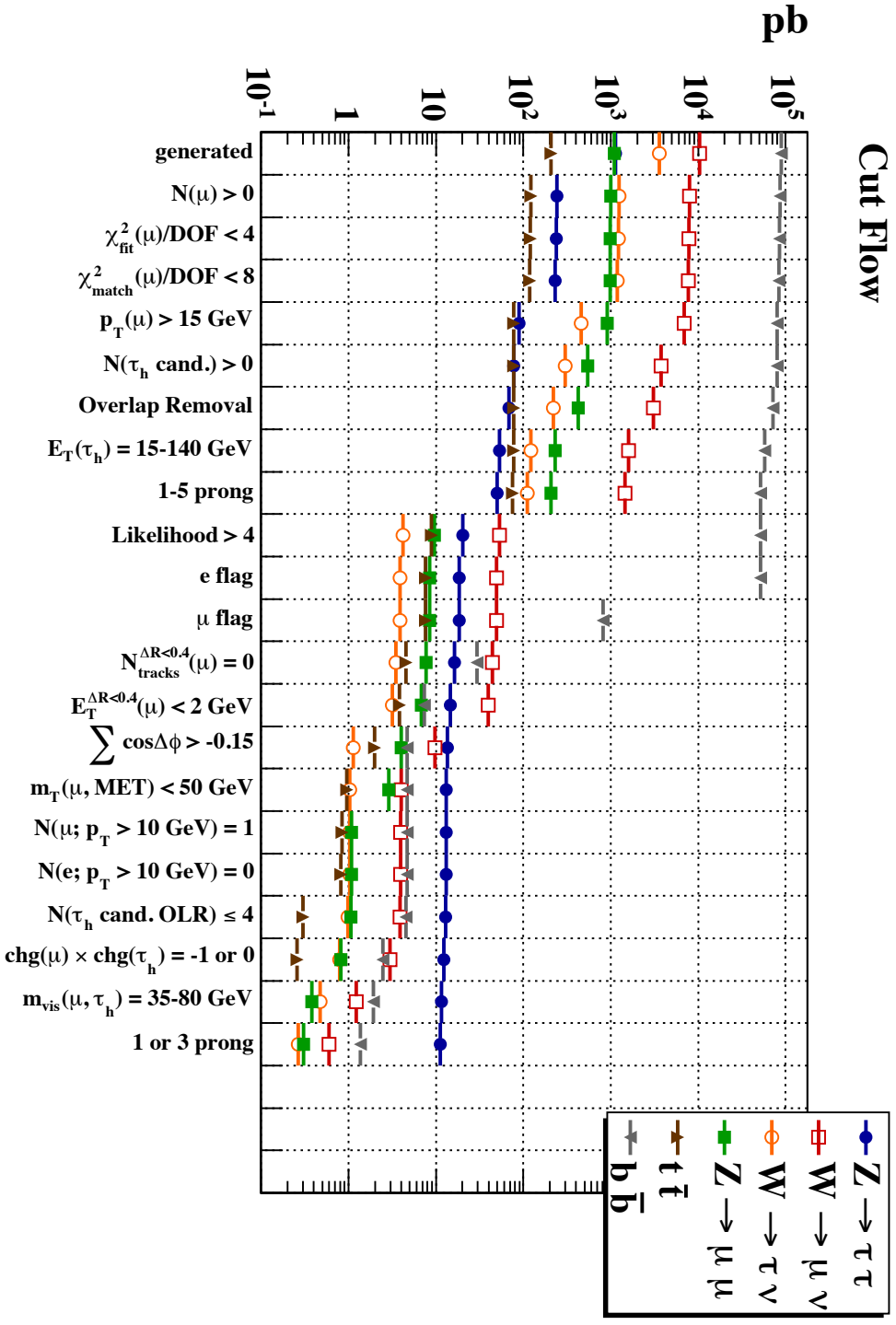

Figure 5.12: The effective cross section passing successive event selections for a preliminary $Z \to \tau\tau \to \mu\tau_{\mathrm{h}}$ event selection (`mc08`, $\sqrt{s} = 10$ TeV) [176].

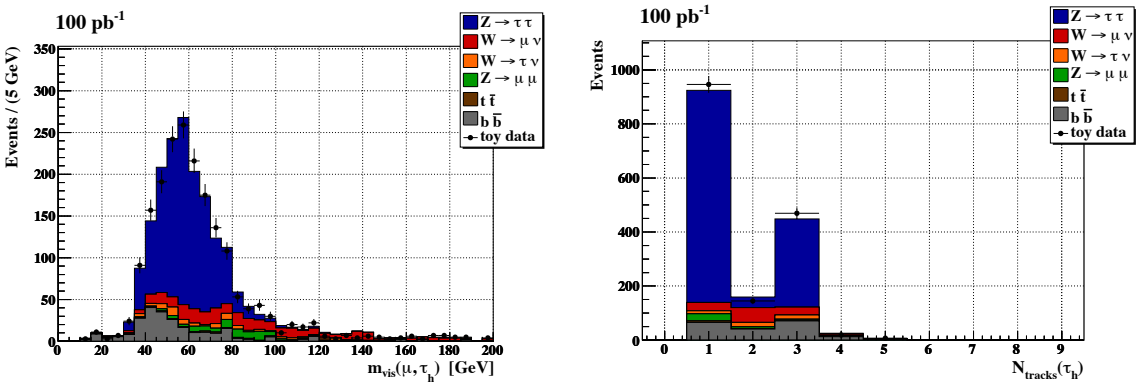

Figure 5.13: The $\mu\tau_{\mathrm{h}}$ visible mass of events passing the entire analysis selection except for a visibile mass window. The number of reconstructed tracks associated to the tau candidate in events passing the entire selection except relaxing the 1 or 3 and OS requirements [176]. Toy data drawn from a Poisson distribution for the expected value in each bin is shown to give a visualization of the expected statistics.

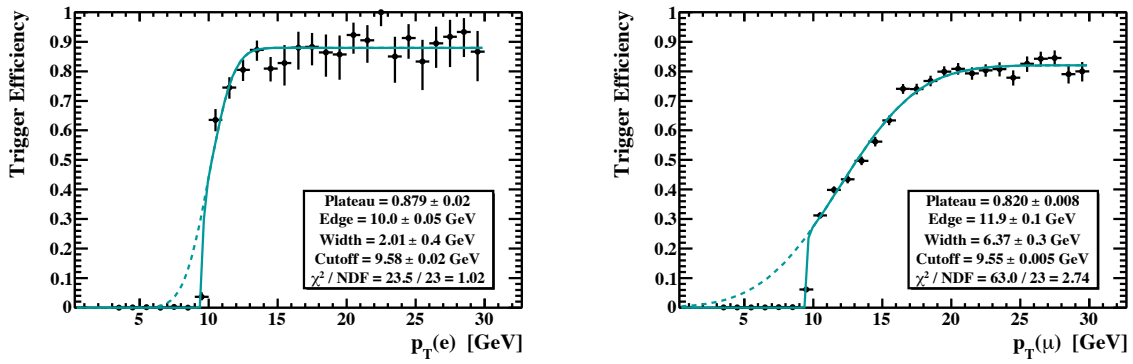

(a) electrons (b) muons

Figure 5.14: The efficiency for true reconstructed leptons in Monte Carlo to pass the trigger using fully simulated Monte Carlo. This efficiency was fit and the parametrtization used to weight fast simulation samples (ATLFAST-II) that did not have a simulated trigger decision (`mc08`) [173].

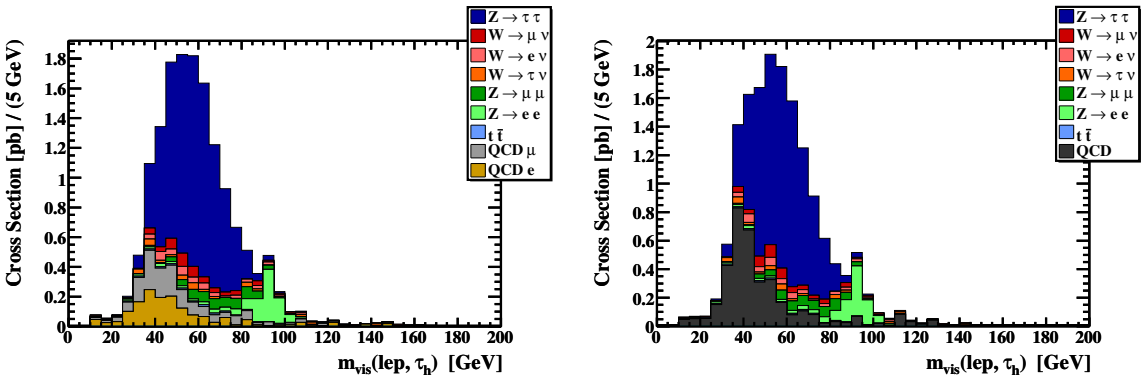

Figure 5.15: The $\mu\tau_h$ visible mass of events passing the entire analysis selection except for a visibile mass window as predicted with the full simulation dijet samples, weighted by fake rates (left), and as predicted with ATLFAST-II dijet Monte Carlo (right) [173].

5.3 Data samples

5.3.1 Data

The year 2010 was the year with the first record-energy collision data at the LHC. Collision data at $\sqrt{s} = 7$ TeV collected from July to October 2010 were used for the first ATLAS measurement of the $Z \to \tau\tau$ cross section. The datasets were processed with the autumn 2010 reprocessing, which uses Athena release 16.0.2.3. The events were triggered with the lowest-p_T unprescaled single electron and muon triggers described in Section 5.4.2. In the $e\tau_h$ channel, run periods E3–I2 were used, while in the $\mu\tau_h$ channel E4–I2 were used. The first periods were not included because initially the trigger conditions varied rapidly. The resulting integrated luminosity [179], after data quality requirements, is about 36 pb^{-1} in both the $e\tau_h$ and $\mu\tau_h$ channels, as is shown for each run period in Table 5.1.

Table 5.1: The `EF_e15_medium` trigger was required for the $e\tau_h$ channel, including a prescale in part of period E. In the $\mu\tau_h$ channel the trigger, `EF_mu10_MG` was used for run period 160899–165632, `EF_mu13_MG` for the run period 165703–167576 and `EF_mu13_MG_tight` for run period 167607–167844, respectively to avoid the use of prescaled triggers. In period E, the $e\tau_h$ channel is using data from period E3 (160613) and above, while the $\mu\tau_h$ channel starts at period E4 (160899) [180].

run period	run number	int. luminosity (pb^{-1}) $e\tau_h$ channel	int. luminosity (pb^{-1}) $\mu\tau_h$ channel
period E	160387–161948	0.752	0.514
period F	162347–162882	1.743	1.743
period G	165591–166383	5.531	5.531
period H	166466–166964	6.984	6.984
period I	167575–167844	20.735	20.735
		35.745	35.507

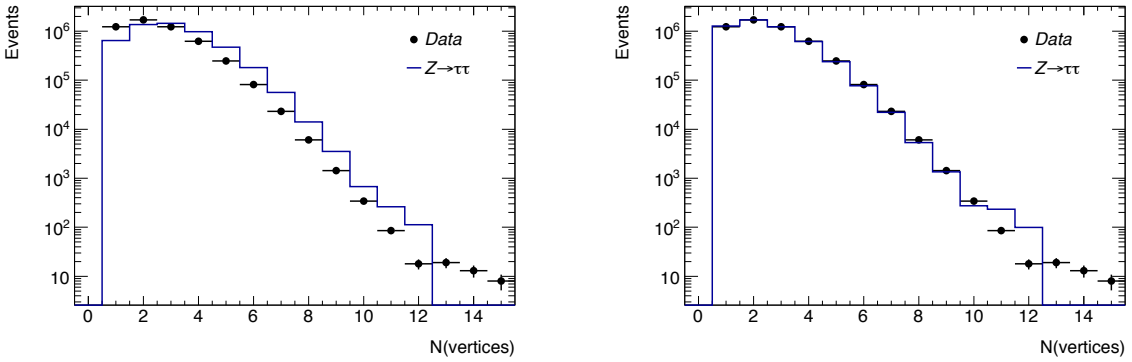

Figure 5.16: Comparison, for data and Monte Carlo, of the distributions of the number of reconstructed vertices in each event before (left) and after (right) vertex re-weighting [180].

5.3.2 Simulation

The Monte Carlo samples[51] were from the `mc10` production campaign. The W and γ^*/Z backgrounds and $Z \to \tau\tau$ signal samples were generated with PYTHIA [125], and were normalized to their corresponding NNLO cross sections [108] calculated using FEWZ [181]. The low-mass γ^*/Z samples were normalized to the NNLO cross sections from Refs. [182, 183]. The diboson samples were generated using Herwig [121]. Other samples used were generated as described in Section 3.6.1.

In each event that is recorded by ATLAS, proton-proton interactions in addition to the one which triggered the read-out can occur, resulting in pile-up interactions characterized by having more than one primary vertex reconstructed per event, as described in Section 3.5.2. The Monte Carlo samples were produced with the so-called bunch-train pile-up setup in which simulated minimum bias interactions were overlaid on top of the hard-scattering event with the following timing structure: individual bunches were separated by 150 ns and contained in trains of eight bunches length. A second bunch train followed with a time separation equal to 225 ns, followed by a longer pause before the next bunch train. The average number of reconstructed primary vertices per bunch crossing in the data ranged from 1–2.2, depending on the period used, while the average number of vertices in the Monte Carlo before re-weighting was 2.8. The Monte Carlo samples were re-weighted such that their distributions of the number of reconstructed vertices per event match the distribution in data (see Figure 5.16).

[51] All of the simulated samples used are listed in the Appendix of Ref. [180].

5.4 $Z \to \tau\tau \to \ell\tau_{\mathrm{h}}$ selection

5.4.1 Event preselection

Primary vertex requirement

Candidate events were required to have at least one reconstructed primary vertex with at least 3 reconstructed tracks.

Jet cleaning

Events may occasionally contain localized high-energy calorimeter deposits not originating from the proton-proton collision. Sources of such apparent energy depositions are, for example, discharges in the hadronic end-cap calorimeter and more rarely, coherent noise in the electromagnetic calorimeter. Cosmic-ray muons undergoing a hard bremsstrahlung are also a potential source of localized energy deposits uncorrelated to the primary proton-proton collisions. The occurrence of these events is very rare, but such spurious energy deposits can have a significant impact on the $E_{\mathrm{T}}^{\mathrm{miss}}$ measurement (by creating high-energy tails), or be incorrectly reconstructed as a jet and, hence, a tau candidate. To prevent these occurrences, dedicated cleaning requirements were applied to events with indications of noise or poor quality jets [184, 180].

5.4.2 Triggering

The analysis made use of unprescaled single-lepton triggers. Events in the $e\tau_{\mathrm{h}}$ channel were required to pass a trigger for a loosely identified electron with $p_{\mathrm{T}} \gtrsim 15$ GeV:

- `EF_e15_medium`.

For the $\mu\tau_{\mathrm{h}}$ channel the lowest-p_{T} unprescaled triggers for a single muon with $p_{\mathrm{T}} \gtrsim 10$–$20$ GeV, in the individual run periods were used:

- `EF_mu10_MG` (periods E4-G1)
- `EF_mu13_MG` (periods G2-I1, until run 167576)
- `EF_mu13_MG_tight` (remaining period I1).

For both channels this resulted in an integrated luminosity of approximately 36 pb^{-1}.

Trigger efficiencies were determined using the tag-and-probe[52] method using $Z \to \ell\ell$ ($\ell = e$ or μ) events, tagging events with a good lepton and a second candidate, and with $W \to \ell\nu$ events, tagging events with significant $E_{\mathrm{T}}^{\mathrm{miss}}$ and a lepton candidate. In Table 5.2 and 5.3, the trigger efficiencies

[52] See the discussion of the tag-and-probe method in Section 3.6.3.

for electrons and muons are shown as measured from data. Correction factors were applied to the Monte Carlo simulation to make the MC trigger efficiency prediction agree with the data. These correction factors were defined as the ratio between the efficiencies measured in data and in Monte Carlo [180].

5.4.3 Object preselection

Selecting the $\ell\tau_{\mathrm{h}}$ final state utilizes the suite of ATLAS reconstruction, including muons, electrons, hadronic tau decays, and missing transverse momentum. Electrons, muons and tau candidates are initially preselected using looser criteria. Pre-selected leptons are used to remove overlapping tau candidates and counted for the dilepton veto (Section 5.4.5). A summary of the preselection can be seen in Table 5.5. After the preselection, the full object selection takes place, including lepton isolation requirements, and the selection of tau candidates (Section 5.4.4). The reconstructed $E_{\mathrm{T}}^{\mathrm{miss}}$ is also utilized in the event selection.

Electrons

The electron identification is based on variables that can efficiently discriminate between electrons and fakes (mis-identified photons and jets). These variables are based on calorimeter information, tracking information or a combination of the two. Three qualities of electrons are provided, with different levels of signal efficiency and purity, namely `loose`, `medium`, and `tight`, subsequently modified for 2010 data analysis (so called `MediumWithTrackMatch` and `TightWithTrackMatch`) [185]. The electrons in this analysis were preselected if they had a cluster with $E_{\mathrm{T}} > 15$ GeV, were within $|\eta| < 2.47$ excluding the transition region between the barrel and end-cap calorimeters ($1.37 < |\eta| < 1.52$) and passed the `MediumWithTrackMatch` identification requirements. Additionally information

Table 5.2: Electron trigger efficiency measured with respect to offline selected electrons in three p_{T} bins [180].

trigger	`EF_e15_medium`
$16-18$ GeV	95.8±2.2(stat.)±0.6(syst.)
$18-20$ GeV	96.5±2.1(stat.)±0.4(syst.)
>20 GeV	99.05±0.22(stat.)±0.08(syst.)

Table 5.3: Muon trigger efficiency measured with respect to offline selected muons with $p_{\mathrm{T}} > 15$ GeV [180].

trigger	efficiency
`EF_mu10_MG`	82.9±0.9(stat.)±0.3(syst.)
`EF_mu13_MG`	84.5±0.4(stat.)±0.1(syst.)
`EF_mu13_MG_tight`	83.1±0.4(stat.)±0.2(syst.)

from the Object Quality maps (OQmaps) [108] was used, removing electrons built from a cluster affected by detector problems[53].

Muons

Muons reconstructed by the Staco algorithm were used in this analysis [69]. Tracks were reconstructed independently by the inner detector and muon spectrometer, and the muon track was formed from the successful combination of a muon spectrometer track with an inner detector one. The preselection of muons required $p_{\mathrm{T}} > 15$ GeV with $|\eta| < 2.4$, corresponding to the trigger acceptance. The longitudinal distance from the primary vertex was required to be less than 10 mm.

Hadronic tau decays

The reconstruction of hadronic tau decays at ATLAS was discussed in detail in Chapter 4. Reconstructed tau candidates were preselected if they had $p_{\mathrm{T}} > 20$ GeV and were located within $|\eta| < 2.47$ but not in the crack region ($1.37 < |\eta| < 1.52$). Information about the full tau candidate selection can be found in Section 5.4.4.

Overlap removal

Because multiple candidates (electron, muon, or tau candidates) were often reconstructed from the same localized response in the ATLAS detector, an overlap removal procedure had to be performed to have a unique hypothesis for each object. Since muons and electrons can be selected with a higher purity than hadronic tau decays, any preselected tau candidate was removed from consideration if it lay within $\Delta R < 0.4$ from any preselected lepton. Electrons were removed if they overlapped with muons within $\Delta R < 0.2$. Finally electron and muon candidates were removed if they lay within $\Delta R < 0.2$ from a harder reconstructed lepton of the same kind.

5.4.4 Object selection

Electron selection

Further requirements were applied on the preselected electrons. The transverse momentum cut was raised to 16 GeV in order to avoid the region immediately surrounding the trigger threshold, which had been found to be poorly modeled by Monte Carlo. Additionally the electron candidates were required to pass the `TightWithTrackMatch` cut identification.

[53] The OQmap for run 167521 was used, for both data and Monte Carlo.

Muon selection

In addition to the preselection requirements, muons had to fulfill requirements of a good quality inner detector track. The inner detector track was required to have at least 1 hit, if expected, in the B layer and the sum of the hits and dead sensors in the pixel detector was required to be greater than 1. The number of SCT hits and dead sensors had to be greater than 5 while the sum of the pixel and SCT holes had to be less than 2, and an additional cut was applied to the fraction of TRT outlier hits to total TRT hits.

Lepton isolation

Fake or real leptons produced in multijet events tend to not be isolated because they are accompanied by the other products of hadronization in a jet. Requiring the leptons to pass isolation requirements suprresses the multijet background to electroweak processes, like $Z \to \tau\tau$.

$I_{p_{\mathrm{T}}}^{0.4}$ denotes the scalar sum of the p_{T} of tracks with $p_{\mathrm{T}} > 1$ GeV and consistent with the primary vertex, within $\Delta R < 0.4$, excluding the track from the lepton candidate itself. $I_{E_{\mathrm{T}}}^{0.4}$ is the scalar sum of the E_{T} of calorimeter cells within $\Delta R < 0.4$, excluding the cells near the lepton candidate itself. Figure 5.17 shows the isolation variables used.

The isolation requirements, chosen to accept $Z \to \tau\tau$ signal and suppress multijet events, are

- for electrons: $I_{p_{\mathrm{T}}}^{0.4}/p_{\mathrm{T}} < 0.06$ and $I_{E_{\mathrm{T}}}^{0.3}/p_{\mathrm{T}} < 0.1$;
- for muons: $I_{p_{\mathrm{T}}}^{0.4}/p_{\mathrm{T}} < 0.06$ and $I_{E_{\mathrm{T}}}^{0.4}/p_{\mathrm{T}} < 0.06$.

The efficiency of these isolation cuts was measured in data using a tag-and-probe method and correction factors were applied to the Monte Carlo to correct the efficiency [180]. The corresponding cut efficiencies are given in Table 5.4.

Table 5.4: Efficiency of isolation variables for electrons and muons in signal Monte Carlo and multijet background after object selection cuts. In brackets is given the statistical error of the last digit [180].

Isolation variable	$Z \to \tau\tau$	Multijet
muon $I_{p_{\mathrm{T}}}^{0.4}/p_{\mathrm{T}} < 0.06$	0.926(2)	0.076(1)
muon $I_{E_{\mathrm{T}}}^{0.4}/p_{\mathrm{T}} < 0.06$	0.872(3)	0.0309(6)
muon combined isolation	0.841(3)	0.0143(4)
electron $I_{p_{\mathrm{T}}}^{0.4}/p_{\mathrm{T}} < 0.06$	0.941(3)	0.232(3)
electron $I_{E_{\mathrm{T}}}^{0.3}/p_{\mathrm{T}} < 0.1$	0.814(4)	0.082(2)
electron combined isolation	0.781(4)	0.046(1)

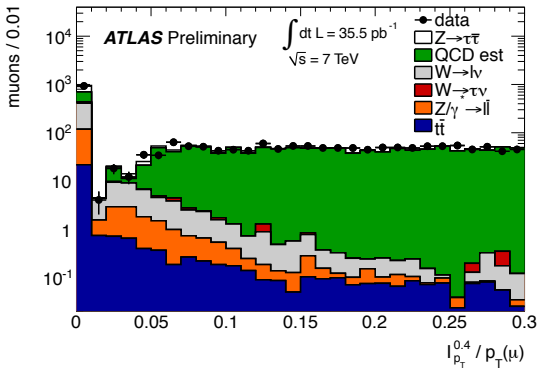

(a) Muon isolation $I^{0.4}_{p_{\mathrm{T}}}$ divided by p_{T}.

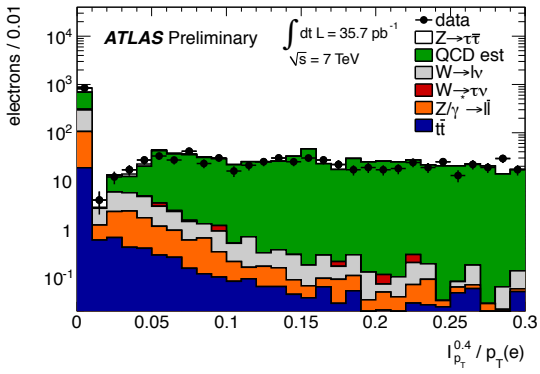

(b) Electron isolation $I^{0.4}_{p_{\mathrm{T}}}$ divided by p_{T}.

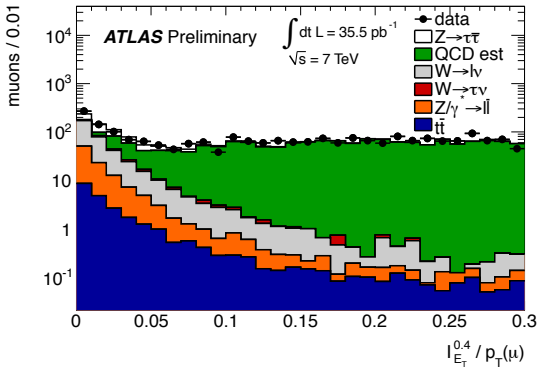

(c) Muon isolation $I^{0.4}_{E_{\mathrm{T}}}$ divided by p_{T}.

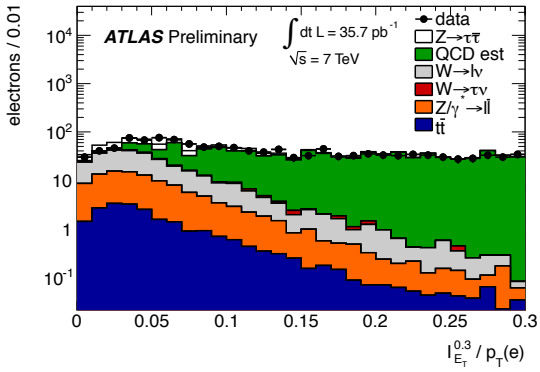

(d) Electron isolation $I^{0.3}_{E_{\mathrm{T}}}$ divided by p_{T}.

Figure 5.17: Distributions of the isolation variables used after selecting one tau candidate and an opposite-sign lepton. The electroweak background is estimated with Monte Carlo. The multijet background is modeled with the same-sign data, corrected with Monte Carlo [180].

Hadronic tau decay selection

The reconstruction of hadronic decays of tau leptons, as described in Chapter 4, was used[54]. From the reconstructed tau candidates, those passing the simple cut-based identification,[55], which uses p_{T}-parametrized cuts on the three variables (R_{EM}, R_{track}, and f_{track}) were selected. The reconstructed tau candidates were required to pass the medium cut-based identification in the 1-prong case or the tight one in the 3-prong case, together with a tight electron veto [186]. In total, these identification requirements result in an efficiency of about 30% for true hadronic tau decays, as determined with Monte Carlo. A correction factor was applied to 1-prong tau candidates in Monte Carlo samples containing true electrons, to correct the probability of electrons being mis-identified as

[54] without JVF-corrected vertex-association, pile-up corrected variables, and other improvements that had not been developed in 2010.

[55] The Winter 2011 version [186].

tau candidates, as measured in data [186]. The highest p_{T} tau candidate passing these identification criteria, with $p_{\mathrm{T}} > 20$ GeV, and within $0 < |\eta| < 1.37$ or $1.52 < |\eta| < 2.47$, was chosen for the signal selection.

Missing transverse momentum

The missing transverse momentum ($E_{\mathrm{T}}^{\mathrm{miss}}$) reconstruction used in this analysis was based on clustered energy deposits in the calorimeter and on reconstructed muon tracks, and was based on the following vectorial sum:

$$E_{\mathrm{T}}^{\mathrm{miss}} = E_{\mathrm{T}}^{\mathrm{miss}}(\texttt{LocHadTopo}) + E_{\mathrm{T}}^{\mathrm{miss}}(\texttt{MuonBoy}) - E_{\mathrm{T}}^{\mathrm{miss}}(\texttt{RefMuon\_Track}).$$

The calorimeter part $E_{\mathrm{T}}^{\mathrm{miss}}(\texttt{LocHadTopo})$ was calculated from the energy deposits of calorimeter cells inside three-dimensional topological clusters [91], calibrated locally to the electromagnetic or hadronic scale depending on the energy deposit classification. $E_{\mathrm{T}}^{\mathrm{miss}}(\texttt{MuonBoy})$ refers to the sum of the combined muon momenta from all isolated combined muons and muons in gaps as well as the sum of all non-isolated muons reconstructed as tracks in the muon spectrometer. A muon was considered isolated if the distance ΔR to the nearest jet was at least 0.3. To avoid double counting because of the isolated muons, the sum of the energy of the calorimeter cells crossed by an isolated muon, $E_{\mathrm{T}}^{\mathrm{miss}}(\texttt{RefMuon\_Track})$, was subtracted from the sum of the other two terms.

Object selection summary

The full preselection and selection requirements are listed in Table 5.5. A summary showing the effect of each of the cuts described in this section on signal Monte Carlo events, normalized to the integrated luminosity used for this study, is listed in Table 5.6. As can be seen, the tau candidate selection is the least efficient step. Figure 5.18 shows the kinematic distributions of the selected objects.

5.4.5 Event selection

Following suppression of the multijets background by the tau identification and lepton isolation cuts, W/Z + jets events dominate the background. These background processes are suppressed with further event-level selection, discussed in the following sections.

Dilepton veto

The background from $Z \to \ell\ell$ + jets events, where a jet fakes tau identification, can be suppressed if the second lepton can be identified and vetoed. This veto additionally suppresses $Z \to \tau\tau \to \ell\ell + \nu$

Table 5.5: Selection summary [180].

Event preselection	
Primary vertex	$N_{\text{vtx}} \geq 1$ with $N_{\text{trk}} \geq 3$
Jet cleaning	Cleaning cuts "medium" with Tau Performance modifications
Trigger	`EF_e15_medium` (e channel)
	`EF_mu10_MG`, `EF_mu13_MG`, `EF_mu13_MGtight` (μ channel)
Pre-selection	
Electrons	$p_{\text{T}} > 15$ GeV
	$\lvert\eta\rvert < 2.47$, but excluding $1.37 < \lvert\eta\rvert < 1.52$
	not in bad OQmaps region, map of run 167521
	`author` 1 or 3
	`MediumWithTrackMatch`
Muons	$p_{\text{T}} > 15$ GeV
	$\lvert\eta\rvert < 2.4$
	`isCombinedMuon`
	$\lvert z_0\rvert < 10$ mm
Tau candidates	$p_{\text{T}} > 20$ GeV
	$\lvert\eta\rvert < 2.47$, but excluding $1.37 < \lvert\eta\rvert < 1.52$
Overlap removal	Order of priority: muon, electrons, tau candidate, jets
Object selection	
Electrons	$p_{\text{T}} > 16$ GeV
	`TightWithTrackMatch` electron
	$I^{0.4}_{p_{\text{T}}}/p_{\text{T}} < 0.06$; $I^{0.3}_{E_{\text{T}}}/p_{\text{T}} < 0.1$
Muons	$p_{\text{T}} > 15$ GeV
	`expectBLayerHit==0` or `nBLHits` > 0
	`nPixHits` + `nDeadPixelSensors` > 1
	`nSCTHits` + `nDeadSCTSensors` > 5
	`nPixHoles` + `nSCTHoles` < 2
	$\lvert\eta\rvert < 1.9$: `nTRTOutliers` / (`nTRTHits` + `nTRTOutliers`) < 0.9
	and `nTRTHits` + `nTRTOutliers` > 5
	$\lvert\eta\rvert \geq 1.9$: (`nTRTHits` + `nTRTOutliers` > 5
	and `nTRTOutliers` / (`nTRTHits` + `nTRTOutliers`) < 0.9)
	or `nTRTHits` + `nTRTOutliers` < 6
	$I^{0.4}_{p_{\text{T}}}/p_{\text{T}} < 0.06$; $I^{0.4}_{E_{\text{T}}}/p_{\text{T}} < 0.06$
Tau candidates	`author` 1 or 3
	passes e veto
	1-prong `medium`, 3-prong `tight` cuts τ-ID
Event selection	
W+jets suppression	$\sum \cos\Delta\phi > -0.15$
	$m_{\text{T}} < 50$ GeV
Dilepton veto	Remove event if N(preselected leptons)> 1
Visible mass cut	35 GeV $< m_{\text{vis}} <$ 75 GeV
Tau candidate selection	$N_{\text{tracks}}(\tau_{\text{h}}) = 1$ or 3
	$\lvert\text{charge}(\tau_{\text{h}})\rvert = 1$
Opposite sign cut	$\text{charge}(\tau_{\text{h}}) \times \text{charge}(\ell) < 0$

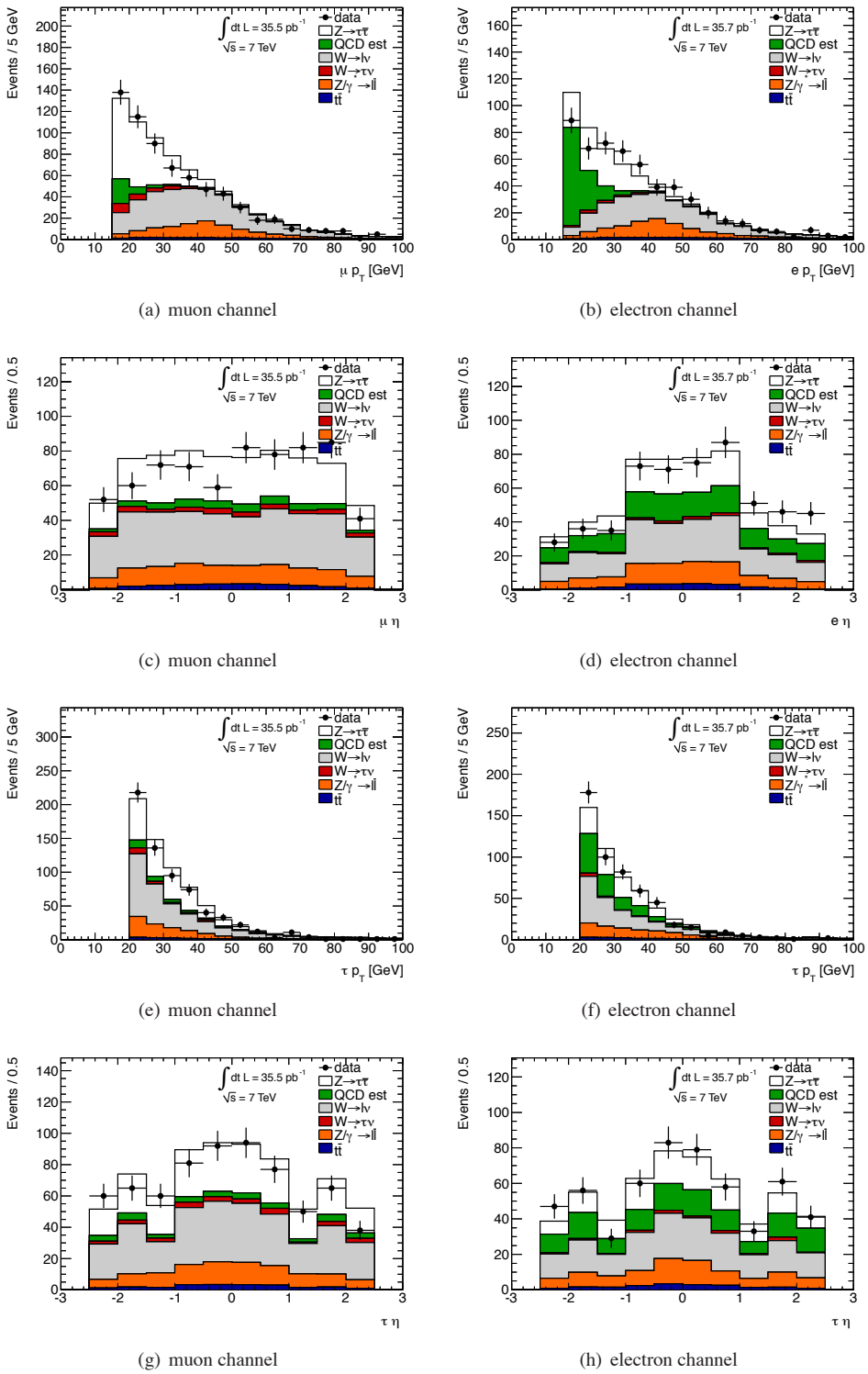

(a) muon channel (b) electron channel

(c) muon channel (d) electron channel

(e) muon channel (f) electron channel

(g) muon channel (h) electron channel

Figure 5.18: Kinematic distributions of the selected leptons and tau candidates following all object selections. The electroweak background is estimated with Monte Carlo. The multijet background is modeled with the same-sign data, corrected with Monte Carlo [180].

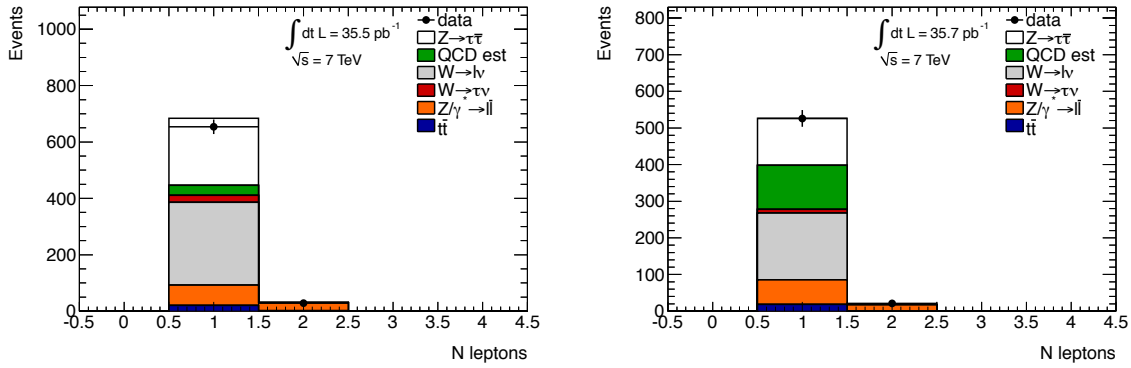

(a) muon channel (b) electron channel

Figure 5.19: Distributions of the number of preselected leptons, counted for the dilepton veto, following all object selections. The electroweak background is estimated with Monte Carlo. The multijet background is modeled with the same-sign data, corrected with Monte Carlo [180].

events, ensuring that the event selection is orthogonal to that from the analysis studying that decay mode. The distribution of the number of preselected leptons can be seen in Figure 5.19. Any event with more than one preselected lepton, as defined in Section 5.4.3, was vetoed. Pre-selected rather than selected leptons were used for the dilepton veto cut. The reason for this was that using selected leptons instead introduced 18% and 2% more background in the $Z \to ee$ and $\mu\mu$ channels while only increasing signal efficiency by 0.1%.

W + jets suppression cuts

The W + jets background is suppressed by requiring that the direction of the $E_{\mathrm{T}}^{\mathrm{miss}}$ be correlated with the direction of the $\ell\tau_{\mathrm{h}}$ decay products, using the transverse mass and $\sum \cos\Delta\phi$ variables discussed in Section 5.2.2. Distributions of these variables using the 2010 data are shown in Figure Fig. 5.20. The cuts required are

$$\sum \cos\Delta\phi = \cos\Delta\phi(\tau_{\mathrm{h}}, E_{\mathrm{T}}^{\mathrm{miss}}) + \cos\Delta\phi(\ell, E_{\mathrm{T}}^{\mathrm{miss}}) > -0.15$$

Table 5.6: Summary of the events passing object selection [180].

Selection	Events ($e\tau_{\mathrm{h}}$ channel 35.7pb^{-1})	Events ($\mu\tau_{\mathrm{h}}$ channel 35.5pb^{-1})
Pre-selected lepton and overlap removal	2497(7)	2478(7)
Pre-selected tau cand. and overlap removal	1179(5)	1133(5)
Selected Lepton	690(4)	1143(5)
Isolated Lepton	531(3)	941(5)
Selected tau candidate	141(2)	258(2)

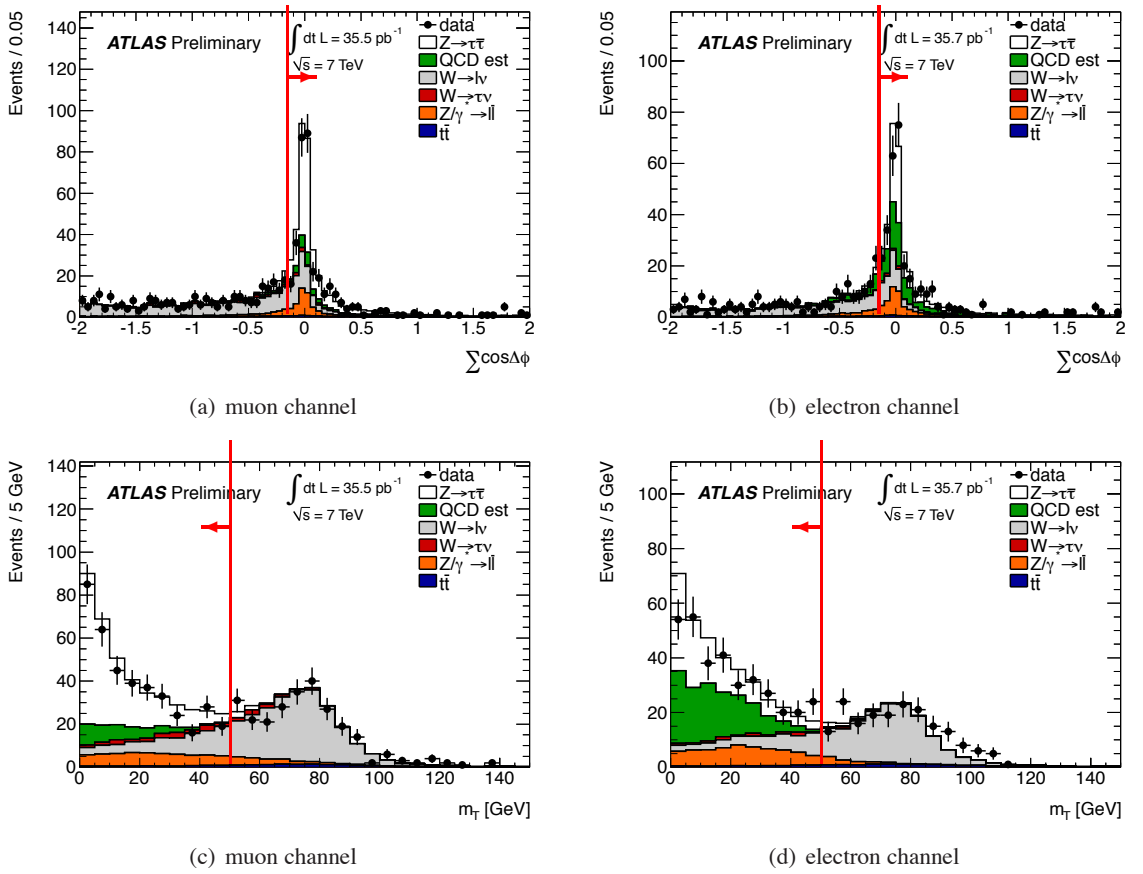

(a) muon channel

(b) electron channel

(c) muon channel

(d) electron channel

Figure 5.20: The distributions of $\sum \cos\Delta\phi$ are shown for the muon (a) and electron (b) channels. The distributions of transverse mass, m_{T}, of the combination of the lepton and the $E_{\mathrm{T}}^{\mathrm{miss}}$ are shown for the muon (c) and electron (d) channels. All of these distributions are shown following the full object selections, the dilepton veto, and requiring opposite sign. The electroweak background is estimated with Monte Carlo. The multijet background is modeled with the same-sign data, corrected with Monte Carlo [180].

and

$$m_{\mathrm{T}} < 50 \text{ GeV}\,.$$

Final selection

A few additional cuts that are characteristic of the $Z \to \tau\tau$ signal were applied to increase its purity. Events were selected that had a reconstructed visible mass of the combination of the chosen tau candidate and the chosen lepton between 35–75 GeV. This window was chosen to be inclusive of the bulk of the signal, while avoiding the background contamination from $Z \to \ell\ell$ accumulating at the Z boson mass near 90 GeV. Figure 5.21 shows distributions of the visible mass.

The chosen tau candidate was required to have 1 or 3 associated tracks and a reconstructed

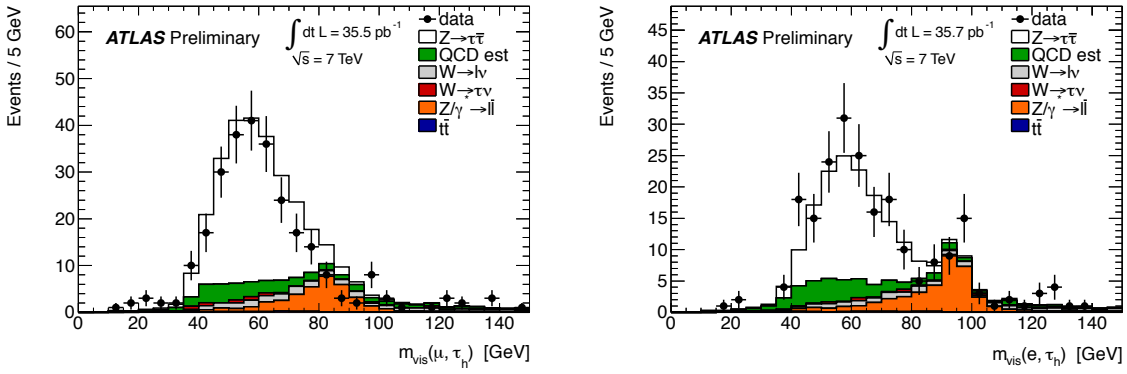

(a) muon channel (b) electron channel

Figure 5.21: The distributions of the visible mass of the combination of the chosen tau candidate and chosen lepton are shown for the muon (a) and electron (b) channels. These distributions are shown following the full object selections and event selections, except for the visible mass window [180].

charge of unit magnitude, characteristic of true hadronic tau decays. The tau candidate charge was reconstructed as the sum of the charges of the associated tracks. Finally, the chosen lepton and tau candidate are required to have opposite-sign charges, as expected from the products of a $Z \to \tau\tau$ decay.

Table 5.5 gives a summary of all selections applied. Table 5.7 shows the number of events passing the cumulative event selections. In these tables the background has been estimated as described in Section 5.7.3.

5.5 Observation of $Z \to \tau\tau \to \ell\tau_{\mathrm{h}}$

Once ATLAS had collected the first few pb^{-1} of integrated luminosity in 2010, a few events were expected to pass the $Z \to \tau\tau \to \ell\tau_{\mathrm{h}}$ selections. The first 10 or so selected events were scanned by hand, and an event display was approved for a particularly clean $Z \to \tau\tau \to \mu\tau_{\mathrm{h}}$ candidate with a 3-prong hadronic tau decay, which is shown in Figure 5.22.

With the first 8.5 pb^{-1}, ATLAS announced observation of $Z \to \tau\tau \to \ell\tau_{\mathrm{h}}$ events [188, 146]. While the previous section showed plots from the event selection with the entire 36 pb^{-1} collected that year, Figure 5.23 shows distributions of the visible mass of the lepton and the tau candidate with the observation data sample.

Table 5.7: Numbers of events passing the cumulative event selections for the $\mu\tau_h$ and $e\tau_h$ channels. The statistical errors on the least significant digits are given in the parentheses. The predictions for individual processes were taken from Monte Carlo, except for multijet, which was estimated from the data with non-isolated leptons as described in Section 5.7.3 [180].

$\mu\tau_h$ channel	data	$\gamma^*/Z \to \tau\tau$	multijets	$\gamma^*/Z \to \mu\mu$	$W \to \mu\nu$	$W \to \tau\nu$	$t\bar{t}$	diboson
object selection	1365	261(3)	163(9)	216(2)	649(6)	54(3)	38.9(5)	8.6(1)
dilepton veto	1291	260(3)	162(8)	125(2)	648(6)	54(3)	34.3(5)	7.8(1)
W suppression cuts	462	231(3)	90(4)	58(1)	66(2)	18(2)	7.8(2)	1.34(5)
$m_{\text{vis}} = 35 - 75$ GeV	327	205(2)	71(3)	23.1(9)	23(1)	10(1)	2.4(1)	0.49(3)
$N_{\text{trk}}(\tau_h) = 1$ or 3, $\lvert Q(\tau_h)\rvert = 1$	247	187(2)	42(3)	15.3(7)	12.1(8)	5(1)	1.4(1)	0.32(2)
opposite sign	213	186(2)	23(3)	11.1(5)	9.3(7)	3.6(8)	1.3(1)	0.28(2)

$e\tau_h$ channel	data	$\gamma^*/Z \to \tau\tau$	multijets	$\gamma^*/Z \to ee$	$W \to e\nu$	$W \to \tau\nu$	$t\bar{t}$	diboson
object selection	1203	141(2)	402(12)	164(1)	409(4)	24(2)	33.0(4)	6.4(1)
dilepton veto	1144	140(2)	400(11)	116(1)	409(4)	24(2)	29.1(4)	5.9(1)
W suppression cuts	449	125(2)	159(6)	70(1)	43(1)	10(1)	6.7(2)	0.98(4)
$m_{\text{vis}} = 35 - 75$ GeV	273	107(1)	95(4)	19.2(7)	12.8(7)	3.7(7)	1.7(1)	0.32(2)
$N_{\text{trk}}(\tau_h) = 1$ or 3, $\lvert Q(\tau_h)\rvert = 1$	180	98.5(1)	53(4)	11.0(5)	6.7(5)	1.8(5)	1.13(9)	0.21(2)
opposite sign	151	98(1)	25(3)	6.9(5)	4.8(4)	1.5(4)	1.02(8)	0.18(1)

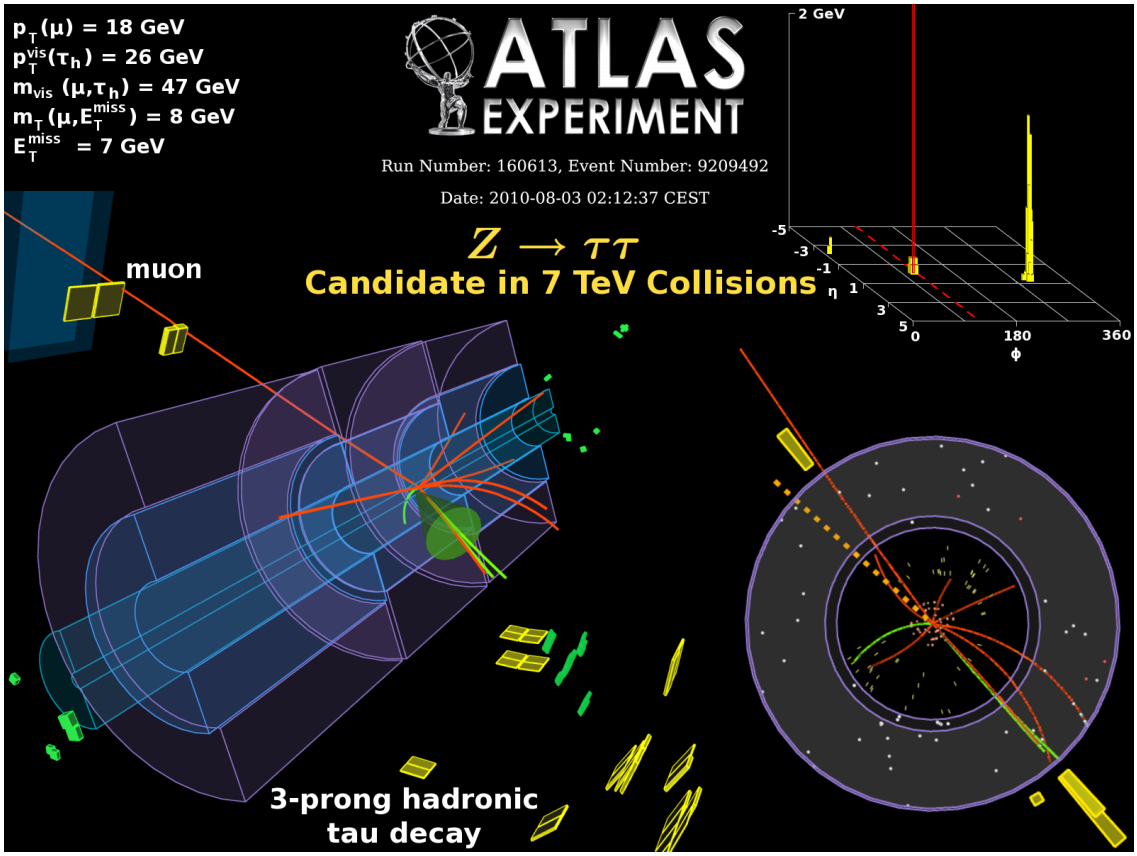

Figure 5.22: An event display of a candidate $Z \to \tau\tau \to \mu\tau_h$ event with a 3-prong hadronic tau decay, in the 2010 dataset [187].

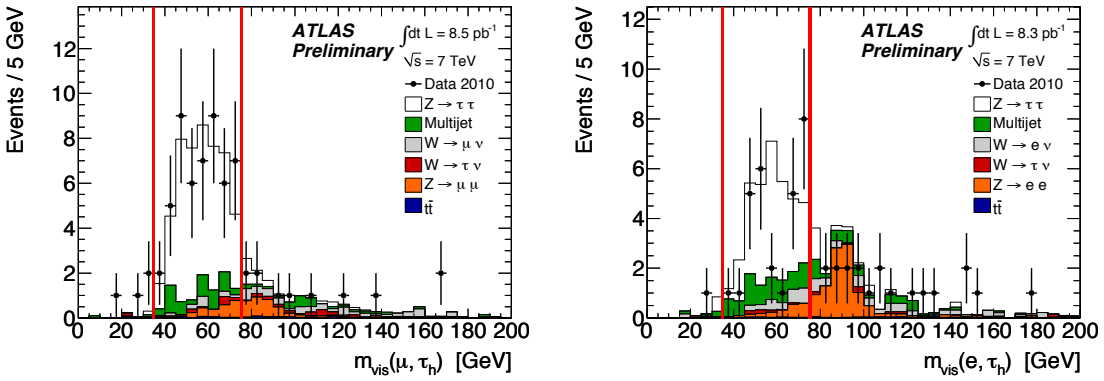

(a) muon channel (b) electron channel

Figure 5.23: The $\mu\tau_h$ visible mass of events passing the full selection for the ATLAS $Z \to \tau\tau$ observation. The red vertical lines indicate the 35–75 GeV mass window used as the final cut [146].

5.6 Kinematics of selected $Z \to \tau\tau \to \ell\tau_{\mathrm{h}}$ events

Using the entire 2010 dataset of approximately 36 pb^{-1}, the observed events, estimated backgrounds, and SM signal expectation for both channels are summarized in Table 5.8. The number of observed events in the data after subtracting the estimated background is

$$164 \pm 16 \text{ (stat.)} \pm 4 \text{ (syst.) events} \quad (\mu\tau_{\mathrm{h}} \text{ channel})$$
$$114 \pm 14 \text{ (stat.)} \pm 3 \text{ (syst.) events} \quad (e\tau_{\mathrm{h}} \text{ channel})$$

which is compatible with the Standard Model signal expectation of

$$186.2 \pm 2.1 \text{ (stat.)} \pm 25.7 \text{ (syst.) events} \quad (\mu\tau_{\mathrm{h}} \text{ channel})$$
$$97.8 \pm 1.4 \text{ (stat.)} \pm 16.2 \text{ (syst.) events} \quad (e\tau_{\mathrm{h}} \text{ channel}) .$$

Figure 5.24 shows distributions of the p_{T} and η of the selected leptons and tau candidates for events passing all signal selection [180]. Distributions of $E_{\mathrm{T}}^{\mathrm{miss}}$ and the $\Delta\phi$ between the selected tau candidate and lepton, in events passing all selections are shown in Figure 5.25. Distributions of the number of tracks associated to the selected tau candidate are shown in Figure 5.26, for events passing all selections except the cut on the number of tracks or the magnitude of the charge for the tau candidate, showing the characteristic 1/3-prong peak for hadronic tau decays.

5.7 Background estimation

5.7.1 Overview

The estimated number of background events from electroweak processes ($W \to \ell\nu$, $W \to \tau\nu$, $Z \to \ell\ell$, diboson) and $t\bar{t}$ was taken from Monte Carlo, provided that these backgrounds were small and the Monte Carlo prediction agreed well with the observed data in regions that are electroweak rich. To

Table 5.8: Summary of the number of selected $Z \to \tau\tau$ candidate events and the expected backgrounds, comparing the two methods for estimating the multijet background described in Section 5.7.

	$\mu\tau_{\mathrm{h}}$ channel (35.5 pb^{-1})	$e\tau_{\mathrm{h}}$ channel (35.7 pb^{-1})
data (after all selections)	213	151
estimated multijet bkg. OS/SS	24 ± 6 (stat.) ± 3 (syst.)	23 ± 6 (stat.) ± 3 (syst.)
estimated multijet bkg. isol. lep.	23 ± 3 (stat.) ± 4 (syst.)	25 ± 3 (stat.) ± 3 (syst.)
estimated $W, Z, t\bar{t}$, diboson background	25 ± 1 (stat.) ± 5 (syst.)	14 ± 1 (stat.) ± 3 (syst.)
data (after bkg. subtraction OS/SS)	164 ± 16(stat.)±4(syst.)	114 ± 14(stat.)±3(syst.)
data (after bkg. subtraction isol. lep.)	164 ± 13(stat.) ± 5(syst.)	111 ± 11(stat.) ± 4(syst.)
SM $Z \to \tau\tau$ expectation	186.2 ± 2.1(stat.) ± 25.7(syst.)	97.8 ± 1.4(stat.) ± 16.2(syst.)

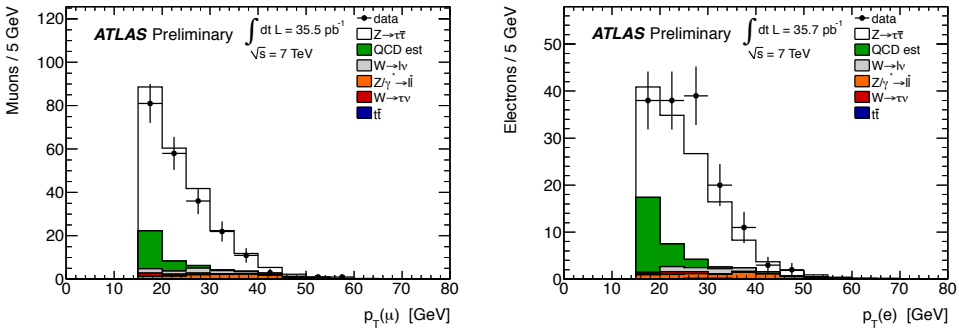

(a) muon channel

(b) electron channel

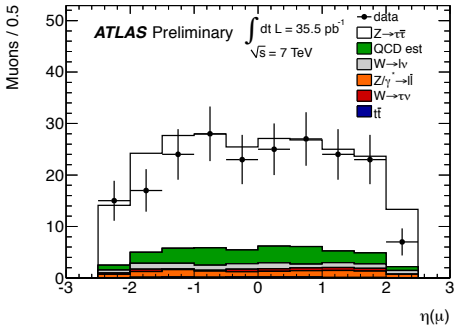

(c) muon channel

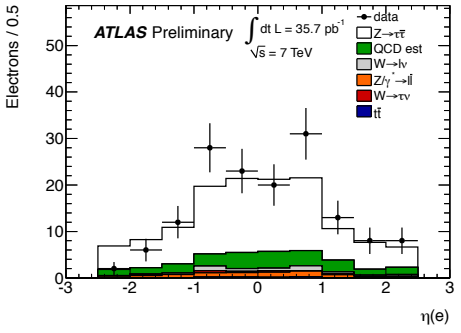

(d) electron channel

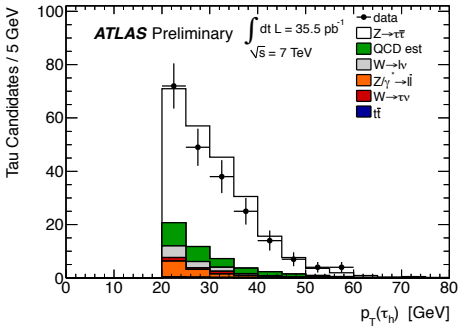

(a) muon channel

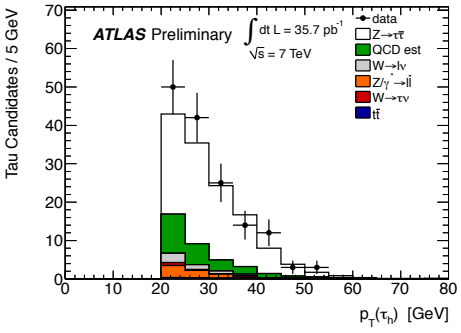

(b) electron channel

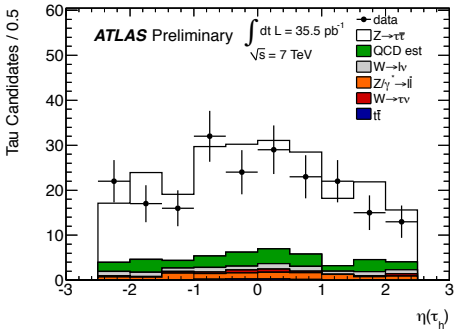

(c) muon channel

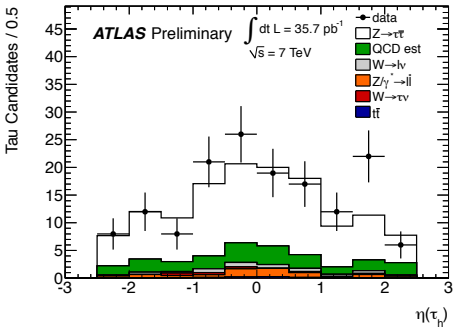

(d) electron channel

Figure 5.24: Distributions of the p_{T} and η of the selected leptons and tau candidates for events passing all signal selection [180].

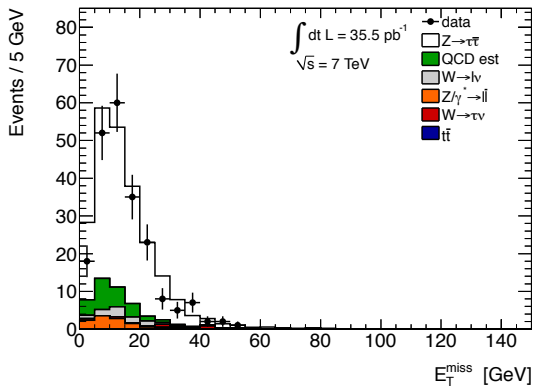

(a) muon channel

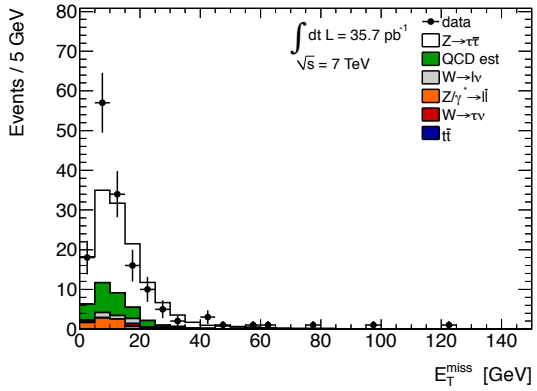

(b) electron channel

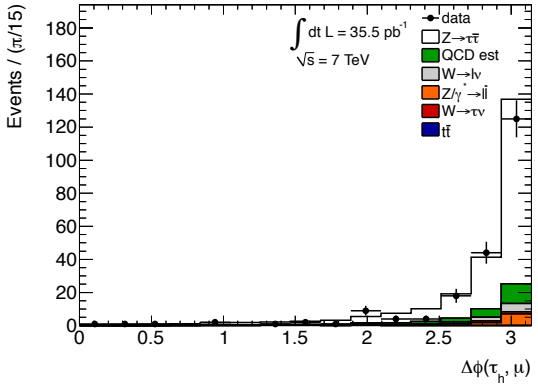

(c) muon channel

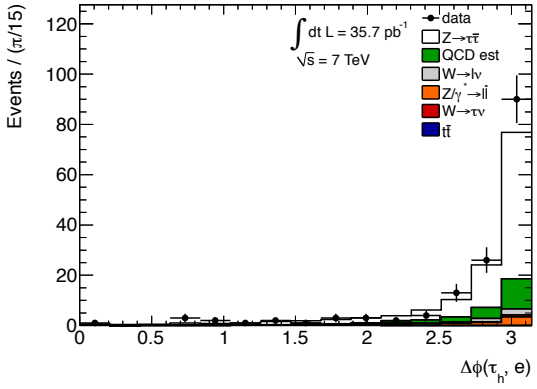

(d) electron channel

Figure 5.25: The distributions of the $E_{\mathrm{T}}^{\mathrm{miss}}$ and $\Delta\phi$ between the selected tau candidate and lepton, in the final visible mass window for the muon (a),(c) and electron (b),(d) channels [180].

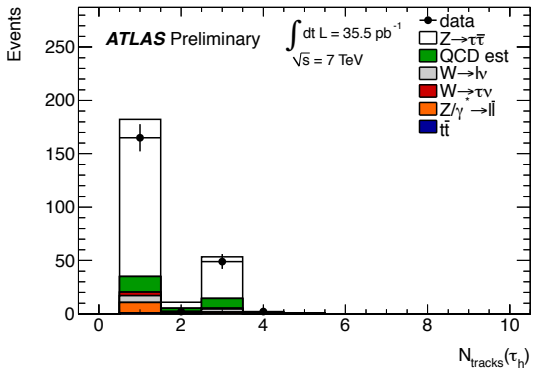

(a) muon channel

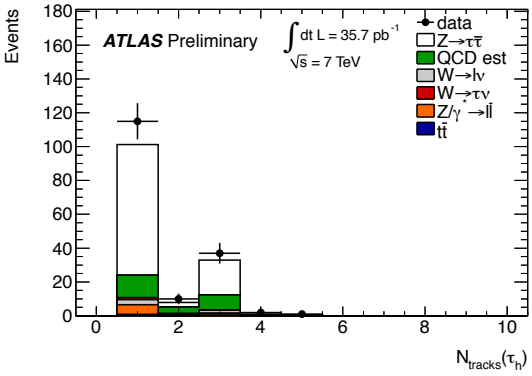

(b) electron channel

Figure 5.26: The final track distribution after all cuts, except without the requirement of 1 or 3 tracks. The product of the reconstructed charges is required to be negative or zero (not same-sign) [180].

account for the mis-modeling of the tau identification fake rate for jets[56], the combined W + jets Monte Carlo samples were normalized with a scale factor derived in a W + jets-rich control region of the data.

Rates of real and fake leptons as well as fake tau candidates produced in multijet events are also not expected to be modeled well with Monte Carlo, as discussed in Section 5.2.1. The estimated number of multijet background events was determined with a data-driven technique, extrapolating from the number of events in the data with a same-sign lepton and tau candidate. with a lepton and tau candidate with the same sign reconstructed charges. It was cross-checked with a second data-driven method, extrapolating from the number of events observed in data with non-isolated leptons.

5.7.2 *W* Monte Carlo scale factor

A very W + jets rich data sample can be selected using the same object selection but varying the event selection, making it possible to check the agreement between the W Monte Carlo and data in normalization and shape of kinematic distributions. This W *control region* (WCR) was constructed to contain events passing the dilepton veto, the cuts on the number of tracks associated to the tau candidate, the charge of the τ candidate, and the charge product (opposite or same sign) but failing both W suppression cuts (see Figure 5.20).

The Monte Carlo agreed with the data reasonably well before imposing the tau identification requirements described in Section 5.4.4. Following tight tau identification, the Monte Carlo was found to overestimate the data. This is illustrated in Fig. 5.27. The W Monte Carlo was therefore corrected by normalizing it to the number of events observed in the data in the W control region, corrected for the contamination from the other electroweak processes predicted from Monte Carlo. That is, the nominal W Monte Carlo samples, both $W \to \ell\nu$ and $W \to \tau\nu$, were scaled by a factor k_W, such that the predicted number of W events in the W control region was equal to the number of events observed in the data, subtracted for the small contamination from $Z \to \ell\ell$, $t\bar{t}$, and diboson:

$$N_W^{\mathrm{WCR}} \to k_W N_W^{\mathrm{WCR}} = N_{\mathrm{data}}^{\mathrm{WCR}} - N_{Z\to\ell\ell,t\bar{t},\mathrm{diboson}}^{\mathrm{WCR}} .$$

Due to the high transverse mass requirement, the multijet contamination was found to be negligible in the W control region.

This procedure was used to determine k_W scale factors for the signal region with a tau candidate passing tight tau identification and an opposite-sign lepton, and also for other control regions. These control regions require individual k_W scale factors to correct the fake rate for tau identification since

[56] Due to the mis-modeling of the jet-width, the tau identification fake rate for jets is not reliable in Monte Carlo. Jets are slightly more wide in data than in MC, as discussed in Section 4.4.1.

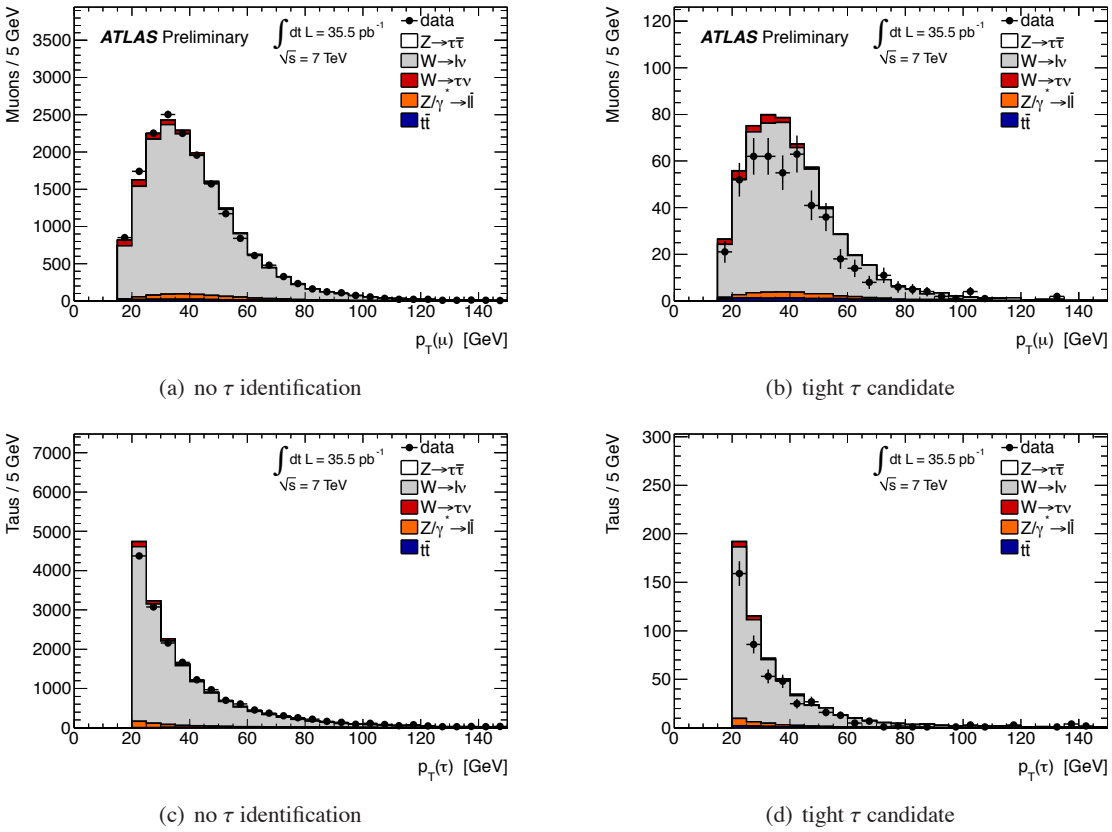

(a) no τ identification

(b) tight τ candidate

(c) no τ identification

(d) tight τ candidate

Figure 5.27: Muon and tau p_{T} distributions in the W control region, following no tau identification (a)/(c) and tight (b)/(d) τ identification. Following tight tau identification, the Monte Carlo overestimates the W contribution. A similar effect is seen in the $e\tau_{\mathrm{h}}$ channel [180].

the tau fake rate depends on the quark/gluon fraction, which varies among the W + jets samples[57]. The measured k_W scale factors are:

$$k_W = \begin{cases} 0.93 \pm 0.04\ (\text{stat.}) & \mu\tau_{\mathrm{h}} \text{ channel, loose + not tight tau, opposite sign} \\ 0.73 \pm 0.06\ (\text{stat.}) & \mu\tau_{\mathrm{h}} \text{ channel, tight tau, opposite sign} \\ 0.94 \pm 0.13\ (\text{stat.}) & \mu\tau_{\mathrm{h}} \text{ channel, tight tau, same sign} \\ 0.97 \pm 0.04\ (\text{stat.}) & e\tau_{\mathrm{h}} \text{ channel, loose + not tight tau, opposite sign} \\ 0.63 \pm 0.07\ (\text{stat.}) & e\tau_{\mathrm{h}} \text{ channel, tight tau, opposite sign} \\ 0.83 \pm 0.15\ (\text{stat.}) & e\tau_{\mathrm{h}} \text{ channel, tight tau, same sign}\,. \end{cases}$$

As a cross-check to the k_W scale factors being consistent with correcting the tau mis-identification rate, instead of applying k_W, a scale factor for the jet to tau fake rate was applied, measured in a

[57] See the discussion of the variation of jet fake rates with composition in Section 4.4.8.

data sample of Z + jets events [158] (see Figure 5.9).

The estimated W + jets background after all cuts is listed in Table 5.10, comparing the estimates using the k_W and tau-by-tau scale factor methods and showing them to be in agreement. The simplest method using the k_W scale factors was chosen as the primary W + jets estimate.

Investigations in methods of using scale factors to correct the rate for jets to fake tau identification later led to the development of the data-driven method for modeling fake backgrounds by applying fake factors to events in the data that fail tau identification, developed for the $Z' \to \tau\tau$ search, which will be discussed in Section 6.4.4.

5.7.3 Multijet background estimation from the same-sign sample

The multijet background was not simulated with Monte Carlo but instead estimated from control regions in the data.

A common method for constructing a data-driven background model is to scale the data in a control region (or side band) by an appropriate weight, measured from the ratios of events in another pair of control regions. It is often called the "*ABCD method*", named for the labels for the four control regions used in the estimate. Essentially, it is the method of applying a single-bin scale factor to a data sample one expects to look like the background to model. It is important that the variables used to select the control regions be largely uncorrelated to give an unbiased model of the background[58]. Examples of uses of the ABCD method are plentiful in ATLAS, especially in

[58] The variables used to define the ABCD regions need to be uncorrelated for the background sample to be modeled, but contaminations in the control regions that are not the background of interest can have correlations so long as

Table 5.9: Scale factors for the jet to tau fake rate obtained in Z + jets events. The fake rate was about 3–7% in the 1-prong case and about 2–3% in the 3-prong case [180].

number of vertices	1-prong medium tau	3-prong tight tau
$1, 2$	0.949 ± 0.220	0.855 ± 0.280
> 2	0.626 ± 0.240	1.151 ± 0.436

Table 5.10: The predicted number of W + jets events in the signal region after all cuts, comparing estimates from the tau-by-tau scale factor and k_W methods [180].

sample	$\mu\tau_{\text{h}}$ channel	
	tau fake rate scale factors	k_W
$W \to \ell\nu$	10.8 ± 0.8 (stat.) ± 2.6 (syst.)	9.3 ± 0.7 (stat.) ± 2.0 (syst.)
$W \to \tau\nu$	4.1 ± 1.0 (stat.) ± 1.1 (syst.)	3.6 ± 0.8 (stat.) ± 0.8 (syst.)
sample	$e\tau_{\text{h}}$ channel	
	tau fake rate scale factor	k_W
$W \to \ell\nu$	6.6 ± 0.6 (stat.) ± 1.6 (syst.)	4.8 ± 0.4 (stat.) ± 1.2 (syst.)
$W \to \tau\nu$	2.0 ± 0.6 (stat.) ± 0.5 (syst.)	1.5 ± 0.4 (stat.) ± 0.4 (syst.)

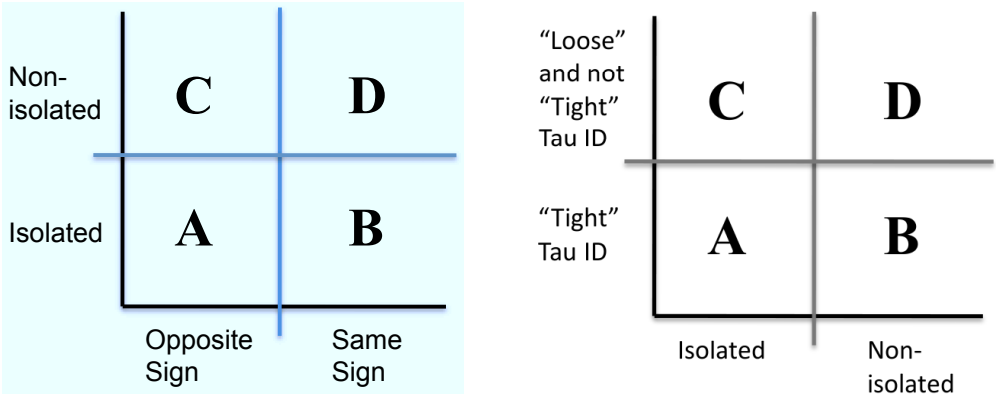

Figure 5.28: Diagrams of the control regions for two ABCD methods for estimating the multijet background. The figure on the left shows the regions for the primary estimate. The figure on the right shows regions for the cross-check method [180].

first observations and measurements because it can be implemented simply and performs well in low count scenarios by grouping the counts into only four bins to determine the normalization[59].

Two complementary ABCD methods, using different control regions, were used to estimate the multijet background. The first method took advantage of the fact that the multijet background is effectively symmetric between the samples with opposite sign (OS) and same sign (SS) charges for the lepton and tau candidate. This property is observed in dijet Monte Carlo samples[60] as well as the data. Then these samples were divided into those that pass or fail lepton isolation requirements, giving the four combinations of regions: {A, B, C, D}, shown in Figure 5.28. A multijet-rich control region is defined to contain the events that fail the lepton isolation requirements, denoted by the union of regions CD. The OS/SS ratio, $R_{\mathrm{OS/SS}}$, is measured in this control region and applied as a weight to the SS sample that passes lepton isolation (B), to predict the multijet background normalization in the signal region (A).

Stated more explicitly, the method relies on the assumption that the OS/SS ratio is the same among multijet events with isolated and non-isolated lepton candidates:

$$\frac{N^{\mathrm{A}}_{\mathrm{multijet}}}{N^{\mathrm{B}}_{\mathrm{multijet}}} = \frac{N^{\mathrm{C}}_{\mathrm{multijet}}}{N^{\mathrm{D}}_{\mathrm{multijet}}} .$$

where N is the number of multijet events in four statistically independent regions, denoted {A, B, C, D} and defined as follows:

- A: signal region with isolated lepton and opposite-sign tau candidate

they can be modeled and are preferably small so they can be subtracted. For example, the $Z \to \ell\ell$ background is obviously OS biased, as is the W + jets.

[59] An other example use of the ABCD method can be found in the first ATLAS $W \to \tau\nu$ cross section measurement [189], as discussed briefly in Section 4.4.2.

[60] Like the dijet samples used in the Monte Carlo studies discussed in Section 5.2.1.

- B: control region with isolated lepton and same-sign tau candidate
- C: control region with non-isolated lepton and opposite-sign tau candidate
- D: control region with non-isolated lepton and same-sign tau candidate.

Regions B, C, and D are nearly signal free, and the regions C and D are very multijet pure. The contamination from other electroweak processes is estimated with Monte Carlo and subtracted in each control region:

$$N^i_{\text{multijet}} = N^i_{\text{data}} - N^i_{Z\to\tau\tau} - N^i_{Z\to\ell\ell,t\bar{t},\text{diboson}} - k_W(N^i_{W\to\ell\nu} + N^i_{W\to\tau\nu}), \quad \text{for } i = \text{B, C, D}\,.$$

In each of the control regions an estimate for the number of multijet events was obtained by correcting for the $Z \to \ell\ell$, $t\bar{t}$ and diboson contributions as predicted from MC, and for $W+$jets $W \to \tau\nu$ contributions by correcting the MC predictions using the k_W normalisation factors discussed previously.

The leptons from the backgrounds $W \to \ell\nu$, $W \to \tau\nu$ and $Z \to \ell\ell$ are typically very well isolated, like $Z \to \tau\tau$. From Monte Carlo, it is estimated that regions C and D are ≈99% multijet pure. These multijet rich regions were used to measure the OS/SS ratio, $R_{\text{OS/SS}}$, for multijet events:

$$R_{\text{OS/SS}} = \frac{N^{\text{C}}_{\text{multijet}}}{N^{\text{D}}_{\text{multijet}}} = \begin{cases} 1.07 \pm 0.04\ (\text{stat.}) \pm 0.04\ (\text{syst.}) & \mu\tau_{\text{h}}\ \text{channel} \\ 1.07 \pm 0.07\ (\text{stat.}) \pm 0.07\ (\text{syst.}) & e\tau_{\text{h}}\ \text{channel}\,. \end{cases}$$

As expected it is consistent with 1. This measured $R_{\text{OS/SS}}$ was then used to scale the multijet estimate from region B to give the prediction in region A:

$$N^{\text{A}}_{\text{multijet}} = \frac{N^{\text{C}}_{\text{multijet}}}{N^{\text{D}}_{\text{multijet}}}\, N^{\text{B}}_{\text{multijet}} = R_{\text{OS/SS}}\, N^{\text{B}}_{\text{multijet}}\,.$$

This yielded the numbers for each region shown in Table 5.11. The expected number of multijet events in the signal region A is

$$N^{\text{A}}_{\text{multijet}} = \begin{cases} 24 \pm 6\ (\text{stat.}) \pm 3\ (\text{syst.}) & \mu\tau_{\text{h}}\ \text{channel} \\ 23 \pm 6\ (\text{stat.}) \pm 3\ (\text{syst.}) & e\tau_{\text{h}}\ \text{channel}\,. \end{cases}$$

This gave the normalization of the multijet background estimate in the signal region. The shapes of kinematic distributions for the multijet background were modeled with the SS events in data (region B if following the isolation requirement), corrected for contamination with MC and scaled to this normalization. This model was used as the primary estimate of the multijet background.

5.7.4 Multijet background estimation from non-isolated leptons

As a cross-check, a second method for estimating the multijet background selected a multijet rich control region by inverting the lepton isolation requirements. Then the number of multijet events in the isolated lepton signal region was estimated by scaling the number observed in the non-isolated region by the expected ratio of isolated to non-isolated leptons. This *isolation ratio* was measured in an independent pair of multijet rich control regions defined by changing the tau selection to choose the leading loose tau candidate and require that it fails medium (tight) tau identification for 1 prong (3 prong) candidates (electron veto is still applied however). This tau candidate selection will be referred to as "loose but not tight". The combinations of requiring an isolated or non-isolated lepton, and a tight or a loose but not tight tau candidate results in four statistically independent regions:

- A: signal region with isolated lepton and tight tau candidate
- B: control region with non-isolated lepton and tight tau candidate
- C: control region with isolated lepton and loose but not tight tau candidate
- D: control region with non-isolated lepton and loose but not tight tau candidate.

Regions B, C, and D are multijet-rich, with some contamination from electroweak processes and $t\bar{t}$. According to Monte Carlo predictions, in region C approximately 50% of this electroweak contamination consists of signal events, constituting about 30% of all events in region C. Since this background estimation method is only a cross-check of the primary method, the theoretical signal cross-section for $Z \to \tau\tau$ was assumed and used to normalize the $Z \to \tau\tau$ contamination in control regions (with its uncertainty propagated as a systematic uncertainty). A summary of the estimates in each control region are shown in Table 5.12.

The key assumption of this method is that for the multijet background, the probability for a jet to fake tau identification should be largely independent of the probability for the fake or true lepton on the other side of the event to be isolated, and therefore the isolation ratio in multijet events is independent of the tau identification requirement:

$$\frac{N^{\mathrm{A}}_{\mathrm{multijet}}}{N^{\mathrm{B}}_{\mathrm{multijet}}} = \frac{N^{\mathrm{C}}_{\mathrm{multijet}}}{N^{\mathrm{D}}_{\mathrm{multijet}}}$$

The validity of this assumption and the possibility of correlations between the lepton isolation and tau identification are considered in Section 5.9.3.

Given these assumptions, the number of multijet events in the signal region A can be estimated by

$$N^{\mathrm{A}}_{\mathrm{multijet}} = \frac{N^{\mathrm{C}}_{\mathrm{multijet}}}{N^{\mathrm{D}}_{\mathrm{multijet}}} N^{\mathrm{B}}_{\mathrm{multijet}} = R_{\mathrm{iso}} N^{\mathrm{B}}_{\mathrm{multijet}} ,$$

where R_{iso} is the isolation ratio measured in regions C and D ($R_{\text{iso}} \sim 1\%$). Since regions B, C, and D are not completely multijet pure, we correct for the expected electroweak contamination from Monte Carlo in each region:

$$N^i_{\text{multijet}} = N^i_{\text{data}} - N^i_{Z\to\tau\tau} - N^i_{Z\to\ell\ell,t\bar{t},\text{diboson}} - k_W(N^i_{W\to\ell\nu} + N^i_{W\to\tau\nu}), \quad \text{for } i = \text{B, C, D}\,.$$

The expected number of multijet events in the signal region A is

$$N^{\text{A}}_{\text{multijet}} = \begin{cases} 23 \pm 3 \text{ (stat.)} \pm 4 \text{ (syst.)} & \mu\tau_{\text{h}} \text{ channel} \\ 25 \pm 3 \text{ (stat.)} \pm 3 \text{ (syst.)} & e\tau_{\text{h}} \text{ channel}\,, \end{cases}$$

in good agreement with the estimate based on the same-sign sample, presented in the previous section. The shapes of the multijet background were modeled with the data in region B, corrected with MC for the small amount of contamination.

Table 5.11: Numbers of events in the control regions discussed in Section 5.7.3. The numbers in parenthesis are the statistical errors in the least significant digits. The multijet expectations are determined by the data-driven method discussed in that section. The other processes are estimated with Monte Carlo [180].

		$\mu\tau_{\mathrm{h}}$ channel		$e\tau_{\mathrm{h}}$ channel	
		isolated lepton	non-isolated lepton	isolated lepton	non-isolated lepton
		region A	region C	region A	region C
	data	213(15)	1521(39)	151(12)	398(20)
	$Z \to \tau\tau$	185(2)	8.4(4)	97(1)	3.2(2)
	$\gamma \to \tau\tau$	0.7(3)	0.05(5)	0.3(2)	0(0)
	multijet	24(6)	1511(39)	23(6)	394(20)
OS events	$W \to \ell\nu$	9.3(7)	0.3(1)	4.8(4)	0.2(1)
	$W \to \tau\nu$	3.6(8)	0.08(8)	1.5(4)	0.04(4)
	$Z \to \ell\ell$	8.7(3)	0.33(6)	4.9(2)	0.12(3)
	$\gamma \to \ell\ell$	2.4(4)	0.16(8)	2.0(3)	0.03(3)
	$t\bar{t}$	1.3(1)	0.99(8)	1.02(8)	0.11(3)
	diboson	0.28(2)	0.052(8)	0.18(1)	0.009(3)
		region B	region D	region B	region D
	data	34(6)	1415(38)	29(5)	367(19)
	$Z \to \tau\tau$	1.3(2)	0.3(8)	1.0(1)	0.23(7)
	$\gamma \to \tau\tau$	0.06(6)	0.09(9)	0.2(1)	0(0)
	multijet	22(6)	1413(38)	21(5)	367(19)
SS events	$W \to \ell\nu$	3.7(5)	0.09(6)	2.3(3)	0(0)
	$W \to \tau\nu$	2.1(7)	0.2(2)	0.3(3)	0(0)
	$Z \to \ell\ell$	1.9(1)	0.11(3)	2.7(3)	0.05(2)
	$\gamma \to \ell\ell$	2.5(4)	0.11(8)	1.3(3)	0.13(11)
	$t\bar{t}$	0.21(4)	0.61(6)	0.1(3)	0.06(18)
	diboson	0.044(7)	0.021(4)	0.029(5)	0.005(3)

Table 5.12: Numbers of events in the control regions discussed in Section 5.7.4. The numbers in parenthesis are the statistical errors in the least significant digits. The multijet expectations are determined by the data-driven method using non-isolated leptons, discussed in that section. The other processes are estimated with Monte Carlo [180].

		$\mu\tau_{\mathrm{h}}$ channel		$e\tau_{\mathrm{h}}$ channel	
		isolated lepton	non-isolated lepton	isolated lepton	non-isolated lepton
		region A	region B	region A	region B
	data	213(15)	1521(39)	151(12)	398(20)
	$Z \to \tau\tau$	185(2)	8.4(4)	97(1)	3.2(2)
	$\gamma \to \tau\tau$	0.7(3)	0.05(5)	0.3(2)	0(0)
	multijet	23(3)	1510(39)	25(3)	394(20)
tight tau candidate	$W \to \ell\nu$	9.3(7)	0.31(12)	4.8(4)	0.2(1)
	$W \to \tau\nu$	3.6(8)	0.08(8)	1.5(4)	0.04(4)
	$Z \to \ell\ell$	8.7(3)	0.33(6)	4.9(2)	0.12(3)
	$\gamma \to \ell\ell$	2.4(4)	0.16(8)	2.0(3)	0.03(3)
	$t\bar{t}$	1.3(1)	0.99(8)	1.02(8)	0.11(3)
	diboson	0.28(2)	0.052(8)	0.18(1)	0.009(3)
		region C	region D	region C	region D
	data	283(17)	9696(98)	225(15)	2159(46)
	$Z \to \tau\tau$	72(1)	4.2(3)	39.5(8)	1.4(2)
	$\gamma* \to \tau\tau$	3(1)	0.3(2)	0	0.03(3)
	multijet	144(17)	9688(98)	139(15)	2156(46)
loose not tight	$W \to \ell\nu$	35(2)	1.8(3)	22(1)	0.6(2)
tau candidate	$W \to \tau\nu$	11(2)	0.5(3)	7.6(1)	0
	$Z \to \ell\ell$	6.3(2)	0.28(5)	9.6(3)	0.20(4)
	$\gamma* \to \ell\ell$	7.5(7)	0.3(1)	5.2(5)	0.2(1)
	$t\bar{t}$	2.3(1)	1.07(8)	1.4(1)	0.22(4)
	diboson	0.31(3)	0.09(1)	0.22(2)	0.019(4)

5.7.5 Summary of backgrounds

The measurements of $Z \to \tau\tau \to \ell\tau_{\mathrm{h}}$ channels were combined with measurements of the $Z \to \tau\tau \to e\mu$ and $Z \to \tau\tau \to \mu\mu$ final states. A summary of the background and $Z \to \tau\tau$ signal expectations for each channel is shown in Table 5.13.

5.8 Method for calculating the cross section

As shown in Appendix A.1.5 when discussing scattering theory, the expected number of observed events from a particular scattering process at a collider can be calculated from the product of the integrated luminosity, the cross section, and correction factors for the acceptance and efficiency. This relation can be used to calculate the measured cross section for a process, given the number of observed events, subtracting the estimated backgrounds. The cross section may be calculated with

$$\sigma(Z \to \tau\tau) \times \mathrm{BR}(\tau \to \ell\nu\nu,\, \tau \to \tau_{\mathrm{h}}\nu) = \frac{N_{\mathrm{obs}} - N_{\mathrm{bkg}}}{A_Z\, C_Z\, \mathcal{L}}\,,$$

where:

- N_{obs} is the number of observed events in data.
- N_{bkg} is the number of estimated background events.
- A_Z denotes the kinematic and geometric acceptance for the signal process. It is determined from generator level Monte Carlo as

  $$A_Z = \frac{N_{\mathrm{fid,dressed}}}{N_{\mathrm{gen}}}$$

  where N_{gen} denotes the number of events generated with LO $\tau\tau$ invariant mass within 66–116 GeV. $N_{\mathrm{fid,dressed}}$ is the number of generated events that result in decay products that fall within the

Table 5.13: A summary of the estimated backgrounds, number of $Z \to \tau\tau$ signal events from Monte Carlo, and the number of observed events for analyses of $Z \to \tau\tau$ in four final states: $\mu\tau_{\mathrm{h}}$, $e\tau_{\mathrm{h}}$, $e\mu$, and $\mu\mu$ [113].

	$\tau_\mu\tau_h$	$\tau_e\tau_h$	$\tau_e\tau_\mu$	$\tau_\mu\tau_\mu$
$\gamma^*/Z \to \ell\ell$	11.1 ± 0.5	6.9 ± 0.4	1.9 ± 0.1	36 ± 1
$W \to \ell\nu$	9.3 ± 0.7	4.8 ± 0.4	0.7 ± 0.2	0.2 ± 0.1
$W \to \tau\nu$	3.6 ± 0.8	1.5 ± 0.4	< 0.2	< 0.2
$t\bar{t}$	1.3 ± 0.1	1.02 ± 0.08	0.15 ± 0.03	0.8 ± 0.1
Diboson	0.28 ± 0.02	0.18 ± 0.01	0.48 ± 0.03	0.13 ± 0.01
Multijet	24 ± 6	23 ± 6	6 ± 4	10 ± 2
$\gamma^*/Z \to \tau\tau$	186 ± 2	98 ± 1	73 ± 1	44 ± 1
Total expected events	235 ± 6	135 ± 6	82 ± 4	91 ± 3
N_{obs}	213	151	85	90

fiducial kinematic region defined in Table 5.14. The generator-level tau lepton decay products in the $N_{\text{fid,dressed}}$ term were further "dressed" by combining their four-vectors with any photons radiated, either from the original tau or from its subsequent decay products simulated with TAUOLA [127], in order to correct for the final state radiation generated with PHOTOS [126].

The central values for the A_Z factor were determined using a default PYTHIA Monte Carlo sample generated with the modified LO MRSTLO* parton distribution function [190] and the corresponding ATLAS MC10 tune [129]. The obtained central values are reported in Table 5.14. The difference in A_Z values between muon and electron channel is essentially due to the exclusion of the calorimeter crack region from the fiducial region for the selection of electrons. The statistical uncertainty on the A_Z correction factors is at the 0.2% level for both channels.

- C_Z is the correction factor that accounts for the efficiency of triggering, reconstructing and identifying decays within the geometrical acceptance. It is defined as

$$C_Z = \frac{N_{\text{reco,pass}}}{N_{\text{fid,dressed}}}$$

where $N_{\text{reco,pass}}$ is the number of reconstructed MC signal events that pass the entire analysis selection. The statistical uncertainty on the C_Z correction factors is 1.5% for the electron channel and 1.2% for the muon channel.

- $\mathcal{L}$ denotes the integrated luminosity for the channel of interest:

$$\mathcal{L} = \int dt\, L\,.$$

The cross section as calculated above gives the total inclusive cross section. The fiducial cross section is independent of the extrapolation to the full phase space with A_Z, and therefore is less affected by theoretical uncertainties in the model. The fiducial cross section is calculated as

$$\sigma_{\text{fid}}(Z \to \tau\tau) \times \text{BR}(\tau \to \ell\nu\nu,\, \tau \to \tau_{\text{h}}\nu) = \frac{N_{\text{obs}} - N_{\text{bkg}}}{C_Z\, \mathcal{L}}\,.$$

Table 5.15 summarizes the quantities used to calculate the cross sections in each channel.

5.9 Systematic uncertainties

Experimental and theoretical systematic uncertainties are propagated to the final expected yields for signal and background. Object-level systematic uncertainties (like the energy scales and resolutions for leptons, hadronic tau decays, and jets) are evaluated by shifting the observables in Monte Carlo

Table 5.14: Central values for the A_Z acceptance factor determined with ATLAS MC10 Monte Carlo generated with PYTHIA and MRSTLO* PDFs, and for the C_Z efficiency factor determined using the same generated sample after full detector simulation and selection [180].

	$\mu\tau_{\mathrm{h}}$ channel	$e\tau_{\mathrm{h}}$ channel
A_Z	0.11691 ± 0.00023 (stat.)	0.10073 ± 0.00021 (stat.)
C_Z	0.2045 ± 0.0024 (stat.)	0.1197 ± 0.0017 (stat.)
fiducial region		
lepton	$p_{\mathrm{T}} > 15$ GeV, $\lvert\eta\rvert < 2.4$	$p_{\mathrm{T}} > 16$ GeV, $\lvert\eta\rvert < 2.47$, excluding $1.37 < \lvert\eta\rvert < 1.52$
hadronic tau decay	$p_{\mathrm{T}}^{\mathrm{vis}} > 20$ GeV, $\lvert\eta\rvert < 2.47$, excluding $1.37 < \lvert\eta\rvert < 1.52$	$p_{\mathrm{T}}^{\mathrm{vis}} > 20$ GeV, $\lvert\eta\rvert < 2.47$, excluding $1.37 < \lvert\eta\rvert < 1.52$
event	$\Sigma \cos\Delta\phi > -0.15$, $m_{\mathrm{T}} < 50$ GeV, $m_{\mathrm{vis}} = 35$–75 GeV	$\Sigma \cos\Delta\phi > -0.15$, $m_{\mathrm{T}} < 50$ GeV, $m_{\mathrm{vis}} = 35$–75 GeV

Table 5.15: A summary of the measured quantities used to calculate the $Z \to \tau\tau$ cross section in four final states: $\mu\tau_{\mathrm{h}}$, $e\tau_{\mathrm{h}}$, $e\mu$, and $\mu\mu$ [113].

	$\tau_\mu\tau_h$	$\tau_e\tau_h$
N_{obs}	213	151
$N_{\mathrm{obs}} - N_{\mathrm{bkg}}$	$164 \pm 16 \pm 4$	$114 \pm 14 \pm 3$
A_Z	0.117 ± 0.004	0.101 ± 0.003
C_Z	0.20 ± 0.03	0.12 ± 0.02
B	0.2250 ± 0.0009	0.2313 ± 0.0009
$\mathcal{L}$	35.5 ± 1.2 pb^{-1}	35.7 ± 1.2 pb^{-1}
	$\tau_e\tau_\mu$	$\tau_\mu\tau_\mu$
N_{obs}	85	90
$N_{\mathrm{obs}} - N_{\mathrm{bkg}}$	$76 \pm 10 \pm 1$	$43 \pm 10 \pm 3$
A_Z	0.114 ± 0.003	0.156 ± 0.006
C_Z	0.29 ± 0.02	0.27 ± 0.02
B	0.0620 ± 0.0002	0.0301 ± 0.0001
$\mathcal{L}$	35.5 ± 1.2 pb^{-1}	35.5 ± 1.2 pb^{-1}

up and down within their uncertainties. Other uncertainties (like the uncertainty in the integrated luminosity or theoretical cross sections) are applied directly to the normalization of the expectation.

The total systematic uncertainties were estimated to be 15%/17% and the statistical uncertainties were 9.8%/12% in the $\mu\tau_{\rm h}/e\tau_{\rm h}$ channels. Table 5.16 summarizes the systematic uncertainties assumed for each channel. The leading systematic uncertainties were the tau identification efficiency and the tau energy scale, which are discussed below with a few other example sources of systematic error. The systematic uncertainties are discussed in detail in Ref. [180].

5.9.1 Cross sections and integrated luminosity

An uncertainty of 5% on the NNLO cross section for Z and $+7\%/-9.5\%$ for $t\bar{t}$ was assumed [191, 192]. The uncertainty on the luminosity was taken to be 3.4% [193]. These uncertainties were not applied to the multijet or W + jets backgrounds since their estimates were data-driven as described in Section 5.7.

5.9.2 Tau energy scale and efficiency

This analysis used the first ATLAS recommended systematic uncertainties on the tau energy scale and identification efficiency for true hadronic tau decays that were estimated with dedicated Monte

Table 5.16: A summary of the systematic uncertainties of the measurement of the $Z \to \tau\tau$ cross section in four final states: $\mu\tau_{\rm h}$, $e\tau_{\rm h}$, $e\mu$, and $\mu\mu$ [113].

Systematic uncertainty	$\tau_\mu\tau_h$	$\tau_e\tau_h$	$\tau_e\tau_\mu$	$\tau_\mu\tau_\mu$
Muon efficiency	3.8%	–	2.2%	8.6%
Muon d_0 (shape and scale)	–	–	–	6.2%
Muon resolution & energy scale	0.2%	–	0.1%	1.0%
Electron efficiency, resolution &				
Charge misidentification	–	9.6%	5.9%	–
τ_h identification efficiency	8.6%	8.6%	–	–
τ_h misidentification	1.1%	0.7%	–	–
Energy scale (e/τ/jets/$E_{\rm T}^{\rm miss}$)	10%	11%	1.7%	0.1%
Multijet estimate method	0.8%	2%	1.0%	1.7%
W normalization factor	0.1%	0.2%	–	–
Object quality selection criteria	1.9%	1.9%	0.4%	0.4%
pile-up description in simulation	0.4%	0.4%	0.5%	0.1%
Theoretical cross section	0.2%	0.1%	0.3%	4.3%
A_Z systematics	3%	3%	3%	4%
Total Systematic uncertainty	15%	17%	7.3%	14%
Statistical uncertainty	9.8%	12%	13%	23%
Luminosity	3.4%	3.4%	3.4%	3.4%

Carlo samples with with systematic shifts or changes of: the event generator, underlying event model, hadronic shower model, amount of detector material, and the topological clustering noise thresholds, as discussed briefly in Section 4.4.5. These studies constrained the energy scale for true hadronic tau decays to a few percent, resulting in a 10%/11% uncertainty on the yield in the $\mu\tau_{\rm h}/e\tau_{\rm h}$ channels. The uncertainty on the efficiency scale factor was constrained to $\approx 10\%$, consistent with 1 [100]. This contributed a 8.6% uncertainty on the yield in both the $\mu\tau_{\rm h}$ and $e\tau_{\rm h}$ channels.

5.9.3 Multijet background estimation from the same-sign sample

The key assumption of the multijet background estimate from the same-sign sample is that the ratio $R_{\rm OS/SS}$ is independent of the lepton isolation. In order check the potential dependence on the isolation of the selected lepton the $R_{\rm OS/SS}$ ratio was measured in bins of lepton isolation. In order to increase the statistics in each of the isolation bins and to suppress the signal at low lepton isolation, the identification on the hadronic tau candidate was reversed. To ensure that there was not an additional dependence on the ratio as a function of hadronic tau identification, $R_{\rm OS/SS}$ was also measured in bins of hadronic tau identification in the anti-isolated lepton region. Figure 5.29 summarizes the results.

A conservative systematic uncertainty was derived by measuring the maximum deviation of $R_{\rm OS/SS}$ as a function of isolation and combining this error in quadrature with the statistical error of the nominally measured value. An error of 5%/10% was measured for the $\mu\tau_{\rm h}/e\tau_{\rm h}$ channels. The systematic error was dominated by the statistical uncertainty from the number of data events in the same-sign sample. This resulted in a net 0.8%/2% systematic error on the $Z \to \tau\tau$ yield in the $\mu\tau_{\rm h}/e\tau_{\rm h}$ channels [180].

5.10 Results

The $Z \to \tau\tau$ cross section was measured independently in four channels: $\mu\tau_{\rm h}$, $e\tau_{\rm h}$, $e\mu$, and $\mu\mu$. The resulting fiducial and total cross sections, calculated as described in the previous section, are shown in Table 5.17.

The cross section measurements were combined with the Best Linear Unbiased Estimate (BLUE) method [194, 195]. The BLUE method combines the results with a linear combination of the individual measurements, with an estimate of the total uncertainty that is unbiased and has the smallest possible variance. This is achieved by constructing the covariance matrix from the statistical and systematic uncertainties for each individual cross section measurement, while accounting for correlations between the uncertainties from each channel. Related systematic uncertainties among the channels such as reconstructed energy scales, identification efficiencies, and trigger efficiencies were

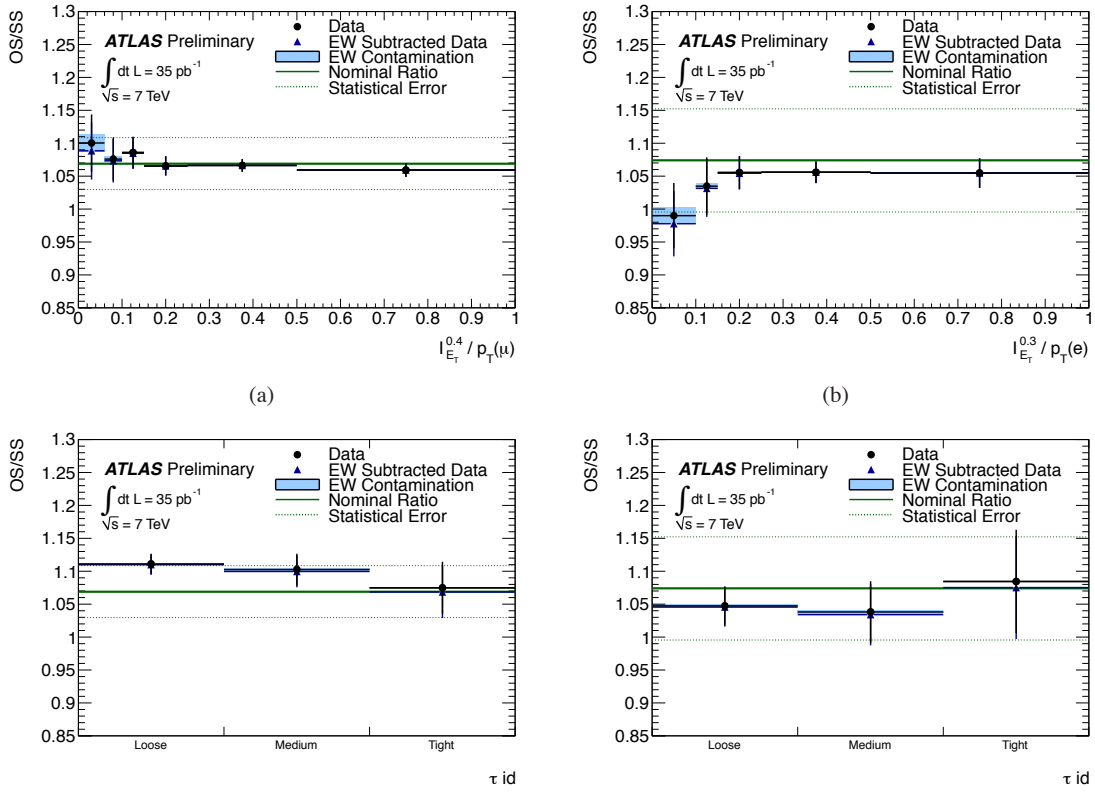

Figure 5.29: Plots demonstrating the stability of $R_{\mathrm{OS/SS}}$ as a function of calorimeters isolation (top) and tau identification requirements (bottom), for the $\mu\tau_{\mathrm{h}}$ (left) and $e\tau_{\mathrm{h}}$ (right) channels [180].

treated as fully correlated. Statistical uncertainties from the MC or data samples are treated as uncorrelated [196].

The combined measured cross section published[61] by ATLAS [113] is

$$\sigma(Z \to \tau\tau, 66 < m_{\tau\tau} < 116 \text{ GeV}) = 0.97 \pm 0.07 \text{ (stat.)} \pm 0.06 \text{ (syst.)} \pm 0.03 \text{ (lumi) nb}\,.$$

A comparison of the individual cross sections with the combined result is shown in Figure 5.30, along with the combined $Z \to \ell\ell$ cross section measured in the $Z \to ee$ and $Z \to \mu\mu$ final states by ATLAS [108]. The measurement is compatible with the NNLO SM theoretical expectation of 0.96 ± 0.05 nb for $\tau\tau$ invariant mass within 66–116 GeV. The result is also comparable with the $Z \to \tau\tau$ cross section measurement published by CMS [198] of[62]

$$\sigma(Z \to \tau\tau, 60 < m_{\tau\tau} < 120 \text{ GeV}) = 1.00 \pm 0.05 \text{ (stat.)} \pm 0.08 \text{ (syst.)} \pm 0.04 \text{ (lumi) nb}\,.$$

[61] The author presented this result at the 2011 International Europhysics Conference on High Energy Physics (EPS) in Grenoble, France [197].

[62] The primary references discussing the topics of this chapter in more detail are

- *A selection strategy for $Z \to \tau\tau \to \mu\tau_{\mathrm{h}}$ with the first 100 inverse picobarns from ATLAS*

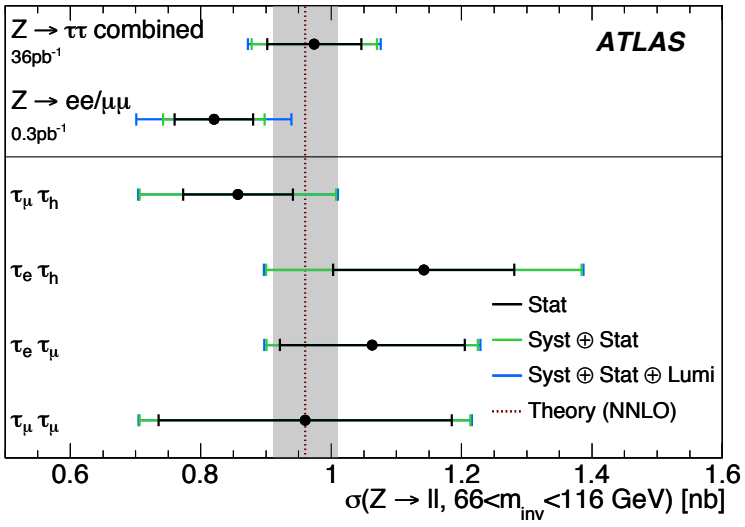

Figure 5.30: The combined measurement of the $Z \to \tau\tau$ cross section in four final states: $\mu\tau_{\rm h}$, $e\tau_{\rm h}$, $e\mu$, and $\mu\mu$ [113]. The combination of the ATLAS measurements of the $Z \to ee/\mu\mu$ cross sections is shown for comparison [108].

ATL-PHYS-INT-2009-044 [176],

- *Benchmark analysis for* $Z \to \tau\tau \to \ell\tau_{\rm h}$ *with the first* 100 pb^{-1} ATL-PHYS-INT-2010-075 [173],
- *Observation of* $Z \to \tau\tau$ *decays with the ATLAS detector - support note for the* $\ell\tau_{\rm h}$ *channel* ATL-COM-PHYS-2010-1033 [188], – support note for ATLAS-CONF-2011-010,
- *Observation of* $Z \to \tau_h\tau_l$ *decays with the ATLAS detector* ATLAS-CONF-2011-010 [146],
- *Measurement of* $Z \to \tau\tau$ *production cross section in proton-proton collisions at* $\sqrt{s} = 7$ *TeV with the ATLAS detector - Support Note for lep-had channels* ATL-COM-PHYS-2011-416 [180],
- *Measurement of the* $Z \to \tau\tau$ *cross section in pp collisions at* $\sqrt{s} = 7$ *TeV with the ATLAS detector* arxiv:1108.2016 [hep-ex] [113].

Table 5.17: A summary of the results of measuring the total and fiducial cross sections for $Z \to \tau\tau$ in four final states: $\mu\tau_{\rm h}$, $e\tau_{\rm h}$, $e\mu$, and $\mu\mu$ [113].

Final State	Fiducial cross section (pb)
$\tau_\mu\tau_h$	$23 \pm 2 \pm 3 \pm 1$
$\tau_e\tau_h$	$27 \pm 3 \pm 5 \pm 1$
$\tau_e\tau_\mu$	$7.5 \pm 1.0 \pm 0.5 \pm 0.3$
$\tau_\mu\tau_\mu$	$4.5 \pm 1.1 \pm 0.6 \pm 0.2$
Final State	Total cross section ($[66, 116]$ GeV) (nb)
$\tau_\mu\tau_h$	$0.86 \pm 0.08 \pm 0.12 \pm 0.03$
$\tau_e\tau_h$	$1.14 \pm 0.14 \pm 0.20 \pm 0.04$
$\tau_e\tau_\mu$	$1.06 \pm 0.14 \pm 0.08 \pm 0.04$
$\tau_\mu\tau_\mu$	$0.96 \pm 0.22 \pm 0.12 \pm 0.03$
$Z \to \tau\tau$	$0.97 \pm 0.07 \pm 0.06 \pm 0.03$

Chapter 6

Search for high-mass resonances decaying to $\tau^+\tau^-$

This chapter describes the first search for new physics in very high-mass ditau events at ATLAS with the 2011 dataset. No significant excess above the SM expectation is observed. The result is interpreted as an upper limit on the cross section times branching fraction to $\tau^+\tau^-$ vs mass for a high-mass resonance. A lower limit is set on the mass of a Sequential Standard Model Z' boson decaying to $\tau^+\tau^-$. The model dependence of these results is discussed.

6.1 Introduction

Many extensions of the Standard Model (SM), motivated by grand unification, predict additional U(1) gauge symmetries which result in new heavy gauge bosons, often denoted Z' [199, 52, 200, 201, 202, 203, 204, 205, 206, 207]. As lepton universality is not necessarily a requirement for these new gauge bosons, it is essential to search in all decay modes. In particular, some models with extended gauge groups that offer an explanation for the high mass of the top quark predict that such bosons preferentially couple to third-generation fermions [204, 208].

The Sequential Standard Model (SSM) is a benchmark model that contains a heavy neutral gauge boson, Z'_{SSM}, with the same couplings to fermions as the Z boson of the SM but with a larger mass. Limits on the cross section times $\tau^+\tau^-$ branching fraction for the Z'_{SSM} are reported as an example of a generic high-mass neutral resonance[63].

Direct searches for high-mass ditau resonances have been performed previously by the CDF [209] and CMS [210] collaborations, excluding a Z'_{SSM} with a mass less than 399 GeV and 468 GeV, at

[63] The model dependence of the limit is discussed in Section 6.7.4.

the 95% Confidence Level (CL)[64], respectively. With the 5 fb^{-1} of integrated luminosity at $\sqrt{s}$ = 7 TeV collected by the ATLAS and CMS expriments in 2011, both [211, 212] collaborations exclude a Z'_{SSM} with a mass less than 1.4 TeV, the ATLAS result being the the subject of this chapter. For comparison, the limits on Z'_{SSM} with the 2011 data from combined searches in the dielectron and dimuon decay channels combined is 2.2 TeV from ATLAS [213] and 2.3 TeV from CMS [214]. $Z' \to \ell\ell$ searches ($\ell = e$ or μ) with 8 TeV data collected in 2012 extended these exclusions to 2.86 TeV from ATLAS [215] and 2.96 TeV from CMS [216], which are currently the most stringent limits on Z' bosons.

Indirect limits on Z' bosons with non-universal flavour couplings have been set using measurements from LEP and LEP II [217] and translate to a lower bound on the Z'_{SSM} mass of 1.09 TeV.

This chapter presents the first search for high-mass resonances decaying into $\tau^+\tau^-$ pairs using the ATLAS detector. The analysis combines searches for $Z' \to \tau\tau$, where both taus decay hadronically ($\tau_{\mathrm{h}}\tau_{\mathrm{h}}$), one tau decays leptonically and the other hadronically ($\ell\tau_{\mathrm{h}}$), and where both taus decay leptonically to the $e\mu$ final state.

The $\tau_{\mathrm{h}}\tau_{\mathrm{h}}$ channel, having a large branching fraction of 42% of $\tau\tau$ decays, is the most sensitive. The $e\tau_{\mathrm{h}}$ and $\mu\tau_{\mathrm{h}}$ channels, with a branching fraction of 22% each for $\tau\tau$ decays, are generally more competitive in new physics searches at lower mass scales, such as for the $H \to \tau\tau$ search [29]. But since the SM backgrounds fall rapidly in reconstructed variables that measures of the mass of a resonance, the $\tau_{\mathrm{h}}\tau_{\mathrm{h}}$ channel contributes more in searches for high-mass new physics. The search gains sensitivity from combining the $\tau_{\mathrm{h}}\tau_{\mathrm{h}}$ and $\ell\tau_{\mathrm{h}}$ channels. The $e\mu$ channel has the weakest sensitivity for a $Z' \to \tau\tau$ because it only gets 2.9% of the branching fraction, but is a comparatively clean channel since the SM background does not involve fake hadronic tau decays.

First, the searches for $Z' \to \tau\tau$ in the $\ell\tau_{\mathrm{h}}$ channels are the focus of this chapter. Then the search in the $\tau_{\mathrm{h}}\tau_{\mathrm{h}}$ channel will be quickly reviewed[65].

6.2 Data samples

6.2.1 Data

In the year 2011, ATLAS recorded over 5 fb^{-1} of integrated luminosity[66], extending the potential for many searches for new physics. The instantaneous luminosity of the LHC climbed from 1×10^{30} to 3.7×10^{33} cm^{-2} s^{-1}, with the average number of interactions per bunch crossing typically ranging from 2 to 20 [114]. The searches for Z' discussed in this chapter use 4.6 fb^{-1} of data after

[64] The limit-setting procedure will be discussed briefly in Section 6.7.3.
[65] See Ref. [97] for more details on the $\tau_{\mathrm{h}}\tau_{\mathrm{h}}$ and $e\mu$ channels.
[66] See the discussion of the ATLAS running periods and datasets in Section 3.5.

making suitable data quality requirements[67] for the operation of the tracking, calorimetry, and muon spectrometer subsystems. Table 6.1 shows the data periods used in the analysis, the triggers used, and the corresponding integrated luminosity. The data were reconstructed with the ATLAS Athena framework [82] release 17, part of the `prod10` reprocessing. The data format used are D3PDs from the Tau Performance group with production tag `p851`.

6.2.2 Simulation

Monte Carlo samples used in this analysis were produced with the ATLAS simulation infrastructure [118] as part of the ATLAS `mc11c` production campaign. The Monte Carlo events were reweighted to match the distribution of the number of reconstructed primary vertices per bunch crossing in data, same as described in Section 5.3.2. Corrections applied to data or Monte Carlo for object reconstruction or trigger modelling are described in Ref. [97].

6.3 Object preselection

All channels use a common *preselection* of objects from the output of common ATLAS reconstruction, which is outlined here. Pre-selected objects are used for overlap removal, carried out in the order of muons, electrons, taus and jets, as described below.

[67] More details on the event-cleaning cuts are given in Ref. [97].

Table 6.1: Data periods, triggers, and the integrated luminosity for the four analysis channels. The $e\mu$ channel uses the same triggers as the $\mu\tau_{\mathrm{h}}$ channel [97].

Periods	Run numbers	EF Trigger	[pb^{-1}]
$\tau_{\mathrm{h}}\tau_{\mathrm{h}}$			
B-E	178109-180776	`EF_tau29_medium1_tau20_medium1` (loose)	215
F-K	182013-187815	`EF_tau29_medium1_tau20_medium1` (default)	2021
L-M	188921-191933	`EF_tau29T_medium1_tau20T_medium1`	2363
All	178109-191933	`EF_tau125_medium1`	4600
$\mu\tau_{\mathrm{h}}$ and $e\mu$			
D-I	179725-186493	`EF_mu18_MG or EF_mu40_MSonly_barrel`	1451
J-M	186516-191933	`EF_mu18_MG_medium or EF_mu40_MSonly_barrel_medium`	3142
$e\tau_{\mathrm{h}}$			
D-J	179725-186755	`EF_e20_medium`	1675
K	186873-187815	`EF_e22_medium`	555
L-M	188921-191933	`EF_e22vh_medium1`	2363

Table 6.2: Summary of object preselection [97].

Muons
StoreGate key: `StacoMuonCollection`
Tau D3PD prefix: `mu_staco_*`
$p_{\mathrm{T}} > 4$ GeV
$|\eta| < 2.5$
`mu_staco_loose == 1`
Require a B-layer hit if expected (`expectBLayerHit == 0 or nBLHits > 0`)
$N(\text{pixel hits}) + N(\text{pixel dead}) \geq 2$
$N(\text{SCT hits}) + N(\text{SCT dead}) \geq 6$
$N(\text{pixel holes}) + N(\text{SCT holes}) \leq 2$
TRT quality cuts:

```
if abs(eta) < 1.9:
    if not ( (nTRTHits + nTRTOutliers > 5) and \
            (nTRTOutliers < 0.9*(nTRTHits + nTRTOutliers))):
        return False
elif (nTRTHits + nTRTOutliers > 5):
    if not (nTRTOutliers < 0.9*(nTRTHits + nTRTOutliers)):
        return False
return True
```

Electrons
StoreGate key: `ElectronAODCollection`
Tau D3PD prefix: `el_*`
$p_{\mathrm{T}} > 15$ GeV
$|\eta| < 2.47$ and not in $1.37 < |\eta| < 1.52$
`el_author` is 1 or 3
`el_mediumPP == 1`
Require a B-layer hit if expected (`expectBLayerHit == 0 or nBLHits > 0`)

Hadronic tau decays
StoreGate key: `TauRecContainer`
Tau D3PD prefix: `tau_*`
$p_{\mathrm{T}} > 25$ GeV
$|\eta| < 2.47$ and not in $1.37 < |\eta| < 1.52$
lead track $|\eta| > 0.05$
`tau_author` is 1 or 3
`tau_numTrack > 0`
Remove candidates overlapping with preselected electrons or muons within $\Delta R < 0.2$

Jets
StoreGate key: `AntiKt4LCTopoJets`
Tau D3PD prefix: `jet_*`
$p_{\mathrm{T}} > 25$ GeV
$|\eta| < 4.5$
$|\mathrm{JVF}| > 0.75$ for jets with $|\eta| < 2.4$
Remove candidates overlapping with preselected electrons or *selected* taus within $\Delta R < 0.2$

6.3.1 Muons

Muon candidates considered were reconstructed with the Staco algorithm[68], which matches tracks reconstructed in the muon spectrometer to tracks found in the inner detector [69]. Muons with $|\eta| < 2.5$, $p_{\mathrm{T}} > 10$ GeV, and passing cuts according to the ATLAS Muon Performance Group recommendations [218] summarized in Table 6.2 were preselected.

6.3.2 Electrons

Electrons are reconstructed[69] in ATLAS by matching inner detector tracks to calorimeter clusters in the EM calorimeter [69]. Electron candidates are preselected if they have $p_{\mathrm{T}} > 15$ GeV, $|\eta| < 2.47$ and are not in the barrel—end-cap transition region region where $1.37 < |\eta| < 1.52$ (also called the "crack" region). The preselection also requires medium^{++} electron identification [88, 89], which has an electron efficiency of approximately 90% and a pion fake rate of 1-3% [90].

6.3.3 Hadronic tau decays

The reconstruction of hadronic tau decays at ATLAS was discussed in detail in Chapter 4. Tau candidates are preselected if they have $p_{\mathrm{T}} > 25$ GeV, $|\eta| < 2.47$ and not in the crack region where $1.37 < |\eta| < 1.52$, and have 1 or 3 core tracks. Core tracks are the tracks associated to the tau candidate, selected to be consistent with the vertex associated with the tau candidate, and within $\Delta R < 0.2$ of the tau axis, defined with respect to the η, ϕ of the calorimeter jet that seeded the tau candidate [101]. Tau candidates are removed from consideration if they overlap with preselected electron or muon candidates within $\Delta R < 0.2$. The final selections for jet rejection using the BDT, the allowed number of tracks, and the minimum p_{T} differ among channels, and are discussed in later sections.

6.3.4 Jets

Jets are reconstructed[70] with the anti-k_{t} algorithm [94], with distance parameter $R = 0.4$, and with three-dimensional topological energy clusters in the calorimeter [91] as input. The energy scale is calibrated with the local hadron calibration scheme (LC) [95], where the energy is split and corrected for each cluster in a jet [93]. Jets are preselected if they have $p_{\mathrm{T}} > 25$ GeV and $|\eta| < 4.5$.

Especially for the highest luminosity runs in the later part of 2011, it is not rare for secondary pile-up interactions to produce jets. For jets within the tracking acceptance, one can select jets with

[68] Muon reconstruction is introduced briefly in Section 3.3.3.
[69] Electron reconstruction is introduced briefly in Section 3.3.4.
[70] Jet reconstruction is introduced briefly in Section 3.3.6.

energy deposits consistent with coming from the primary reconstructed vertex by requiring a high JVF, discussed in Section 3.3.6. Jets within $|\eta| < 2.4$ are required to have $|\text{JVF}| > 0.75$. Finally, in each channel jet candidates are removed that overlap with *preselected* electron or *selected* hadronic tau candidates within $\Delta R < 0.2$, where the final tau selection depends on the channel[71]

6.3.5 Missing transverse energy

The signal events are characterized by true missing transverse momentum ($E_{\text{T}}^{\text{miss}}$) due to the presence of neutrinos. This analysis uses the ATLAS refined $E_{\text{T}}^{\text{miss}}$ reconstruction (`MET_RefFinal_BDTMedium`), where the $E_{\text{T}}^{\text{miss}}$ is calculated from the vector sum of the transverse momentum of all the high-p_{T} objects reconstructed in the event, as well as a term for the remaining soft activity in the calorimeter. In the refined calculation scheme [105], each type of object is calibrated independently (electrons, muons, taus, etc.), with tau candidates calibrated at the tau energy scale if they pass the `JetBDTSigMedium` identification criteria.

6.4 Search in the $\ell\tau_{\text{h}}$ channels

6.4.1 Triggering

For the search in the $\ell\tau_{\text{h}}$ channels, events passing single-lepton triggers were selected. The analysis of the $\mu\tau_{\text{h}}$ channel required events to pass the following unprescaled single muon triggers:

- `EF_mu18_MG or EF_mu40_MSonly_barrel` for data in periods D-I,
- `EF_mu18_MG_medium or EF_mu40_MSonly_barrel_medium` for data in periods J-M.

The first trigger requires a combined muon with $p_{\text{T}} \gtrsim 20$ GeV, while the second trigger only requires a candidate in the muon spectrometer and has slower turn-on with p_{T}. Together, the trigger requirements have approximately 80% efficiency in the barrel and 90% efficiency in the end-caps, limited mainly by geometric acceptance [219].

The search in the $e\tau_{\text{h}}$ channel required events to pass the following unprescaled single electron triggers for a loosely identified electron with $p_{\text{T}} \gtrsim 15$ GeV:

- `EF_e20_medium` for data in periods D-J,
- `EF_e22_medium` for data in period K,
- `EF_e22vh_medium1` for data in periods L-M,

[71] Selected jets are only used in this analysis directly in the jet-veto of the $e\mu$ channel, however, tau candidates failing identification, which essentially define the selected jet candidates not overlapping with taus, are considered in the data-driven background estimations used in these analyses.

which have efficiencies [220] between 94–98% for electrons passing `el_tightPP`.

6.4.2 Object selection

Objects are preselected as discussed in Section 6.3. Before exploring the event selection, requirements are further made of the lepton and hadronic tau candidates, defining *selected* leptons and taus. Preselected leptons are used in the overlap removal done for tau preselection, and they are used later in the event selection to veto on the presence of additional leptons.

Muon selection

For the $\mu\tau_{\text{h}}$ channel, selected muons are defined as those with

- $p_{\text{T}} > 25$ GeV,
- having a combined muon spectrometer and inner detector offline candidate (`mu_staco_isCombinedMuon == 1`),
- `etcone20`$/p_{\text{T}} < 4\%$.

To suppress the presence of leptons produced in jets, the calorimeter isolation requirement listed above is required, where `etcone20` denotes the sum of the transverse energy of the calorimeter cells within $\Delta R < 0.2$ of the muon track.

Electron selection

For the $e\tau_{\text{h}}$ channel, selected electrons are defined as those with

- $p_{\text{T}} > 30$ GeV,
- passing tight electron identification (`el_tightPP == 1`).

To suppress real or fake electrons produced in jets, the following calorimeter and tracking isolation cuts are applied to selected electrons:

- $\begin{cases} \text{corrected } \texttt{etcone20}/p_{\text{T}} < 5\% & \text{if } p_{\text{T}} < 100 \text{ GeV} \\ \text{corrected } \texttt{etcone20} < 5 \text{ GeV} & \text{if } p_{\text{T}} \geq 100 \text{ GeV} \end{cases}$,
- `ptcone40`$/p_{\text{T}} < 5\%$,

where `etcone20` denotes the sum of the transverse energy of the calorimeter cells within $\Delta R < 0.2$ of the electron track, corrected for leakage with a p_{T}-dependent correction and for pile-up with an N(vertex)-dependent correction [221]. The variable `ptcone40` denotes the sum of the p_{T} of tracks

with $p_{\mathrm{T}} > 1$ GeV, within $\Delta R < 0.4$ of the electron track, and associated to the same vertex as the electron candidate. The vertex requirement makes the track-based isolation inherently more robust against pile-up than the calorimeter-based isolation, and can therefore utilize a larger ΔR-cone. Beginning for electrons with $p_{\mathrm{T}} > 100$ GeV, the p_{T}-dependent calorimeter isolation requirement becomes a constant cut on the magnitude of the isolation measures.

Hadronic tau selection

The $\ell\tau_{\mathrm{h}}$ channels use only 1-prong hadronic tau candidates which comprise 50% of the tau decay branching fraction (80% of the hadronic tau decay branching fraction) and better signal purity than 3-prong decays. 3-prong tau decays also have poor reconstruction efficiency that is falling with p_{T} as it becomes harder to reconstruct each of the 3 collimated tracks, as discussed in Section 4.4.7.

Tau candidates are required to have $p_{\mathrm{T}} > 35$ GeV and pass a BDT selection optimized for rejecting jets (the medium working point). In addition to not overlapping with preselected muons, tau candidates must pass the ATLAS cut-based muon veto, which requires a loose matching between the track momentum and calorimeter energy by having a low f_{track}, but only for candidates that have EM fraction, f_{EM}, near 0 or 1 [102]. The f_{EM} must also be greater than 0.1 if the visible mass of the lepton and tau candidate are near the Z peak [97].

For the $e\tau_{\mathrm{h}}$ channel, to suppress the rate of electrons faking taus, we use the medium ATLAS BDT-based electron veto discussed in Section 4.3.5. Since the dominant background source of true electrons, $Z \to ee$, falls quickly with p_{T}, the loose veto is used for tau candidates with $p_{\mathrm{T}} > 100$ GeV.

A final cleaning cut removes tau candidates from consideration that are very near $\eta \approx 0$, where there is a small crack dividing the A and C sides of the inner detector and calorimeter barrels. A large fraction of reconstructed hadronic tau candidates in this region are faked by electrons that are not removed by overlap removal due to poor electron identification in this region and poor efficiency for high-threshold hits in the TRT. Tau candidates with leading tracks within $|\eta| < 0.05$ are vetoed.

The hadronic tau selection can be summarized as

- $p_{\mathrm{T}} > 35$ GeV.
- 1 core-track,
- `tau_JetBDTSigMedium == 1`,
- `tau_muonVeto == 0`,
- $f_{\mathrm{EM}} > 0.1$ if $80\,\mathrm{GeV} < m(\mu, \tau_{\mathrm{h}}) < 100\,\mathrm{GeV}$, (only for the $\mu\tau_{\mathrm{h}}$ channel)

- $\begin{cases} \texttt{tau\_EleBDTMedium == 0} & \text{if } p_{\mathrm{T}} < 100 \text{ GeV} \\ \texttt{tau\_EleBDTLoose == 0} & \text{if } p_{\mathrm{T}} \geq 100 \text{ GeV} \end{cases}$, (only for the $e\tau_{\mathrm{h}}$ channel)
- lead track $|\eta| > 0.05$.

6.4.3 Event selection

The *event preselection* defining the kinematic region explored is: events with exactly one selected electron or muon, no additional preselected electrons or muons (see Section 6.3), and having exactly one selected 1-prong hadronic tau decay.

Distributions of kinematic variables for the $\mu\tau_{\mathrm{h}}$ channel are shown in Figures 6.1 and 6.2. Distributions for the $e\tau_{\mathrm{h}}$ channel are shown in Figures 6.3 and 6.4. The plots in this section show the estimated background composition, using data-driven methods for the multijet and W/Z + jets backgrounds, and Monte Carlo simulation to predict the remaining backgrounds. The plots of the ratio of the observed over the expected counts contain bands meant to help visualize the dominant systematic uncertainties, as discussed in Section 6.6.

Hypothetical $Z' \to \tau\tau$ events produce high-p_{T} tau decay products that are back-to-back in the transverse plane. Figure 6.1 (top) shows the distribution of the absolute difference in ϕ between the selected muon and hadronic tau. Events with back-to-back candidates are selected by requiring $|\Delta\phi(\mu, \tau_{\mathrm{h}})| > 2.7$. Next, the hadronic tau and the muon are required to have opposite sign charges. Figure 6.1(middle) shows the distribution of the product of the charges of the selected muon and hadronic tau.

Because the sample of electrons is less pure than muons, and because electrons fake tau candidates more readily than muons, the $e\tau_{\mathrm{h}}$ channel has more significant fake backgrounds than $\mu\tau_{\mathrm{h}}$. Additional event-level cuts were chosen for the $e\tau_{\mathrm{h}}$ channel[72]. The $Z \to ee$ and multijet contributions are reduced to a negligible level by requiring $E_{\mathrm{T}}^{\mathrm{miss}} > 30$ GeV. The W + jets background is suppressed by requiring $m_{\mathrm{T}} < 50$ GeV, where m_{T} is the transverse mass of the electron-$E_{\mathrm{T}}^{\mathrm{miss}}$ system, defined as

$$m_{\mathrm{T}}(e, E_{\mathrm{T}}^{\mathrm{miss}}) = \sqrt{2\, p_{\mathrm{T}}(e)\, p_{\mathrm{T}}(\tau_{\mathrm{h}})(1 - \cos\Delta\phi)}\,,$$

where $\Delta\phi$ is the angle between the electron and $E_{\mathrm{T}}^{\mathrm{miss}}$ in the transverse plane.

This summarizes our *baseline event selection*. It provides a region dominated by $Z \to \tau\tau$ and W/Z + jets, without yet focusing on high-mass events. The total transverse mass of the four-vector sum of the muon, the hadronic tau decay, and the missing transverse momentum, $m_{\mathrm{T}}^{\mathrm{tot}}(\ell, \tau_{\mathrm{h}}, E_{\mathrm{T}}^{\mathrm{miss}})$, is calculated.

[72] An updated result with the 2012 analysis will proabably harmonize the $\ell\tau_{\mathrm{h}}$ event selection. Part of the reason the $\mu\tau_{\mathrm{h}}$ and $e\tau_{\mathrm{h}}$ channels have different selections, is that they were approved in succession and not together.

The data were blinded in the regions where,

- $p_{\mathrm{T}}(\tau_{\mathrm{h}}) > 140$ GeV,
- or $p_{\mathrm{T}}(\ell) > 140$ GeV,
- or $E_{\mathrm{T}}^{\mathrm{miss}} > 140$ GeV,
- or $m_{\mathrm{T}}^{\mathrm{tot}}(\ell, \tau_{\mathrm{h}}, E_{\mathrm{T}}^{\mathrm{miss}}) > 300$ GeV,

to verify that the background modeling is well controlled outside of a high-mass signal region, and then the selections were frozen.

After the baseline event selection, a cut on $m_{\mathrm{T}}^{\mathrm{tot}}$ was optimized to give the best expected upper limit, as described later in Section 6.7, on the strength parameter of a SSM Z' in bins of its mass. The primary signal region which excludes the highest Z'_{SSM} mass at the 95% confidence level requires $m_{\mathrm{T}}^{\mathrm{tot}} > 600$ GeV for the $\mu\tau_{\mathrm{h}}$ channel and $m_{\mathrm{T}}^{\mathrm{tot}} > 500$ GeV for the $e\tau_{\mathrm{h}}$ channel, with cuts stepping down to 400 GeV to exclude lower masses most effectively, as shown in Table 6.6.

The event selection can be summarized as

1. exactly one selected muon
2. no additional preselected electrons or muons
3. exactly one selected 1-prong hadronic tau decay
4. $|\Delta\phi(\ell, \tau_{\mathrm{h}})| > 2.7$
5. opposite sign charges for the ℓ and τ_{h}
6. $E_{\mathrm{T}}^{\mathrm{miss}} > 30$ GeV (only for the $e\tau_{\mathrm{h}}$ channel)
7. $m_{\mathrm{T}}(e, E_{\mathrm{T}}^{\mathrm{miss}}) < 50$ GeV (only for the $e\tau_{\mathrm{h}}$ channel)
8. $m_{\mathrm{T}}^{\mathrm{tot}}(\ell, \tau_{\mathrm{h}}, E_{\mathrm{T}}^{\mathrm{miss}}) > 400$–$600$ GeV (depending on the signal mass)

Table 6.3 shows the number of events passing each step in the event selection with the predictions for each background. Table 6.4 shows the signal expectations passing high-mass thresholds on $m_{\mathrm{T}}^{\mathrm{tot}}$.

6.4.4 Background estimation

Overview

The dominant backgrounds involving fake hadronic tau decays from multijet and W+jets events are modeled in data-driven ways. Data-driven estimates are required because the rate for jets to pass tau identification is mis-modeled by the ATLAS full simulation, as discussed briefly in Section 4.4.1.

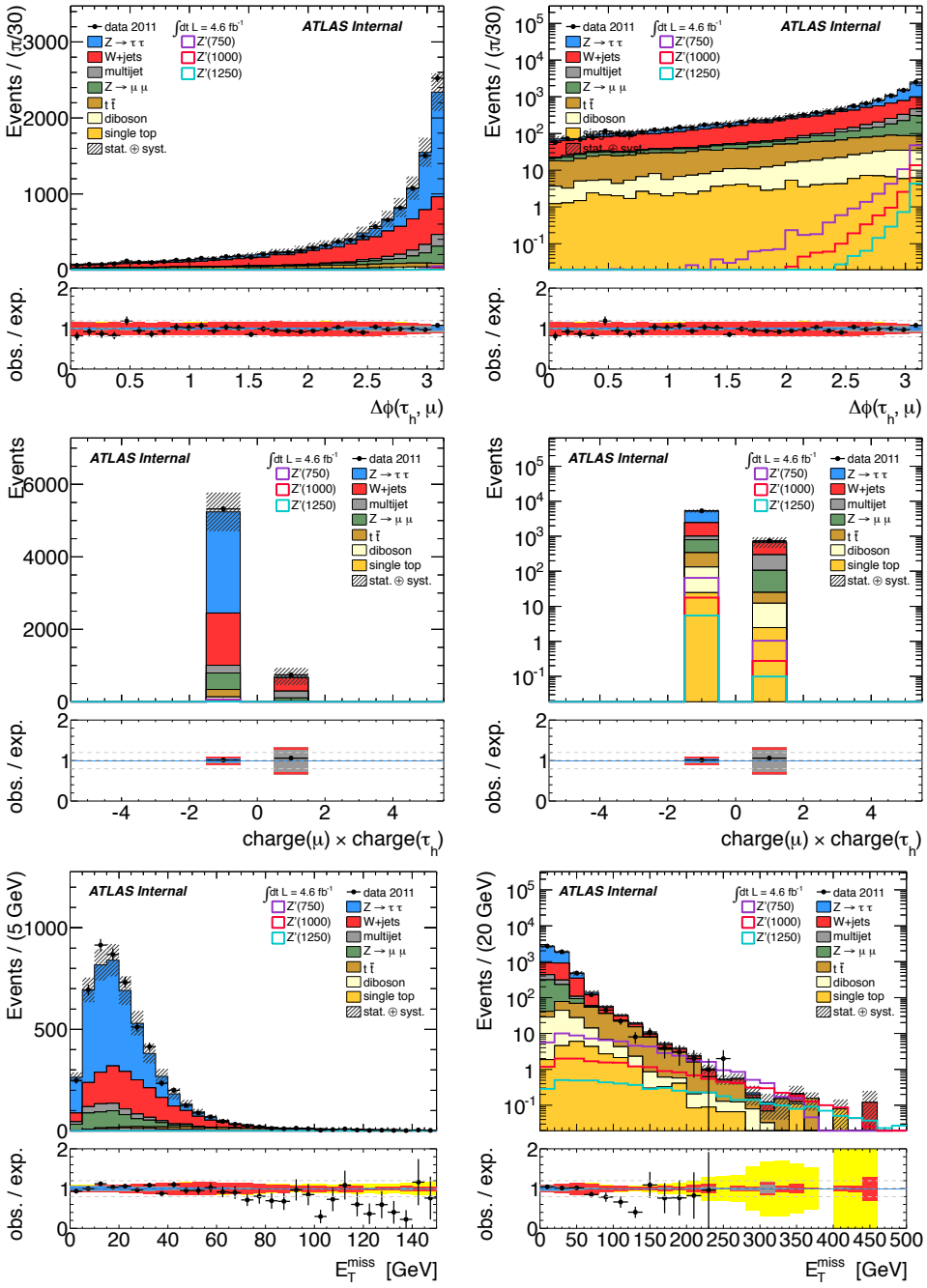

Figure 6.1: Kinematic distributions for the $\mu\tau_{\mathrm{h}}$ channel. (top) The distribution of the absolute difference in ϕ between the selected muon and tau candidate in events with exactly one selected muon, no additional preselected electrons or muons, and exactly one selected 1-prong tau. (middle) The distribution of the product of the reconstructed charges of the selected electron and tau candidate in events with the event preselection listed above, and requiring $\Delta\phi(\mu, \tau_{\mathrm{h}}) > 2.7$. (bottom) The distribution of the $E_{\mathrm{T}}^{\mathrm{miss}}$ in events with the above selection, and requiring opposite-sign charges for the μ and τ_{h} (the $\mu\tau_{\mathrm{h}}$ baseline event selection) [97].

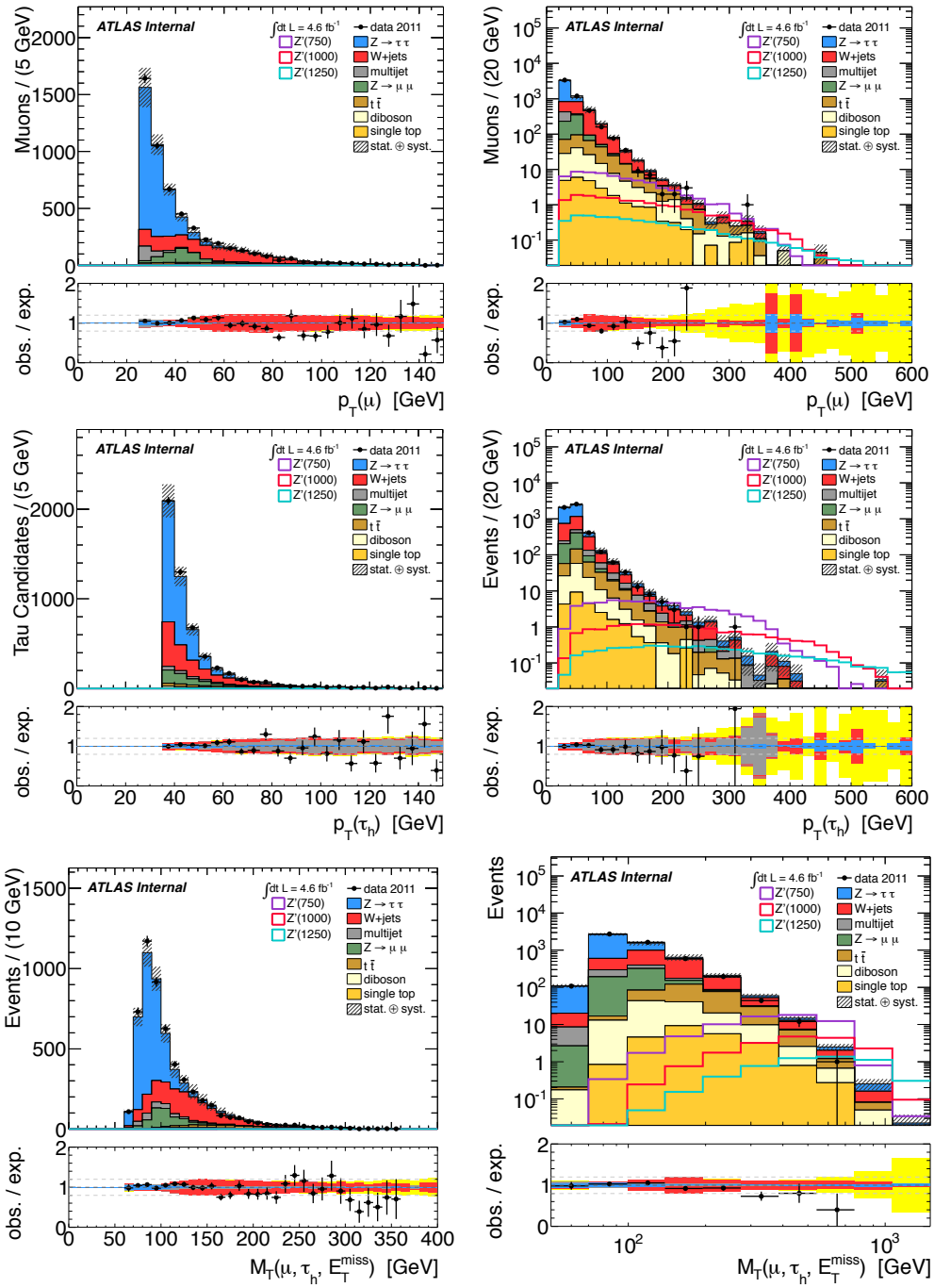

Figure 6.2: Kinematic distributions for the $\mu\tau_{\mathrm{h}}$ channel. (top) The distribution of $p_{\mathrm{T}}(\mu)$, (middle) the distribution of $p_{\mathrm{T}}(\tau_{\mathrm{h}})$, and (bottom) the distribution of $m_{\mathrm{T}}^{\mathrm{tot}}(\mu, \tau_{\mathrm{h}}, E_{\mathrm{T}}^{\mathrm{miss}})$ in events passing the $\mu\tau_{\mathrm{h}}$ baseline event selection ($M_{\mathrm{T}} \equiv m_{\mathrm{T}}^{\mathrm{tot}}$) [97].

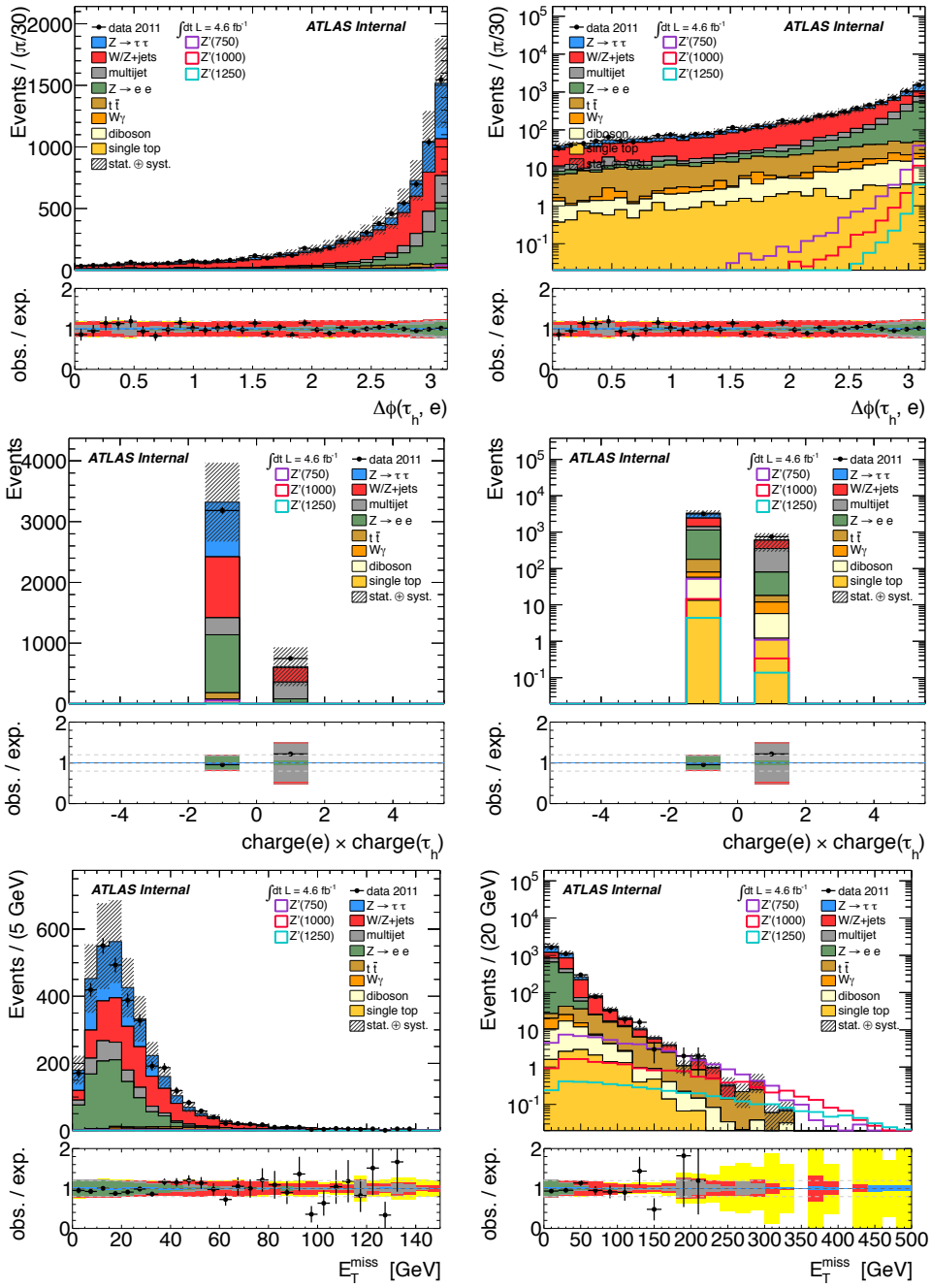

Figure 6.3: Kinematic distributions for the $e\tau_{\mathrm{h}}$ channel. (top) The distribution of the absolute difference in ϕ between the selected electron and tau candidate in events with exactly one selected electron, no additional preselected electrons or muons, and exactly one selected 1-prong tau. (middle) The distribution of the product of the reconstructed charges of the selected electron and tau candidate in events with the event preselection listed above, and requiring $\Delta\phi(e, \tau_{\mathrm{h}}) > 2.7$. (bottom) The distribution of the $E_{\mathrm{T}}^{\mathrm{miss}}$ in events with the above selection, and requiring opposite-sign charges for the e and τ_{h} [97].

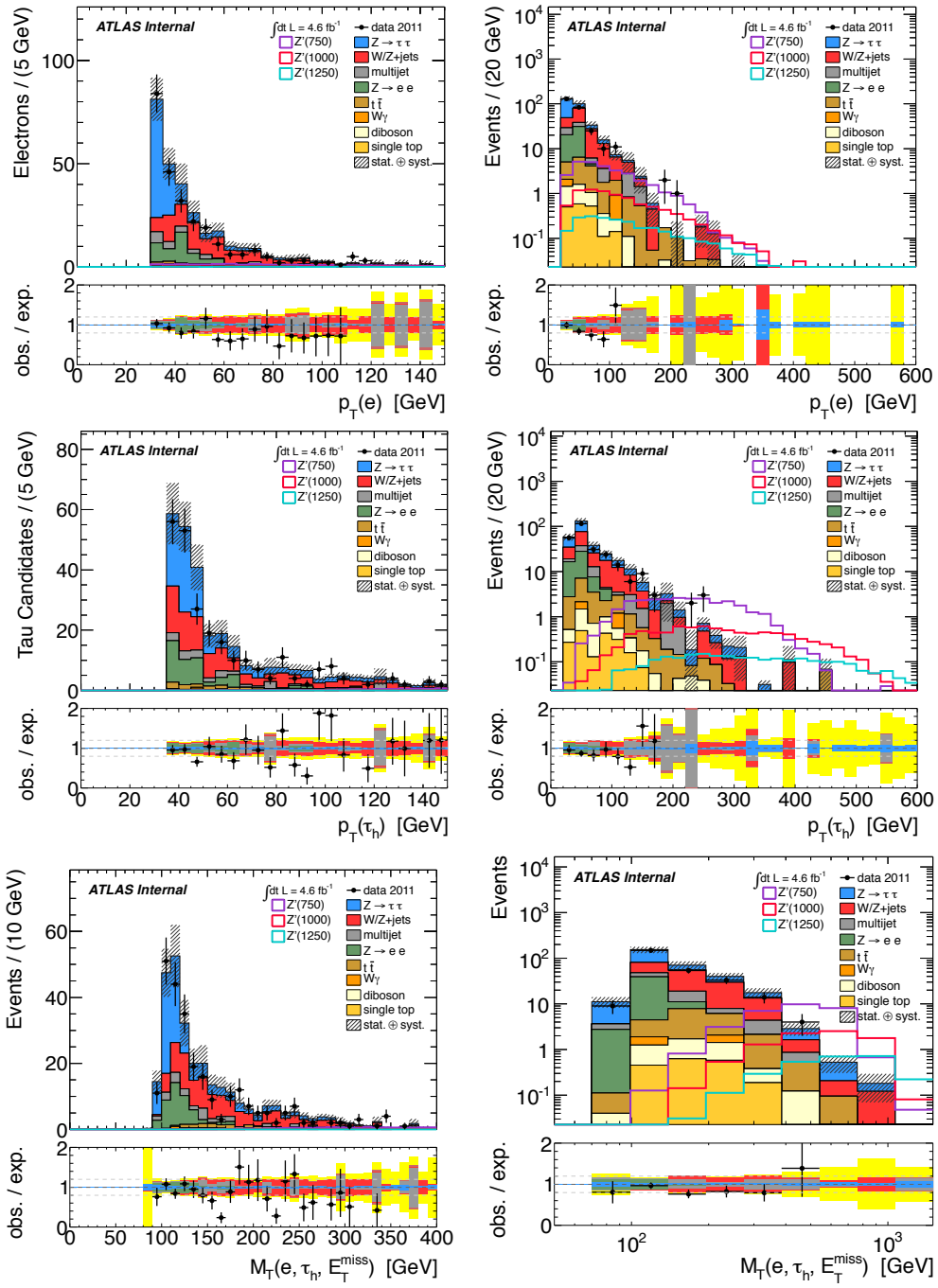

Figure 6.4: Kinematic distributions for the $e\tau_{\mathrm{h}}$ channel. (top) The distribution of $p_{\mathrm{T}}(e)$, (middle) the distribution of $p_{\mathrm{T}}(\tau_{\mathrm{h}})$, and (bottom) the distribution of $m_{\mathrm{T}}^{\mathrm{tot}}(e, \tau_{\mathrm{h}}, E_{\mathrm{T}}^{\mathrm{miss}})$ in events passing the $e\tau_{\mathrm{h}}$ baseline event selection ($M_{\mathrm{T}} \equiv m_{\mathrm{T}}^{\mathrm{tot}}$) [97].

Table 6.3: The number of events passing each step in the event selection of the $\ell\tau_{\mathrm{h}}$ channels. The numbers in parentheses denote the statistical uncertainty in the least significant digits [97].

$\mu\tau_{\mathrm{h}}$ channel	data	total SM	$Z \to \tau\tau$	W+jets	multijet	$Z \to \mu\mu$	$t\bar{t}$	diboson	single top	$Z'(1000)$
one μ, one τ_{h}	11605	11653(47)	3867(35)	4913(21)	583(5)	897(21)	963(7)	323(4)	108(3)	18.7(2)
$\lvert\Delta\phi(\mu,\tau_{\mathrm{h}})\rvert > 2.7$	6061	5941(38)	2829(31)	1811(14)	403(4)	533(17)	221(3)	117(2)	27(1)	17.9(2)
opposite sign μ and τ_{h}	5320	5242(37)	2791(31)	1446(13)	213(3)	452(16)	208(3)	107(2)	24(1)	17.6(2)
$m_{\mathrm{T}}^{\mathrm{tot}} > 200$ GeV	229	263(5)	30.0(5)	114(4)	5.5(4)	5(1)	76(2)	22.3(8)	9.4(9)	16.5(2)
$m_{\mathrm{T}}^{\mathrm{tot}} > 300$ GeV	31	53(2)	7.3(2)	18(2)	0.6(1)	0.3(2)	17.6(9)	6.7(6)	3.0(5)	14.1(2)
$m_{\mathrm{T}}^{\mathrm{tot}} > 400$ GeV	13	15(1)	2.31(5)	5.0(8)	0.15(7)	0.1(1)	4.5(4)	1.7(2)	0.9(3)	11.0(2)
$m_{\mathrm{T}}^{\mathrm{tot}} > 500$ GeV	1	4.5(5)	0.82(3)	1.6(5)	0.02(2)	< 0.1	1.2(2)	0.6(1)	0.3(2)	8.0(1)
$m_{\mathrm{T}}^{\mathrm{tot}} > 600$ GeV	1	1.4(3)	0.36(2)	0.3(2)	< 0.01		0.3(1)	0.23(7)	0.2(1)	5.5(1)
$m_{\mathrm{T}}^{\mathrm{tot}} > 700$ GeV	1	0.5(1)	0.17(1)	0.07(7)			0.03(3)	0.13(5)	0.1(1)	3.38(9)

$e\tau_{\mathrm{h}}$ channel	data	total SM	$Z \to \tau\tau$	W/Z+jets	multijet	$Z \to ee$	$t\bar{t}$	$W\gamma$	diboson	single top	$Z'(1000)$
one e, one τ_{h}	7295	7270(51)	1340(20)	3251(21)	766(22)	1280(35)	402(4)	68(6)	115(2)	49(2)	15.6(2)
$\lvert\Delta\phi(e,\tau_{\mathrm{h}})\rvert > 2.7$	3929	3933(43)	918(17)	1242(15)	556(18)	1020(32)	106(2)	28(4)	48(1)	15(1)	14.9(2)
opposite sign e and τ_{h}	3183	3322(40)	902(17)	1004(14)	279(13)	958(31)	99.9(2)	22(4)	44(1)	13.3(9)	14.6(2)
$E_{\mathrm{T}}^{\mathrm{miss}} > 30$ GeV	832	817(15)	158(6)	388(8)	39(6)	101(10)	85(2)	9(2)	26.8(9)	10.7(9)	12.8(2)
$m_{\mathrm{T}}(e, E_{\mathrm{T}}^{\mathrm{miss}}) < 50$ GeV	263	298(10)	113(5)	101(5)	22(4)	41(6)	15.1(7)	1.3(9)	3.1(2)	1.9(3)	8.7(1)
$m_{\mathrm{T}}^{\mathrm{tot}} > 200$ GeV	46	59(4)	15.6(7)	31(2)	4(2)	0.03(2)	5.7(5)	0.6(6)	1.1(1)	0.8(2)	8.5(1)
$m_{\mathrm{T}}^{\mathrm{tot}} > 300$ GeV	14	14(2)	4.4(3)	6(1)	2(1)	0.02(2)	1.4(2)	< 0.1	0.29(7)	0.11(8)	7.7(1)
$m_{\mathrm{T}}^{\mathrm{tot}} > 400$ GeV	4	3.0(8)	1.42(4)	0.8(6)	0.3(3)	< 0.01	0.4(1)		0.14(5)	< 0.1	6.5(1)
$m_{\mathrm{T}}^{\mathrm{tot}} > 500$ GeV	0	1.6(4)	0.57(2)	0.8(4)	< 0.1		0.13(7)		0.06(3)		5.0(1)
$m_{\mathrm{T}}^{\mathrm{tot}} > 600$ GeV	0	0.5(2)	0.23(2)	0.2(2)			0.04(4)		0.02(2)		3.67(9)

Table 6.4: The number of expected SM and signal events passing possible $m_{\mathrm{T}}^{\mathrm{tot}}$ cuts in the $\ell\tau_{\mathrm{h}}$ channels. The numbers in parentheses denote the statistical uncertainty in the least significant digits. The bold numbers denote the expected signal for the chosen mass cuts shown in Table 6.6 [97].

$\mu\tau_{\mathrm{h}}$ channel	total SM	$Z'(500)$	$Z'(625)$	$Z'(750)$	$Z'(875)$	$Z'(1000)$	$Z'(1125)$	$Z'(1250)$	$Z'(1375)$	$Z'(1500)$	$Z'(1625)$	$Z'(1750)$
$m_{\mathrm{T}}^{\mathrm{tot}} > 400$ GeV	15(1)	**42(1)**	**44(1)**	29.1(5)	17.4(4)	11.0(2)	6.1(1)	3.94(5)	2.35(4)	1.39(3)	0.85(2)	0.52(1)
$m_{\mathrm{T}}^{\mathrm{tot}} > 500$ GeV	4.5(5)	5.8(5)	18.1(9)	**17.0(4)**	**11.5(3)**	8.0(1)	4.7(1)	3.14(5)	1.94(4)	1.17(2)	0.73(1)	0.450(9)
$m_{\mathrm{T}}^{\mathrm{tot}} > 600$ GeV	1.4(3)	1.0(2)	3.9(4)	8.3(3)	6.9(2)	**5.5(1)**	**3.38(9)**	**2.36(4)**	**1.55(4)**	**0.96(2)**	**0.60(1)**	**0.374(8)**
$m_{\mathrm{T}}^{\mathrm{tot}} > 700$ GeV	0.5(1)	0.3(1)	1.0(2)	2.3(1)	3.4(2)	3.38(9)	2.38(8)	1.78(4)	1.19(3)	0.76(2)	0.48(1)	0.314(7)

$e\tau_{\mathrm{h}}$ channel	total SM	$Z'(500)$	$Z'(625)$	$Z'(750)$	$Z'(875)$	$Z'(1000)$	$Z'(1125)$	$Z'(1250)$	$Z'(1375)$	$Z'(1500)$	$Z'(1625)$	$Z'(1750)$
$m_{\mathrm{T}}^{\mathrm{tot}} > 400$ GeV	3.0(8)	**32(1)**	**28(1)**	**17.7(4)**	10.5(3)	6.5(1)	3.6(1)	2.15(4)	1.24(3)	0.75(2)	0.46(1)	0.283(7)
$m_{\mathrm{T}}^{\mathrm{tot}} > 500$ GeV	1.6(4)	5.0(5)	12.3(7)	11.1(3)	**7.9(3)**	**5.0(1)**	**2.88(9)**	**1.82(4)**	**1.07(3)**	**0.65(2)**	**0.41(1)**	**0.258(7)**
$m_{\mathrm{T}}^{\mathrm{tot}} > 600$ GeV	0.5(2)	0.7(2)	3.7(4)	5.5(2)	5.2(2)	3.67(9)	2.25(8)	1.45(3)	0.90(3)	0.55(2)	0.35(1)	0.223(6)

The multijet and W/Z + jets backgrounds are estimated with data-driven techniques involving fake factors parameterizing the rate for jets to fake lepton isolation and tau identification. The fake-factor method populates the tail of the background model with high-mass events from data, that typically outnumber the contribution of that background to the signal region because more events fail the tau identification or lepton isolation than pass. Fake factor methods have precedence in other ATLAS analyses, including using fake factors for muon isolation and electron identification to predict the W+jets background to $WW \to \ell\ell$ [222, 223]. A fake-factor method is also used in the ATLAS search for exotic excesses in same-sign dileptons [224].

The remaining backgrounds considered ($Z \to \tau\tau$, $Z \to \mu\mu$, $t\bar{t}$, single top, and diboson) are modeled with ATLAS fully simulated Monte Carlo samples.

Multijet background

The background from multijet events is demonstrated to be negligible at high $m_{\mathrm{T}}^{\mathrm{tot}}$, but it is also important to model its contribution at lower mass for modeling control regions. Multijet events are unique among our backgrounds because the leptons produced in jets are often not isolated in the calorimeter. The ratio of the number of isolated leptons to the number of non-isolated leptons in a multijet-rich region of data (*multijet control region* or multijet–CR) is measured, and used to predict the number of leptons from multijet events passing isolation requirements. The multijet–CR is defined as

- exactly one selected lepton ignoring the isolation requirements,
- no additional preselected electrons or muons
- at least one preselected hadronic tau candidate,
- zero selected 1-prong hadronic tau candidates,
- $E_{\mathrm{T}}^{\mathrm{miss}} < 30$ GeV,
- $m_{\mathrm{T}}(\ell, E_{\mathrm{T}}^{\mathrm{miss}}) < 30$ GeV,
- $|d_0(\mu)| > 0.08$ mm (only in the $\mu\tau_{\mathrm{h}}$ channel).

The selected leptons in this control sample are then divided into two categories: those that pass and those that fail the lepton isolation requirements discussed in Section 6.4.2. These are used to define a *fake factor*, $f_{\ell\text{–iso}}$, for lepton isolation as the number of isolated leptons in the data, divided by the number of non-isolated leptons, binned in p_{T} and η:

$$f_{\ell\text{–iso}}(p_{\mathrm{T}}, \eta) \equiv \left. \frac{N^{\text{pass } \ell\text{–iso}}(p_{\mathrm{T}}, \eta)}{N^{\text{fail } \ell\text{–iso}}(p_{\mathrm{T}}, \eta)} \right|_{\text{multijet–CR}} .$$

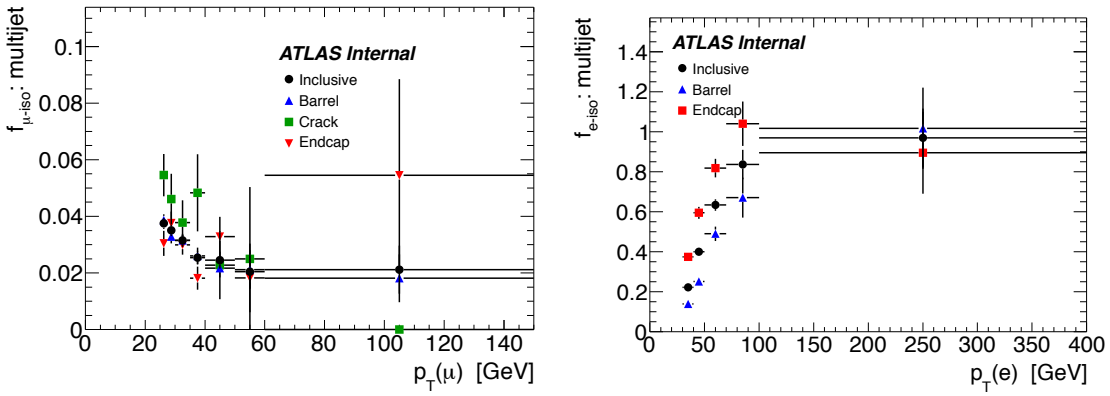

Figure 6.5: Lepton isolation fake factors derived in the multijet control region for the $\mu\tau_{\text{h}}$ channel (left) and the $e\tau_{\text{h}}$ channel (right)[97].

The lepton isolation fake factors are shown in Figure 6.5.

The number of multijet events passing lepton isolation and event selections is predicted by multiplying the number of events that fail isolation but pass all other selection criteria by fake factors binned in p_{T} and η:

$$N_{\text{multijet}}(p_{\text{T}}, \eta, x) = f_{\ell\text{–iso}}(p_{\text{T}}, \eta) \cdot N_{\text{multijet}}^{\text{fail } \ell\text{–iso}}(p_{\text{T}}, \eta, x)\,.$$

The sample of non-isolated leptons in the data is corrected by subtracting the expected contamination of electroweak processes in Monte Carlo:

$$N_{\text{multijet}}(p_{\text{T}}, \eta, x) = f_{\ell\text{–iso}}(p_{\text{T}}, \eta) \cdot \left(N_{\text{data}}^{\text{fail } \ell\text{–iso}}(p_{\text{T}}, \eta, x) - N_{\text{MC}}^{\text{fail } \ell\text{–iso}}(p_{\text{T}}, \eta, x)\right).$$

This correction is approximately 3% of the number of isolated muons, 25% of the number of isolated electrons, and negligible for the number of non-isolated leptons. Since this relation is true, bin-by-bin, the shape of the multijet background in any kinematic variable, $x \in \{\Delta\phi, m_{\text{T}}^{\text{tot}}, \ldots\}$, is modeled from the events in the data with non-isolated leptons, with Monte Carlo modeling the other contamination subtracted.

Figure 6.6 shows the multijet estimate in the distributions of $m_{\text{T}}(\ell, E_{\text{T}}^{\text{miss}})$ and $d_0(\ell)$, after the event preselection, where it is 583 ± 5 (stat.) events, or 5% of the expected background in the $\mu\tau_{\text{h}}$ channel, and 766 ± 22 (stat.) events, or 10% of the expected background in the $e\tau_{\text{h}}$ channel. In Figure 6.6 (bottom-right), tau identification and electron veto requirements are also loosened.

After baseline event selection in the $\mu\tau_{\text{h}}$ channel, the expected multijet background falls to less than 0.02 of an event for events with $m_{\text{T}}^{\text{tot}} \gtrsim 500$ GeV, and it is therefore considered negligible in the signal region with $m_{\text{T}}^{\text{tot}}(\mu, \tau_{\text{h}}, E_{\text{T}}^{\text{miss}}) > 600$ GeV, as is also shown in Figure 6.7 (left).

This method assumes that the ratio of the number of isolated leptons to the number of non-isolated leptons in multijet events is not strongly correlated with the cuts used to enrich the multijet

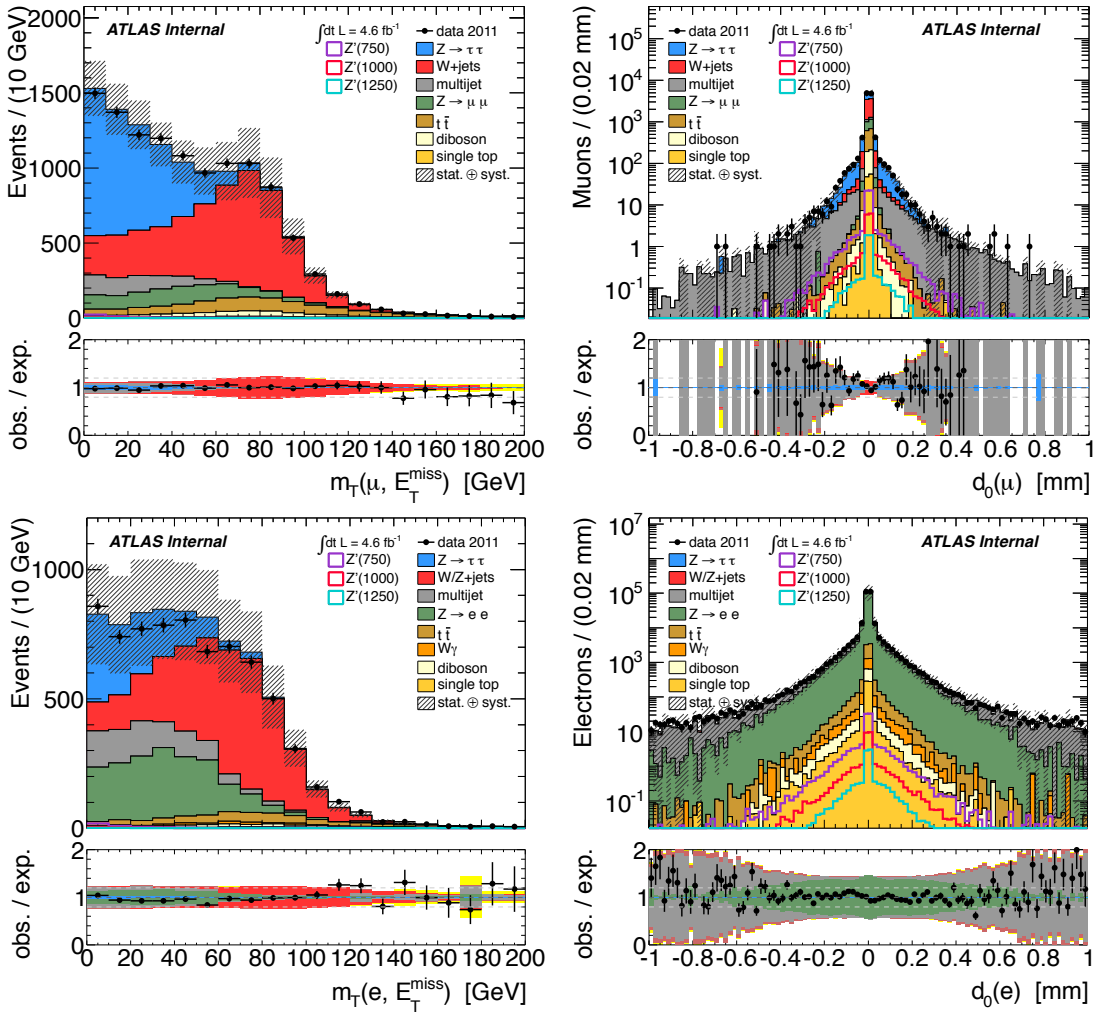

Figure 6.6: (left) The distribution of the transverse mass of the combination of the selected lepton and the $E_{\mathrm{T}}^{\mathrm{miss}}$, $m_{\mathrm{T}}(\ell, E_{\mathrm{T}}^{\mathrm{miss}})$. (right) The distribution of the impact parameter, d_0 of the selected lepton. These plots include the requirements of: exactly one selected muon, no additional preselected electrons or muons, and exactly one selected 1-prong tau, except the (bottom-right) has the tau identification completely removed including the electon-veto [97].

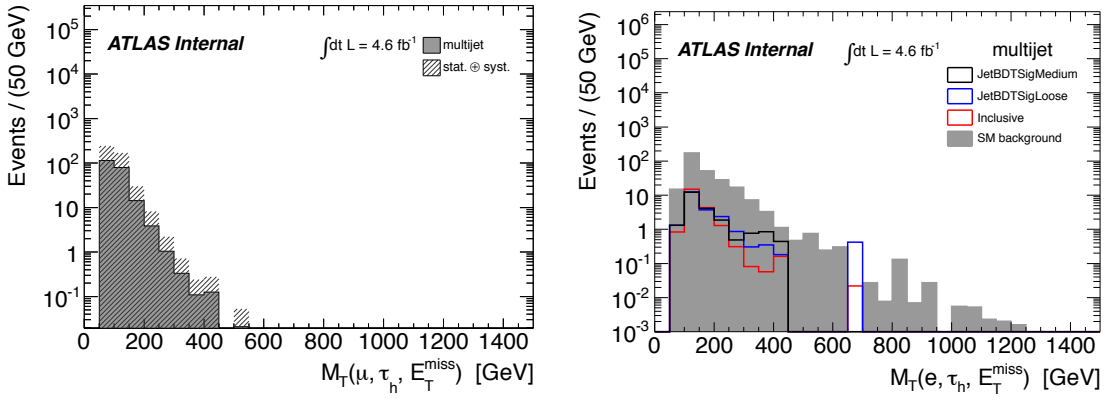

Figure 6.7: Plots demonstrating that the multijet backgrounds are negligible at high mass for events passing the baseline event selections. (left) The $m_{\mathrm{T}}^{\mathrm{tot}}$ distribution of the multijet estimate in $\mu\tau_{\mathrm{h}}$ channel, showing that the multijet background falls to $\mathcal{O}(10^{-2})$ events for $m_{\mathrm{T}}^{\mathrm{tot}} \gtrsim 400$ GeV. (right) The $m_{\mathrm{T}}^{\mathrm{tot}}$ distribution of the multijet estimate in $e\tau_{\mathrm{h}}$ channel, with predictions for medium (used in the nominal selection), loose, and no jet-tau discrimination, The loosened $m_{\mathrm{T}}^{\mathrm{tot}}$ distributions are scaled to the integral predicted by the nominal selection, `JetBDTSigMedium`. ($M_{\mathrm{T}} \equiv m_{\mathrm{T}}^{\mathrm{tot}}$) [97].

control sample. This assumption was justified by studies showing no significant dependence of the isolation fake factors on the thresholds of the m_{T} and d_0 cuts [97]. However, the analysis allows for a conservative 100% systematic on the isolation fake-factor method, which has negligible effect on the final limit because the multijet background is less than a hundredth of an event (see Table 6.3).

In the $e\tau_{\mathrm{h}}$ channel, the multijet background is less clearly neglible than in the $\mu\tau_{\mathrm{h}}$ channel, but it is still dominated by the $Z \to \tau\tau$ and W/Z + jets backgrounds and falling quickly to $\mathcal{O}(0.1)$ events with $m_{\mathrm{T}}^{\mathrm{tot}} \gtrsim 500$ GeV. The multijet background prediction was cross-checked by enriching the statistics in the high-mass tail by relaxing the tau identification from requiring the medium BDT jet-discriminant used in the selection, to loose, and to the inclusive reconstructed 1-prong taus. The loosened $m_{\mathrm{T}}^{\mathrm{tot}}$ distributions, shown in Figure 6.7 (right), are scaled to the integral predicted by the nominal selection, and are consistent in shape as could be expected because the tau identification efficiency and rejection are reasonably flat vs p_{T} for 1-prong candidates[73]. The loosened distributions indicate that the multijet $m_{\mathrm{T}}^{\mathrm{tot}}$ distribution continues to fall to less than 0.1 events with $m_{\mathrm{T}}^{\mathrm{tot}} \gtrsim 500$ GeV, and is therefore considered negligible in the primary signal region with an expected SM background of 1.6 events. The multijet estimate of 0.3 ± 0.3 events from the nominal selection (medium BDT, which turned out to be the most conservative) is used for the secondary signal region of $m_{\mathrm{T}}^{\mathrm{tot}} > 400$ GeV.

The multijet background was also cross-checked with a combined estimate of the W/Z + jets and the multijet backgrounds, using a single fake factor for tau identification, discussed in the following

[73] See Figure 4.27 in Section 4.4.7.

sub-section.

W+jets background

The dominant background throughout most of the high-$m_{\mathrm{T}}^{\mathrm{tot}}$ tail comes from W + jets events. It is estimated with a data-driven technique using fake factors parameterizing the rate for jets to fake tau identification, similar to the lepton-isolation fake-factor method used to estimate the multijet background.

Fundamentally, using a data-driven method to predict the rate of fake hadronic tau decays is necessary for the same reason the k_W scale factor was needed to correct normalization of the W + jets MC in the $Z \to \tau\tau$ cross section measurement discussed in Section 5.7.2, because the rate of jets faking tau identification is mis-modeled in Monte Carlo[74] The larger dataset in 2011 allows one to make a tau-by-tau correction, binned in p_{T} and η. Moreover, building the model from the events failing identification populates the tail of the background model with high-mass events from data, that typically outnumber the contribution of that background to the signal region because more events fail the tau identification or lepton isolation than pass.

A W + jets rich region of data can be selected by requiring high m_{T} for the lepton-$E_{\mathrm{T}}^{\mathrm{miss}}$ combination[75] The *W+jets control region* (or W–CR) is defined by selecting events which have

- exactly one selected muon,
- no additional preselected muons or electrons,
- at least one preselected hadronic tau candidate,
- $m_{\mathrm{T}}(\ell, E_{\mathrm{T}}^{\mathrm{miss}}) = 70$–$200$ GeV,

The preselected tau candidates in this region are divided into two categories: those that pass the medium BDT tau identification, and those that fail. A fake factor f_τ for hadronic tau identification is defined as the number of tau candidates that pass divided by the number that fail identification, binned in p_{T} and η:

$$f_\tau(p_{\mathrm{T}}, \eta) \equiv \left.\frac{N^{\text{pass } \tau\text{–ID}}(p_{\mathrm{T}}, \eta)}{N^{\text{fail } \tau\text{–ID}}(p_{\mathrm{T}}, \eta)}\right|_{\text{W–CR}} .$$

The tau identification fake factors are shown in Figure 6.8. To predict the number of W+jet events passing tau identification and event selection, the W+jet events that fail tau identification are weighted by their fake factor:

$$N_{W+\text{jet}}(p_{\mathrm{T}}, \eta, x) = f_\tau(p_{\mathrm{T}}, \eta) \cdot N_{W+\text{jet}}^{\text{fail } \tau\text{–ID}}(p_{\mathrm{T}}, \eta, x) \,,$$

[74] The tau identification fake rate for jets is mis-modeled, ultimately because jets are slightly more wide in data than in the simulation. See the discussion in Section 4.4.1.

[75] As shown in Figure 6.7, which shows the W + jets peak at high m_{T} in the sample passing tau identification. It is $\mathcal{O}(10)$ times larger in the sample failing tau identification.

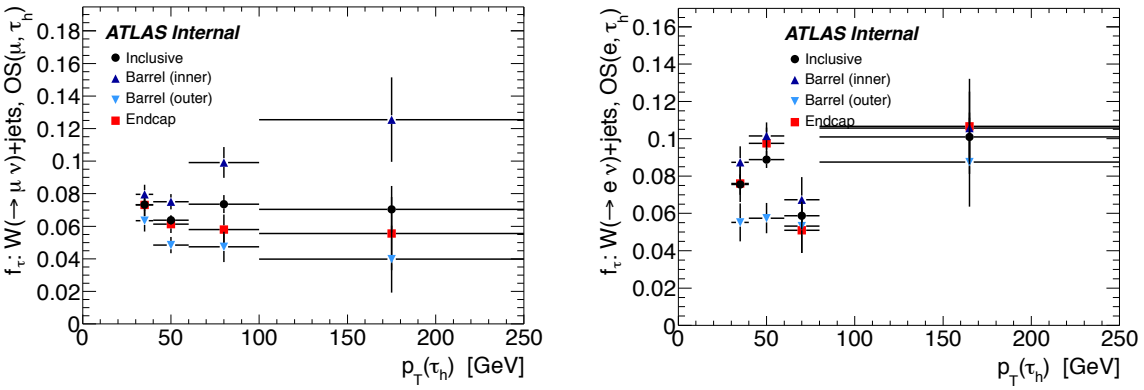

Figure 6.8: Tau identification fake factors derived in the W + jets control region. The binning in η is defined as inner barrel: $|\eta| < 0.8$, outer barrel: $0.8 < |\eta| < 1.37$, crack: $1.37 < |\eta| < 1.52$, and end-cap: $1.52 < |\eta| < 2.47$ [97].

where x is any kinematic variable ($\Delta\phi, m_{\mathrm{T}}^{\mathrm{tot}}, \ldots$).

The sample of failing tau candidates in the data was corrected for contaminations from other electroweak processes as well as from multijet events:

$$N_{W+\mathrm{jet}}(p_{\mathrm{T}}, \eta, x) = f_\tau(p_{\mathrm{T}}, \eta) \cdot \left(N_{\mathrm{data}}^{\text{fail } \tau\text{-ID}}(p_{\mathrm{T}}, \eta, x) - N_{\mathrm{multijet}}^{\text{fail } \tau\text{-ID}}(p_{\mathrm{T}}, \eta, x) - N_{\mathrm{MC}}^{\text{fail } \tau\text{-ID}}(p_{\mathrm{T}}, \eta, x) \right).$$

The multijet contamination is estimated using the lepton-isolation fake-factor method described in the previous sub-section. The shape of the W + jets background in any kinematic variable, x, is modeled from the events in the data that failed tau identification, with the multijet estimate and Monte Carlo modeling of the other contamination subtracted.

Figure 6.9 illustrates the procedure for the data-driven background estimates. First the multijet contamination is estimated from the rate of non-isolated muons in both the sample that passes tau identification, and the sample that fails tau identification. Then the corrected number of tau candidates failing identification is weighted to predict the W + jets background.

This method assumes the tau identification fake factor is not strongly correlated with the cuts used to enrich the W + jets control sample where they were measured. This assumption was justified by studies showing no significant dependence of the fake factors on the thresholds of the m_{T} cuts (see Figure 6.10). Also, the Alpgen W + jets Monte Carlo does not show a strong dependence of the generator-level quark-gluon fraction that would cause a sample dependence of the fake factor, as shown in the plots of the true quark-gluon fraction in MC in Figure 4.36.

Figure 6.6 shows the normalization of the W + jets estimate in the distribution of $m_{\mathrm{T}}(\mu, E_{\mathrm{T}}^{\mathrm{miss}})$ after event preselection, showing a modeling that is consistent with the estimates of multijet, $Z \to \tau\tau$, and other backgrounds. An advantage of the fake-factor method is the larger sample of tau candidates that fail tau identification than those that pass, however, the statistical uncertainty (71%)

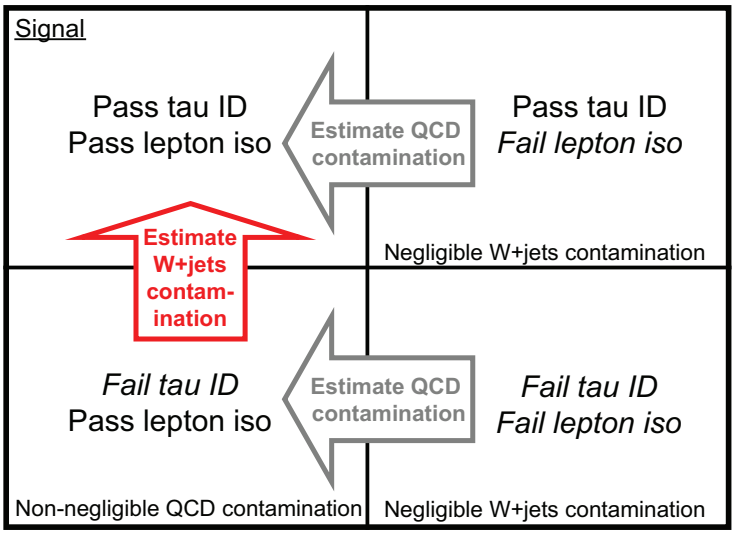

Figure 6.9: A diagram illustrating the combined use of the two data-driven methods to predict the multijet and W + jets backgrounds. First, the multijet contamination is estimated from the rate of non-isolated leptons in both the signal sample that passes tau identification, and the sample that fails. Then, the corrected number of tau candidates failing identification is weighted to predict the W + jets background.

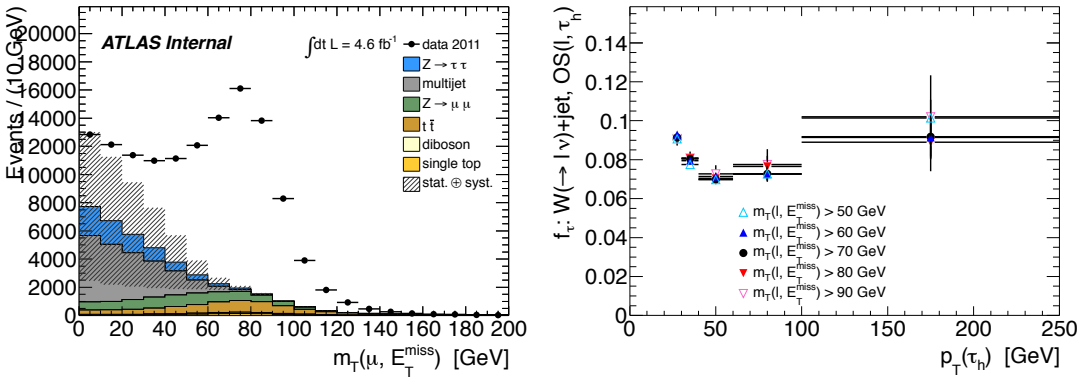

Figure 6.10: (left) The distribution of $m_{\mathrm{T}}(\mu, E_{\mathrm{T}}^{\mathrm{miss}})$ near the W + jets control region, before applying a cut of $m_{\mathrm{T}}(\mu, E_{\mathrm{T}}^{\mathrm{miss}}) > 70$ GeV. (right) Tau identification fake factors derived from modified control regions with various $m_{\mathrm{T}}(\mu, E_{\mathrm{T}}^{\mathrm{miss}})$ cuts applied, showing that the fake factors do not have a strong dependence on $m_{\mathrm{T}}(\mu, E_{\mathrm{T}}^{\mathrm{miss}})$ [97].

from the count of candidates failing tau identification in the data in the high-mass signal region, remains the dominant uncertainty for this background. The W + jets background has a 30% total systematic uncertainty coming from the sum in quadrature of a 20% systematic uncertainty on the consistency of the fake factors measured in the W + jets control region and a control region Z + jets events, added with a 20% statistical uncertainty on the count of high-p_{T} events in the W+jet control region [97].

Single-fake-factor method

The W/Z + jets background was also cross-checked with a combined estimate of the W/Z + jets and the multijet backgrounds, using a single fake factor for tau identification. One might have estimated the background from *all fake* hadronic tau candidates, from both multijet and W/Z + jets events, with a fake factor applied to tau candidates, without estimating the multijet background independently and subtracting it. If one estimates the combined fake backgrounds with a *single*[76] set of tau identification fake factors from the W + jets control region, this should over-predict the background in regions where the multijet contamination is significant, since multijet events have a higher gluon-fraction which lowers the tau identification fake rate. This single-fake-factor method[77] should improve at higher-$p_{\mathrm{T}}(\tau_{\mathrm{h}})$, where the quark-fraction increases, and the fake factors for W + jets and multijet events become more similar[78].

Figures 6.11 (top) show that as expected, the low-$m_{\mathrm{T}}^{\mathrm{tot}}$ and low-$p_{\mathrm{T}}(\tau_{\mathrm{h}})$ part of the distribution is over-estimated, due to the significant multijet contribution, and the estimate improves at higher mass. Figure 6.11 (bottom) compares the high-mass parts of the $m_{\mathrm{T}}^{\mathrm{tot}}$ distributions using the nominal ("double fake factor") estimate described above, and using the single-fake-factor estimate.

The single-fake-factor method provides a cross-check for the $e\tau_{\mathrm{h}}$ channel, that avoids the coupling of the estimates of the multijet and W/Z + jets backgrounds in the contamination subtraction that is done. The predictions are consistent and are summarized in Table 6.5.

$Z/\gamma^*(\rightarrow \ell\ell)$ + jets background

In the $\mu\tau_{\mathrm{h}}$ channel, the Z + jets background is steeply falling in $m_{\mathrm{T}}^{\mathrm{tot}}$ and negligible at high-$m_{\mathrm{T}}^{\mathrm{tot}}$ in either case where a jet or a lepton fakes the tau candidate as estimated with Monte Carlo generated with Alpgen (see Figure 6.12).

[76] As opposed to using both W + jets tau fake factors and multijet isolation fake factors (or another multijet estimate). This effectively means that the right-side of the diagram in Figure 6.9 is ignored, and that the multijet contamination is not separately corrected for, but instead is covered with tau identification fake factors.

[77] A recent ATLAS Higgs search with taus does a similar estimate of the backgrounds with fake hadoric tau candidates [225]. In that method, fake factors appropriate for multijet and W/Z + jets are mixed to give a single set of fake factors. For this method, only the W/Z + jets fake factor is used.

[78] Recall from Figures 4.31 and 4.36, that the tau identification fake factors derived in W + jets and multijet control regions become more similar, ultimately because they get more quark-enriched.

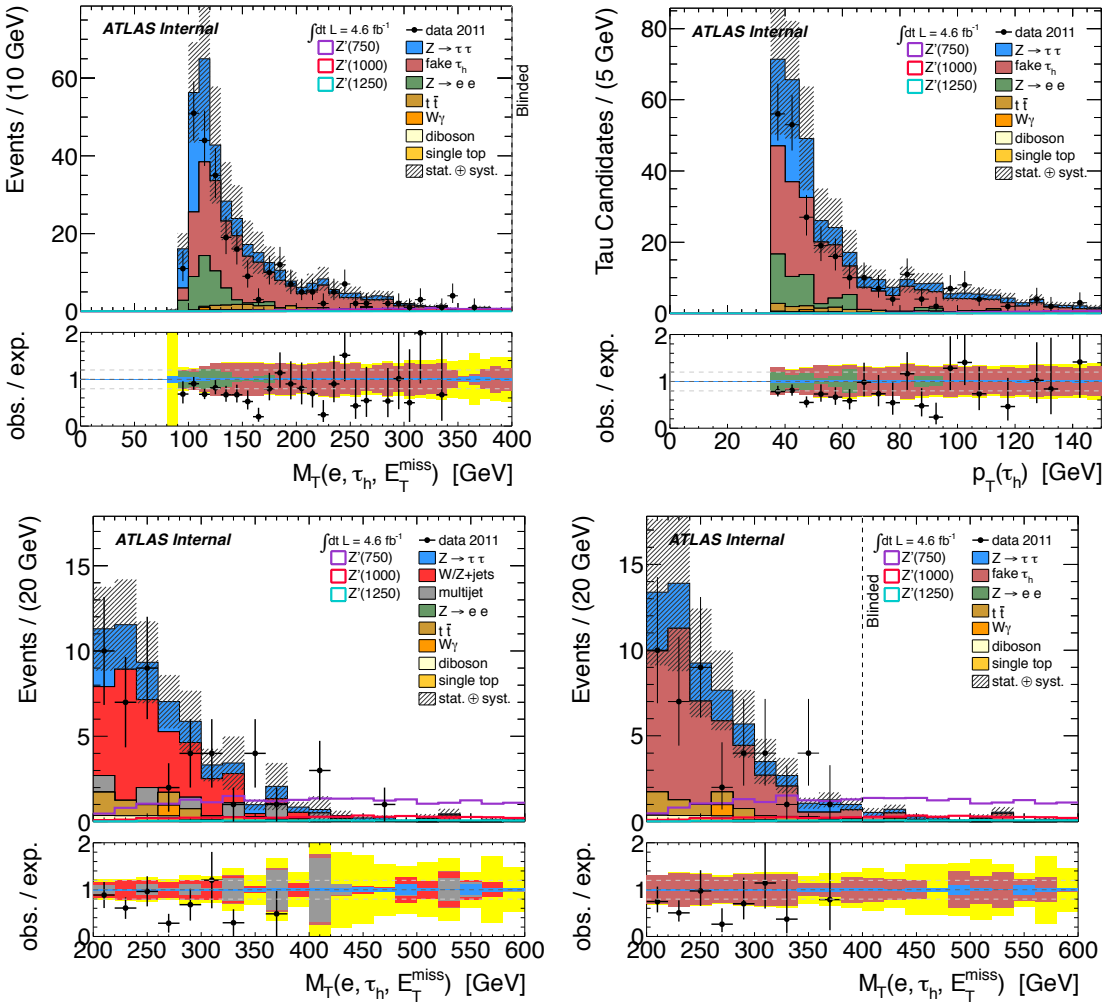

Figure 6.11: Kinematic distributions for events passing the $e\tau_{\mathrm{h}}$ baseline event selection, comparing estimates of the fake backgrounds with the nominal double-fake-factor method and the single-fake-factor method. The distribution of $m_{\mathrm{T}}^{\mathrm{tot}}(e, \tau_{\mathrm{h}}, E_{\mathrm{T}}^{\mathrm{miss}})$ (top-left) and $p_{\mathrm{T}}(\tau_{\mathrm{h}})$ (top-right) using the single-fake-factor method. The high-mass tail of the $m_{\mathrm{T}}^{\mathrm{tot}}$ distribution using the nominal double-fake-factor method (bottom-left) and the single-fake-factor method (bottom-right) ($M_{\mathrm{T}} \equiv m_{\mathrm{T}}^{\mathrm{tot}}$) [97]. The "Fake τ_{h}" estimate is meant to cover fake hadronic tau decays from W + jets and multijet events. Because it uses a tau fake factor derived in a W + jets sample, which is rich in quark-initiated jets, the fake estimate should over estimate the multijet contribution, which is more gluon-rich.

Table 6.5: Comparison of estimates of the fake hadronic tau background for the $e\tau_{\mathrm{h}}$ channel, showing the nominal fake background estimate (double fake factor) and the single-fake-factor method [97].

	double fake factor			single fake factor
	W/Z + jets	multijet	total	fake τ_{h}
$m_{\mathrm{T}}^{\mathrm{tot}} > 400$ GeV	0.8(6)	0.3(3)	1.1(4)	1.3(4)
$m_{\mathrm{T}}^{\mathrm{tot}} > 500$ GeV	0.8(4)	< 0.1	0.8(4)	0.9(4)

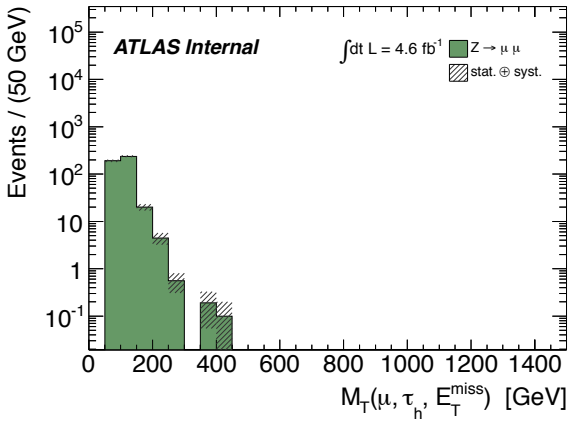

Figure 6.12: The distribution of $m_{\mathrm{T}}^{\mathrm{tot}}(\mu, \tau_{\mathrm{h}}, E_{\mathrm{T}}^{\mathrm{miss}})$ for the $Z \to \mu\mu$ background of the $\mu\tau_{\mathrm{h}}$ channel. The $Z \to \mu\mu$ background is negligible at high $m_{\mathrm{T}}^{\mathrm{tot}}$, falling to 0.1 events with $m_{\mathrm{T}}^{\mathrm{tot}} \gtrsim 400$ GeV compared to a total expected SM background of 15 ± 1 events. ($M_{\mathrm{T}} \equiv m_{\mathrm{T}}^{\mathrm{tot}}$) [97].

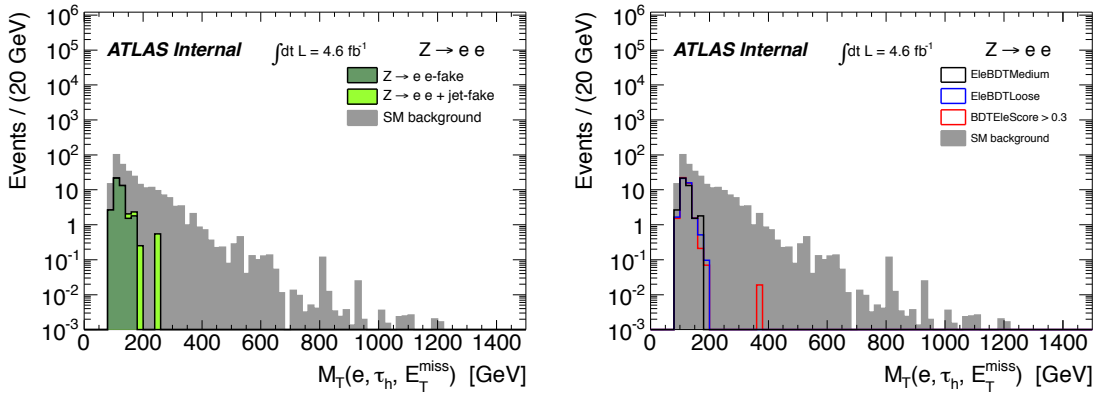

Figure 6.13: Plots demonstrating that the $Z \to ee$ background is negligible at high mass for events passing the $e\tau_{\mathrm{h}}$ baseline event selection. (left) The $m_{\mathrm{T}}^{\mathrm{tot}}$ distribution of the $Z \to ee$ modeled with Alpgen Monte Carlo, divided into cases where the reconstructed tau candidate matched a true electron or a jet. (right) The $m_{\mathrm{T}}^{\mathrm{tot}}$ distribution of the expected $Z \to ee$ background, with predictions for medium (used in the nominal selection), loose, and no electron-veto applied to the hadronic tau candidate. For the (right), the reconstructed tau candidate is required to match a true Monte Carlo electron [97].

In the $e\tau_{\mathrm{h}}$ channel, it was recognized that the Z + jets background is dominated by events where one of the electrons from $Z \to ee$ fakes the tau candidate, and results in a background with low $m_{\mathrm{T}}^{\mathrm{tot}}$ near the Z mass. The contribution from Z + jets with a jet faking the tau candidate is small, being $\mathcal{O}(1\%)$ of the Z + jets background (see Figure 6.13 (left)). The Monte Carlo estimate was filtered for events where the tau candidate is matched to a true electron, so that jet fake contribution is covered by the data-driven W + jets tau fake factor estimate.

The prediction for the $Z \to ee$ background, where an electron fakes the reconstructed hadronic tau decay, was cross-checked by enriching the statistics in the high-mass tail by relaxing the electron veto in the Monte Carlo. Figure 6.13 (right) shows the distributions of $m_{\mathrm{T}}^{\mathrm{tot}}$ in events with the nominal medium electron veto, the loose veto, and with an even looser requirement of `BDTEleScore` > 0.3, each scaled to the expectation passing medium. The shapes of the loosened distributions are statistically consistent and show that the $Z \to ee$ background continues to fall to less than 0.02 events with $m_{\mathrm{T}}^{\mathrm{tot}} \gtrsim 300$ GeV, and is therefore considered negligible in the signal region with $m_{\mathrm{T}}^{\mathrm{tot}}(e, \tau_{\mathrm{h}}, E_{\mathrm{T}}^{\mathrm{miss}}) > 500$ GeV and an expected SM background of 1.6 events.

Other backgrounds

The remaining backgrounds to this channel are estimated with ATLAS full simulation Monte Carlo samples.

- ***Z*/$\gamma^*(\to \tau\tau)$ + jets** This process surpasses W+jets as the largest background for events with $m_{\mathrm{T}}^{\mathrm{tot}} \gtrsim 600$ GeV. We estimate it using fully simulated Monte Carlo generated with Alpgen. The samples are binned in the number of additional hard final-state partons (`NpX`), and binned in the true ditau mass. The available statistics in low-mass, low-`NpX` samples are up to 10M events, decreasing to 20k events in the high-mass, high-`NpX` samples, sufficient to give only a 5% statistical uncertainty on this background. While data-driven methods are used to estimate some of the other backgrounds with fake hadronic taus, the Monte Carlo scale factor for tau identification of real taus is consistent with 1.0 (see Section 4.4.6), which justifies using a Monte Carlo based estimate without additional corrections.

- ***t*$\bar{t}$ and single top** While subdominant throughout the cutflow, the background from top-quark events is of the same order as the W+jets and $Z/\gamma^*(\to \tau\tau)$ backgrounds in the high $m_{\mathrm{T}}^{\mathrm{tot}}(\ell, \tau_{\mathrm{h}}, E_{\mathrm{T}}^{\mathrm{miss}})$ signal region, and is estimated with Monte Carlo generated with MC@NLO for $t\bar{t}$ and AcerMC for single top events. The background is well normalized in control regions in regions where $t\bar{t}$ dominates the sample, including at high values of $E_{\mathrm{T}}^{\mathrm{miss}}$, $m_{\mathrm{T}}(\mu, E_{\mathrm{T}}^{\mathrm{miss}})$, and $N(\mathrm{jets})$[79].

- **Diboson** This background is small compared to the total background and is estimated with Monte Carlo generated with MC@NLO.

[79] See in $E_{\mathrm{T}}^{\mathrm{miss}}$ plots in Figures 6.1 and 6.3 and the additional plots in Ref. [97].

6.5 Search in the $\tau_h\tau_h$ channel

6.5.1 Triggering

In the $\tau_h\tau_h$ channel, events are triggered by either a ditau trigger with p_T thresholds of 20 and 29 GeV, or a single-tau trigger with $p_T > 125$ GeV.

6.5.2 Object selection

Selected tau candidates in the $\tau_h\tau_h$ channel must have $p_T > 50$ GeV, pass the loose BDT identification, have one or three tracks and a charge magnitude of one. At least two selected taus are required in the event. If more than two are found, the two leading p_T selected taus are chosen to be used in the analysis.

6.5.3 Event selection

Events are selected which have two loosely identified hadronic tau decays with $p_T > 50$ GeV that have opposite-signed charges, and $\Delta\phi > 2.7$, where $\Delta\phi$ is the angle between the reconstructed tau decays in the transverse plane. Events are vetoed that have any preselected electrons or muons, as described in Section 6.3. The total transverse mass of the combination of the two tau decays and the E_T^{miss}, m_T^{tot}, is calculated, and shown in Figure 6.14. High-m_T^{tot} signal regions are optimized as a function of the mass of the Z' signal, shown in Table 6.6.

6.5.4 Background estimation

The two main backgrounds are multijet and $Z \to \tau\tau$. The contribution from $Z \to \tau\tau$ is irreducible and taken directly from simulation, as the tau identification efficiency is well-modeled with Monte Carlo. The multijet background shape is estimated from a fit to data in the high purity same-sign control region, and normalized in a side band of m_T^{tot}. The other backgrounds make very minor contributions and are estimated directly from simulation.

Table 6.6: Mass-dependent cuts on m_T^{tot} for different Z' signal masses [97].

SSM Z' mass [GeV]	500	625	750	875	1000	1125	1250
$\tau_h\tau_h$ channel	350	400	500	500	625	625	700
$\mu\tau_h$ channel	400	400	500	500	600	600	600
$e\tau_h$ channel	400	400	400	500	500	500	500
$e\mu$ channel	300	350	350	350	500	500	500

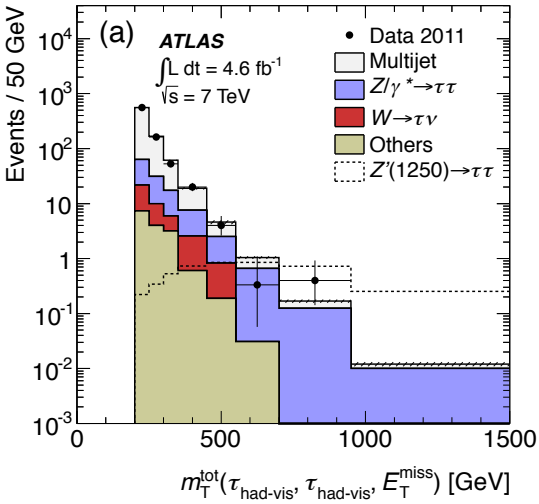

Figure 6.14: The $m_{\mathrm{T}}^{\mathrm{tot}}(\tau_{\mathrm{h}}, \tau_{\mathrm{h}}, E_{\mathrm{T}}^{\mathrm{miss}})$ distribution for the $\tau_{\mathrm{h}}\tau_{\mathrm{h}}$ channel after the full selection (excluding the final $m_{\mathrm{T}}^{\mathrm{tot}}$ window). The estimated contributions from SM processes and Z'_{SSM} signal are stacked and theobserved events in data are overlayed. The uncertainty on the data/MC ratio includes only the statistical uncertainty from the data and the MC simulated samples, while the uncertainty on the multijet contribution is not included [211].

6.6 Systematic uncertainties

Experimental and theoretical systematic uncertainties are propagated to the final expected yields for signal and background, some object-by-object, in a similar way as discussed for the $Z \to \tau\tau$ cross section measurement in Section 5.9.

The systematic uncertainties on the background processes have little effect on the final mass limit, due to the very low number of expected events. The uncertainties on the signal, however, have a significant impact on the signal sensitivity. The experimental systematic uncertainties can be split into efficiency uncertainties, which primarily result in scaling of the samples and have little impact on variable distributions, and energy scale uncertainties, which can impact the shape of key variables and cause changes in efficiency through cut acceptance.

The dominant uncertainty on the signal is the uncertainty on the tau identification efficiency, which increases with the Z' mass (due to the inflation with p_{T}, see Section 4.4.7) and contributes 15% in the $\tau_{\mathrm{h}}\tau_{\mathrm{h}}$ channel and 8–10% in the $\ell\tau_{\mathrm{h}}$ channel for a $Z'_{\mathrm{SSM}}$with a mass of 1250 GeV. The dominant systematic uncertainties on the irreducible $Z \to \tau\tau$ background (with little effect on the expected Z'_{SSM} mass limit) are 14–20% ($\tau_{\mathrm{h}}\tau_{\mathrm{h}}$ channel) and 11–14% ($\ell\tau_{\mathrm{h}}$ channels) on the energy scale, 14% ($\tau_{\mathrm{h}}\tau_{\mathrm{h}}$ channel) and 6% ($\ell\tau_{\mathrm{h}}$ channels) on the tau identification efficiency[80], and 11% on

[80] A more detailed discussion of the uncertainty on the tau identification efficiency at high-p_{T} is given in Section 4.4.7.

the NNLO production cross section for high-mass $Z \to \tau\tau$ including the uncertainties on both the EW and QCD k-factors [97]. A summary of the effects of systematic uncertainties on the Z' signal and background predictions in all channels is shown in Table 6.7. A more detailed breakdown of how each uncertainty effects each background for the $\ell\tau_{\mathrm{h}}$ channels is shown in Tables 6.8 and 6.9.

Table 6.7: Uncertainties on the estimated signal and total background contributions in percent for each channel. The following signal masses, chosen to be close to the region where the limits are set, are used: 1250 GeV for $\tau_{\mathrm{h}}\tau_{\mathrm{h}}$ (hh); 1000 GeV for $\ell\tau_{\mathrm{h}}$ (μh) and $e\tau_{\mathrm{h}}$ (eh); and 750 GeV for $e\mu$. A dash denotes that the uncertainty is not applicable. The statistical uncertainty corresponds to the uncertainty due to limited sample size in the MC and control regions [211].

Uncertainty [%]	Signal				Background			
	hh	μh	eh	$e\mu$	hh	μh	eh	$e\mu$
Stat. uncertainty	1	2	2	3	5	20	23	7
Eff. and fake rate	16	10	8	1	12	16	4	3
Energy scale and res.	5	7	6	2	$^{+22}_{-11}$	3	8	5
Theory cross section	8	6	6	5	9	4	4	5
Luminosity	4	4	4	4	2	2	2	4
Data-driven methods	–	–	–	–	$^{+21}_{-11}$	6	16	–

Table 6.8: The final predicted event yields for the $\mu\tau_h$ channel and their systematic uncertainties, for the primary signal region with $m_T^{tot} > 600$ GeV. The first line of numbers reports the number of expected events. The uncertainties are reported as percent of that background. The syst. uncert. denotes the total systematic uncertainty on the estimate of each background, calculated from the sum in quadrature of the individual systematic uncertainties, listed below that. The stat. uncert. denotes the statistical uncertainty either from the number of Monte Carlo events, or the events used in a data-driven model. The total uncert. denotes the total uncertainty on the estimate of each background, calculated from the sum in quadrature of the statistical and the total systematic uncertainty [97].

	W+jets	$Z \to \tau\tau$	$t\bar{t}$	diboson	single top	$Z'(1000)$
expected events	0.3	0.4	0.3	0.2	0.2	5.5
total. uncert.	77	18	46	33	95	13
stat. uncert.	71	5	35	29	74	2
syst. uncert.	30	17	30	15	59	12
μ efficiency	-	0	0	0	0	2
μ p_T resolution ID	-	0	0	2	0	2
μ p_T resolution MS	-	0	0	1	0	2
τ_h efficiency	-	6	5	5	0	10
jet$\to \tau_h$ fake rate	-	0	11	0	0	0
$e \to \tau_h$ fake rate	-	0	25	11	58	0
jet energy scale	-	11	2	2	0	6
jet energy resolution	-	1	0	2	0	2
cluster energy scale	-	0	1	2	0	2
luminosity	-	2	2	2	2	2
theo. cross section	-	11	10	7	13	-
τ_h fake factor	30	-	-	-	-	-

Table 6.9: The final predicted event yields for the $e\tau_h$ channel and their systematic uncertainties, for the primary signal region with $m_T^{tot} > 500$ GeV. The first line of numbers reports the number of expected events. The uncertainties are reported as percent of that background. The syst. uncert. denotes the total systematic uncertainty on the estimate of each background, calculated from the sum in quadrature of the individual systematic uncertainties, listed below that. The stat. uncert. denotes the statistical uncertainty either from the number of Monte Carlo events, or the events used in a data-driven model. The total uncert. denotes the total uncertainty on the estimate of each background, calculated from the sum in quadrature of the statistical and the total systematic uncertainty [97].

	W/Z+jets	$Z \to \tau\tau$	$t\bar{t}$	diboson	$Z'(1000)$
expected events	0.8	0.6	0.1	0.1	5.0
total. uncert.	52	19	72	55	10
stat. uncert.	43	4	54	50	2
syst. uncert.	30	19	48	23	10
e efficiency	-	1	1	1	1
e energy scale	-	0	0	0	0
e energy resolution	-	0	0	0	0
τ_h efficiency	-	6	5	6	8
jet$\to \tau_h$ fake rate	-	0	21	0	0
$e \to \tau_h$ fake rate	-	0	23	17	0
jet energy scale	-	14	24	11	6
jet energy resolution	-	1	25	6	0
cluster energy scale	-	0	5	0	1
luminosity	-	2	2	2	2
theo. cross section	-	11	10	7	-
τ_h fake factor	30	-	-	-	-

6.7 Results

6.7.1 Observed events

Table 6.10 shows a summary of the number of observed events in each channel, in the primary signal regions optimized for the highest Z'_{SSM} mass that can be excluded independently in that channel. In the $\tau_{\mathrm{h}}\tau_{\mathrm{h}}$ channel 0.97 ± 0.27 events are expected and 2 events are observed. In the $\mu\tau_{\mathrm{h}}$ and $e\tau_{\mathrm{h}}$ channels, 1.4 ± 0.4 and 1.6 ± 0.5 events are expected, with 1 and 0 events observed, respectively. In all cases, the number of observed events is consistent with the expected Standard Model backgrounds. Therefore, upper limits are set on the production of a high-mass resonance decaying to $\tau^+\tau^-$ pairs.

6.7.2 Likelihood model

The statistical combination of the channels employs a likelihood function constructed as the product of Poisson probability terms describing the total number of events observed in each channel. The Poisson probability in each channel is evaluated for the observed number of data events given the signal plus background expectation. Systematic uncertainties on the expected number of events are incorporated into the likelihood via Gaussian-distributed nuisance parameters.

The combined Likelihood is parameterized as

$$L(\mu, \alpha_i; n_c) = \prod_c \mathrm{Poisson}\big(n_c; \mu\,(s_c + \Delta s_c) + b_c + \Delta b_c\big) \prod_i \mathrm{Gaussian}(\alpha_i; 0, 1)\,,$$

Table 6.10: A summary of the number of events observed and the number of background events expected in the primary signal regions optimized for the highest Z'_{SSM} mass that can be excluded independently in each channel. The total uncertainties on each estimated contribution are shown. The signal efficiency denotes the expected number of signal events divided by the product of the production cross section, the ditau branching fraction and the integrated luminosity: $\sigma(pp \to Z'_{\mathrm{SSM}}) \times \mathrm{BR}(Z'_{\mathrm{SSM}} \to \tau\tau) \times \int L\,dt$ [211].

	$\tau_{\mathrm{had}}\tau_{\mathrm{had}}$	$\tau_\mu\tau_{\mathrm{had}}$	$\tau_e\tau_{\mathrm{had}}$	$\tau_e\tau_\mu$
$m_{Z'}$ [GeV]	1250	1000	1000	750
$m_{\mathrm{T}}^{\mathrm{tot}}$ threshold [GeV]	700	600	500	350
$Z/\gamma^* \to \tau\tau$	0.73±0.23	0.36±0.06	0.57±0.11	0.55±0.07
W+jets	< 0.03	0.28±0.22	0.8 ±0.4	0.33±0.10
$Z(\to \ell\ell)$+jets	< 0.01	< 0.1	< 0.01	0.06±0.02
$t\bar{t}$	< 0.02	0.33±0.15	0.13±0.09	0.97±0.22
Diboson	< 0.01	0.23±0.07	0.06±0.03	1.69±0.24
Single top	< 0.01	0.19±0.18	< 0.1	< 0.1
Multijet	0.24±0.15	< 0.01	< 0.1	< 0.01
Total expected background	0.97±0.27	1.4 ±0.4	1.6 ±0.5	3.6 ±0.4
Events observed	2	1	0	5
Expected signal events	6.3 ±1.1	5.5 ±0.7	5.0 ±0.5	6.72±0.26
Signal efficiency (%)	4.3	1.1	1.0	0.4

where c is summed over the channels, i is summed over the systematic uncertainties, n_c is the number of events observed in a channel, s_c and b_c are the expected number of signal and background events, and Δs_c and Δb_c are linear functions of nuisance parameters, α_i:

$$\Delta s_c = \sum_i \alpha_i \, \delta s_{ci} \quad \text{and} \quad \Delta b_c = \sum_i \alpha_i \, \delta b_{ci} \, .$$

Here δs_{ci} and δb_{ci} denote the change in normalization of the signal and background models, respectively, when the nuisance parameter $\alpha_i = \pm 1$, corresponding to a shift of one standard deviation under the Gaussian constraints[81]. Correlations across channels are taken into account by using common nuisance parameters among the channels. A signal-strength parameter, μ, multiplies the expected signal for all channels. Theoretical uncertainties on the signal cross section are not included in the calculation of the experimental limit as they are model-dependent.

6.7.3 Limit-setting procedure

Bayesian[82] credibility intervals are determined leading to 95% CL upper limits on the cross section times branching fraction for a high-mass resonance decaying into a $\tau^+\tau^-$ pair as a function of the resonance mass.

The upper limit of the Bayesian credibility interval for the signal strength with 95% confidence, μ_{up}, is determined by

$$0.95 = \int_0^{\mu_{\text{up}}} d\mu \, p(\mu; n_c)$$

where the posterior probability distribution for the signal-strength parameter given the observed data, $p(\mu; n_c)$, is determined by marginalizing the nuisance parameters [136]:

$$p(\mu; n_c) \propto \int d\alpha_i \, L(\mu, \alpha_i; n_c) \, \pi(\mu)$$

for which a positive uniform prior probability distribution is assumed for $\pi(\mu)$[83]. The Bayesian Analysis Toolkit (BAT) [230] was used to implement the sampling of the posterior using the method of Markov Chain Monte Carlo (MCMC) [231, 232].

[81] The example model is somewhat simplified because the actual model can be bifurcated to have a different variations depending on if α is positive or negative. This only concerns systematic uncertainties that have significantly different up and down variations, and was only used for the jet energy scale and multijet shape uncertainties in the $\tau_{\text{h}}\tau_{\text{h}}$ channel. The `HistFactory` tool of the `RooStats` framework to was used to configure and build the model described for calculating CLs limits. See the `HistFactory` manual [226] for a detailed description of the parametrizations of the likelihood. The same configuration but an independent implementation using bifurcated Gaussians with two width parameters was used to calculate the Bayesian limits.

[82] As a cross-check, frequentist upper limits were also evaluated using the CLs technique [227, 228] as described in Ref. [97], giving similar results also excluding a Z'_{SSM} with a mass up to 1.4 TeV.

[83] The impact of the choice of the prior on the signal-strength parameter has been evaluated by also considering the reference prior [229] which prior improves the combined mass limit by approximately 50 GeV or 3.6%.

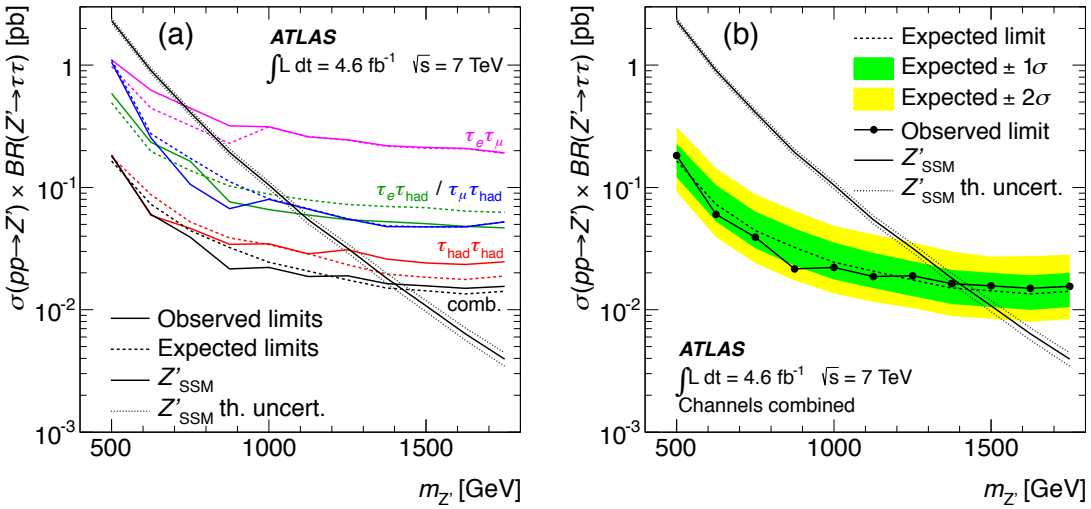

Figure 6.15: (left) The expected (dashed) and observed (solid) 95% credibility upper limits on the cross section times $\tau^+\tau^-$ branching fraction, in the $\tau_h\tau_h$, $\mu\tau_h$, $e\tau_h$, and $e\mu$ channels, and for their combination. The expected Z'_{SSM} production cross section and its corresponding theoretical uncertainty (dotted) are also included. (right) The expected and observed upper limits for the combination including 1σ and 2σ uncertainty bands. Z'_{SSM} masses up to 1.40 TeV are excluded, in agreement with the expected limit in the absence of a signal of 1.42 TeV [211].

Figure 6.15 (left) shows limits derived independently in each channel and their improvement in combination. Figure 6.15 (right) shows the combined expected limit and a band showing its estimated statistical variance, evaluated by generating Monte Carlo pseudo-experiments. As a result[84], SSM Z' bosons are excluded with masses less than 1.4 TeV at 95% CL. CMS performed a similar search, also excluding SSM Z' bosons decaying to $\tau^+\tau^-$ with masses less than 1.4 TeV [212].

6.7.4 Model dependence

The exclusion is nearly model-independent such that theorists with a model for a high-mass $\tau^+\tau^-$ resonance should be able to calculate the cross section as a function of mass of their model and compare it to the excluded cross section. Using the predicted cross section of Z'_{SSM} at NNLO as a function of mass, the upper limit on the signal-strength parameter was converted to the cross section times $\tau^+\tau^-$ branching fraction excluded at 95% CL shown in Figures 6.15. The exclusion is model-independent insofar as it applies to models predicting a high-mass $\tau^+\tau^-$ resonances with a width small compared to its mass[85], modulo the effects of the polarization of the out-going tau

[84] The author presented this result at the Tau2012 International Workshop on Tau Lepton Physics in Nagoya, Japan [233].

[85] The mass has to be small enough to be produced on-resonance at the LHC ($m \lesssim \sqrt{\hat{s}}$) and not in the higher-mass, contact interaction regime [234].

leptons. Any such model will result in back-to-back tau decays that can only vary in the initial polarization of the tau leptons depending on the type of coupling the signal has to taus.

The polarization of the out-going tau leptons can have a significant effect on the fraction of the momentum carried by the visible decay products because the tau lepton decays through a left-handed coupling to the W boson [235]. Hence changing the polarization of the tau leptons in this analysis would affect the signal acceptance, mainly through the thresholds applied to the transverse momentum of the visible tau decay products and on $m_{\mathrm{T}}^{\mathrm{tot}}$. For $Z \to \tau\tau$ decays, the tau polarization is determined by the relative strengths of the vector and axial couplings, C_{V} and C_{A}, parameterized by the Weinberg angle. For charged leptons these are defined as [236, 136]

$$C_{\mathrm{V}} = -1 + 4\,\sin^2\theta_{\mathrm{W}} \approx -0.08 \qquad \text{and} \qquad C_{\mathrm{A}} = -1\,.$$

In the SSM, the Z' has the same vector and axial coupling strengths as the Z of the SM. However, for a generic Z' with chiral couplings, C_{V} and C_{A} can have other values. To determine the extent of the effect of tau polarization on signal acceptance, the two extreme cases for chiral couplings are considered:

- $C_{\mathrm{V}} = +1$ and $C_{\mathrm{A}} = -1$, purely left-handed coupling (V − A),
- $C_{\mathrm{V}} = +1$ and $C_{\mathrm{A}} = +1$, purely right-handed coupling (V + A).

Monte Carlo $Z' \to \tau\tau$ samples were generated using PYTHIA 6.4 for each signal mass point with SSM (nominal), V − A, and V + A couplings. For hadronic tau decays, the visible fraction of momentum (the part not carried by neutrinos) is slightly larger for V − A than for V + A. (see Figure 6.16 (top-left)). For leptonic decays, the opposite is true but to a lesser degree (see Figure 6.16 (top-right)). The net impact of the tau polarizations on the final $m_{\mathrm{T}}^{\mathrm{tot}}$ distribution for a 1250 GeV Z' is shown in Figure 6.16 for the $\tau_{\mathrm{h}}\tau_{\mathrm{h}}$ channel (bottom-left) and the $\ell\tau_{\mathrm{h}}$ channels (bottom-right). The acceptance varies by ±10–20% as a result of the change in couplings, as shown in Figure 6.17.

The impact of the different chiral couplings on the excluded cross section times $\tau^+\tau^-$ branching fraction is shown in Figure 6.18, with dashed lines indicating the spread in expected limits in the case of V − A or V + A couplings. The mass limit is improved by ≈ 30 GeV or 2.1% for V − A couplings, since the observable fraction momentum is larger, and degraded by ≈ 50 GeV or 3.6% for V + A couplings[86].

[86] The primary references discussing the topics of this chapter in more detail are

- *A search for high-mass resonances decaying to $\tau^+\tau^-$ in pp collisions at $\sqrt{s} = 7$ TeV with the ATLAS detector* `ATL-COM-PHYS-2012-394` [97] – support note for the $Z' \to \tau\tau$ search with 2011 data,
- *A search for high-mass resonances decaying to $\tau^+\tau^-$ in the ATLAS detector* `ATLAS-CONF-2012-067` [237] –

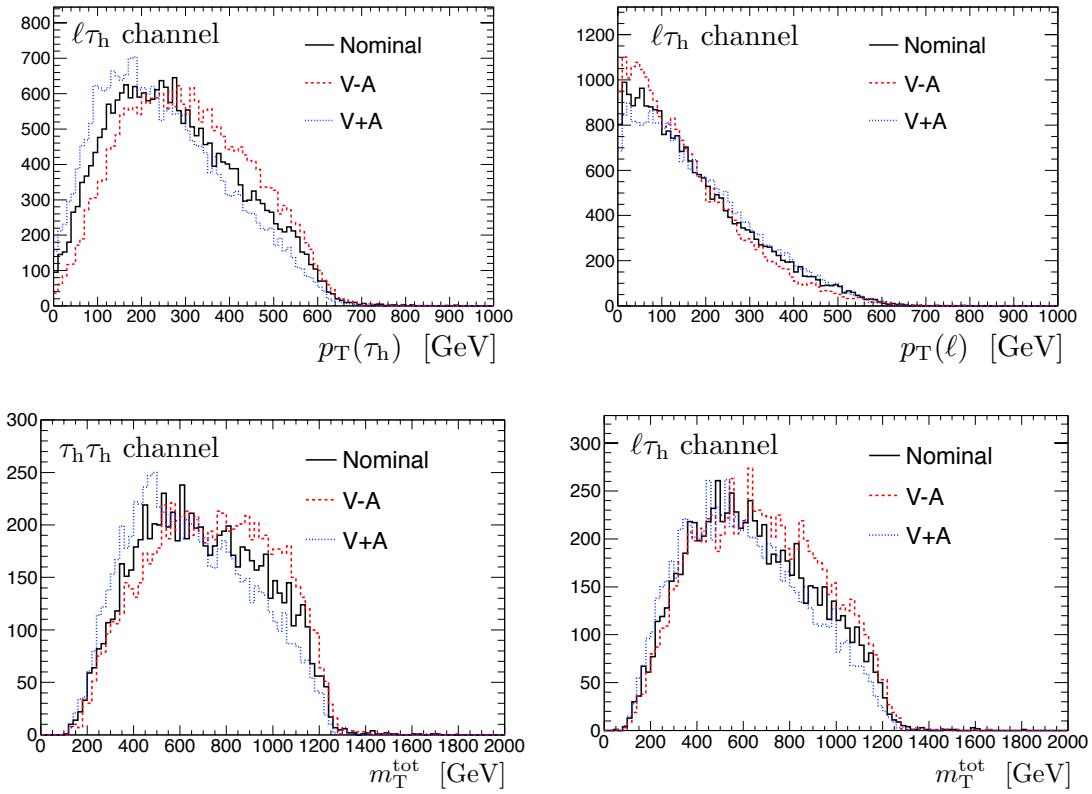

Figure 6.16: Generator-level kinematic distributions for a Z'_{SSM} with a mass of 1250 GeV, after the baseline event selection, with SSM (nominal), V − A, and V + A couplings. (top-left) and (top-right) show the visible p_T of hadronic tau decay and lepton, respectively, in the $\ell\tau_h$ channel. (bottom-left) and (and bottom-right) compare the m_T^{tot} distributions in the $\tau_h\tau_h$ and $\ell\tau_h$ channels, respectively. [97].

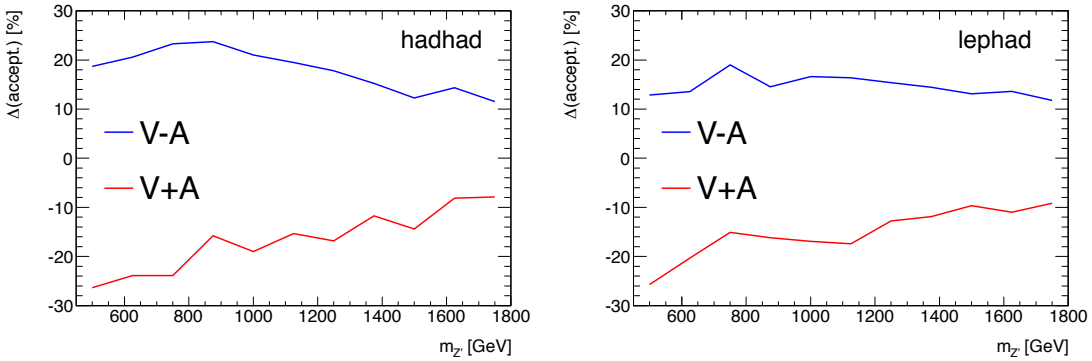

Figure 6.17: The relative change in signal acceptance for the V − A and V + A samples (in % of the nominal SSM signal) vs. the Z' mass for the $\tau_h\tau_h$ channel (left) and the $\ell\tau_h$ channel (right) [97].

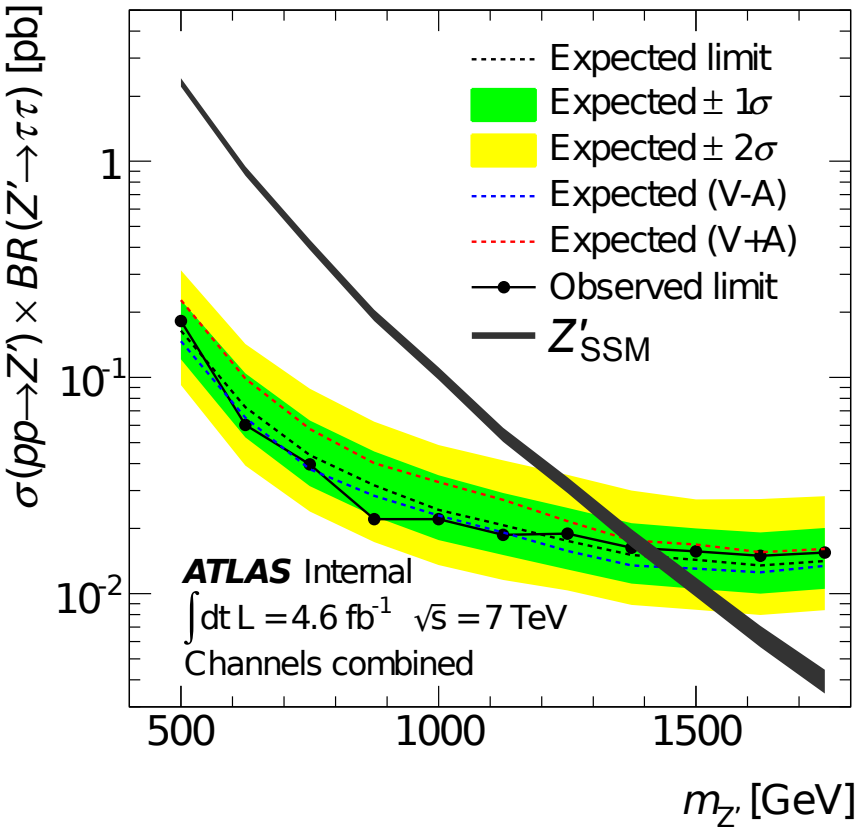

Figure 6.18: The expected and observed upper limits for the combination, showing the change in expected limit for V − A and V + A couplings [97].

conference note.

- *A search for high-mass resonances decaying to $\tau^+\tau^-$ in pp collisions at $\sqrt{s} = 7$ TeV with the ATLAS detector* `arxiv:1210.6604 [hep-ex]` [211] – publication.

Chapter 7

Conclusion

The start-up and last few years of running of the LHC have been a huge success for particle physics. Many properties of the SM have been measured and validated at a new energy scale. Figure 7.1 shows a summary of many of the SM cross section measurements made at ATLAS in the 2011 and 2012 data. A new particle has been observed, and so far, it looks consistent with the SM Higgs boson. This thesis has presented a summary of many of the aspects of tau performance at ATLAS, a $Z \to \tau\tau$ cross section measurement with the 2010 ATLAS dataset, and an upper limit on the cross section times branching ratio for a hypothetical high-mass resonance (Z') decaying to $\tau^+\tau^-$. The $Z' \to \tau\tau$ result is one of several searches for exotic phenomena at ATLAS, many of which are summarized in Figure 7.2. It is the first search for exotic phenomena at ATLAS with reconstructed hadronic tau decays in the final state.

There has not yet been any evidence for new physics beyond the SM among the searches for supersymmetry or other exotic phenomena at the LHC, but exclusions in the TeV scale are just beginning. The LHC is scheduled to begin a new run in 2015 with a target energy of $\sqrt{s} = 13$ TeV. The experiments are busily preparing updgrades to the experiments, updates to the trigger system, and getting ready for new analyses.

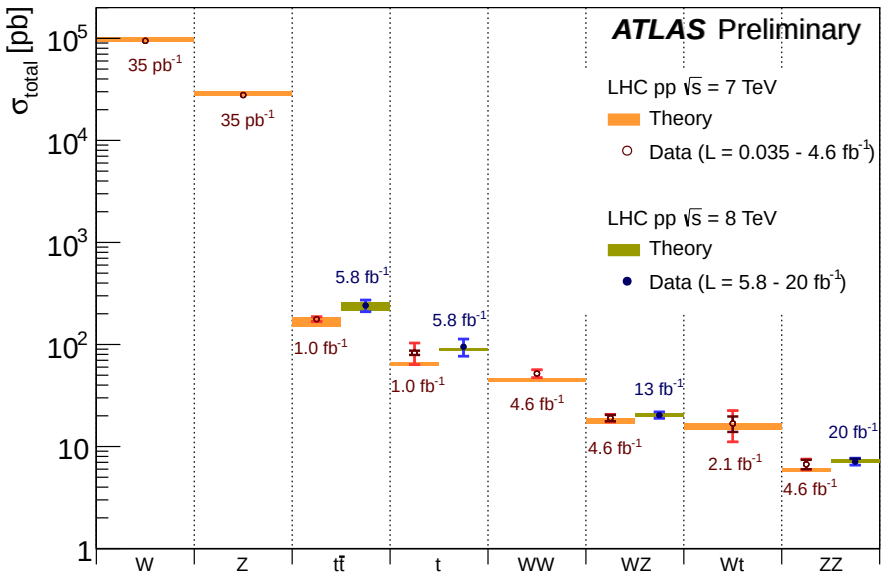

Figure 7.1: Summary of several Standard Model total production cross section measurements, correcting for leptonic branching fractions, compared to the corresponding theoretical expectations. The W and Z vector-boson inclusive cross sections were measured with 35 pb^{-1} of integrated luminosity from the 2010 dataset. All other measurements were performed using the 2011 dataset or the 2012 dataset. The luminosity used for each measurement is indicated close to the data point [238].

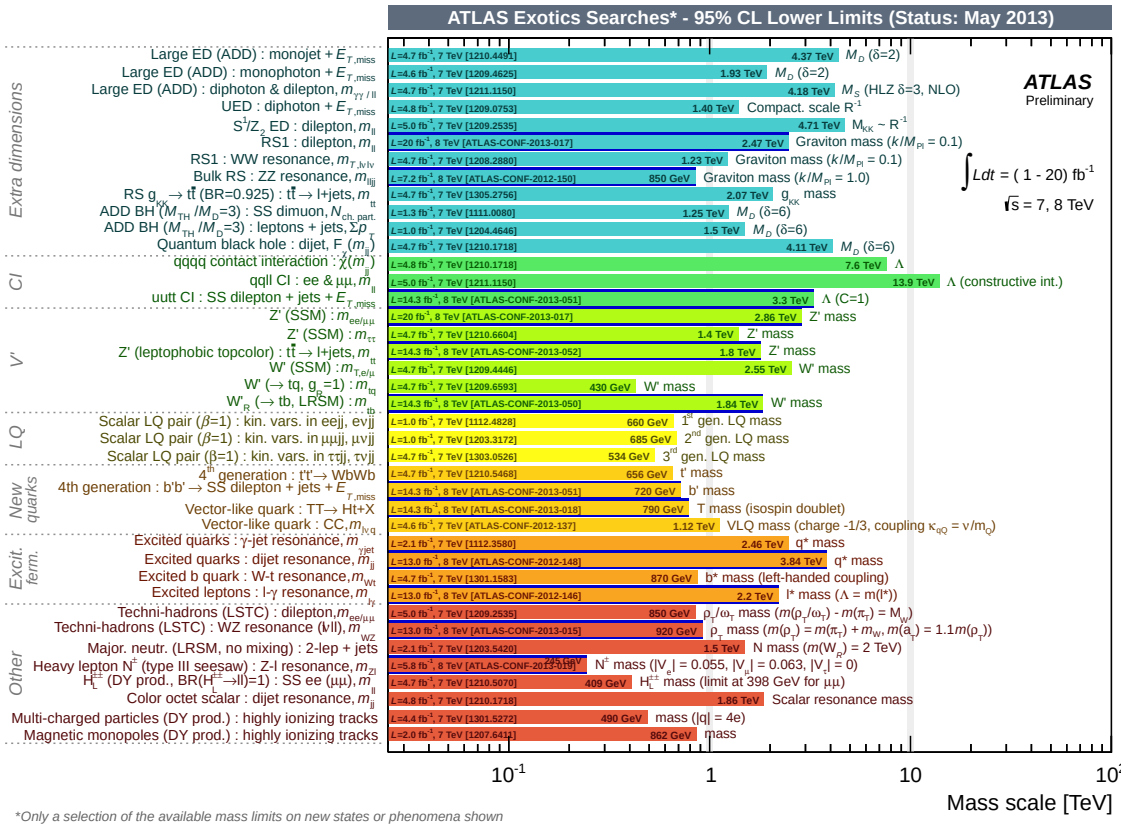

Figure 7.2: Mass reach of several ATLAS searches for new phenomena other than Supersymmetry. Dark blue lines indicate 8 TeV data results with the 2012 data [238].

Appendix A

A review of the Standard Model

Here, I outline my understanding of the highlights in the recent history of rational discourse and scientific experiment that have led physicists to the current, concise, yet often precise, but mysterious model we have for the dynamics of nature's most elementary constituents. I discuss the questions: What is quantum mechanics? And, how did we arrive at the Standard Model? The Standard Model (SM) is the culmination of several incremental breakthroughs in particle physics, many of which will be noted in what follows, but quickly. I begin the discussion with quantum mechanics, because it marks such a huge shift from the classical paradigm, and it's a good story[87].

A.1 Quantum mechanics

A.1.1 A brief history

Quantum mechanics has its roots in the first investigations of the particulate nature of matter and energy at the end of the 19^{th} century, including: Boltzmann's development of statistical mechanics, J.J. Thomson's discovery that cathode rays are composed electrons in 1897 [245], and Planck's studies of thermal radiation. In 1900, in order to explain anomalous measurements of the spectrum of thermal radiation of hot objects (so called "black-body radiation"), Planck predicted that the energy from thermal radiation is quantized in discrete units, $h\nu$, where ν is the frequency of the electromagnetic radiation and h was a new constant (now called "Planck's constant") representing the quantum unit of action [246, 247]. Einstein later used Planck's hypothesis of the quantization of the energy of radiation to explain the photoelectric-effect [248], drawing into question whether light should fundamentally be described by a wave as in classical electrodynamics.

[87] Some especially useful references in writing this summary have been Refs. [239, 240, 241, 236, 242, 243, 244, 33, 136].

Rutherford's scattering experiments of 1911 [249] led Bohr to develop a model of the atom in 1913 that resembles a tiny solar system, with nuclei confined to the center and electrons traveling in bound orbitals [250, 251, 252]. While the Bohr model correctly predicted the Rydberg formula for the atomic spectrum of hydrogen [253], a more satisfactory motivation of its energy levels and a description of its fine-structure would have to wait.

Louis de Broglie's discovery of electron diffraction in 1925 brought the notion of wave-particle duality to matter consisting of fermions [254], in comparison to photons whose wave-particle nature was already known from classical electrodynamics and the discoveries of Planck and Einstein. These observations were first consistently formalized that year in the matrix mechanics of Heisenberg, Born, and Jordan [255, 256, 257], marking the birth of modern quantum mechanics. Their formalism allows for the wave-like interference effects observable in phenomena consisting of quantum particles because, according to the Born rule [258], the probability to observe a system in a specific state is given by the square of a quantum amplitude, which can in general be the sum of complex numbers giving the square of the amplitude negative terms. Pauli then used this formalism in 1926 to predict the atomic spectrum of hydrogen, including the first-order perturbative corrections to the energy due to external electric and magnetic fields [259].

Independently in 1926, Schrödinger developed his theory of wave mechanics and used it to describe the orbital structure of hydrogen [260, 261]. That same year, Schrödinger proved that his wave mechanics and Heisenberg's matrix mechanics were equivalent formulations of the modern theory of quantum mechanics [262]. In 1927, Heisenberg published his uncertainty principle that highlights an important consequence of quantum mechanics: that not all observables are compatible, meaning that some observables, like momentum and position in the same direction, cannot be predicted simultaneously to arbitrary precision, but must always have the product of their quantum mechanical uncertainties be of the order of Planck's constant or greater [263].

Dirac developed the first relativistic quantum theory of electrons when he introduced the Dirac equation in 1928 and used it to predict the existence of antimatter [264, 265]. This laid much of the groundwork for what would later become the modern theory of Quantum Electrodynamics (QED).

Two early seminal textbooks attempt to clarify the principles underlying quantum mechanics. The first is Dirac's *The Principles of Quantum Mechanics* (published in 1930) [266], which pedagogically motivates the necessity of quantum mechanics to describe superpositions of states. The second is John von Neumann's *The Mathematical Foundations of Quantum Mechanics* (published in 1932) [267], written during his time as a founding member of the Institute for Advanced Studies. In his book, von Neumann axiomatized quantum mechanics as fundamentally describing the linear algebra of state vectors in a Hilbert space (or a direct product of them in multi-particle systems).

Observables are represented by Hermitian operators with possible outcomes corresponding to their eigenvalues:

$$\hat{H}\ |n\rangle = E_n\ |n\rangle\ ,$$

and the probability of observing an outcome is given by the Born rule:

$$P(n) = |\ \langle n|\psi\rangle\ |^2\ .$$

In the book's introduction, von Neumann comments on the success quantum theory had already had in predicting experiments throughout the 1920s, but he also noted the conceptual revolution the theory was bringing [267]:

> And, what was fundamentally of greater significance, was that the general opinion in theoretical physics had accepted the idea that the principle of continuity ("natura non facit saltus"), prevailing in the perceived macrocosmic world, is merely simulated by an averaging process in a world which in truth is discontinuous by its very nature.

With these stable foundations, the known consequences of quantum theory continued to build. In 1940, Pauli discovered the *spin-statistics theorem*[88] which fundamentally constrains the statistics obeyed by identical particles: whether their state is even (bosons) or odd (fermions) under exchange, depends directly on the spin of the particles. Integer-spin particles must be bosons, and half-integer-spin particles must be fermions [268]. This single fact has the dramatic observable consequence that the spin-$\frac{1}{2}$ fermions of the SM form stable matter by stacking their states in bound systems like nuclei, atoms, and molecules, while the spin-1, force-carrying bosons are free to fill the same state.

This and other developments have led to rapid progress in the last century in the understanding and applications of quantum theory. Some of the applications of quantum mechanics include: forming the framework for understanding chemical bonding in the field of computational chemistry, describing many of the electrical properties of semiconductors underlying the current technology of electrical transistors and memory devices, the development of lasers, and of course, successfully modeling the outcomes of generations of scientific experiments studying a range of phenomena from cold ion traps to high-energy particle colliders.

A.1.2 The measurement problem

Since quantum mechanics fundamentally involves some notion of probability and introduces some strange concepts (*e.g.* superpositions), there has been a lot of trouble over how to interpret the theory. Problems like—what do the elements of randomness in the theory say about reality? and

[88] The source and consequences of the spin-statistics theorem are discussed in more detail in Appendix A.1.4.

specifically, how is the outcome of a measurement determined?—are still debated among physicists today.

The *Copenhagen interpretation* of quantum mechanics grew out of discussions between Bohr, Heisenberg, and others in the years 1924–1927. It postulates that isolated quantum systems evolve under unitary evolution according to the Schödinger equation, but that when a system is *measured* by an outside agent, the wave function (read state vector) instantly *collapses* into a single eigenstate of the observable, a non-unitary operation.

A particularly bizarre consequence of this is highlighted by the Einstein-Podolsky-Rosen (EPR) thought experiment published in 1935 [269], where an isolated quantum system of two bodies is in a coherent quantum state, *i.e.* the two bodies are *entangled*. Then, the two bodies are brought sufficiently far apart that they are causally separated. One is then asked what the outcome will be of measurements of two non-commuting observables, if one observable is measured from one body and the second simultaneously from the other (*i.e.* outside the light cone of the first measurement). A common hypothetical implementation of the experiment is to measure orthogonal components of the spins of a spin-0 system that decays into two spin-$\frac{1}{2}$ particles[89] or decays into two photons which are correlated to have opposite polarizations. EPR point out that assuming that: (1) the laws of physics are only allowed to act *locally*, meaning the measurement of one decay product cannot have an immediate effect on the other, and that (2) the physical observables in question are *real* or have *counterfactual definiteness* in the sense that it is meaningful to talk about the status of observables independent of a particular measurement, *is in direct contradiction* with the entangled observables being non-commuting. Because according to quantum mechanics, non-commuting observables will satisfy an uncertainty relationship. The authors were so repulsed by the idea of two observables not having simultaneous reality that they were "thus forced to conclude that the quantum-mechanical description of physical reality given by wave functions is not complete" [269].

Years later, in 1964, John S. Bell followed the reasoning of the EPR thought experiment, and proved his now famous *Bell's theorem* [270] which shows that any theory with observables that have local elements of reality, or that depend on other so called "*local hidden variables*", will not predict the correlations required by quantum mechanics. This is quantified in the relationships called the "*Bell's inequalities*" for simultaneous measurements of non-commuting observables. And so while quantum mechanics served as a very predictive framework, it remained controversial whether the theory is complete if one wants to retain the common notions of locality and counterfactual definiteness. Remarkably, the experiments of John Clauser and Stuart Freedman in 1972 [271] and Alain Aspect in 1982 [272, 273] definitively showed that Bell's inequalities are violated in actual

[89] This means the system is in the singlet state: $\frac{1}{\sqrt{2}}(\uparrow\downarrow - \downarrow\uparrow)$.

implementations of EPR-like experiments, using laser-excited cascade sources of two photons with correlated polarizations. After which, it became clear that nature *does not* respect together the concepts of locality and counterfactual definiteness, and that therefore a theory relying on local hidden variables cannot describe quantum phenomena.

In the Copenhagen interpretation of quantum mechanics, this paradox is avoided by not claiming that quantum mechanics describes reality, that it only describes the probabilities of measurements, and therefore does not have counterfactual definiteness. Further, it rejects locality[90] by allowing for instantaneous wave function collapse to describe measurements of entangled states, what Einstein called "spooky action at a distance". While still controversial, the Copenhagen interpretation of quantum mechanics has been regarded as the standard interpretation among physicists since its inception.

Some of the mystery of apparent wave function collapse has been resolved by the modern theory of *decoherence*, which explains why superpositions of eigenstates of position or charge[91] (or other macroscopic observables) are never observed, due to the interactions of a quantum system and the many more degrees of freedom in its environment (including the measuring device). H. Dieter Zeh was one of the first to suggest the plausibility of this mechanism in his paper published in 1970, where he says [275]:

> Superpositions of states with different charge therefore cannot be observed for similar reasons as those valid for superpositions of macroscopically different states: They cannot be dynamically stable because of the significantly different interaction of their components with their environment.

In the 1980s, the theory of decoherence was worked out in more detail in the work of Zurek [276, 277] and Joos and Zeh [278], and is summarized in a textbook by Giulini, Joos, Kiefer, Kupsch, Stamatescu, and Zeh [279]. Essentially, because measurement inherently involves breaking the isolation of a quantum system, the process of decoherence rapidly takes a system in a pure quantum state to being an incoherent mixture of states, where each state is weighted by the squares of the amplitudes for each possible measurement.

In the modern version of the Copenhagen interpretation, the process leading to wave function collapse is recognized as an emergent phenomena from the dephasing effects of decoherence, but which of the possible eigenstates is actually observed in any given measurement is still inherently

[90] Although accepting the Copenhagen interpretation requires a strict loss of locality, it preserves *causality* because the results of the entangled measurements, while correlated, are inherently random and therefore cannot be used to send signals faster than light.

[91] The basis of states that are eigenstates of position and charge are selected out of any other arbitrary basis, fundamentally because the Lagrangian describing the interactions of a system has terms that are local in that basis [274].

indeterministic. The Copenhagen interpretation still views that during a measurement, the terms in a state vector representing the other possibilities not observed in a measurement are dropped, and the state is immediately re-normalized in the observed eigenstate (including any required non-local collapse for entangled systems).

One of the alternative interpretations of quantum mechanics, the *many-worlds interpretation*, first developed by Hugh Everett in 1957 [280] and popularized Bryce DeWitt in the 1970s [281], removes the non-unitary operation of wave function collapse entirely from the theory. It postulates that since any isolated quantum system evolves unitarily under the Schrödinger equation, the state of universe itself being a closed system, evolves unitarily under the Schrödinger equation, continuously. The many worlds interpretation has influenced and been heavily influenced by the development of the theory of decoherence. Decoherence explains why superpositions of observable eigenstates decouple in the presence of an environment with many more degrees of freedom, although the state of the total system, including the environment, remains a pure quantum state evolving under the Schrödinger equation. According to the many worlds interpretation, these decoupled mixtures of states are each independently *real* although they are effectively disconnected observationally. This leads to the fantastic claim that all possibilities from all possible interactions have a corresponding branch in the immensely fragmented universal state vector of the multiverse, but it remains a controversial proposal among physicists[92]. The many worlds interpretation succeeds in removing the ad hoc wave collapse from quantum mechanics; the multiverse continues to evolve unitarily. It also succeeds in preserving locality because interference and the coordinated acts of entangled systems happen naturally when different terms in the universal state vector are coherent.

There are also other interpretations of quantum mechanics including *de Broglie-Bohm theory*, *the theory of consistent histories*, and others that generally try to straddle some labored construction to preserve locality or a notion of realism or both, but people are thinking[93]. And so it remains that while quantum mechanics has formed a highly predictive framework for predicting experiments, the metaphysical implications of the theory and what a state vector actually corresponds to in reality are not understood.

[92] As I heard one put it once during lunch in the Penn faculty lounge: "Are we supposed to believe that there is a universe where I am throwing my food at you?"

[93] There has even been a recent claim that quantum mechanics cannot be interpreted statistically [282].

A.1.3 Fields

In physics, a *field*[94] generally means a mathematical structure which has a tensor (scalar, vector, or higher rank) defined at every point on a manifold. Most often, the manifold is space-time. A field being a concept used throughout classical physics, examples of scalar fields include the temperature of some body or the Newtonian gravitational potential in some space. Examples of vector fields include the velocity of wind or electric and magnetic fields.

In Quantum Field Theory (QFT), the field itself plays the leading role as the dynamical variable. Naively, one may have thought to start with the position and momentum of particles as the fundamental dynamical variables, but instead particles emerge from the theory, and can be thought of as the minimum quanta of excitation in a given field, localized in space-time and momentum-space in wave packets. According to the process of canonical quantization[95] the dynamical variables of a quantum theory are operators in a Hilbert space. From this, one can calculate decay rates and scattering cross sections of relativistic quantum systems, as will be discussed in Appendix A.1.5.

QFTs can be made compatible with Einstein's special theory of relativity [284], describing relativistic dynamics, by requiring that the operators defining the four-momentum of the system satisfy the Poincaré algebra, the implications of which will be discussed in the following section. It is still an open question: what is the unique[96] quantum theory that in the classical limit reduces to Einstein's general theory of relativity [285], the modern classical field theory of gravity. General relativity is particular as a field theory in that it relates the stress-energy tensor field to the metric of space-time. A resolution of this issue of how to quantize gravity has been a primary pursuit in research in theoretical physics since the developments of relativity and quantum theory.

As we will discuss in Appendix A.1.6, in particle physics, it is useful to use QFTs with a particular type of symmetry among the internal degrees of freedom of the field (components of the tensor) called a "*gauge symmetry*". The U(1) gauge invariance of the classical electromagnetic potential has been know since the 19$^{\text{th}}$ century, but many thought the electromagnetic force fields ($\vec{E}$ and $\vec{B}$, or $F^{\mu\nu}$ covariantly) were fundamental and the potential fields (A^{μ}), used to derive them, were just a mathematical tool. This issue was shown to be testable in principle when Werner Ehrenberg and Raymond E. Siday first predicted the *Aharonov-Bohm effect* in 1949 [286], which was was later

[94] Not to be confused with the more basic concept of a field from abstract algebra, which defines a field as "a ring whose nonzero elements form an abelian group under multiplication", or equivalently as "a mathematical set on which the usual operations addition, subtraction, and multiplication are defined for all elements, and division for non-zero elements" (paraphrasing Wikipedia [283]). Tensors themselves are formally constructed as being linear functions of vectors, which rely on the mathematical concepts of vectors spaces, which in turn depend on the definition of a vector sum and scalar product, which depend on the concept of an algebraic field.

[95] Canonical quantization is discussed briefly in Appendix A.1.4.

[96] String theory is considered by many as a candidate for the quantum theory of gravity, but it is still being understood and is only defined perturbatively. Most agree that a quantum theory of gravity will require new frameworks beyond QFT.

independently predicted by Yakir Aharonov and David Bohm in 1959 [287]. The effect is predicted to occur in a thought experiment where an electron travels through a region where $\vec{B} = 0$ effectively, but the vector potential $\vec{A}$ is not trivial, like near the outside of a long solenoid or through the hole along the axis of symmetry of a toroid. Due to traveling through such a region, quantum mechanics predicts that an electron should take on a phase-shift. In an electron interference experiment, like a Young's double-slit, arranged with such a vector potential, the phase-shift should be observable. The effect was first experimentally verified by Robert G. Chambers in 1960 [288], and confirmed later by Peshkin *et al.* [289] and Osakabe *et al.* [290]. Physicists now view the gauge fields as more fundamental and the effects of force fields as being a result of the constraints of the gauge symmetry.

A.1.4 The importance of symmetry

Complementary to the conceptual revolutions that were happening in modern physics during the late 19^{th} and early 20^{th} century due to the development of the theories of quantum mechanics and general relativity, several ideas in mathematics also advanced at that time and have forever changed how theories of physics are constructed. Most importantly were several developments that deepened the understanding of the implications of symmetry on physical systems, including a maturing of the fields of variational calculus, differential geometry, group theory, and algebraic geometry.

Noether's theorem

Foremost is *Noether's theorem* of differential symmetries, proved by Emmy Noether in 1915 and published in 1918 [291], which explained that physical quantities that are conserved in time, like energy or momentum, are fundamentally a consequence of the symmetries of the theory. It says that any differentiable symmetry of the action of a physical system has a corresponding conservation law. It generalizes the constants of motion observed in Lagrangian and Hamiltonian mechanics. For example, energy conservation is a consequence of time-translation invariance; angular momentum conservation is a consequence of rotation invariance, etc. (see Table A.1). This revolutionized how physicists describe their theories in the most fundamental and compact form: by specifying the symmetries obeyed by a system. The study of differential and continuous symmetries is the study of *Lie groups*[97], a field founded by the work of Sophus Lie and Friedrich Engel, and extended by Élie Cartan, who succeeded in classifying all the simple Lie groups, which can each be thought of as a differentiable manifold that is simply connected, and where each point on the manifold represents an

[97] Many Lie groups are especially useful in physics, for example to describe gauge invariance, as discussed in Appendix A.1.6. Examples of Lie groups include the special orthogonal and special unitary groups, $\mathrm{SO}(n)/\mathrm{SU}(n)$, which are the set of all $n \times n$ orthogonal/unitary matrices with determinate 1, which describe the group of rotations in the space $\mathbb{R}^n/\mathbb{C}^n$, respectively.

element of a non-abelian group[98]. Much of the mathematical properties of Lie groups were proved or conjectured independently by Wilhelm Killing.

Poincaré invariance ⇒ representations

Many important constraints on the types of models that are capable of describing fundamental physics are a result of requring the theory be covariant with respect to the Poincaré group, the group of isometries of Minkowski spacetime, and therefore consistently describe relativistic dynamics.

In 1939, Eugene Wigner classified the irreducible unitary representations of the Poincaré group [293]. Under the constraint that the states are eigenstates of mass, the valid representations are the familiar scalars, spinors, vectors, and 2-forms. Combined with consequences of the spin-statistics theorem, this fundamentally limits the types of fields and spins allowed in a relativistic QFT (see Table A.2).

Poincaré invariance ⇒ canonical commutation relations

Another essential implication of the requirements of Poincaré invariance is evident in the practice of *canonical quantization*. A quantum field, ϕ, and its conjugate momentum, π, become operators in a Hilbert space: $\hat{\phi}$, $\hat{\pi}$; consequently, the classical expressions for the four-momentum of the field, P^μ, and its Lorentz charges, $M^{\mu\nu}$, can be derived as operators. Requiring that $\hat{P}^\mu$ and $\hat{M}^{\mu\nu}$ satisfy the Poincaré Lie algebra as generators enforces a set of commutation relations from which one can

[98] It is remarkable that the study and classification of Lie groups effectively unified concepts in differential geometry and abstract algebra, and eventually led to Felix Klein's proposal of his influential Erlangen program [292], where he proposed that geometries be classified by their associated symmetries.

Table A.1: Conserved Noether currents in the Standard Model.

symmetry	Lie group		Noether charge
space-time translations	$\mathrm{R}^{1,3}$	$\Longleftrightarrow$	four-momentum
spacial rotations	SO(3)	$\Longleftrightarrow$	angular momentum
gauge	$\mathrm{U(1)_{EM}}$	$\Longleftrightarrow$	EM charge
gauge	$\mathrm{U(1)_Y}$	$\Longleftrightarrow$	weak hypercharge
gauge	$\mathrm{SU(2)_L}$	$\Longleftrightarrow$	weak isospin
gauge	$\mathrm{SU(3)_C}$	$\Longleftrightarrow$	color

Table A.2: A modern summary of Wigner's classification of the irreducible unitary representations of the Poincaré group.

representation	spin	statistics	typical field	example
scalar	0	boson	ϕ	Higgs
spinor	1/2	fermion	ψ_a	quarks, leptons
vector	1	boson	A_μ	vector bosons
vector × spinor	3/2	fermion	$\psi_{\mu\alpha}$	gravitino
vector × vector	2	boson	$g_{\mu\nu}$	graviton

derive the *equal time commutation relations* that are often assumed in QFT textbooks:

$$\begin{aligned}\left[\hat{\phi}(t,\vec{x}),\ \hat{\phi}(t,\vec{y})\right] &= \left[\hat{\pi}(t,\vec{x}),\ \hat{\pi}(t,\vec{y})\right] = 0\,,\\ \left[\hat{\phi}(t,\vec{x}),\ \hat{\pi}(t,\vec{y})\right] &= i\,\hbar\,\delta^3(\vec{x}-\vec{y})\,,\end{aligned}$$

for a scalar boson field, ϕ, for example.

This is also how one can motivate the constraints of the spin-statistics theorem. For spinor representations, one is forced to satisfy anti-commutation relations instead of commutation relations for the field and its conjugate momentum, ultimately due to sign constraints in the forms of the single-particle plane-wave solutions of the Dirac equation. Consequently anti-commutation relations also have to be satisfied by creation and anihilation opperators for single particles excitations of a spinor field:

$$\begin{aligned}\left\{\hat{b}(\vec{k},s),\hat{b}(\vec{k}',s')\right\} &= \left\{\hat{b}^\dagger(\vec{k},s),\hat{b}^\dagger(\vec{k}',s')\right\} = 0\,,\\ \left\{\hat{b}(\vec{k},s),\hat{b}^\dagger(\vec{k}',s')\right\} &= \delta^3(\vec{k}-\vec{k}')\,\delta_{ss'}\,.\end{aligned}$$

From the first line with creation opperators, $\hat{b}^\dagger$,

$$\left\{\hat{b}^\dagger(\vec{k},s),\hat{b}^\dagger(\vec{k}',s')\right\} = \hat{b}^\dagger(\vec{k},s)\,\hat{b}^\dagger(\vec{k}',s') + \hat{b}^\dagger(\vec{k}',s')\,\hat{b}^\dagger(\vec{k},s) = 0$$

$$\Rightarrow \qquad \hat{b}^\dagger(\vec{k},s)\,\hat{b}^\dagger(\vec{k}',s') = -\hat{b}^\dagger(\vec{k}',s')\,\hat{b}^\dagger(\vec{k},s)$$

one can see the interesting consequence that a state created with two spinors is anti-symmetric under exchange, and is said to obey "fermion statistics". Boson fields, on the other hand, satisfy (normal) commutation relations, and are symmetric under exchange. Another point to note is that if a state has two identical fermion creation operators applied:

$$\hat{b}^{\dagger 2} = \frac{1}{2}\left\{\hat{b}^\dagger,\hat{b}^\dagger\right\} = 0\,,$$

the amplitude is destroyed. Therefore no two identical fermions (spinors) can be in the same state.

Coleman-Mandula theorem

The Coleman-Mandula theorem [294] prohibits types of symmetries for a relativistic QFT that are not a simple direct product of the Poincaré group and internal symmetries. Therefore, the Coleman-Mandula theorem limits the symmetry groups of relativistic QFTs to direct products of the form:

$$\text{(Poincaré group)} \times \prod\text{(internal symmetry groups)}\,.$$

Internal symmetries are often described by gauge symmetries, as discussed in Appendix A.1.6, and are represented by unitary Lie groups such as U(1), SU(2), etc. In the case of the SM, the total

symmetry group of the field theory is [99]

$$(\text{Poincaré group}) \times \mathrm{SU}(3)_{\mathrm{C}} \times \mathrm{SU}(2)_{\mathrm{L}} \times \mathrm{U}(1)_{\mathrm{Y}} \,,$$

which will be discussed in more detail in Appendix A.2. According to the assumptions of the Coleman-Mandula theorem, a QFT cannot have symmetries that mix the internal degrees of symmetry and Poincaré symmetry, which is satisfied by the fields being Wigner representations: scalars, vectors, and spinors.

The Haag-Lopuszanski-Sohnius theorem (HLS) [38], generalizes the assumptions of the Coleman-Mandula theorem to not only consider symmetries that have a Lie algebra, but to also consider symmetries that have a Lie superalgebra, which in general can have anti-commutation relations among the generators. The HLS theorem demonstrates that the only consistent combination of Poincaré and internal symmetries that is not a simple direct product is the *supersymmetry algebra*. This is one of the motivations for considering supersymmetry as a natural extension of the SM, discussed briefly in Section 2.5.1.

A.1.5 Scattering theory

QED and renormalization

Having discussed how naturally constrained the framework of QFT is, let us survey how it developed and discuss an important way it is predictive. The first successful relativistic QFT to be developed was Quantum Electrodynamics (QED), which has its roots in the formulations of Dirac.

QED initially seemed to not be a predictive theory because perturbation series describing any interactions appeared to be divergent. These so-called "*ultraviolet*" divergences are a symptom of the fact that QFT describes interactions as ideal points in space-time and describes space-time as an ideal continuum. An example of the problem is evident even in the classical EM self-energy of a point charge. Certain statistical and quantum mechanical constructions are ill defined in the small-distance/high-energy continuum limit, unless the limit is taken very carefully. The problem deals directly with the fact that to evaluate the quantum mechanical amplitude for a particle to propagate from a point A to a point B involves an infinite sum of amplitudes of the possible intermediate processes. Analogously the amplitude for the fundamental QED interaction, the photon-electron vertex, involves an infinite sum of processes within an effective vertex (see the illustrations in Figure A.1).

In the latter half of the 1940s, a series of developments by Julian Schwinger [297, 298, 299] and independently by Sin-Itiro Tomonaga [300, 301, 302, 303, 304], using the canonical operator formalism, and also independently by Richard Feynman [305, 306], using his path integral formulation

[99] The Poincaré group itself is often written as $\mathrm{R}^{1,3} \times \mathrm{O}(1,3)$, the direct product of space-time translations and Lorentz boosts/rotations.

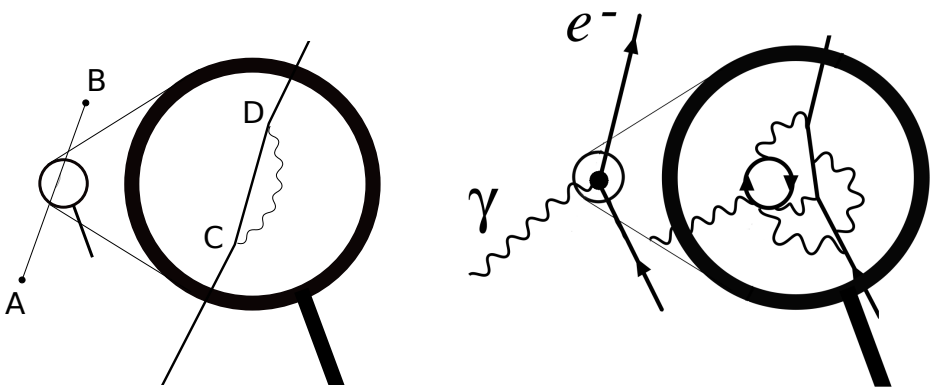

Figure A.1: Diagrams illustrating that the QED fermion propagator (left) and the QED vertex (right) are inherently an infinite sum of indistinguisable quantum amplitudes that result in an effective mass and coupling, respectively, when renormalized [295, 296].

of quantum mechanics [307], showed that the divergent terms could be *renormalized* to give finite predictions. In 1949, Freeman Dyson proved the equivalence of the operator and path integral formulations of QED [308], and he formalized perturbative problems in QED as depending on the Dyson series for the expansion of the S-matrix [309]:

$$\begin{aligned}\hat{S} &= \mathrm{T}\left[\exp\left(-i\int d^4x'\,\hat{\mathcal{H}}_{\mathrm{I}}(x')\right)\right] \\ &= \sum_{n=0}^{\infty}\frac{(-i)^n}{n!}\int\ldots\int d^4x_1\ldots d^4x_n\,\mathrm{T}\left[\hat{\mathcal{H}}_{\mathrm{I}}(x'_1)\ldots\hat{\mathcal{H}}_{\mathrm{I}}(x'_n)\right]\,,\end{aligned}$$

to which we will return.

Renormalization involves rescaling the field strengths, masses, and couplings that are the input parameters in the Lagrangian of a theory to account for the *finite* shifts in the effective mass or coupling due to the infinite sum of quantum corrections. Not only does renormalization succeed in producing finite results in QED, it additionally predicts that the effective coupling should scale with the energy exchanged in an interaction. Essentially, an electron has a cloud of radiated photons and e^+e^- pairs from quantum corrections that effectively screens part of the EM coupling. A higher-energy interaction probes deeper into this virtual cloud, resulting in an effective coupling that rises with the energy exchanged. The scaling of couplings with energy is described by the *renormalization group*.

Initially physicists were generally skeptical about the mathematical soundness of renormalization as a way to remove infinities in the theory. Beginning in the 1970s, however, physicists began to better appreciate the role of the renormalization group and its applications in effective field theories. Kenneth G. Wilson [310, 311, 312] and others demonstrated the usefulness of the renormalization group in statistical field theories applied to the physics of condensed matter, where it provides

important insights into the behavior of phase transitions.

Green's functions

It turns out that many calculations in QFT reduce to calculating *Green's functions*, also called "*n-point correlation functions*", which are defined as the vacuum expectation value of n field operators. The 2-point function is simply the Feynman propagator:

$$G^{(2)}(x,y) = \quad x \quad \text{—(blob)—} \quad y \ ,$$

which can be interpreted as the quantum amplitude for a particle created at a space-time position x to propagate to a position y. The blob in the middle of the propagator indicates a sum over all possible intermediate quantum processes that result in the same final state. A rather beautiful calculation, shown in detail in many QFT textbooks[100], proves that the n-point correlation function, being the vacuum expectation value of the product of n Heisenberg[101] field operators, in the vacuum of the interacting Hamiltonian, $|\Omega\rangle$, can be expanded and factored as follows:

$$\begin{aligned} G^{(n)}(x_1,\ldots,x_n) &= \langle\Omega|\mathrm{T}\left[\hat{\phi}_{\mathrm{H}}(x_1)\ldots\hat{\phi}_{\mathrm{H}}(x_n)\right]|\Omega\rangle \\ &= \frac{\langle 0|\mathrm{T}\left[\hat{\phi}_{\mathrm{I}}(x_1)\ldots\hat{\phi}_{\mathrm{I}}(x_n)\,\hat{S}\right]|0\rangle}{\langle 0|\hat{S}|0\rangle} \\ &= \frac{\sum(\text{external diagrams})\cdot\cancel{\exp\left(\sum(\text{vacuum bubbles})\right)}}{\cancel{\exp\left(\sum(\text{vacuum bubbles})\right)}} \\ &= \sum(\text{external diagrams})\,, \end{aligned}$$

where in the above, we have expanded the in-coming and out-going states as momentum eigenstates in the interaction picture[102], with plane-wave solutions of the free Hamiltonian. The Dyson series for the S-matrix defined above gives the perturbative expansion for small coupling, where each term results in diagrams with more interaction vertices suppressed by more factors of the coupling constant. When expanded, the series results in diagrams with products of so called "*vacuum bubbles*" that are not connected to the external part of the diagram like

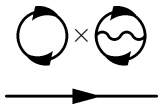

,

[100] See, for example, Peskin and Schroeder [313] or David Tong's lecture notes [314].

[101] In the Heisenberg picture the operators carry the time dependence in the Hilbert space and state vectors are stationary.

[102] In the interaction picture the operators carry the time dependence only due to the interaction terms in the Hamiltonian, and are stationary in the free theory. The state vector carries the time-dependence due to the free Hamiltonian.

but these vacuum bubbles factor into exponentials and cancel in the numerator and denominator. Therefore in the sum over all diagrams, one only has to consider diagrams with parts that are externally connected. Further, due to the *cluster decomposition theorem* [315, 316], diagrams that do not connect all points, but instead have two or more disconnected parts, contribute only a part of measure zero to the total amplitude, because the amplitude vanishes for diagrams with space-like separated parts, ultimately a consequence of locality in QFT.

For example, $G^{(2)}$ for QED is given by:

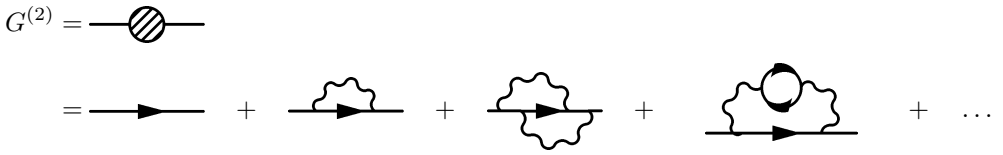

$G^{(4)}$, describing $2 \to 2$ interactions, is given by

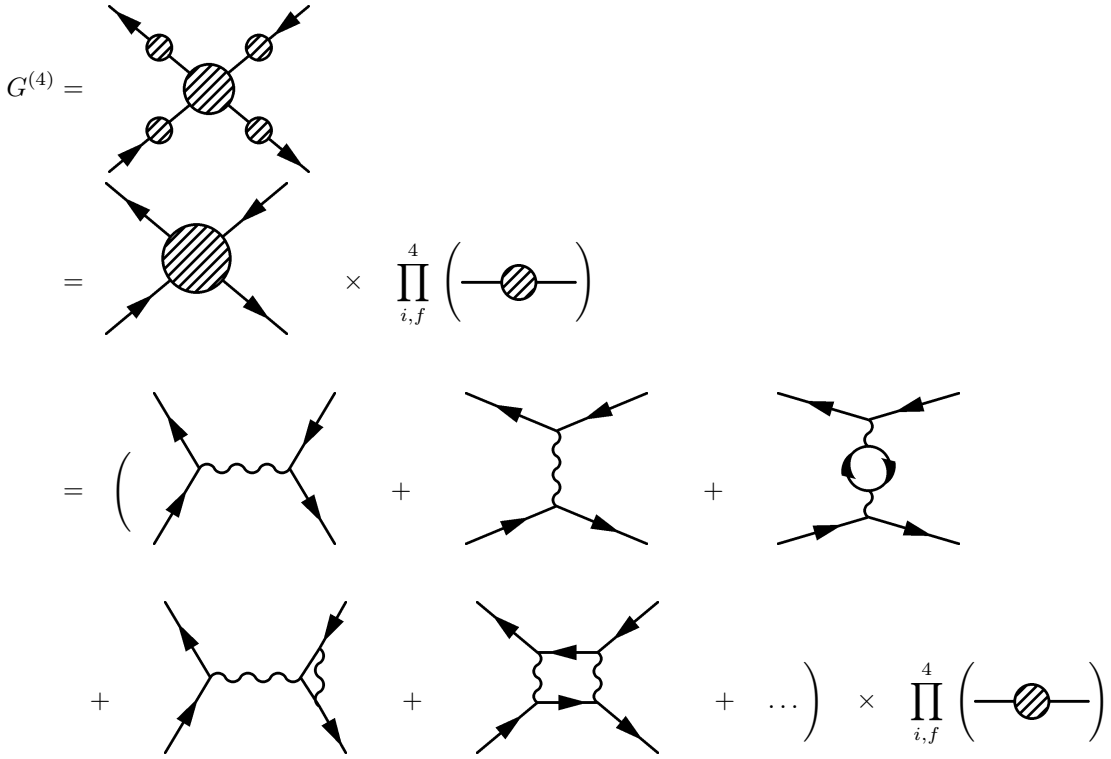

The reduction formula

Again assuming that in the problems of interest, the in-coming and out-going states will be in a narrow wave-packet superposition of momentum eigenstates, one can show that the matrix elements of the S-matrix that give the quantum amplitude for some scattering process can be expressed

according to the *Lehmann-Symanzik-Zimmermann (LSZ) reduction formula* [317] as

$$
\begin{aligned}
S_{fi} &= \langle f|\hat{S}|i\rangle \\
&= \tilde{G}^{(n)}(-p_f,\ldots,p_i)\prod_f\left(\tilde{G}^{(2)}(p_f)\right)^{-1}\prod_i\left(\tilde{G}^{(2)}(p_i)\right)^{-1} \\
&= \quad\times\prod_{i,f}^{n}\left(\quad\right)^{-1} \\
&= \quad -i\mathcal{M} \\
&= -i\,\mathcal{M}\,(2\,\pi)^4\,\delta^4\left(\sum p_i-\sum p_f\right)\,,
\end{aligned}
$$

where $\tilde{G}^{(n)}$ denotes the momentum-space Fourier transform of the space-time n-point correlation function:

$$\tilde{G}^{(n)}(p_1,\ldots,p_n)\equiv\prod_i^n\left[\int\frac{d^4p_i}{(2\,\pi)^4}e^{-i\,p_i\cdot x_i}\right]\,G^{(n)}(x_1,\ldots,x_n)\,.$$

The expansion of the in-coming and out-going states as momentum eigenstates introduces inverse factors of the propagators that cancel the factors of propagators appearing in $G^{(n)}$. The irreducible matrix element, $\mathcal{M}$, is defined as the remaining part of the diagram, with the external lines held on mass-shell, but summing over all connected intermediate possible diagrams, and integrating over all possible virtual momenta. An overall momentum-conserving δ-function will always result, and a factor of $-i$ is often factored out by convention.

Scattering cross sections

The scattering theory developed from QFT is especially useful for describing the event rates in experiments at particle colliders. At particle colliders like the LHC, two anti-parallel beams of particles of known energies are squeezed to cross in a small cross-sectional area of the order of a few hundred square microns. In such a scenario one can show that the differential collision rate for some process, dN/dt, factors into the luminosity, L, that characterizes the flux of particles in the beam per area per time, and the differential cross section, $d\sigma$, an area proportional to the rate for that process:

$$dN=\varepsilon\,L\,dt\,d\sigma\,.$$

The factor, ε, is a dimensionless variable to account for experimental inefficiencies in reconstructing/identifying/selecting the process. The differential scattering cross section of $2 \to n$ process can be calculated from the $n+2$-point function, which can be expressed in terms of its irreducible matrix element as

$$d\sigma = \prod_f \left(\frac{d^3 p_f}{(2\,\pi)^3\, 2\, E_f} \right) \frac{|\mathcal{M}|^2}{4\, E_1\, E_2\, |v_1 - v_2|}\, (2\,\pi)^4\, \delta^4\Big(p_1 + p_2 - \sum_f p_f\Big)\,.$$

In the case of $2 \to 2$ scattering with energies high enough to neglect the masses of the in-coming or out-going particles, one can further simplfy $d\sigma$ to

$$\left.\frac{d\sigma}{d\Omega}\right|_{\rm CM} = \frac{1}{64\,\pi^2\, E_{\rm CM}^2}\, |\mathcal{M}|^2\,,$$

where CM denotes that the $d\sigma$ is valid in the center-of-momentum reference frame, and $E_{\rm CM}$ is the center-of-momentum energy of the incoming two particles.

Integrating dN over some running time for the experiment and over the kinematic phase-space of the process in question gives the theoretical prediction for the expected number of events observed:

$$\begin{aligned} N &= \int dt\, L \int d\sigma\, \varepsilon \\ &= \left(\int dt\, L \right) A\, C\, \sigma\,, \end{aligned}$$

where A is a dimensionless variable to account for the *acceptance*, the fraction of events produced in the instrumented fiducial volume selected in the experiment:

$$A = \frac{\int dt\, L \int_{\rm fiducial} d\sigma}{\int dt\, L \int d\sigma} = \frac{\int dt\, L \int_{\rm fiducial} d\Omega\, \frac{d\sigma}{d\Omega}}{\sigma \int dt\, L}\,,$$

and C is a dimensionless variable to account for the overall experimental *efficiency* to reconstruct and identify events from the process:

$$C = \frac{\int dt\, L \int_{\rm fiducial} d\sigma\, \varepsilon}{\int dt\, L \int_{\rm fiducial} d\sigma} = \frac{\int dt\, L \int_{\rm fiducial} d\Omega\, \frac{d\sigma}{d\Omega}\, \varepsilon(\Omega)}{\int dt\, L \int_{\rm fiducial} d\sigma}\,.$$

In practice, high-energy physics experiments generally estimate these integrals numerically with Monte Carlo methods, using matrix-element event generators and often very detailed simulations[103] of the geometry, material, and instrumentation of the experiments. The integrated luminosity, $\int dt\, L$, is measured independently [179, 318].

A.1.6 Gauge invariance

$\mathrm{U(1)_{EM}}$ local gauge invariance

As discussed previously, gauge invariance plays an important role in constructing the SM. As an example, consider the $\mathrm{U(1)_{EM}}$ gauge invariance of electrodynamics. The fundamental representation

[103] See the brief discussion of ATLAS simulation in Section 3.6.

of U(1) is a complex number with unit modulus, which can be written $e^{i\,\theta}$, where θ is a real number. So U(1) gauge invariance demands that the action be unchanged by a transformation that shifts the phase of the fermion fields:

$$\psi(x) \to \psi'(x) = e^{i\,\theta(x)}\,\psi(x)\,.$$

Note that we are additionally requiring that the gauge invariance be *local*, since $\theta(x)$ being an arbitrary function implies that the phase can be transformed independently at every point in space-time. Consider the impact this has on the Lagrangian for a free Dirac fermion:

$$\mathcal{L} = i\,\bar{\psi}\,\gamma^{\mu}\,\partial_{\mu}\,\psi - m\,\bar{\psi}\,\psi\,.$$

The conjugate field, $\bar{\psi}$, transforms as

$$\bar{\psi}(x) \to e^{-i\,\theta(x)}\,\psi(x)\,.$$

and the phase shift is just right to cancel in the $m\,\bar{\psi}\,\psi$ term. But in the kinetic term, one needs to consider the transformation of $\partial_{\mu}\,\psi$, which accumulates an additional term because we allowed the phase to be local:

$$\partial_{\mu}\,\psi(x) \to e^{i\,\theta}\,\partial_{\mu}\,\psi + i\,e^{i\,\theta}\,\psi\,\partial_{\mu}\,\theta\,.$$

This second term breaks the gauge invariance of the Lagrangian.

Posit that one can introduce an additional four-vector field, A_{μ}, to cancel this second term, making the derivative gauge invariant. The *covariant derivative* is defined:

$$D_{\mu}\,\psi \equiv (\partial_{\mu} - i\,q\,A_{\mu})\,\psi\,,$$

where A_{μ} is referred to as the "*connection*" in the covariant derivative. Let us express the U(1) transformation of A_{μ} as

$$A_{\mu} \to A_{\mu} + \delta A_{\mu}$$

Consider how $D_{\mu}\,\psi$ transforms under U(1):

$$\begin{aligned}
D_{\mu}\,\psi' &= \partial_{\mu}\,\psi' - i\,q\,A'_{\mu}\,\psi' \\
&= e^{i\,\theta}\,\partial_{\mu}\,\psi + i\,e^{i\,\theta}\,\psi\,\partial_{\mu}\,\theta - i\,q\,A_{\mu}\,e^{i\,\theta}\,\psi - i\,q\,\delta A_{\mu}\,e^{i\,\theta}\,\psi \\
&= e^{i\,\theta}\,\underbrace{(\partial_{\mu} - iq\,A_{\mu})}_{D_{\mu}\,\psi}\,\psi + i\,e^{i\,\theta}\,\psi\,\underbrace{(\partial_{\mu}\,\theta - q\,\delta A_{\mu})}_{0} \\
&= e^{i\,\theta}\,D_{\mu}\,\psi\,.
\end{aligned}$$

Note that now the phase will cancel with the $\bar{\psi}$ only if we require the term on the right to be zero, and this constrains how A_{μ} can transform:

$$\Rightarrow \qquad \delta A_{\mu} = \frac{1}{q}\,\partial_{\mu}\,\theta$$

$$\Rightarrow \qquad A_\mu \to A_\mu + \frac{1}{q}\,\partial_\mu\,\theta\,.$$

Now if we replace the derivative in the Lagrangian for the Dirac field with the covariant derivative under U(1), then the entire Lagrangian will be gauge invariant:

$$\begin{aligned}\mathcal{L} &= i\,\bar{\psi}\,\gamma^\mu\,D_\mu\,\psi - m\,\bar{\psi}\,\psi \\ &= i\,\bar{\psi}\,\gamma^\mu\,\partial_\mu\,\psi - m\,\bar{\psi}\,\psi + q\,\bar{\psi}\,\gamma^\mu\,\psi\,A_\mu \\ &= \mathcal{L}_{\text{QED}}\,.\end{aligned}$$

Note that this results in a Lagrangian that no longer describes a free Dirac fermion, but has an additional interaction term between the fermion, ψ, and the gauge boson field, A_μ, describing the photon. The Lagrangian for QED can be derived by requiring local $\text{U}(1)_{\text{EM}}$ gauge invariance.

This is an example of the general fact that demanding local gauge invariance under some gauge group requires the introduction of *gauge boson fields* to serve as the connections in the corresponding covariant derivatives.

Yang-Mills gauge theories

While the importance of the $\text{U}(1)_{\text{EM}}$ gauge invariance of electrodynamics is something that has been recognized since the development of classical electrodynamics, considering gauge invariance under general SU(n) transformations as *the* guiding principle in constructing theories of elementary interactions was first proposed in 1954 by Yang and Mills, in an attempt to describe the isospin invariance observed among the spectrum of hadrons [1].

Any unitary transformation among the internal degrees of freedom of a field, ψ_i, can be written as

$$\psi_i \to \exp\left(i\,\theta^a\,T^a_{ij}\right)\;\psi_j\,,$$

where T^a_{ij} are the generators of the gauge symmetry group, and θ^a are dimensionless real parameters. For infinitesimal transformations, one can expand the exponential:

$$\psi_i \to \left(1 + i\,\theta^a\,T^a_{ij}\right)\;\psi_j\,.$$

One can define a covariant derivative:

$$D_\mu\,\psi_i \equiv \partial_\mu\,\psi_i + i\,g\,A^a_\mu\,T^a_{ij}\,\psi_j\,.$$

where gauge boson fields, A^a_μ, serve as connections and g is a free dimensionless coupling parameter. Then one can show[104] that the covariant derivate $D_\mu\,\psi_i$ will transform with the same phase factor

[104] See, for example, Peskin chapter 15 [313], and Martin chapter 10 [243].

as the fermion field it acts on, provided that the gauge fields transform as

$$A^a_\mu \to A^a_\mu - \frac{1}{g}\,\partial_\mu\,\theta^a - f^{abc}\,\theta^b\,A^c_\mu\,,$$

where f^{abc} are the structure constants of the Lie algebra of the gauge group. Note that for abelian groups, the structure constants are zero, which is why there was not a third term in the example for $\mathrm{U(1)_{EM}}$ discussed above. It follows that one can construct Lagrangian terms that are both Lorentz and gauge invariant with space-time tensors constructed from A^a_μ, called the "*field strength tensors*":

$$F^a_{\mu\nu} \equiv \partial_\mu\,A^a_\nu - \partial_\nu\,A^a_\mu - g\,f^{abc}\,A^b_\mu\,A^c_\nu$$

which transform as

$$F^a_{\mu\nu} \to F^a_{\mu\nu} - f^{abc}\,\theta^b\,F^c_{\mu\nu}\,.$$

The kinetic energy term of the Lagrangian for the gauge fields can be expressed as

$$\mathcal{L}_{\text{gauge}} = -\frac{1}{4}\,F^{a\mu\nu}\,F^a_{\mu\nu}\,.$$

and is Lorentz and gauge invariant.

Specifying the gauge symmetry, and the field content of the fermions fully determines a Yang-Mills theory:

$$\begin{aligned}\mathcal{L}_{\text{Yang-Mills}} &= \mathcal{L}_{\text{gauge}} + \mathcal{L}_{\text{fermions}} \\ &= -\frac{1}{4}\,F^{a\mu\nu}\,F^a_{\mu\nu} + i\,\bar{\psi}_i\,\gamma^\mu\,D_\mu\,\psi_i + m\,\bar{\psi}_i\,\psi_i\,.\end{aligned}$$

The gauge symmetry determines the gauge boson fields of the theory. Combining this with a set of given Dirac fields describing the fermions determines the allowed interaction terms of the Lagrangian, by using gauge-covariant derivatives. In this way, the structure of the gauge symmetry of a theory specifies the structure of its interactions.

A.2 The Standard Model

A.2.1 Quarks, leptons, and gauge bosons

In the SM, the fermions are described by spinor representations of the Poincaré group. The boson force carriers are described by gauge fields that are a result of requiring invariance of the action under a specific gauge group, which specifies a particular symmetry among the internal degrees of freedom of the spinor fields:

$$\mathrm{SU(3)_C \times SU(2)_L \times U(1)_Y}\quad.$$

Gauge invariance requires the introduction of gauge boson fields G^α_μ, W^a_μ, and B_μ, which serve as the connections in the covariant derivatives needed in the terms for the fermion kinetic energies[105].

[105] See the discussion of gauge invariance and covariant derivatives in Appendix A.1.6.

$$\begin{array}{ccccc} \mathrm{SU}(3)_\mathrm{C} & \times & \mathrm{SU}(2)_\mathrm{L} & \times & \mathrm{U}(1)_\mathrm{Y} \\ \Downarrow & & \Downarrow & & \Downarrow \\ G^\alpha_\mu \;:\; (\,\mathbf{8},\mathbf{1},0\,) & & W^a_\mu \;:\; (\,\mathbf{1},\mathbf{3},0\,) & & B_\mu \;:\; (\,\mathbf{1},\mathbf{1},0\,) \\ \alpha \in \{\,1,\,2,\,\ldots,\,8\,\} & & a \in \{\,1,\,2,\,3\,\} & & \end{array}$$

The gauge-covariant derivative is

$$D_\mu\,\psi \equiv \left(\partial_\mu + i\,g_1\,B_\mu\,Y_{\mathrm{L/R}} + \Big[i\,g_2\,W^a_\mu\,T^a\Big]_\mathrm{L} + \Big[i\,g_3\,G^a_\mu\,\tau^a\Big]_\mathrm{C}\right)\psi\,.$$

Besides this particular gauge invariance, another peculiar feature of the SM is the structure of the representations of the fermions. The bracketed terms only appear for interaction terms with fermions that have the relevant Noether charges for that gauge symmetry. Some fermions transform as singlets under part of the SM gauge symmetries, and therefore not all fermions participate in all the gauge interactions. The types of fermions happen to divide evenly between *quarks*, which carry *red*, *green*, and *blue* color charges in a triplet representation of $\mathrm{SU}(3)_\mathrm{C}$, and *leptons* which transform as color singlets. Table A.3 shows the gauge-group representations of the SM fermions. Another important feature is that only the left-chiral part of the fermions (as denoted by the L) form doublet representations of SU(2), while the right-chiral part of the fields are singlets. Finally, Y denotes the *hypercharge* quantum number carried by all fermions as a consequence of their $\mathrm{U}(1)_\mathrm{Y}$ invariance, but note that the left- and right-chiral parts of the fields form separate singlets. These chiral ingredients of the SM are what allow for parity and CP violation in the weak interactions.

Table A.3: Gauge-group representations of the SM fermions. The rows are components of weak iso-spin, and the columns are components of color. The sets of three numbers on right denote if the fields have a singlet or triplet representation of $\mathrm{SU}(3)_\mathrm{C}$, doublet or singlet representation of $\mathrm{SU}(2)_\mathrm{L}$, and their weak hypercharge quantum number respectively.

Left-handed quarks:	$\begin{pmatrix} u^\mathrm{r}_\mathrm{L} & u^\mathrm{g}_\mathrm{L} & u^\mathrm{b}_\mathrm{L} \\ d^\mathrm{r}_\mathrm{L} & d^\mathrm{g}_\mathrm{L} & d^\mathrm{b}_\mathrm{L} \end{pmatrix}$, $\begin{pmatrix} c^\mathrm{r}_\mathrm{L} & c^\mathrm{g}_\mathrm{L} & c^\mathrm{b}_\mathrm{L} \\ s^\mathrm{r}_\mathrm{L} & s^\mathrm{g}_\mathrm{L} & s^\mathrm{b}_\mathrm{L} \end{pmatrix}$, $\begin{pmatrix} t^\mathrm{r}_\mathrm{L} & t^\mathrm{g}_\mathrm{L} & t^\mathrm{b}_\mathrm{L} \\ b^\mathrm{r}_\mathrm{L} & b^\mathrm{g}_\mathrm{L} & b^\mathrm{b}_\mathrm{L} \end{pmatrix}$	:	$(\,\mathbf{3},\mathbf{2},\frac{1}{6}\,)$
Right-handed quarks:	$\begin{pmatrix} u^\mathrm{r}_\mathrm{R} & u^\mathrm{g}_\mathrm{R} & u^\mathrm{b}_\mathrm{R} \end{pmatrix}$, $\begin{pmatrix} c^\mathrm{r}_\mathrm{R} & c^\mathrm{g}_\mathrm{R} & c^\mathrm{b}_\mathrm{R} \end{pmatrix}$, $\begin{pmatrix} t^\mathrm{r}_\mathrm{R} & t^\mathrm{g}_\mathrm{R} & t^\mathrm{b}_\mathrm{R} \end{pmatrix}$	:	$(\,\mathbf{3},\mathbf{1},\frac{2}{3}\,)$
	$\begin{pmatrix} d^\mathrm{r}_\mathrm{R} & d^\mathrm{g}_\mathrm{R} & d^\mathrm{b}_\mathrm{R} \end{pmatrix}$, $\begin{pmatrix} s^\mathrm{r}_\mathrm{R} & s^\mathrm{g}_\mathrm{R} & s^\mathrm{b}_\mathrm{R} \end{pmatrix}$, $\begin{pmatrix} b^\mathrm{r}_\mathrm{R} & b^\mathrm{g}_\mathrm{R} & b^\mathrm{b}_\mathrm{R} \end{pmatrix}$	:	$(\,\mathbf{3},\mathbf{1},-\frac{1}{3}\,)$
Left-handed leptons:	$\begin{pmatrix} \nu_{e\mathrm{L}} \\ e_\mathrm{L} \end{pmatrix}$, $\begin{pmatrix} \nu_{\mu\mathrm{L}} \\ \mu_\mathrm{L} \end{pmatrix}$, $\begin{pmatrix} \nu_{\tau\mathrm{L}} \\ \tau_\mathrm{L} \end{pmatrix}$	:	$(\,\mathbf{1},\mathbf{2},-\frac{1}{2}\,)$
Right-handed leptons:	e_R, μ_R, τ_R	:	$(\,\mathbf{1},\mathbf{1},-1\,)$

A.2.2 The Standard Model Lagrangian

The SM is a Yang-Mills theory with the gauge group: $\mathrm{SU(3)_C} \times \mathrm{SU(2)_L} \times \mathrm{U(1)_Y}$, and with the particular combination of triplet/doublet/singlet representations of fermions discussed in the previous section. Additionally, an SU(2) doublet of complex scalar Higgs fields is coupled to the electroweak gauge bosons and to the fermions following the Higgs mechanism discussed in the following section.

The full Lagrangian density is

$$
\begin{aligned}
&\text{kinetic energies and self-interactions of the gauge bosons} \\
\mathcal{L}_{\mathrm{SM}} = &-\frac{1}{4}\, B_{\mu\nu}\, B^{\mu\nu} - \frac{1}{4}\, W^a_{\mu\nu}\, W^{a\mu\nu} - \frac{1}{4}\, G^\alpha_{\mu\nu}\, G^{\alpha\mu\nu} \\
&\text{kinetic energies and electroweak interactions of the left-handed fermions} \\
&+ \bar{L}_i\, \gamma^\mu \Big(i\, \partial_\mu - \frac{1}{2}\, g_1\, Y_{i\mathrm{L}}\, B_\mu - \frac{1}{2}\, g_2\, \sigma^a\, W^a_\mu \Big) L_i \\
&\text{kinetic energies and electroweak interactions of the right-handed fermions} \\
&+ \bar{R}_i\, \gamma^\mu \Big(i\, \partial_\mu - \frac{1}{2}\, g_1\, Y_{i\mathrm{R}}\, B_\mu \Big) R_i \\
&\text{strong interactions between quarks and gluons} \\
&+ \frac{i\, g_3}{2}\, \bar{Q}_j\, \gamma^\mu\, \lambda^\alpha\, G^\alpha_\mu\, Q_j \\
&\text{electroweak boson masses and Higgs couplings} \\
&+ \frac{1}{2} \left| \Big(i\, \partial_\mu - \frac{1}{2}\, g_1\, B_\mu - \frac{1}{2}\, g_2\, \sigma^a\, W^a_\mu \Big) \Phi \right|^2 - V(\Phi) \\
&\text{fermion masses and Higgs couplings} \\
&- \Big(y^{\mathrm{d}}_{k\ell}\, \bar{L}_k\, \Phi\, R_\ell + y^{\mathrm{u}}_{k\ell}\, \bar{R}_k\, \tilde{\Phi}\, L_\ell + h.c. \Big) \,.
\end{aligned}
$$

It is important to note that there are several types of spaces being indexed above. Some remarks about notation:

- $B_{\mu\nu}$, $W^a_{\mu\nu}$, and $G^\alpha_{\mu\nu}$ are the field strength tensors defined for the gauge field of $\mathrm{U(1)_Y}$:

$$B_{\mu\nu} \equiv \partial_\mu\, B_\nu - \partial_\nu\, B_\mu \,,$$

  for the 3 gauge fields of $\mathrm{SU(2)_L}$:

$$W^a_{\mu\nu} \equiv \partial_\mu\, W^a_\nu - \partial_\nu\, W^a_\mu - g_2\, \epsilon^{abc}\, W^b_\mu\, W^c_\nu \quad \text{for } a \in \{\, 1,\, 2,\, 3\,\} \,,$$

  and for the 8 gauge fields of $\mathrm{SU(3)_C}$:

$$G^\alpha_{\mu\nu} \equiv \partial_\mu\, G^\alpha_\nu - \partial_\nu\, G^\alpha_\mu + g_3\, f^{\alpha\beta\gamma}\, G^\beta_\mu\, G^\gamma_\nu \quad \text{for } \alpha \in \{\, 1,\, 2,\, \ldots,\, 8\,\} \,,$$

  with $f^{\alpha\beta\gamma}$ being the structure constants of SU(3).

- L and R denote the left and right projections of the Dirac fermion fields, including quarks and leptons. Q denote the Dirac fermion fields for the quarks, which have left- and right-chiral parts: $Q = L + R$. But note that the strong interactions are not chiral.

- μ and ν are four-vector indices, which result from the fact that the gauge fields transform as four-vector representations of the gauge symmetries of the Standard Model ($\mathrm{SU(3)_C} \times \mathrm{SU(2)_L} \times \mathrm{U(1)_Y}$).

- a, b, c index the 3 generators of SU(2), expanded in terms of the Pauli matrices:

$$T^a = \frac{1}{2}\,\sigma^a \quad \text{for } a \in \{\,1,\,2,\,3\,\}\,.$$

- α, β, γ index the 8 generators of SU(3), expanded in terms of the Gell-Mann matrices:

$$\tau^\alpha = \frac{1}{2}\,\lambda^\alpha \quad \text{for } \alpha \in \{\,1,\,2,\,\ldots,\,8\,\}\,.$$

- i, j, k, ℓ sum over the generations of the Standard Model. In the chiral terms related to the electroweak and Higgs interactions, coupling to the left- and right-handed spinors: L and R, the sums over generations include both leptons and quarks. In the strong interaction term, j only indexes generations of the quarks, since the leptons do not interact strongly.

- There are 3 types of indexes left implied (*i.e.* being contracted but not written explicitly):

  1. the 4 components of the spinors of the fermion fields: L, R, Q, and their corresponding Dirac matrices: γ^μ,
  2. the 2 components of the $\mathrm{SU(2)_L}$ doublets: L, R, Φ, and their corresponding Pauli matrices: σ^a,
  3. the 3 components of the $\mathrm{SU(3)_C}$ triplets: Q_j, and their corresponding Gell-Mann matrices: λ^α.

- Φ is the SM Higgs doublet:

$$\Phi \equiv \begin{pmatrix} \phi^+ \\ \phi^0 \end{pmatrix} \;:\; (\,\mathbf{1}, \mathbf{2}, \frac{1}{2}\,)\,,$$

  and it is conventional to define

$$\tilde{\Phi} \equiv \begin{pmatrix} 0 & 1 \\ -1 & 0 \end{pmatrix} \Phi^* = \begin{pmatrix} \phi^{0*} \\ -\phi^{+*} \end{pmatrix}\,.$$

- *h.c.* denotes the Hermitian conjugate of the previous terms in the parenthesis.

Expanding this Lagrangian in the Dyson series for the S-matrix gives the interaction vertices shown in Figure A.2.

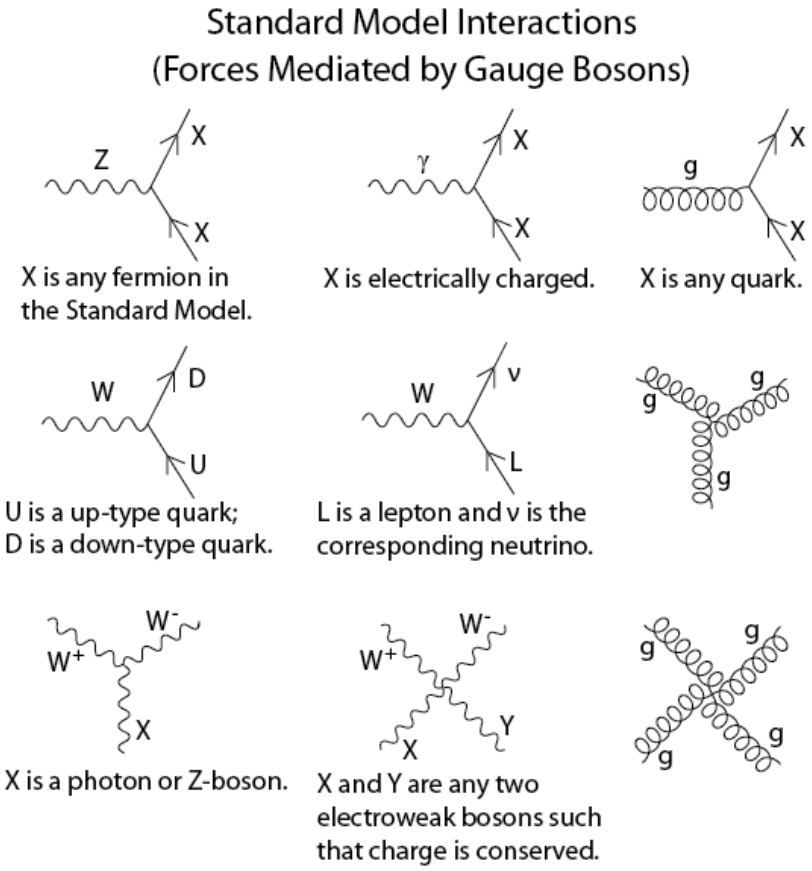

Figure A.2: The interactions of the Standard Model [319].

A.2.3 The Higgs mechanism

Motivation

Terms in the Lagrangian that would represent Lorentz invariant masses for the gauge bosons would look like

$$\frac{1}{2}\, m_A^2\, A^\mu\, A_\mu\,.$$

But because the gauge bosons have non-trivial gauge transformations:

$$A_\mu \to A_\mu + \frac{1}{e}\,\partial_\mu\,\theta\,,$$

such terms are not gauge invariant. It seemed that requiring gauge invariance excludes the theory from describing massive gauge bosons, but gauge invariance is seen as the motivating principle behind the existence of boson fields in Yang-Mills theories. The mystery of how to incorporate massive boson fields into gauge invariant theories was solved by the Higgs mechanism.

Also note that in the SM, Dirac fermion mass terms are no longer gauge invariant[106] because they are not gauge singlets:

$$m\,\bar{\psi}\,\psi = m\,(\bar{\psi}_{\rm L}\,\psi_{\rm R} + \bar{\psi}_{\rm R}\,\psi_{\rm L})$$

The left-handed fermions form $\mathrm{SU}(2)_{\rm L}$ doublets, while the right-handed are $\mathrm{SU}(2)_{\rm L}$ singlets, so their products do not close.

Goldstone's theorem and the Higgs mechanism

In 1960, *spontaneous symmetry breaking* (discussed more bellow) was described by Yoichiro Nambu [320] to explain the apparent breakdown of EM gauge invariance in the BCS theory of superconductivity [321, 322]. Further, he suggested that an analogus mechanism could used in particle physics to explain the approximate but broken symmetries among the spectrum of hadrons, and suggested the lightest meson, the pion was a boson predicted to exist as a consequence chiral symmetry breaking of the strong interactions [323, 324]. In 1961, Jeffery Goldstone [325] generalized Nambu's ideas to any spontaneously broken symmetry of relativistic QFT. He motivated that spontaneous breaking of a symmetry in a relativistic field theory always results in *massless* spin-zero bosons, called "*Goldstone bosons*", and proved the conclusion was a theorem of QFT the following year with Abdus Salam and Steven Weinberg [326].

In 1964, three groups: Robert Brout and Francois Englert [2]; Peter Higgs [3, 4]; and Gerald Guralnik, Carl R. Hagen, and Tom Kibble [5], independently demonstrated an exception to Goldstone's theorem, showing that Goldstone bosons do not occur when a spontaneously broken symmetry is *local*. Instead, the Goldstone mode provides the third polarization of a massive vector field, resulting in *massive* gauge bosons. The other mode of the original scalar doublet remains as a massive spin-zero particle, the Higgs boson. This is the Englert-Brout-Higgs-Guralnik-Hagen-Kibble mechanism, or *Higgs mechanism*. In the SM, the Higgs boson also couples to the fermions, generating their bare masses, as discussed briefly later in Appendix A.2.6 and A.2.7.

Electroweak symmetry breaking in the SM

The Higgs mechanism is utilized in the unified model of the electroweak interactions of Sheldon Glashow [6], Steven Weinberg [7], and Abdus Salam [8, 9, 10], that forms the modern basis of the Standard Model. As implemented in the SM, the Higgs mechanism couples the $\mathrm{SU}(2)_{\rm L}$ and the $\mathrm{U}(1)_{\rm Y}$ parts of the gauge symmetry through a Higgs field that is a complex scalar invariant under

[106] A fermion mass term, $m\,\bar{\psi}\,\psi$, is gauge invariant in QED, see Appendix A.1.6, but is not gauge invariant in the SM.

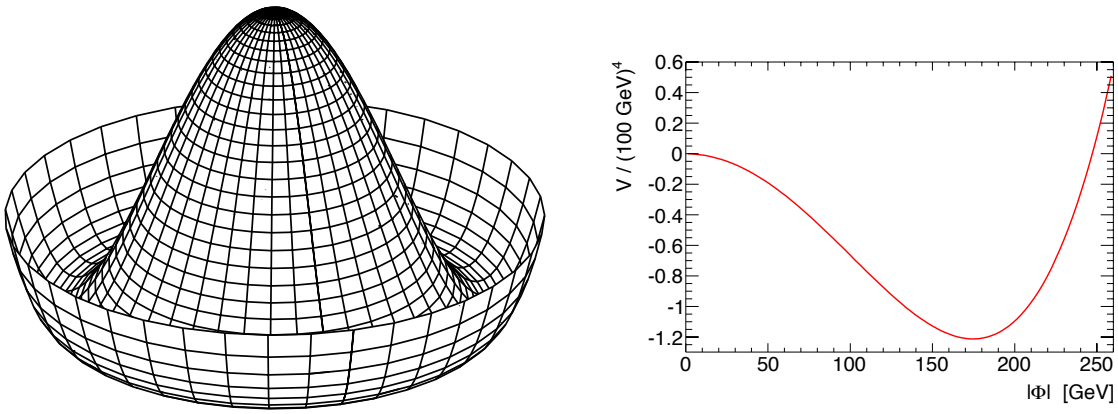

Figure A.3: Illustration of the Higgs potential, $V(\Phi)$. (left) The shape of the potential in any two components of: $\mathrm{Re}(\phi^+)$, $\mathrm{Im}(\phi^+)$, $\mathrm{Re}(\phi^0)$, $\mathrm{Im}(\phi^0)$. (right) A plot of the Higgs potential assuming $m_H = 126$ GeV, as shown in Table A.5 [327].

$\mathrm{U(1)_Y}$ and an $\mathrm{SU(2)_L}$ doublet:

$$\Phi \equiv \begin{pmatrix} \phi^+ \\ \phi^0 \end{pmatrix} \;\; : \;\; (\, \mathbf{1}, \mathbf{2}, \frac{1}{2}\,) \,,$$

where both ϕ^+ and ϕ^0 are complex numbers. The potential of the Higgs field is expanded as

$$V(\Phi) = \mu^2 \, \Phi^\dagger \, \Phi + \lambda \, \left| \Phi^\dagger \, \Phi \right|^2 \,.$$

To spontaneously break the symmetry, the potential $V(\Phi)$ is chosen to have an unstable maximum at $\Phi = 0$ by requiring that $\mu^2 < 0$ (see Figure A.3). Finding the minimum of the potential:

$$\mu^2 + 2\,\lambda \;\; \Phi^\dagger \Phi \big|_{\mathrm{min}} = 0$$

gives degenerate minima with

$$\Phi^\dagger \, \Phi = |\Phi|^2 = |\phi^+|^2 + |\phi^0|^2 = \frac{-\mu^2}{2\,\lambda} \,.$$

At energies low compared to the local maximum in the potential, the vacuum settles into the degenerate minima, a process called "*spontaneous symmetry breaking*". The freedom in phase of the minimum results in the $\mathrm{U(1)_{EM}}$ symmetry after electroweak symmetry breaking:

$$\mathrm{SU(2)_L} \times \mathrm{U(1)_Y} \;\; \rightarrow \;\; \mathrm{U(1)_{EM}} \;\; .$$

For purposes of notation, one can choose all of the vacuum expectation value to be real and in one component of the Higgs doublet:

$$\langle \Phi \rangle = \begin{pmatrix} 0 \\ v/\sqrt{2} \end{pmatrix} \,,$$

The vacuum expectation value can be expressed in terms of the parameters in the Higgs potential:

$$\langle \Phi^\dagger \, \Phi \rangle = \frac{v^2}{2} = \frac{-\mu^2}{2\,\lambda}$$

$$\Rightarrow \qquad v \equiv \sqrt{\frac{-\mu^2}{\lambda}} \, .$$

Now, one can expand Φ around this new vacuum, to find the spectrum of excitations in the low-energy theory:

$$\Phi(x) = \frac{1}{\sqrt{2}} \begin{pmatrix} 0 \\ v + h(x) \end{pmatrix} .$$

Massive gauge bosons

To see the effect the non-zero Higgs vacuum has on the gauge bosons, one can expand the appropriate term in the Lagrangian:

$$\begin{aligned} \left| \left(-\frac{1}{2}\, g_1 \, B_\mu - \frac{1}{2}\, g_2 \, \sigma^a \, W_\mu^a \right) \Phi \right|^2 &= \frac{1}{8} \left| \begin{pmatrix} g_1 \, B_\mu + g_2 \, W_\mu^3 & g_2 \, (W_\mu^1 - i W_\mu^2) \\ g_2 \, (W_\mu^1 + i W_\mu^2) & g_1 \, B_\mu - g_2 \, W_\mu^3 \end{pmatrix} \begin{pmatrix} 0 \\ v \end{pmatrix} \right|^2 \\ &= \frac{1}{8}\, g_2^2 \, v^2 \, (W_\mu^1 - i W_\mu^2)(W_\mu^1 + i W_\mu^2) \\ &\quad + \frac{1}{8}\, v^2 \, (g_2 \, W_\mu^3 - g_1 \, B_\mu)(g_2 \, W_\mu^3 - g_1 \, B_\mu) \, . \end{aligned}$$

Let

$$W_\mu^\pm \equiv \frac{1}{\sqrt{2}} (W_\mu^1 \mp i \, W_\mu^2) \, ,$$

and

$$Z_\mu \equiv \frac{1}{\sqrt{g_1^2 + g_2^2}} (g_2 \, W_\mu^2 - g_1 \, B_\mu) \, .$$

Then the above Lagrangian terms become

$$\underbrace{\frac{1}{4}\, v^2 \, g_2^2}_{\frac{1}{2}\, m_W^2} \, W_\mu^+ \, W^{-\mu} + \underbrace{\frac{1}{4}\, v^2 \, (g_1^2 + g_2^2)^2}_{\frac{1}{2}\, m_Z^2} \, Z_\mu \, Z^\mu \, .$$

Here we recognize the appropriate terms for generating the tree-level masses for the $W^\pm$ and Z bosons:

$$\Rightarrow \qquad m_W = \frac{v \, g_2}{\sqrt{2}} \quad \text{and} \quad m_Z = \frac{v}{\sqrt{2}} \sqrt{g_1^2 + g_2^2} \, .$$

The Higgs boson

Plugging the vacuum expectation into $V(\Phi)$ and finding the coefficient for the h^2 term reveals that a tree-level mass is also generated for the boson associated with the Higgs field:

$$\begin{aligned} V &= \frac{\mu^2}{2}(v+h)^2 + \frac{\lambda}{4}(v+h)^4 \\ &\sim \frac{\mu^2}{2}h^2 + \frac{\lambda}{4}6\,v^2\,h^2\,, \text{ to order } h^2 \\ &= \frac{\mu^2}{2}h^2 + \frac{3}{2}\left(\frac{-\mu^2}{v^2}\right)v^2\,h^2 \\ &= -\mu^2\,h^2 = \frac{1}{2}m_{\mathrm{H}}^2\,h^2 \\ \Rightarrow \qquad & m_{\mathrm{H}} = \sqrt{-2\,\mu^2} = \sqrt{2\,\lambda\,v^2}\,. \end{aligned}$$

A.2.4 Electroweak theory

A unified theory of the electroweak interactions, the cornerstone of the SM, was the culmination of several incremental developments including Fermi's four-fermion interaction model for β-decay in 1934 [328] and the first direct detection of neutrinos in 1956 at the Cowan-Reines nuclear reactor experiment [329]. Tsung Dao Lee and Chen Ning Yang published a systematic review of parity conservation in 1956 [330], noting that parity conservation could be verified and constrained by atomic electromagnetic interactions, but it had not been tested for weak interactions. They further suggested experiments that could probe for parity conservation in β-decays and meson or hyperon decays. The following year, teams led by Chien-Shiung Wu [331] and Leon Lederman [332] discovered the parity violation of the weak interactions in β-decays of cobalt-60 and muon decays, respectively.

One of the most important features of the unified theory of the electroweak interactions is that the gauge group is chiral; the left-chiral part of the fermion fields forms SU(2) doublets, allowing the theory to have parity-violating and CP-violating interactions. E. C. George Sudarshan and Robert Marshak were first to propose a vector–axial-vector (V-A) chiral couplings for the weak interaction in 1958 [333], followed by similar theories by Murray Gell-Mann and Feynman [334] and by Nambu [335]. In 1961, Glashow [6] was the first to suggest the SU(2)×U(1) gauge structure to unify the electromagnetic and weak interactions. Weinberg [7] and Salam [10] incorporated the Higgs mechanism into Glashow's electroweak theory in 1967, formulating the modern basis of the SM.

Bejamin Lee demonstrated the first renormalizable theory with a spontaneously broken global symmetry in 1969 [336]. In 1972, during his doctoral studies advised by Martinus Veltman, Gerardus 't Hooft proved that all Yang-Mills theories with massive gauge bosons produced via the Higgs

mechanism, including the SM, are renormalizable [337, 338]. Then, 't Hooft and Veltman introduced *dimensional regularization* as a new general method for regularizing gauge theories [339].

By the early 1970s, these theoretical developments formed the consensus that the weak interactions should be mediated by gauge bosons in analogy with the photon from QED, but that the bosons needed to be sufficiently massive to limit the range of weak interactions to nuclear scales. While charged-current interactions were known to exist from neutrino-production processes like β-decay, neutral currents had not been observed until 1973, when the Gargamelle experiment first observed neutral currents exchanged in a bubble chamber exposed to a beam of neutrinos [340, 341].

Measuring the ratio of charged and neutral currents at Gargamelle resulted in the first measurement of the *Weinberg angle* that parametrizes the mixing of the W^3_μ and B_μ bosons in the Glashow-Weinberg-Salam model:

$$\begin{pmatrix} Z_\mu \\ A_\mu \end{pmatrix} = \begin{pmatrix} \cos\theta_\mathrm{W} & -\sin\theta_\mathrm{W} \\ \sin\theta_\mathrm{W} & \cos\theta_\mathrm{W} \end{pmatrix} \begin{pmatrix} W^3_\mu \\ B_\mu \end{pmatrix}$$

where the Weinberg angle is determined by the ratios of the weak couplings and boson masses by the following relationships:

$$\begin{aligned} \Rightarrow \qquad \sin\theta_\mathrm{W} &= \frac{g_1}{\sqrt{g_1^2+g_2^2}} \\ \cos\theta_\mathrm{W} &= \frac{g_2}{\sqrt{g_1^2+g_2^2}} = \frac{m_W}{m_Z} \\ \tan\theta_\mathrm{W} &= \frac{g_1}{g_2}\,. \end{aligned}$$

The coupling of the resulting electromagnetic interaction, mediated by the A^μ boson, is related to the fundamental couplings by

$$e \equiv \sqrt{4\,\pi\,\alpha} \;\equiv\; g_1\,\cos\theta_\mathrm{W} \;\equiv\; g_2\,\sin\theta_\mathrm{W}\,,$$

where $\alpha \approx 1/137$ is the traditional EM fine-structure constant. The fundamental coupling g_2 is related to Fermi's effective coupling constant for charged-current interactions by

$$\frac{G_\mathrm{F}}{\sqrt{2}} \equiv \frac{g_2^2}{8\,m_W^2}\,.$$

Knowing these couplings and the newly measured Weinberg angle allowed for the first quantitative prediction of $W^\pm$ and Z boson masses:

$$m_W^2 = \frac{\sqrt{2}}{G_\mathrm{F}}\,\frac{g_2^2}{8} = \frac{\sqrt{2}}{G_\mathrm{F}}\,\frac{e^2}{8\,\sin^2\theta_\mathrm{W}} = \frac{\pi\,\alpha}{\sqrt{2}\,G_\mathrm{F}}\,\frac{1}{\sin^2\theta_\mathrm{W}}$$

$$\Rightarrow \qquad m_W = \sqrt{\frac{\pi\,\alpha}{\sqrt{2}\,G_\mathrm{F}}}\,\frac{1}{\sin\theta_\mathrm{W}} \approx (37\ \mathrm{GeV})\,\frac{1}{0.48} \approx 80\ \mathrm{GeV}$$

and

$$m_Z = \frac{m_W}{\cos\theta_{\rm W}} \approx \frac{80\ {\rm GeV}}{0.88} \approx 90\ {\rm GeV}\,.$$

In 1976, this led to Carlo Rubbia to suggest converting the CERN SPS pp-collider to the first $p\bar{p}$-collider to directly produce the $W^\pm$ and Z gauge bosons. In 1983, after the construction of the first anti-proton factory and the commissioning of the accelerator complex at CERN, the UA1 [342, 343, 344, 345] and UA2 [346, 347] collaborations discovered the $W^\pm$ and Z bosons in high-$p_{\rm T}$ lepton events, with masses clearly consistent with the Glashow-Weinberg-Salam prediction, firmly establishing the SM [348].

A.2.5 Strong interactions

The quark model and confinement

Meanwhile, physicists studying hadrons in the 1950s and 1960s were beginning to suspect more and more that hadrons are composite from studying the spectrum of hadrons and their decays, but theorists were still struggling to find a theory of the strong interactions that bind hadrons. In 1957, Murray Gell-Mann and Arthur Rosenfeld published the first review review of particle physics, cataloging the particle spectrums and decay rates observed [349]. In 1964, Gell-Mann [350] and George Zweig [351, 352] independently proposed the *quark model* which classified hadrons as composite states of 3-quark *baryons* or quark-antiquark *mesons*. Inelastic electron-proton collision experiments at the Stanford Linear Accelerator Center (SLAC)[107] in 1969 verified the composite structure of the proton [353, 354].

One of the most important implications of identifying the symmetries of a system is that one can then predict its degenerate states. Even when a symmetry is approximate, the spectrum of possible

[107] Now: SLAC National Accelerator Laboratory.

Table A.4: Approximate values of the electroweak parameters. Only three of the dimensionless and one of the $\sim$ GeV parameters are fundamental, and the remaining can be derived [136].

$g_1 \approx 0.36$	$m_W \approx 80.4$ GeV
$g_2 \approx 0.65$	$m_Z \approx 91.2$ GeV
$e \approx 0.31$	$v \approx 246$ GeV
$\sin^2\theta_{\rm W} \approx 0.23$	$\sqrt{2}\,G_{\rm F} \approx (246\ {\rm GeV})^{-2}$

Table A.5: The SM parameters of the Higgs vacuum potential, assuming the Higgs-like particle observed at the LHC, as discussed in Section 2.3.2, is the SM Higgs boson. Two of the three parameters: μ, λ, and $m_{\rm H}$ are fundamental and one can be derived.

$m_{\rm H} \approx 126$ GeV	$-\mu^2 \approx (126\ {\rm GeV})^2/2$
	$\lambda \approx 0.13$

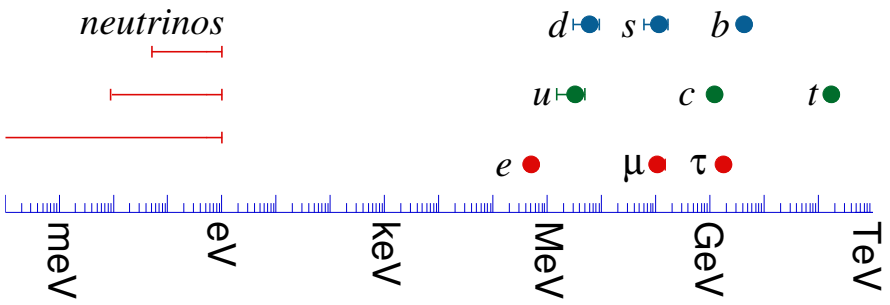

Figure A.4: Mass range of the SM fermions [355]. For approximate values of the masses, see Table A.6.

states of a system will cluster into approximate representations of the symmetries of the system. In the 1960s, the known hadrons consisted of combinations of u, d, and s quarks, which each have relatively small masses (1–100 MeV, see Table A.6). An effective way to predict the spectrum of hadrons is to consider SU(3) transformations of the u, d, s flavors (ignoring color for the moment). This $\mathrm{SU}(3)_{\mathrm{flavor}}$ symmetry is approximate because of the differences in the masses and charges of the quarks breaks the symmetry (see Figure A.6).

When a quark and anti-quark combine to form a meson, they transform as an octet and a singlet of states under $\mathrm{SU}(3)_{\mathrm{flavor}}$ rotations: $\mathbf{3} \otimes \bar{\mathbf{3}} = \mathbf{8} \oplus \mathbf{1}$ (see Figure A.5). The two neutral $s = 0$ octet states and the singlet mix in general, as is the case for the η/η' and ϕ/ω mesons. When three quarks combine to form a baryon, they transform as a fully symmetric[108] decuplet, two octets that

[108] Symmetry under exchange is not an issue for mesons because quarks and anti-quarks are distinguishable, but combinations of quarks in a baryon are not in general.

Table A.6: Masses and electroweak charges of the SM fermions [136]. For a visualization of the range of masses, see Figure A.4.

name	approx. bare mass	T_{L}^3	Y_{L}	Y_{R}	Q
quarks					
up (u)	1–3 MeV	+1/2	+1/6	+2/3	+2/3
down (d)	4–6 MeV	-1/2	+1/6	-1/3	-1/3
charm (c)	1,300 MeV	+1/2	+1/6	+2/3	+2/3
strange (s)	100 MeV	-1/2	+1/6	-1/3	-1/3
top (t)	173,000 MeV	+1/2	+1/6	+2/3	+2/3
bottom (b)	4,200 MeV	-1/2	+1/6	-1/3	-1/3
leptons					
ν_e	$\lesssim 1$ eV	+1/2	-1/2	0	0
e	0.5 MeV	-1/2	-1/2	-1	-1
ν_μ	$\lesssim 1$ eV	+1/2	-1/2	0	0
μ	106 MeV	-1/2	-1/2	-1	-1
ν_τ	$\lesssim 1$ eV	+1/2	-1/2	0	0
τ	1,776 MeV	-1/2	-1/2	-1	-1

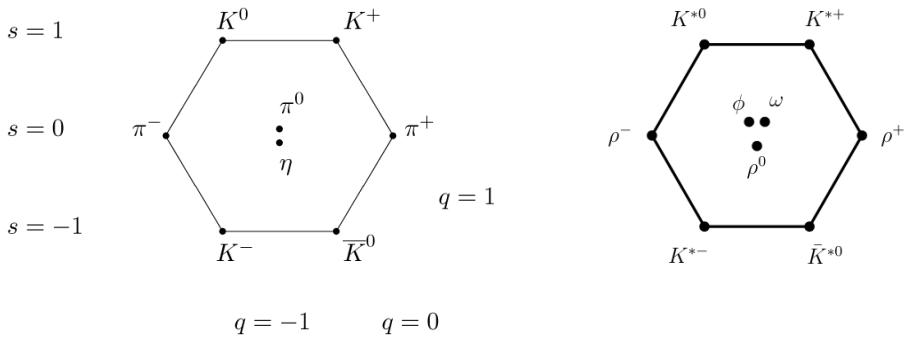

Figure A.5: (left) Pseudoscalar mesons ($J^{PC} = 0^{-+}$). (right) Pseudovector mesons ($J^{PC} = 1^{--}$) [357].

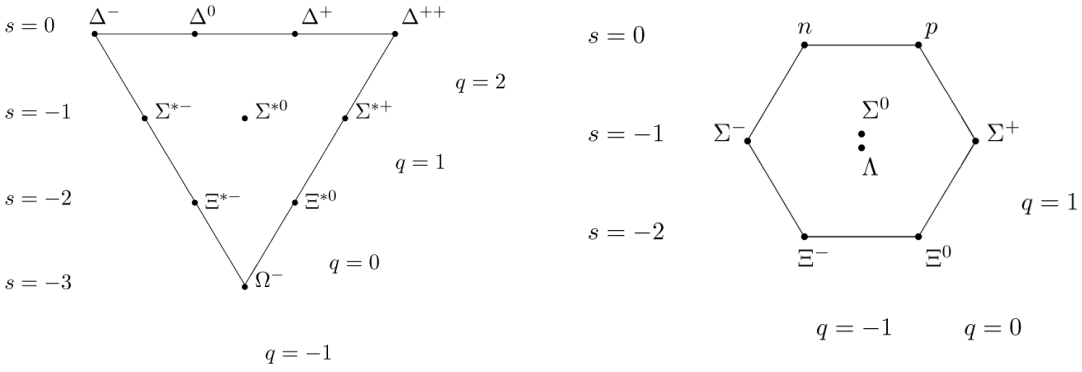

Figure A.6: (left) Spin-3/2 baryon decuplet. (right) Spin-1/2 baryon octet [357].

are symmetric under exchange of the first two or the last two quarks, and a fully antisymmetric singlet: $\mathbf{3} \otimes \mathbf{3} \otimes \mathbf{3} = \mathbf{10}_S \oplus \mathbf{8}_M \oplus \mathbf{8}_M \oplus \mathbf{1}_A$ (see Figure A.6). When the Ω^- baryon (consisting of a *sss* combination of quarks) was discovered at Brookhaven National Laboratory (BNL) in 1964 [356], it completed the symmetric decuplet predicted by the quark model and established the model's success.

In 1964, Oscar Greenberg noted that the antisymmetry under exchange required of fermions by the spin-statistics theorem could not be accounted for in states that appeared fully symmetric like the Δ^{++} ($= |uuu, \uparrow\uparrow\uparrow\rangle$) baryon [358]. The next year, Moo-Young Han and Nambu proposed a new conserved current called "*color*" to solve this symmetry problem for baryons [359]. The red/green/blue color charges form a triplet representation of an independent SU(3) symmetry. Baryons are always in the fully antisymmetric color singlet of $\mathbf{3}\otimes\mathbf{3}\otimes\mathbf{3}$, and therefore the remaining spin and flavor parts of the state-vector must be a fully symmetric combination like for the Δ^{++}. For the baryon octet, the mixed symmetry octets of spin and flavor are combined to give a fully symmetric combination.

Further, Han and Nambu suggested that the strong force was mediated by the eight SU(3) gauge bosons that later became known as "*gluons*". These developments marked the beginning of the formation of the theory of *Quantum Chromodynmaics* (QCD), and by 1973 it was seen as integrated into the SM [15]. In 1979, the TASSO Collaboration discovered evidence for the gluon in events with a 3-jet signature [360, 361].

The strong force is sufficiently strong compared to the masses of the lightest quarks that when quarks in a hadron are given enough energy to overcome the binding energy of the hadron, they also have sufficient energy to pair-produce other quarks until the color charge is neutralized and all quarks are bound into color singlets. This feature of the strong interactions is called "*confinement*"—that all quarks are bound in color-singlet combinations and never bare. The process of an energetic colored state fragmenting into additional hadrons is called "*hadronization*". A "*jet*" refers to the collection of nearby hadrons, which will be relatively colinear due to the boost of the outgoing high-p_{T} quark or gluon that hadronized to produce them[109]. In high-energy collisions producing strongly interacting particles, the cross section is dominated by dijet production, as predicted by Sterman and Weinberg in 1977 [362]. High-p_{T} dijet production was first observed at UA2 [363] in 1982 and UA1 [364] in 1983.

The parton picture and asymptotic freedom

The organization of hadrons into multiplets, discussed previously, concerned the *valence* quark content of hadrons. But the proton, for example, also derives much of its physical properties from a cloud of virtual particles it carries with it from quantum corrections. Back in 1969, Bjorken [365] and Feynman [366] both argued that high-energy experiments demonstrated that quarks were real particles because at high enough collision energies, quarks should not care that they are in a bound system and the physics should be described by collisions between free quarks or gluons within hadrons, which Feynman collectively called "*partons*". Eventually this *asymptotic freedom* was explained by Politzer [11] and Gross and Wilczek [12, 13, 14] as being a consequence of the strong interaction having a negative β-function, which characterizes the renormalization group equation that governs the scaling of the coupling constant with energy. Strong interactions get weaker at higher energies.

According to the *factorization theorem* [367, 368], asymptotic freedom allows one to factor the amplitude of high-energy hadron collisions into the cross section for the parton-level interaction, convolved with Parton Distribution Functions (PDFs), $f_i(x)$, which describe the probability for a parton of flavor i to carry fraction x of the total momentum of the hadron. Below the factorization

[109] Jet reconstruction at ATLAS will be discussed briefly in Section 3.3.6.

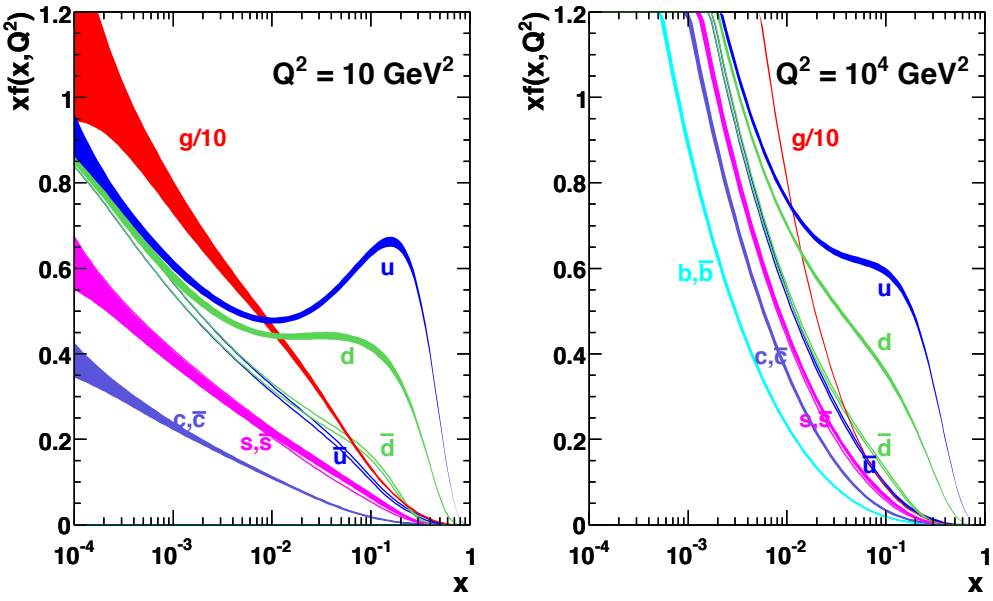

Figure A.7: NLO PDFs for the proton at $Q^2 = 10$ GeV^2 (left) and $Q^2 = 10^4$ GeV^2 (right) [54].

scale, the QCD behavior is non-perturbative, but at high-Q^2 (the scale of the momentum-transfer squared), the amplitude can be factored as:

$$\sigma(pp \to X) = \sum_{ij} \int dx_1\, dx_2\, f_i(x)\, f_j(x)\, \hat{\sigma}(ij \to X)\,,$$

where the PDFs depend on the Q^2 scale of the factorization. PDFs can be evolved to different Q^2 scales using the Dokshitzer-Gribov-Lipatov-Altarelli-Parisi (DGLAP) [369, 370, 371] and the Balitsky-Fadin-Kuraev-Lipatov (BFKL) [372, 373] equations. Examples of proton PDFs for the collisions at the LHC are shown in Figure A.7. Proton PDFs are best constrained at electron-proton colliders like HERA. Because PDFs are necessary to calculate cross sections for collisions with hadrons, the measurement of PDFs and the estimation of their uncertainties is an active area research relevant for searches for new physics at the LHC [54].

A.2.6 Quark flavor mixing

The Cabibbo angle

Excited mesons and baryons have preferences for certain weak decays. In 1963, Nicola Cabibbo proposed a way to preserve a universal coupling for the charged-current weak interaction, if the quark eigenstates of the charged-current weak interaction are mixtures of the mass eigenstates of

the total Hamiltonian:

$$\begin{pmatrix} d' \\ s' \end{pmatrix} = \begin{pmatrix} \cos\theta_{\mathrm{C}} & \sin\theta_{\mathrm{C}} \\ -\sin\theta_{\mathrm{C}} & \cos\theta_{\mathrm{C}} \end{pmatrix} \begin{pmatrix} d \\ s \end{pmatrix} .$$

By comparing the relative branching fractions of certain leptonic decay modes, such as $K^+ \to \mu^+ \nu$ and $\pi^+ \to \mu^+ \nu$, Cabibbo was able to single-out charged-current weak interactions to estimate the *Cabibbo mixing angle*: $\theta_{\mathrm{C}} \approx 0.23$ [374].

Three generations of quarks

In 1970, Glashow, Iliopoulos, and Maiani proposed that a fourth quark: *charm*, completing the second weak-isospin doublet with the strange quark, was necesary to cancel box diagrams contributing to neutral kaon decays to suppress unobserved flavor-changing neutral currents [375]. In 1974, the charm quark was discovered by two independent teams led by Burton Richter at SLAC [376] and Samuel Ting at BNL [377]. Both laboratories produced J/ψ mesons[110] ($c\bar{c}$) on resonance in e^+e^- collisions. The b-quark of the third quark doublet was discovered in 1977 by a team led by Lederman when the Υ meson ($b\bar{b}$) was first produced at Fermilab [378].

Complementary discoveries about the three generations of leptons were also made, as discussed briefly in the following section. It has come to seem that nature has *three generations of fermions* (as shown Figure 2.1 and Table A.3), three doublets that each have the same quantum numbers but higher masses for each successive generation.

The completion of the three doublets with the discovery of the top quark had to wait until 1995 for the operation of the world's first superconducting proton-antiproton collider, the Tevatron, where the top quark was discovered by the CDF [379] and DØ [380] collaborations. Note that high-energy experiments had to climb orders of magnitude in collision energy to discover all the known flavors of quarks because their mass hierarchy spans 5 orders of magnitude, with the most massive quark being the top quark with a mass of about 173 GeV (see Figure A.4).

The CKM matrix

In 1973, Kobayashi and Maskawa generalized the quark-flavor-mixing formalism of Cabibbo to include three generations, defining the *Cabibbo-Kobayashi-Maskawa (CKM) matrix* [381]:

$$\begin{pmatrix} d' \\ s' \\ b' \end{pmatrix} = V_{\mathrm{CKM}} \begin{pmatrix} d \\ s \\ b \end{pmatrix} = \begin{pmatrix} V_{ud} & V_{us} & V_{ub} \\ V_{cd} & V_{cs} & V_{cb} \\ V_{td} & V_{ts} & V_{tb} \end{pmatrix} \begin{pmatrix} d \\ s \\ b \end{pmatrix} .$$

The primed states on the left are the eigenstates of the charged-current weak interaction and the states on the right are mass eigenstates that are slightly mixed among the weak eigenstates. While

[110] Now dubbed "J/ψ", the $c\bar{c}$ meson was first called "J" by the BNL team and "ψ" by the team at SLAC.

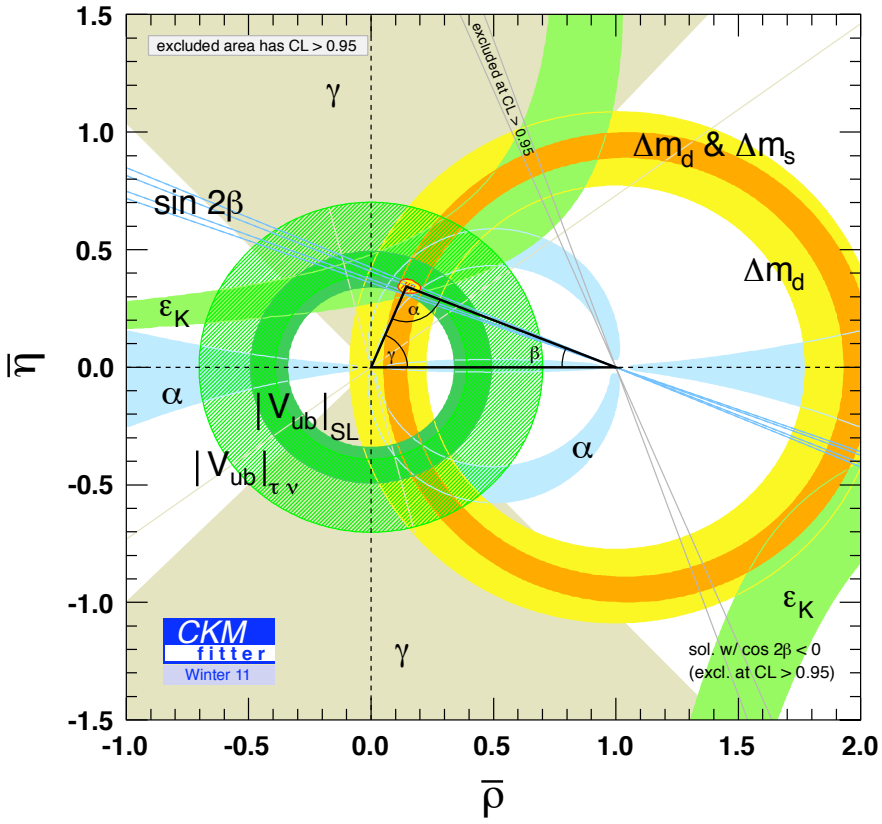

Figure A.8: Constraints on the CKM $(\bar{\rho}, \bar{\eta})$ coordinates from the global SM CKM-fit. Regions outside the colored areas have been excluded at 95 %. For the combined fit the yellow area inscribed by the contour line represents points with CL ¡ 95%. The shaded area inside this region represents points with CL ¡ 68.3% [382].

the elements of the CKM matrix are in general complex numbers, considering their magnitudes demonstrates that the matrix is approximately diagonal:

$$\begin{pmatrix} |V_{ud}| & |V_{us}| & |V_{ub}| \\ |V_{cd}| & |V_{cs}| & |V_{cb}| \\ |V_{td}| & |V_{ts}| & |V_{tb}| \end{pmatrix} \approx \begin{pmatrix} 0.97 & 0.23 & 0.003 \\ 0.23 & 0.97 & 0.040 \\ 0.01 & 0.04 & 0.999 \end{pmatrix} .$$

This means that when the quark doublets are considered in terms of their mass eigenstates, exchanges of $W^{\pm}$ bosons prefer to flip the flavor of quarks within their doublets (like $c \leftrightarrow s$) but CKM-suppressed transitions (like $c \leftrightarrow d$) do occur.

The Wolfenstein parametrization [383, 384] is a common parametrization of the CKM matrix

using four real parameters: $\bar{\rho}$, $\bar{\eta}$, A, and λ that are conveniently each $\mathcal{O}(1)$:

$$\begin{aligned} \bar{\rho} + i\,\bar{\eta} &\equiv -\frac{V_{ud}\,V_{ub}^*}{V_{cd}\,V_{cb}^*}\,, \\ \lambda^2 &\equiv \frac{|V_{us}|^2}{|V_{ud}|^2 + |V_{us}|^2}\,, \\ A^2\,\lambda^4 &\equiv \frac{|V_{cb}|^2}{|V_{ud}|^2 + |V_{us}|^2}\,. \end{aligned}$$

The $\bar{\rho}$ and $\bar{\eta}$ determine the position of the free third point of the relevant *unitary triangle* that can be derived from the constraint that the CKM matrix is unitary (see Figure A.8). The CKM matrix is now reasonably well constrained by several heavy-flavor measurements from the Belle and BaBar experiments at B-factories, as well as the Tevatron experiments, which are combined by the CKMFitter Group [382].

Relation to the Yukawa couplings

In the SM, the Higgs mechanism not only gives rise to the gauge boson masses, it also generates masses for the fermions. The flavor mixing descrbribed by the CKM matrix is actually a result of the Yukawa couplings of the Higgs to the fermions fields not being diagonal. After EW symmetry breaking, the fermion-mass matrix can be calculated in terms of the Higgs vacuum expectation value and the Yukawa couplings:

$$M_{ij}^x = \frac{v}{\sqrt{2}}\,y_{ij}^x\,,$$

where $x \in \{\mathrm{u}, \mathrm{d}, \mathrm{e}\}$ give three matrices for the up-type quarks, down-type quarks, and charged leptons. The indices i, j run over the three generations, allowing them to mix.

By the diagonalization theorem, the mass matrix can be put in diagonal-form with unitary transformation matrices:

$$U_{\mathrm{L}}^\dagger\,M\,U_{\mathrm{R}} = M_{\mathrm{D}}\,.$$

In this notation the CKM matrix is given by

$$V_{\mathrm{CKM}} = U_{\mathrm{L}}^{\mathrm{u}\dagger}\,U_{\mathrm{L}}^{\mathrm{d}}\,.$$

A.2.7 Neutrino flavor mixing

Three generations of leptons

In 1962, Leon Lederman, Melvin Schwartz, and Jack Steinberger showed that neutrinos come in more than one flavor [385] by demonstrating that neutrinos from charged-pion decays to muons always created muons when they are detected (never electrons or taus[111]). In 1975, the τ lepton

[111] The experiment was at the AGS accelerator at BNL and over laboratory distances where neutrino oscillation was neglible.

was discovered by Martin Perl and collaborators at SLAC [386, 387, 388]. In 1990, after performing precision measurements of the width of Z boson at LEP, the ALEPH Collaboration constrained the number of neutrino generations to which the Z can decay to 3 [389]. The updated result in 2006 combining all four LEP experiments is consistent with the number of neutrino types with masses less than half the Z mass being 2.984 ± 0.008 [235]. The ν_τ was not observed directly until it was discovered by the DONUT Collaboration at Fermilab in 2001 [390]. Completing the third generation, it is the last lepton to be discovered. Together, these results conclude that like the quark sector, the leptons seem to come in three generations.

Neutrino oscillation

In the 1950s, it was realized that the rate of neutrino production from fusion processes in the Sun was large and that the neutrino flux may be detectable on Earth. The Solar Standard Model, describing the fusion rates in the sun, was worked out in more detail, and John Bahcall predicted the flux of solar electron neutrinos on Earth with energies of a few 100 keV to be $\sim 8 \times 10^{10}$ cm^{-2} s^{-1} [391, 392]. The first experiment sensitive to this flux was the Homestake Mine experiment by Ray Davis Jr. In 1968, Davis measured the solar neutrino flux on Earth to be $\sim 2.5 \times 10^{10}$ cm^{-2} s^{-1} [393, 394], roughly a third of Bahcall's predicted value. This issue remained unresolved for over 30 years, known as the *solar neutrino problem* [395].

In analogy with the CKM matrix for the quark sector, if the neutrino flavor eigenstates are a mixture of mass eigenstates, and if those mass eigenstates have different masses, then the mass eigenstates will drift in and out of phase as they propagate through free space, modulating the probability to observe a given flavor. This phenomena is called "*neutrino oscillation*", and was first proposed by Bruno Pontecorvo in 1957 [396]. A hypothetical explanation of the solar neutrino problem was that solar neutrinos were oscillating to other flavors in-flight to Earth. Solar neutrinos (100 keV to 20 MeV) are not energetic enough for the ν_μ and ν_τ flavors to participate in charge-current interactions, because it requires the production of heavy charged leptons. The existing solar neutrino experiments like Davis' were only sensitive to the ν_e-flux, and therefore observed a deficit[112].

In 1998, Super-Kamiokande observed another deficit in the expected flux of several GeV atmospheric neutrinos produced in cosmic ray showers, hypothetically due to ν_μ-disappearance by oscillating to other flavors [31]. The Sudbury Neutrino Observatory (SNO) put an end to the mystery by being the first solar neutrino experiment sensitive to both charged- and neutral-current

[112] Solar neutrino oscillations are additionally complicated by the high-density environment of the sun, which due to the MSW effect on neutrinos traveling through matter [397, 398], adiabatically rotates the electron neutrinos created in fusion processes in the sun into nearly pure ν_2 mass eigenstates by the time they exit the sun. Therefore, solar neutrino experiments are really measuring the flavor fractions of the ν_2 mass eigenstate.

interactions, and therefore could measure the total solar ν-flux and the ν_e-flux independently. In 2001, SNO reported its first measurements of the solar neutrino flux, consistent with the neutrino oscillation hypothesis [32]. Therefore, the weak eigenstates of neutrinos must be a mix of mass eigenstates with differing masses.

This was the first conclusive evidence that (at least some of) the neutrino masses are non-zero, which is technically beyond the Standard Model physics, since the SM does not have any right-handed neutrinos. Extending the SM to include massive neutrinos is reasonably straight-forward and allows for a flavor-mixing matrix like CKM for the quark sector. However, there are two types of massive fermions: Dirac or Majorana, with different mass terms for the Lagrangian. While it is now well known to physicsts that neutrinos have mass, measuring the related parameters and constraining the neutrino sector is still an active area of research [33, 399].

The PMNS matrix

The mixing of the neutrino flavor and mass eigenstates is described by the *Pontecorvo-Maki-Nakagawa-Sakata (PMNS) matrix* [396, 400, 401]:

$$\begin{pmatrix} \nu_e \\ \nu_\mu \\ \nu_\tau \end{pmatrix} = U_{\text{PMNS}} \begin{pmatrix} \nu_1 \\ \nu_2 \\ \nu_3 \end{pmatrix} = \begin{pmatrix} U_{e1} & U_{e2} & U_{e3} \\ U_{\mu 1} & U_{\mu 2} & U_{\mu 3} \\ U_{\tau 1} & U_{\tau 2} & U_{\tau 3} \end{pmatrix} \begin{pmatrix} \nu_1 \\ \nu_2 \\ \nu_3 \end{pmatrix}$$

The standard parametrization of the PMNS matrix has 3 Eulerian angles for the mixing between mass states: θ_{12}, θ_{23}, θ_{13}, which have been experimentally measured (see Table A.7), and 3 unknown phase factors: α_1, α_2, δ. The α_1 and α_2 parameters are physically meaningful only if neutrinos are Majorana particles (if the neutrino is identical to its antiparticle), which is currently unknown, and do not enter into oscillation phenomena regardless. If neutrinos are Majorana, then these factors influence the rate of neutrinoless double-beta decay. The phase factor δ is non-zero only if neutrino oscillation violates CP symmetry.

Neutrino oscillation is best observable at various distances depending on the energies and mixing parameters of the neutrinos. The parameters θ_{12} and Δm^2_{21} dominate the effects of solar neutrino oscillation and have been measured most precisely by the SNO [32, 402] and KamLAND [403] collaborations. Atmospheric neutrino oscillations are the result of θ_{23} and $|\Delta m^2_{32}|$, measured by the Super-K [31, 404], K2K, and MINOS experiments, among others. In 2011, T2K reported an indication that the last unobserved neutrino parameter θ_{13} was non-zero [405]. The following year (in April of 2012), the Daya Bay Reactor Neutrino Experiment measured θ_{13}, with 5σ evidence of it being non-zero [406]. Recently, the result from Daya Bay has been combined with measurements from RENO, T2K, MINOS, and Double Chooz [407]. Approximate values of the measured neutrino

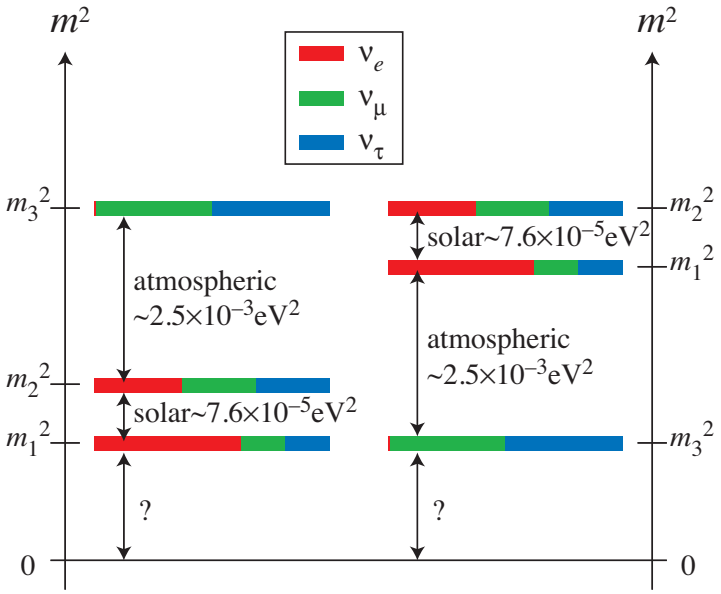

Figure A.9: An illustration of the two possible neutrino mass hierarchies: normal (left) with $m_1 < m_2 < m_3$ and inverted (right) with $m_3 < m_1 < m_2$ [355].

parameters are summarized in Table A.7.

Approximate values of the magnitudes of the elements of the PMNS matrix are [136]

$$\begin{pmatrix} |U_{e1}| & |U_{e2}| & |U_{e3}| \\ |U_{\mu 1}| & |U_{\mu 2}| & |U_{\mu 3}| \\ |U_{\tau 1}| & |U_{\tau 2}| & |U_{\tau 3}| \end{pmatrix} \approx \begin{pmatrix} 0.8 & 0.5 & 0.15 \\ 0.4 & 0.6 & 0.7 \\ 0.4 & 0.6 & 0.7 \end{pmatrix}.$$

Note that unlike the CKM matrix, the PMNS matrix is far from being diagonal, and instead appears to be maximally mixed. The ν_1 mass eigenstate is mostly the ν_e flavor. ν_2 is almost evenly divided between all three flavors. Lastly, ν_3 has barely any ν_e and is approximately evenly shared between the other two flavors. The magnitude of $|\Delta m^2_{32}|$ is ~ 30 times larger than Δm^2_{21}, and its sign is not known, allowing for the two possible mass hierarchies shown in Figure A.9.

Table A.7: Approximate values of the measured neutrino mixing parameters. The remaining unknown parameters are α_1, α_2, δ, and the sign of Δm^2_{32} [136].

mixing angles	mass differences
$\sin^2(2\,\theta_{12}) \equiv \sin^2(2\,\theta_{\rm sol}) \approx 0.86$	$\Delta m^2_{21} \equiv \Delta m^2_{\rm sol} \approx 7.6 \times 10^{-5}$ eV^2
$\sin^2(2\,\theta_{23}) \equiv \sin^2(2\,\theta_{\rm atm}) > 0.92$	$\lvert\Delta m^2_{32}\rvert \equiv \lvert\Delta m^2_{\rm atm}\rvert \approx 2.5 \times 10^{-3}$ eV^2
$\sin^2(2\,\theta_{13}) \approx 0.09$	$\lvert\Delta m^2_{31}\rvert \approx \lvert\Delta m^2_{32}\rvert$

Appendix B

Tau identification variables

This appendix defines all identification variables used by the jet and electron discriminants.The variables are:

Electromagnetic radius (R_{EM}): the transverse energy weighted shower width in the electromagnetic (EM) calorimeter:

$$R_{\mathrm{EM}} = \frac{\sum_{i\in\{\mathrm{EM\ 0-2}\}}^{\Delta R_i<0.4} E_{\mathrm{T},i}\,\Delta R_i}{\sum_{i\in\{\mathrm{EM\ 0-2}\}}^{\Delta R_i<0.4} E_{\mathrm{T},i}}, \tag{B.1}$$

where i runs over cells in the first three layers of the EM calorimeter (pre-sampler, layer 1, and layer 2), associated to the tau candidate.

Track radius (R_{track}): the p_{T} weighted track width:

$$R_{\mathrm{track}} = \frac{\sum_{i}^{\Delta R_i<0.4} p_{\mathrm{T},i}\,\Delta R_i}{\sum_{i}^{\Delta R_i<0.4} p_{\mathrm{T},i}}, \tag{B.2}$$

where i runs over all core and isolation tracks of the tau candidate, and $p_{\mathrm{T},i}$ is the track transverse momentum. Note that for candidates with only one track, R_{track} simplifies to the ΔR between the track and the tau candidate axis.

Leading track momentum fraction (f_{track}):

$$f_{\mathrm{track}} = \frac{p_{\mathrm{T},1}^{\mathrm{track}}}{p_{\mathrm{T}}^{\tau}}, \tag{B.3}$$

where $p_{\mathrm{T},1}^{\mathrm{track}}$ is the transverse momentum of the leading p_{T} core track and p_{T}^{τ} is the transverse momentum of the tau candidate, calibrated at the EM energy scale. Note that for candidates with one track, f_{track} is the fraction of the candidate's momentum attributed to the track, compared to the total momentum of the candidate, which can have contributions from the calorimeter deposits from π^0s and other neutrals.

Core energy fraction (f_{core}): the fraction of transverse energy within ($\Delta R < 0.1$) of the tau candidate:

$$f_{\text{core}} = \frac{\sum_{i\in\{\text{all}\}}^{\Delta R_i<0.1} E_{\text{T},i}}{\sum_{j\in\{\text{all}\}}^{\Delta R_j<0.4} E_{\text{T},j}}, \tag{B.4}$$

where i runs over all cells associated to the tau candidate within $\Delta R < 0.1$ and j runs over all cells in the wide cone. The calorimeter cells associated to a tau candidate are those which are clustered in the topological clusters that are constituents of the jet that seeded tau reconstruction. ΔR_i is defined between a calorimeter cell and the tau candidate axis. $E_{\text{T},i}$ is the cell transverse energy, calibrated at the EM scale. Note that an unconventional definition of the core cone is used for f_{core}, as it provides better discrimination.

Electromagnetic fraction (f_{EM}): the fraction of transverse energy of the tau candidate deposited in the EM calorimeter:

$$f_{\text{EM}} = \frac{\sum_{i\in\{\text{EM 0-2}\}}^{\Delta R_i<0.4} E_{\text{T},i}}{\sum_{j\in\{\text{all}\}}^{\Delta R_j<0.4} E_{\text{T},j}}, \tag{B.5}$$

where $E_{\text{T},i}$ ($E_{\text{T},j}$) is the transverse energy deposited in cell i (j), and i runs over the cells in the first three layers of the EM calorimeter, while j runs over the cells in all layers of the calorimeter.

Cluster mass ($m_{\text{eff. clusters}}$): the invariant mass computed from the constituent clusters of the seed jet, calibrated at the LC energy scale. To minimise the effect of pileup, only the first N leading E_{T} clusters (effective clusters) are used in the calculation, defined as

$$N = \frac{(\sum_i E_{\text{T}i})^2}{\sum_i E_{\text{T}i}^2}, \tag{B.6}$$

where i runs over all clusters associated to the tau candidate, and N is rounded up to the nearest integer.

Track mass (m_{tracks}): the invariant mass of the track system, where the tracks used for the invariant mass calculation use both core and isolation tracks.

Transverse flight path significance ($S_{\text{T}}^{\text{flight}}$): the decay length significance of the secondary vertex for multi-prong tau candidates in the transverse plane:

$$S_{\text{T}}^{\text{flight}} = \frac{L_{\text{T}}^{\text{flight}}}{\delta L_{\text{T}}^{\text{flight}}}, \tag{B.7}$$

where $L_{\text{T}}^{\text{flight}}$ is the reconstructed signed decay length, and $\delta L_{\text{T}}^{\text{flight}}$ is its estimated uncertainty. Only core tracks are used for the secondary vertex fit.

TRT HT fraction (f_{HT}): the ratio of high-threshold to low-threshold hits (including outlier hits), in the Transition Radiation Tracker (TRT), for the leading p_{T} core track.

$$f_{\mathrm{HT}} = \frac{\text{High-threshold TRT hits}}{\text{Low-threshold TRT hits}} \tag{B.8}$$

Since electrons are lighter than pions, and therefore have higher Lorentz γ factors, they are more likely to produce the transition radiation that causes high-threshold hits in the TRT [76]. This variable can be used to discriminate hadronic 1-prong tau candidates from electrons.

Number of isolation tracks ($N^{\mathrm{iso}}_{\mathrm{track}}$): the number of tracks in the isolation annulus.

Hadronic radius (R_{Had}): the transverse energy weighted shower width in the hadronic calorimeter

$$R_{\mathrm{Had}} = \frac{\sum_{i\in\{\mathrm{Had,EM3}\}}^{\Delta R_i<0.4} E_{\mathrm{T},i}\,\Delta R_i}{\sum_{i\in\{\mathrm{Had,EM3}\}}^{\Delta R_i<0.4} E_{\mathrm{T},i}}, \tag{B.9}$$

where i runs over cells associated to the tau candidate in the hadronic calorimeter and also layer 3 of the EM calorimeter. Only cells in the *wide cone*, defined as $\Delta R < 0.4$ from the tau candidate axis, are considered.

Calorimetric radius (R_{Cal}): the shower width in the electromagnetic and hadronic calorimeter weighted by the transverse energy of each calorimeter part.

$$R_{\mathrm{Cal}} = \frac{\sum_{i\in\{\mathrm{all}\}}^{\Delta R_i<0.4} E_{\mathrm{T},i}\,\Delta R_i}{\sum_{i\in\{\mathrm{all}\}}^{\Delta R_i<0.4} E_{\mathrm{T},i}}, \tag{B.10}$$

where i runs over cells in all layers of the EM and hadronic calorimeters. Only cells in the wide cone are considered.

Leading track IP significance ($S_{\text{lead track}}$): the impact parameter significance of the leading track of the tau candidate:

$$S_{\text{lead track}} = \frac{d_0}{\delta d_0}, \tag{B.11}$$

where d_0 is the distance of closest approach of the track to the reconstructed primary vertex in the transverse plane, and δd_0 is its estimated uncertainty.

First 2(3) leading clusters energy ratio ($f_{\text{2 lead clusters}}$($f_{\text{3 lead clusters}}$)): the ratio of the energy of the first two (three) leading clusters (highest energy first) over the total energy of all clusters associated to the tau candidate.

Maximum ΔR (ΔR_{max}): the maximal ΔR between a core track and the tau candidate axis.

Hadronic track fraction (f_{Had}^{track}): the ratio of the hadronic transverse energy over the transverse momentum of the leading track:

$$f_{\mathrm{Had}}^{track} = \frac{\sum_{i\in\{\mathrm{Had}\}}^{\Delta R_i<0.4} E_{\mathrm{T},i}}{p_{\mathrm{T},1}^{\mathrm{track}}}, \tag{B.12}$$

where i runs over all cells in the hadronic calorimeter within the wide cone.

Maximum strip E_{T} ($E_{\mathrm{T,max}}^{\mathrm{strip}}$): the maximum transverse energy deposited in a cell in the pre-sampler layer of the electromagnetic calorimeter, which is not associated with that of the leading track.

Electromagnetic track fraction (f_{EM}^{track}): the ratio of the transverse energy deposited in the electromagnetic calorimeter over the transverse momentum of the leading track:

$$f_{\mathrm{EM}}^{track} = \frac{\sum_{i\in\{\mathrm{EM}\}}^{\Delta R_i<0.4} E_{\mathrm{T},i}}{p_{\mathrm{T},1}^{\mathrm{track}}}, \tag{B.13}$$

where i runs over all cells in the EM calorimeter within the wide cone.

Ring isolation (f_{iso}):

$$f_{\mathrm{iso}} = \frac{\sum_{i\in\{\mathrm{EM\ 0-2}\}}^{0.1<\Delta R<0.2} E_{\mathrm{T},i}}{\sum_{j\in\{\mathrm{EM\ 0-2}\}}^{\Delta R<0.4} E_{\mathrm{T},j}}, \tag{B.14}$$

where i runs over cells in the first three layers of the EM calorimeter in the annulus $0.1 < \Delta R < 0.2$ around the tau candidate axis and j runs over EM cells in the wide cone.

Corrected cluster isolation energy ($E_{\mathrm{T,corr}}^{\mathrm{iso}}$): the transverse energy of isolated clusters:

$$E_{\mathrm{T,corr}}^{\mathrm{iso}} = E_{\mathrm{T}}^{\mathrm{iso}} - \delta E_{\mathrm{T}}^{\mathrm{iso}} = \sum_{i}^{0.2<\Delta R_i<0.4} E_{\mathrm{T},i} - \delta E_{\mathrm{T}}^{\mathrm{iso}} \tag{B.15}$$

where i runs over all clusters associated to the tau candidate. ΔR_i is defined between the cluster and the tau candidate axis. The pileup correction term is defined as $\delta E_{\mathrm{T}}^{\mathrm{iso}} = (1-\mathrm{JVF}) \times \sum p_{T,trk}$, where JVF is the jet vertex fraction of the jet seed of the tau candidate, calculated with respect to the primary vertex and $\sum p_{T,trk}$ the sum of the transverse momentum of the tracks associated to that jet.

C List of Tables

D List of Figures

Bibliography

[1] C. N. Yang and R. L. Mills, *Conservation of isotopic spin and isotopic gauge invariance*, Phys. Rev. **96** (1954) 191–195. 2.2, A.1.6

[2] F. Englert and R. Brout, *Broken symmetry and the mass of gauge vector mesons*, Phys. Rev. Lett. **13** (1964) 321–323. 2.2, A.2.3

[3] P. Higgs, *Broken symmetries, massless particles and gauge fields*, Physics Letters **12** (1964) 132–133. 2.2, A.2.3

[4] P. W. Higgs, *Broken symmetries and the masses of gauge bosons*, Phys. Rev. Lett. **13** (1964) 508–509. 2.2, A.2.3

[5] G. S. Guralnik, C. R. Hagen, and T. W. B. Kibble, *Global conservation laws and massless particles*, Phys. Rev. Lett. **13** (1964) 585–587. 2.2, A.2.3

[6] S. Glashow, *Partial symmetries of weak interactions*, Nucl.Phys. **22** (1961) 579–588. 2.2, A.2.3, A.2.4

[7] S. Weinberg, *A model of leptons*, Phys. Rev. Lett. **19** (1967) 1264–1266. 2.2, A.2.3, A.2.4

[8] A. Salam and J. C. Ward, *Gauge theory of elementary interactions*, Phys. Rev. 136 (1964) 763–768. 2.2, A.2.3

[9] A. Salam and J. C. Ward, *Electromagnetic and weak interactions*, Phys.Lett. **13** (1964) 168–171. 2.2, A.2.3

[10] A. Salam, *Weak and electromagnetic interactions*, Svartholm: Elementary Particle Theory, Proceedings Of The Nobel Symposium Held 1968 At Lerum, Sweden, Stockholm (1968) 367–377. 2.2, A.2.3, A.2.4

[11] H. D. Politzer, *Reliable perturbative results for strong interactions?*, Phys. Rev. Lett. **30** (1973) 1346–1349. 2.2, A.2.5

[12] D. J. Gross and F. Wilczek, *Ultraviolet behavior of non-abelian gauge theories*, Phys. Rev. Lett. **30** (1973) 1343–1346. 2.2, A.2.5

[13] D. J. Gross and F. Wilczek, *Asymptotically free gauge theories. I*, Phys. Rev. D **8** (1973) 3633–3652. 2.2, A.2.5

[14] D. J. Gross and F. Wilczek, *Asymptotically free gauge theories. II*, Phys. Rev. D **9** (1974) 980–993. 2.2, A.2.5

[15] S. Weinberg, *Non-abelian gauge theories of the strong interactions*, Phys. Rev. Lett. **31** (1973) 494–497. 2.2, A.2.5

[16] A. Chao *et al.*, *2001 Snowmass accelerator R&D report*, SLAC-PUB-9483, 2001. 2.2

[17] ALEPH, DELPHI, L3, and OPAL Collaborations, *Search for the standard model Higgs boson at LEP*, Phys.Lett.B **565** (2003) 61–75, arXiv:hep-ex/0306033 [hep-ex]. 2.3.1, 2.3

[18] CDF and DØ Collaborations, *Updated combination of CDF and DØ searches for standard model Higgs boson production with up to 10.0 fb^{-1} of data*, arXiv:1207.0449 [hep-ex]. 1

[19] CDF and DØ Collaborations, *Combined CDF and DØ upper limits on standard model Higgs-boson production with up to 4.2 fb^{-1} of data*, arXiv:0903.4001 [hep-ex]. 2.3

[20] ALEPH, CDF, DØ, DELPHI, L3, OPAL, and SLD Collaborations, *Precision electroweak measurements and constraints on the standard model*, arXiv:0911.2604 [hep-ex]. 2.4

[21] ATLAS Collaboration, *Combined search for the Standard Model Higgs boson in pp collisions at $\sqrt{s} = 7$ TeV with the ATLAS detector*, Phys.Rev. **D**86 (2012) 032003, arXiv:1207.0319 [hep-ex]. 2.3.2

[22] CMS Collaboration, *Combined results of searches for the standard model Higgs boson in pp collisions at $\sqrt{s} = 7$ TeV*, Phys.Lett. **B**710 (2012) 26–48, arXiv:1202.1488 [hep-ex]. 2.3.2

[23] ATLAS Collaboration, *Observation of a new particle in the search for the Standard Model Higgs boson with the ATLAS detector at the LHC*, Phys.Lett.B **716** (2012) 1–29, arXiv:1207.7214 [hep-ex]. 2.3.2, 2.5, 2.6, 2.7, 2.3.2, 2.3.2

[24] CMS Collaboration, *Observation of a new boson at a mass of 125 GeV with the CMS experiment at the LHC*, Phys.Lett.B **716** (2012) 30–61, arXiv:1207.7235 [hep-ex]. 2.3.2

[25] A. Denner, S. Heinemeyer, I. Puljak, D. Rebuzzi, and M. Spira, *Standard Model Higgs boson branching ratios with uncertainties*, Eur.Phys.J.C **71** (2011) 1753, arXiv:1107.5909 [hep-ph]. 2.5

[26] LHC Higgs Cross Section Working Group Collaboration, S. Dittmaier et al., *Handbook of LHC Higgs Cross Sections: 1. Inclusive Observables*, arXiv:1101.0593 [hep-ph]. 2.5

[27] S. Dittmaier et al., *Handbook of LHC Higgs Cross Sections: 2. Differential Distributions*, arXiv:1201.3084 [hep-ph]. 2.1

[28] ATLAS Collaboration, *Observation of an excess of events in the search for the Standard Model Higgs boson in the $\gamma\gamma$ channel with the ATLAS detector*, ATLAS-CONF-2012-091, 2012. 2.6

[29] ATLAS Collaboration, *Search for the Standard Model Higgs boson in $H \to \tau\tau$ in proton-proton collisions with the ATLAS detector*, ATLAS-CONF-2012-160, 2012. 2.3.2, 6.1

[30] *Search for the Standard Model Higgs boson in produced in association with a vector boson and decaying to bottom quarks with the ATLAS detector*, ATLAS-CONF-2012-161, 2012. 2.3.2

[31] Super-Kamiokande Collaboration, *Evidence for oscillation of atmospheric neutrinos*, Phys. Rev. Lett. **81** (1998) 1562–1567. 2.4.1, A.2.7

[32] SNO Collaboration, *Measurement of the rate of $\nu_e + d \to p + p + e^-$ interactions produced by ^8B solar neutrinos at the Sudbury Neutrino Observatory*, Phys. Rev. Lett. **87** (2001) 071301. 2.4.1, A.2.7

[33] P. Langacker, *The Standard Model and Beyond*. CRC Press, 2010. 2.4.2, 2.4.3, 2.5.3, 87, A.2.7

[34] T. Hambye and K. Riesselmann, *SM Higgs mass bounds from theory*, arXiv:hep-ph/9708416 [hep-ph]. 2.8, 2.4.3

[35] C. F. Kolda and H. Murayama, *The Higgs mass and new physics scales in the minimal standard model*, JHEP **0**007 (2000) 035, arXiv:hep-ph/0003170 [hep-ph]. 2.4.3

[36] A. D. Sakharov, *Violation of CP in variance, C asymmetry, and baryon asymmetry of the universe*, Journal of Experimental and Theoretical Physics **5** (1967) 24–27. Republished in Soviet Physics Uspekhi 34 (5): 392–393. 2.4.4

[37] Planck Collaboration, *Planck 2013 results. I. Overview of products and scientific results*, arXiv:1303.5062 [astro-ph.CO]. 2.4.5

[38] R. Haag, J. T. Lopuszański, and M. Sohnius, *All possible generators of supersymmetries of the S-matrix*, Nuclear Physics B **88** (1975) 257–274. 2.5.1, A.1.4

[39] S. P. Martin, *A Supersymmetry primer*, arXiv:hep-ph/9709356 [hep-ph]. 2.9

[40] U. Amaldi, A. Böhm, L. S. Durkin, P. Langacker, A. K. Mann, W. J. Marciano, A. Sirlin, and H. H. Williams, *Comprehensive analysis of data pertaining to the weak neutral current and the intermediate-vector-boson masses*, Phys. Rev. D **36** (1987) 1385–1407. 2.5.2

[41] U. Amaldi, W. de Boer, and H. Fürstenau, *Comparison of grand unified theories with electroweak and strong coupling constants measured at LEP*, Physics Letters B **260** (1991) 447–455. 2.5.2

[42] S. Dimopoulos and H. Georgi, *Softly Broken Supersymmetry and SU(5)*, Nucl.Phys.B **193** (1981) 150. 2.5.2

[43] J. Ellis, K. Enqvist, G. Gelmini, C. Kounnas, A. Masiero, D. V. Nanopoulos, and A. Y. Smirnov, *Towards a supersymmetric cosmology*, Physics Letters B **147** (1984) 27–33. 2.5.2

[44] S. Dimopoulos, S. A. Raby, and F. Wilczek, *Unification of couplings*, Physics Today **44** (1991) 25–33. 2.5.2

[45] W. de Boer and C. Sander, *Global electroweak fits and gauge coupling unification*, Phys.Lett.B **585** (2004) 276–286, arXiv:hep-ph/0307049 [hep-ph]. 2.5.2

[46] J. C. Pati and A. Salam, *Lepton number as the fourth "color"*, Phys. Rev. D **10** (1974) 275–289. 2.5.3

[47] H. Georgi and S. L. Glashow, *Unity of all elementary-particle forces*, Physical Review Letters **32** (1974) 438–441. 2.5.3

[48] H. Georgi, H. R. Quinn, and S. Weinberg, *Hierarchy of interactions in unified gauge theories*, Physical Review Letters **33** (1974) 451–454. 2.5.3

[49] R. Slansky, *Group theory for unified model building*, Phys.Rept. **79** (1981) 1–128. 2.5.3

[50] J. C. Baez and J. Huerta, *The Algebra of Grand Unified Theories*, Bull.Am.Math.Soc. **47** (2010) 483–552, arXiv:0904.1556 [hep-th]. 2.5.3

[51] D. London and J. L. Rosner, *Extra gauge bosons in E_6*, Phys.Rev.D **34** (1986) 1530–1546. 2.5.3

[52] J. L. Hewett and T. G. Rizzo, *Low-energy phenomenology of superstring-inspired* E_6 *models*, Phys. Reports **183** (1989) 193–381. 2.5.3, 6.1

[53] B. A. Ovrut, A. Purves, and S. Spinner, *Wilson lines and a canonical basis of SU(4) heterotic standard models*, JHEP **1211** (2012) 026, arXiv:1203.1325 [hep-th]. 2.5.3

[54] A. Martin, W. Stirling, R. Thorne, and G. Watt, *Parton distributions for the LHC*, Eur.Phys.J.C **63** (2009) 189–285, arXiv:0901.0002 [hep-ph]. 3.1, A.7, A.2.5

[55] A. Martin, W. Stirling, R. Thorne, and G. Watt, *Martin-Stirling-Thorne-Watt Parton Distribution Functions*, http://mstwpdf.hepforge.org, 2013. See also `http://www.hep.phy.cam.ac.uk/~wjs/plots/plots.html`. 3.1

[56] M. L. Perl, *The Superconducting Super Collider Project*, SLAC-PUB-3943, 1986. 7

[57] SSC, *Site-specific conceptual design of the superconducting super collider*. SSC, Dallas, TX, 1990. 7

[58] J.-L. Caron, *Overall view of LHC experiments.*, LHC-PHO-1998-349, May, 1998. 3.2

[59] C. Lefevre, *LHC: the guide*, https://cds.cern.ch/record/1092437, 2008. 3.1

[60] T. Berners-Lee, *Information Management: A Proposal*, http://www.w3.org/History/1989/proposal.html. March 1989. 8

[61] CERN, *Statement concerning CERN W3 software release into public domain*, CERN-IT-9304003. 30 April 1993. 8

[62] M. Benedikt, P. Collier, V. Mertens, J. Poole, and K. Schindl, *LHC Design Report*. CERN, Geneva, 2004. 3.3, 3.1

[63] J. J. Goodson, *Search for supersymmetry in states with large missing transverse momentum and three leptons including a Z boson*. PhD thesis, Stony Brook U., 2012. CERN-THESIS-2012-053. 3.3

[64] LHC Machine Outreach, *Relative beam sizes around IP1 (ATLAS) in collision*, http://lhc-machine-outreach.web.cern.ch/lhc-machine-outreach/collisions.htm, 2012. 3.4

[65] ATLAS Collaboration, *ATLAS online beam spot public results*, https://twiki.cern.ch/twiki/bin/view/AtlasPublic/OnlineBeamSpotPublicResults, 2013. 10

[66] L. R. Evans and P. Bryant, *LHC Machine*, JINST **3** (2008) S08001. 3.1, 3.4

[67] ATLAS Collaboration, *ATLAS detector and physics performance: Technical Design Report*. CERN, Geneva, 1999. 3.2.1

[68] ATLAS Collaboration, *The ATLAS experiment at the CERN Large Hadron Collider*, JINST **3** (2008) S08003. 3.5, 3.2.1, 11, 3.2.2, 3.2, 3.7, 3.2.3, 3.3, 3.8, 3.9, 3.10, 3.11, 3.2.4, 3.3.2, 3.3.3, 3.3.4, 3.3.5, 3.4

[69] ATLAS Collaboration, *Expected performance of the ATLAS experiment: detector, trigger and physics*. CERN, Geneva, 2008. arXiv:0901.0512. 3.2.1, 3.3.3, 3.3.4, 40, 5.1.1, 5.4.3, 6.3.1, 6.3.2

[70] ATLAS Outreach, *ATLAS Fact Sheet*, https://cds.cern.ch/record/1457044, 2010. 3.2.1, 3.6

[71] CMS Collaboration, *The CMS experiment at the CERN LHC*, Journal of Instrumentation **3** (2008) no. 08, S08004. 3.2.2, 3.2

[72] H. M. Gray, *The charged particle multiplicity at center of mass energies from 900 GeV to 7 TeV measured with the ATLAS experiment at the Large Hadron Collider*. PhD thesis, California Institute of Technology, Pasadena, USA, 2010. CERN-THESIS-2010-163. 3.7

[73] R. Reece, *TRT low threshold calibration*, ATL-INDET-INT-2008-002, 2008. 12

[74] R. Reece, J. Adelman, S. Fratina, D. Guest, and E. Klinkby, *TRT straw hit efficiency*, ATL-COM-INDET-2011-088, 2011. 12, 3.2.3

[75] ATLAS Collaboration, *Performance of the ATLAS detector using first collision data*, JHEP **1009** (2010) 056, arXiv:1005.5254 [hep-ex]. 12, 3.8, 3.2.3, 3.5.1

[76] ATLAS TRT Collaboration, *The ATLAS Transition Radiation Tracker (TRT) proportional drift tube: design and performance*, Journal of Instrumentation **3** (2008) no. 02, P02013. http://stacks.iop.org/1748-0221/3/i=02/a=P02013. 3.2.3, B

[77] ATLAS TRT Collaboration, *The ATLAS TRT barrel detector*, Journal of Instrumentation **3** (2008) no. 02, P02014. http://stacks.iop.org/1748-0221/3/i=02/a=P02014. 3.2.3

[78] ATLAS TRT Collaboration, *The ATLAS TRT end-cap detectors*, Journal of Instrumentation **3** (2008) no. 10, P10003. http://stacks.iop.org/1748-0221/3/i=10/a=P10003. 3.2.3

[79] ATLAS TRT Collaboration, *The ATLAS TRT electronics*, Journal of Instrumentation **3** (2008) no. 06, P06007. http://stacks.iop.org/1748-0221/3/i=06/a=P06007. 3.2.3

[80] *Particle identification performance of the ATLAS Transition Radiation Tracker*, ATLAS-CONF-2011-128, 2011. 3.2.3

[81] ATLAS Collaboration, *Muon Momentum Resolution in the First Pass Reconstruction of the 2010 p-p Collision data*, ATLAS-CONF-2011-046, 2011. 3.2.3, 3.2.5

[82] *Atlas Computing: technical design report*. CERN, Geneva, 2005. 3.3.1, 3.24, 6.2.1

[83] A. Salzburger, *The ATLAS Track Extrapolation Package*, ATL-SOFT-PUB-2007-005, 2007. 3.13, 3.3.2

[84] T. Cornelissen, M. Elsing, S. Fleischmann, W. Liebig, E. Moyse, and A. Salzburger, *Concepts, design, and implementation of the ATLAS New Tracking (NEWT)*, ATL-SOFT-PUB-2007-007, 2007. 3.3.2

[85] ATLAS Collaboration, *Search for the Standard Model Higgs boson in the decay channel* $H \to ZZ^{(*)} \to 4\ell$ *with 4.8* fb^{-1} *of pp collisions at* $\sqrt{s} = 7$ *TeV*, ATLAS-CONF-2011-162, 2011. 3.14

[86] ATLAS Collaboration, *ATLAS public event displays*, https://twiki.cern.ch/twiki/bin/view/AtlasPublic/EventDisplayStandAlone, 2009–2012. 3.14, 3.15, 3.18, 3.23

[87] ATLAS Collaboration, *Muon reconstruction efficiency in reprocessed 2010 LHC proton-proton collision data recorded with the ATLAS detector*, ATLAS-CONF-2011-063, 2011. 3.3.3

[88] ATLAS Egamma Performance Group, *Egamma performance twiki*, https://twiki.cern.ch/twiki/bin/view/AtlasProtected/ElectronGamma, 2012. 3.3.4, 6.3.2

[89] ATLAS Egamma Performance Group, *ATLAS egamma performance TechnicalitiesForMedium1*, https://twiki.cern.ch/twiki/bin/viewauth/AtlasProtected/TechnicalitiesForMedium1, 2011. 3.3.4, 6.3.2

[90] ATLAS Collaboration, *Electron performance measurements with the ATLAS detector using the 2010 LHC proton-proton collision data*, Eur.Phys.J. **C**72 (2012) 1909, arXiv:1110.3174 [hep-ex]. 3.3.4, 3.25, 4.4.5, 6.3.2

[91] W. Lampl, S. Laplace, D. Lelas, P. Loch, H. Ma, S. Menke, S. Rajagopalan, D. Rousseau, S. Snyder, and G. Unal, *Calorimeter clustering algorithms: description and performance*, ATL-LARG-PUB-2008-002, 2008. 3.3.5, 3.3.6, 4.2.2, 5.4.4, 6.3.4

[92] ATLAS Collaboration, *ATLAS topological clustering*, https://twiki.cern.ch/twiki/bin/view/Atlas/TopologicalClustering, 2013. 3.16

[93] ATLAS Collaboration, *Jet energy measurement with the ATLAS detector in proton-proton collisions at* $\sqrt{s} = 7$ *TeV*, arXiv:1112.6426 [hep-ex]. Submitted to EPJC. 3.3.6, 4.2.3, 6.3.4

[94] M. Cacciari, G. P. Salam, and G. Soyez, *The anti-k_t jet clustering algorithm*, JHEP **0**4 (2008) 063, arXiv:0802.1189 [hep-ph]. 3.3.6, 4.2.2, 6.3.4

[95] Barillari, T et al., *Local hadronic calibration*, ATL-LARG-PUB-2009-001-2, 2008. 3.3.6, 4.4.5, 6.3.4

[96] ATLAS JetEtMiss Performance Group, *JetEtMiss performance twiki*, https://twiki.cern.ch/twiki/bin/view/AtlasProtected/JetEtMiss, 2012. 17

[97] W. Davey, J. Dingfelder, A. Florez, J. Glatzer, G. Palacino, R. Reece, A. Tuna, P. Wagner, and H. Williams, *A search for high-mass resonances decaying to $\tau^+\tau^-$ in pp collisions at $\sqrt{s} = 7$ TeV with the ATLAS detector*, ATL-COM-PHYS-2012-394, 2012. Support note for ATLAS-CONF-2012-067 and arXiv:1210.6604 [hep-ex]. 17, 4.4.7, 4.5, 4.27, 4.28, 4.29, 4.30, 4.4.7, 4.31, 4.36, 38, 65, 6.2.2, 67, 6.1, 6.2, 6.4.2, 6.1, 6.2, 6.3, 6.4, 6.3, 6.4, 6.5, 6.6, 6.7, 6.4.4, 6.8, 6.10, 6.4.4, 6.11, 6.5, 6.12, 6.13, 79, 6.6, 6.6, 6.8, 6.9, 82, 86, 6.16, 6.17, 6.18

[98] D. W. Miller, A. Schwartzman, and D. Su, *Jet-vertex association algorithm*, ATL-COM-PHYS-2008-008, 2008. 3.3.6

[99] D. W. Miller, *Measurement of hadronic event shapes and jet substructure in proton-proton collisions at 7 TeV center-of-mass energy with the ATLAS detector at the Large Hadron Collider*. PhD thesis, Stanford University, Menlo Park, CA, 2011. CERN-THESIS-2011-144. 3.3.6, 3.17

[100] ATLAS Collaboration, *Reconstruction, energy calibration, and identification of hadronically decaying tau leptons*, ATLAS-CONF-2011-077, 2011. 3.3.7, 4.2.1, 4.4, 4.3.1, 4.3.3, 4.3, 4.12, 4.13, 4.14, 4.3.4, 4.3.4, 30, 4.19, 4.4.5, 4.4.6, 4.25, 4.4.9, 38, 5.9.2

[101] ATLAS Collaboration, *Performance of the reconstruction and identification of hadronic tau decays with ATLAS*, ATLAS-CONF-2011-152, 2011. 3.3.7, 3.3.7, 4.2.1, 4.16, 4.4.1, 4.23, 4.4.5, 4.4.6, 4.4.7, 4.4.9, 4.40, 4.41, 4.43, 38, 6.3.3

[102] ATLAS Collaboration, *Performance of the reconstruction and identification of hadronic tau decays in ATLAS with 2011 data*, ATLAS-CONF-2012-142, 2012. 3.3.7, 3.5.2, 4.2.1, 4.2.5, 4.5, 4.3.5, 4.16, 4.4.1, 4.22, 4.4.4, 4.4, 4.26, 38, 6.4.2

[103] W. Davey, P.-O. DeViveiros, M. Flechl, H. Fox, F. Friedrich, J. Keller, S. Lai, H. Maddocks, T. Mitani, A. Pingel, R. Reece, Y. Sakurai, F. Scutti, S. Tsuno, A. Tuna, H. Weits, S. Xella, and S. Wahrmund, *Identification of the hadronic decays of tau leptons in 2012 data*, ATL-COM-PHYS-2012-1821, 2012. 3.3.7, 4.2.1, 4.4.6, 38, 4.45

[104] ATLAS Collaboration, *Measurement of the top quark pair production cross section in pp collisions at $\sqrt{s} = 7$ TeV in $\mu+\tau$ final states with ATLAS.*, ATLAS-CONF-2011-119, 2011. 3.18

[105] ATLAS Collaboration, *Performance of missing transverse momentum reconstruction in proton-proton collisions at 7 TeV with ATLAS*, Eur.Phys.J.C **72** (2012) 1844, arXiv:1108.5602 [hep-ex]. 3.3.8, 6.3.5

[106] S. Kama, *Evolution of the trigger and data acquisition system in the ATLAS experiment*, ATL-DAQ-PROC-2012-061, 2012. 3.19, 3.4.3

[107] ATLAS Collaboration, *ATLAS trigger operation public results*, https://twiki.cern.ch/twiki/bin/view/AtlasPublic/TriggerOperationPublicResults, 2013. 3.20

[108] ATLAS Collaboration, *Measurement of the $W \to \ell\nu$ and $Z/\gamma^* \to \ell\ell$ production cross sections in proton-proton collisions at $\sqrt{s} = 7$ TeV with the ATLAS detector*, JHEP **1012** (2010) 060, arXiv:1010.2130 [hep-ex]. 3.5.1, 5.3.2, 5.4.3, 5.10, 5.30

[109] ATLAS Collaboration, *Measurement of the inclusive $W^{\pm}$ and Z/γ^* cross sections in the electron and muon decay channels in pp collisions at $\sqrt{s} = 7$ TeV with the ATLAS detector*, Phys.Rev.D **85** (2012) 072004, arXiv:1109.5141 [hep-ex]. 3.5.1

[110] ATLAS Collaboration, *Measurement of the transverse momentum distribution of Z/γ^* bosons in proton-proton collisions at $\sqrt{s} = 7$ TeV with the ATLAS detector*, Phys.Lett.B **705** (2011) 415–434, arXiv:1107.2381 [hep-ex]. 3.5.1

[111] ATLAS Collaboration, *Measurement of the transverse momentum distribution of W bosons in pp collisions at $\sqrt{s} = 7$ TeV with the ATLAS detector*, Phys.Rev.D **85** (2012) 012005, arXiv:1108.6308 [hep-ex]. 3.5.1

[112] ATLAS Collaboration, *Measurement of the top quark-pair production cross section with ATLAS in pp collisions at $\sqrt{s} = 7$ TeV*, Eur.Phys.J.C **71** (2011) 1577, arXiv:1012.1792 [hep-ex]. 3.5.1

[113] ATLAS Collaboration, *Measurement of the $Z \to \tau\tau$ cross section in pp collisions at $\sqrt{s} = 7$ TeV with the ATLAS detector*, Phys.Rev.D **84** (2011) 112006, arXiv:1108.2016 [hep-ex]. 3.5.1, 4.3.3, 4.4.2, 5.13, 5.15, 5.16, 5.10, 5.30, 62, 5.17

[114] ATLAS Collaboration, *Luminosity public results*, https://twiki.cern.ch/twiki/bin/view/AtlasPublic/LuminosityPublicResults, 2013. 3.21, 3.22, 6.2.1

[115] ATLAS Collaboration, *ATLAS data summary*, https://atlas.web.cern.ch/Atlas/GROUPS/DATAPREPARATION/DataSummary, 2013. 3.4

[116] ATLAS Collaboration, *Performance of the ATLAS inner detector track and vertex reconstruction in the high pile-up LHC environment*, ATLAS-CONF-2012-042, 2012. 3.5.2

[117] E. Barberio, S. Bedikian, E. Coniavitis, M. Dam, W. Davey, E. N. Dawe, S. Demers, M. Flechl, F. Friedrich, J. Godfrey, K. Hanawa, M. Janus, D. Jennens, J. Keller, S. Lai, M. Morgenstern, K. Nakamura, D. C. O'Neil, M. I. Pedraza Morales, R. Reece, N. Rompotis, M. Simonyan, A. Saavedra, K. G. Tan, M. Trottier-McDonald, S. Tsuno, D. Varouchas, M. Volpi, M. Wolter, S. Xella, and D. Zanzi, *Identification of hadronic tau decays for summer 2011*, ATL-PHYS-INT-2011-090, 2011. Support note for ATLAS-CONF-2011-152. 3.5.2, 4.7, 4.42, 4.7

[118] ATLAS Collaboration, *The ATLAS simulation infrastructure*, Eur.Phys.J.C **70** (2010) , arXiv:1005.4568 [physics.ins-det]. 3.6.1, 6.2.2

[119] M. L. Mangano, M. Moretti, F. Piccinini, R. Pittau, and A. D. Polosa, *ALPGEN, a generator for hard multiparton processes in hadronic collisions*, JHEP **07** (2003) 001, arXiv:0206293 [hep-ph]. 3.6.1

[120] S. Frixione and B. R. Webber, *Matching NLO QCD computations and parton shower simulations*, JHEP **0206** (2002) 029. 3.6.1

[121] G. Corcella *et al.*, *HERWIG 6.5 release note*, arXiv:hep-ph/0210213. 3.6.1, 5.3.2

[122] J. M. Butterworth, J. R. Forshaw, and M. H. Seymour, *Multiparton interactions in photoproduction at HERA*, Z.Phys.C **72** (1996) 637–646, arXiv:hep-ph/9601371. 3.6.1

[123] ATLAS Collaboration, *First tuning of HERWIG/JIMMY to ATLAS data*, ATL-PHYS-PUB-2010-014, 2010. 3.6.1

[124] B. P. Kersevan and E. Richter-Was, *The Monte Carlo event generator AcerMC version 2.0 with interfaces to PYTHIA 6.2 and HERWIG 6.5*, arXiv:hep-ph/0405247 [hep-ph]. 3.6.1

[125] T. Sjostrand, S. Mrenna, and P. Skands, *PYTHIA 6.4 physics and manual*, JHEP **05** (2006) 026, arXiv:0603175 [hep-ph]. 3.6.1, 4.4.1, 5.3.2

[126] P. Golonka and Z. Was, *PHOTOS Monte Carlo: A Precision tool for QED corrections in Z and W decays*, Eur.Phys.J. C **45** (2006) 97–107, arXiv:hep-ph/0506026 [hep-ph]. 3.6.1, 5.8

[127] N. Davidson, G. Nanava, T. Przedzinski, E. Richter-Was, and Z. Was, *Universal Interface of TAUOLA Technical and Physics Documentation*, Comput.Phys.Commun. **183** (2012) 821–843, arXiv:1002.0543 [hep-ph]. 3.6.1, 4.4.7, 5.8

[128] S. Agostinelli *et al.*, *GEANT4: A simulation toolkit*, Nucl. Instr. and Meth. A **506** (2003) 250. 3.6.2

[129] ATLAS Collaboration, *Charged particle multiplicities in pp interactions at* $\sqrt{s} = 0.9$ *and 7 TeV in a diffractive limited phase space measured with the ATLAS detector at the LHC and a new PYTHIA 6 tune*, ATLAS-CONF-2010-031, 2010. 3.6.2, 4.4.1, 5.8

[130] WLCG, *Worldwide LHC Computing Grid*, http://wlcg.web.cern.ch, 2013. 3.26, 3.7.1

[131] H. Sakamoto, *The ATLAS distributed computing: the challenges of the future*, ATL-SOFT-PROC-2013-001, 2013. 3.26

[132] I. Bird, *Computing for the Large Hadron Collider*, Annual Review of Nuclear and Particle Science **61** 99–118. 3.27

[133] *ROOT*, http://root.cern.ch, 2013. 3.7.1, 4.3.4

[134] K. Cranmer, *Athena analysis tutorial*, USATLAS Analysis Jamboree, May, 2007. 3.28

[135] I. Ueda, *The Present and Future Challenges of Distributed Computing in the ATLAS experiment*, ATL-SOFT-PROC-2012-069, 2012. 3.5

[136] J. Beringer *et al.* (Particle Data Group), *The Review of Particle Physics*, Phys.Rev.D **86** (2012) 010001. 4.1, 6.7.3, 6.7.4, 87, A.4, A.6, A.2.7, A.7

[137] ATLAS Collaboration, *Measurement of inclusive jet and dijet cross sections in proton-proton collisions at 7 TeV centre-of-mass energy with the ATLAS detector*, Eur.Phys.J.C (2010) , arXiv:1009.5908 [hep-ex]. 22

[138] ATLAS Collaboration, *Measurement of the $W \to \tau\nu$ cross section in pp collisions at $\sqrt{s} = 7$ TeV with the ATLAS detector*, Phys.Lett.B **706** (2012) 276–294, arXiv:1108.4101 [hep-ex]. 22, 4.4.2

[139] ATLAS Tau Performance Group, *Standard tau notation for public documents*, https://twiki.cern.ch/twiki/bin/viewauth/AtlasProtected/TauWG, 2012. 23

[140] A. Christov, Y. Coadou, Z. Czyczula, M. Janus, L. Janyst, A. Kaczmarska, A. Kalinowski, J. Komaragiri, S. Lai, W. Mader, N. Meyer, E. Richter-Was, C. Ruwiedel, and M. Wolter, *Performance of the tau reconstruction and identification algorithm with release 14.2.20 and mc08 data*, ATL-COM-PHYS-2009-229, 2009. 4.2, 4.3, 4.2.2

[141] ATLAS Collaboration, *Tau reconstruction and identification performance in ATLAS*, ATLAS-CONF-2010-086, 2010. 4.3.2

[142] ATLAS Collaboration, *Tau identification performance with the ATLAS detector*, ATL-COM-PHYS-2010-599, 2010. Support note for ATLAS-CONF-2010-086. 4.3.2, 4.1

[143] R. Reece, *Cut-based tau ID: status and plans*, Talk given at an ATLAS tau working group meeting, CERN. Nov 11, 2010. 4.6, 4.3.3, 4.10

[144] ATLAS Collaboration, *Reconstruction of hadronic tau candidates in QCD events at ATLAS with 7 TeV proton-proton collisions*, ATLAS-CONF-2010-059, 2010. 4.3.2, 4.4.1, 4.17, 38

[145] ATLAS Collaboration, *Observation of $W \to \tau\nu$ decays with the ATLAS experiment*, ATLAS-CONF-2010-097, 2010. 4.3.2, 4.4.2, 4.18

[146] ATLAS Collaboration, *Observation of $Z \to \tau_h\tau_l$ decays with the ATLAS detector*, ATLAS-CONF-2011-010, 2011. 4.3.2, 5.5, 5.23, 62

[147] ATLAS Collaboration, *Reconstruction, energy calibration, and identification of hadronic tau decays for winter 2011*, ATL-PHYS-INT-2011-068, 2011. Support note for ATLAS-CONF-2011-077. 4.8, 4.9, 4.2, 4.15, 4.3.4, 4.4.3, 4.20, 4.21, 4.37

[148] A. Kalinowski and K. Benslama, *Tau identification with the logarithmic likelihood method*, ATL-PHYS-INT-2008-037, 2008. 4.3.4, 5.5, 5.6

[149] L. Breiman, J. Friedman, C. Stone, and R. Olshen, *Classification and Regression Trees*. Chapman & Hall, 1984. 4.3.4

[150] A. Hoecker, P. Speckmayer, J. Stelzer, J. Therhaag, E. von Toerne, H. Voss, M. Backes, T. Carli, O. Cohen, A. Christov, D. Dannheim, K. Danielowski, S. Henrot-Versille, M. Jachowski, K. Kraszewski, A. Krasznahorkay, Jr., M. Kruk, Y. Mahalalel, R. Ospanov, X. Prudent, A. Robert, D. Schouten, F. Tegenfeldt, A. Voigt, K. Voss, M. Wolter, and A. Zemla, *TMVA - Toolkit for Multivariate Data Analysis*, arXiv:physics/0703039. 4.3.4

[151] Y. Freund and R. Shapire, *Experiments with a New Boosting Algorithm*, in *Proceedings 13th International Conference on Machine Learning*. 1996. 4.3.4

[152] E. Dawe, D. O'Neil, and S. Protopopescu, *Using boosted decision trees for hadronic tau identification*, ATL-PHYS-INT-2011-004, 2011. 4.3.4

[153] Z. Czyczula and M. Dam, *Cut-based electron veto algorithm for the track-seeded part of tauRec*, ATL-PHYS-INT-2009-023, 2009. 4.3.5

[154] *Commissioning of the ATLAS tau-tepton reconstruction using 900 GeV minimum-bias data*, ATLAS-CONF-2010-012, 2010. 4.4.1, 4.17, 38

[155] ATLAS Collaboration, *Properties of jets and inputs to jet reconstruction and calibration with the ATLAS detector using proton-proton collisions at* $\sqrt{s} = 7$ *TeV*, ATLAS-CONF-2010-053, 2010. 4.4.1

[156] ATLAS Collaboration, *Jet shapes in ATLAS and MC modeling*, ATL-PHYS-PUB-2011-010, 2011. 4.4.1

[157] ATLAS Collaboration, *Study of jet shapes in inclusive jet production in pp collisions at* $\sqrt{s} = 7$ *TeV using the ATLAS detector*, Phys.Rev.D **83** (2011) 052003, arXiv:1101.0070 [hep-ex]. 4.4.1, 4.33

[158] F. Friedrich, W. Mader, and A. Straessner, *Determination of the tau identification fake rate using* $Z(\to \ell\ell)$*+jets events with the ATLAS detector*, ATL-PHYS-INT-2011-070, 2011. 4.4.3, 5.7.2

[159] ATLAS Collaboration, *Determination of the tau energy scale and the associated systematic uncertainty in proton-proton collisions at* $\sqrt{s} = 7$ *TeV with the ATLAS detector at the LHC in 2011*, ATLAS-CONF-2012-054, 2012. 4.24, 4.4.5, 5.1.1

[160] ATLAS Collaboration, *Determination of the tau energy scale and the associated systematic uncertainty in proton-proton collisions at* $\sqrt{s} = 8$ *TeV with the ATLAS detector at the LHC in 2012*, ATLAS-CONF-2013-044, 2013. 4.4.5

[161] ATLAS Collaboration, *Measurement of hadronic tau decay identification efficiency using* $W \to \tau\nu$ *events*, ATLAS-CONF-2011-093, 2011. 4.4.6

[162] A. Tuna, *Talks in the ATLAS tau performance group on high-*p_{T} *tau efficiency on 2011-07-18, 2011-08-05, and 2011-08-23*, Talk given at an ATLAS tau working group meetings, CERN. 4.4.7

[163] R. Alon, L. Asquith, S. Baker, E. Bergeaas Kuutmann, B. Chapleau, S. Chekanov, A. R. Davison, E. Duchovni, T. Farooque, J. Ferrando, L. S. Gomez Fajardo, M. Karagoz, S. Livermore, A. Lewis, D. W. Miller, K. Moenig, E. Oliver, J. Proudfoot, C. Sandoval, A. Schwartzman, P. Sinervo, M. Villaplana, and M. Vos, *Backup note for jet mass and substructure in QCD jets with the ATLAS experiment*, ATL-COM-PHYS-2011-1319, 2011. 4.4.7

[164] M. Begel, A. Gaponenko, I. Hinchliffe, F. Paige, C. Ruwiedel, M. Shapiro, and S. Zenz, *A study of release 16 tracking performance in jets using 2010 data*, ATL-COM-INDET-2011-028, 2011. 4.4.7

[165] ATLAS Collaboration, *Light-quark and gluon jets in ATLAS*, ATLAS-CONF-2011-053, 2011. 4.4.8

[166] ATLAS Collaboration, *Light-quark and gluon Jets: calorimeter response, jet energy scale systematics and properties*, ATLAS-CONF-2012-138, 2012. 4.32, 4.4.8

[167] A. Tuna, *Jet fake rates in a search for* $Z \to \tau\tau \to \ell\tau_{\mathrm{h}}$ *and exploring quark-gluon composition to motivate systematics*, Talk given at the ATLAS tau performance / $H \to \tau\tau$ workshop, Oxford, England. March 21, 2012. 4.4.8, 4.4.8

[168] J. Gallicchio and M. D. Schwartz, *Quark and gluon tagging at the LHC*, Phys.Rev.Lett. **107** (2011) 172001, arXiv:1106.3076 [hep-ph]. 4.4.8, 4.33

[169] J. Gallicchio and M. D. Schwartz, *Pure samples of quark and gluon jets at the LHC*, JHEP **1110** (2011) 103, arXiv:1104.1175 [hep-ph]. 4.4.8, 4.4.8, 4.35

[170] R. Reece, *Introducing tau^{++}: a more natural pile-up proof tau*, Talk given at an ATLAS tau working group meeting, CERN. May 17, 2011. 4.6, 4.4.9

[171] R. Reece, *Progress in local track-based pile-up correction to calorimeter isolation*, Talk given at an ATLAS tau working group meeting, CERN. November 22, 2011. 4.4.9, 4.44

[172] D. Cavalli and C. Pizio, *$Z \to \tau\tau$ in first ATLAS data*, ATL-PHYS-INT-2009-005, 2008. 5.1.1, 40, 50, 5.2.3

[173] P. Bechtle, D. Cavalli, Y. Coadou, S. Consonni, W. Davey, G. Fischer, A. Goussiou, J. Griffiths, K. Jakobs, A. Kaczmarska, S. Kuehn, S. Lai, W. Mader, C. Pizio, R. Reece, E. Richter-Was, S. Tsuno, and H. H. Williams, *Benchmark analysis for $Z \to \tau\tau \to \ell\tau_{\mathrm{h}}$ with the first* 100 pb^{-1}, ATL-PHYS-INT-2010-075, 2010. 5.1.1, 5.2.3, 5.14, 5.15, 62

[174] A. Nairz, L. Goossens, M. Branco, D. Cameron, P. Salgado, D. Barberis, K. Bos, and G. Poulard, *ATLAS computing system commissioning: real-time data processing and distribution tests*, Journal of Physics: Conference Series **110** (2008) no. 9, 092019. http://stacks.iop.org/1742-6596/110/i=9/a=092019. 42

[175] D. Costanzo, I. Hinchliffe, and S. Menke, *Analysis model forum report*, ATL-GEN-INT-2008-001, 2008. 42

[176] R. Reece and H. H. Williams, *A selection strategy for $Z \to \tau\tau \to \mu\tau_{\mathrm{h}}$ with the first 100 inverse picobarns from ATLAS*, ATL-PHYS-INT-2009-044, 2009. 5.1, 5.2, 5.3, 5.4, 5.5, 5.2.1, 5.6, 5.7, 5.8, 5.9, 5.2.2, 5.2.2, 5.10, 5.11, 5.2.3, 5.12, 5.13, 62

[177] A. Kaczmarska and E. Richter-Was, *Prospects for physics measurements with the $Z \to \tau\tau(e, \tau_{\mathrm{had}})$ process for* 100 pb^{-1} *with the ATLAS detector*, ATL-PHYS-INT-2009-019, 2008. 50, 5.2.3

[178] D. Adams, S. Asai, D. Cavalli, M. Dhrssen, K. Edmonds, S. Elles, M. Fehling, U. Felzmann, L. Gladilin, L. Helary, M. Hohlfeld, S. Horvat, K. Jakobs, M. Kaneda, G. Kirsch, S. Kuehn, J. F. Marchand, C. Pizio, X. Portell, D. Rebuzzi, E. Schmidt, A. Shibata, I. Vivarelli, S. Winkelmann, and S. Yamamoto, *The ATLFAST-II performance in release 14: particle signatures and selected benchmark processes*, ATL-PHYS-INT-2009-110, 2009. 5.2.3

[179] ATLAS Collaboration, *Luminosity determination in pp collisions at $\sqrt{s} = 7$ TeV using the ATLAS detector at the LHC*, Eur.Phys.J.C **71** (2011) 1630, arXiv:1101.2185 [hep-ex]. 5.3.1, A.1.5

[180] C. Boddy, D. Capriotti, D. Cavalli, E. Coniavitis, S. Consonni, S. Dhaliwal, D. Evangelakou, S. Farrington, F. Friedrich, J. Griffiths, A. Kaczmarska, J. Kretzschmar, S. Kuehn, S. Lai, A. Larner, Z. Liang, J. Novakova, X. Prudent, E. Ptacek, R. Reece, F. Seifert, T. Schwindt, M. Trottier-McDonald, T. Vickey, M. Wolter, and S. Yacoob, *Measurement of $Z \to \tau\tau$ production cross section in proton-proton collisions at $\sqrt{s} = 7$ TeV with the ATLAS detector - Support Note for lep-had channels*, ATL-COM-PHYS-2011-416, 2010. Support note for arXiv:1108.2016 [hep-ex]. 5.1, 5.16, 51, 5.4.1, 5.4.2, 5.2, 5.3, 5.4.4, 5.4, 5.17, 5.5, 5.18, 5.19, 5.6, 5.20, 5.21, 5.7, 5.6, 5.24, 5.25, 5.26, 5.27, 5.9, 5.10, 5.28, 5.11, 5.12, 5.14, 5.9, 5.9.3, 5.29, 62

[181] C. Anastasiou, L. Dixon, K. Melnikov, and F. Petriello, *High-precision QCD at hadron colliders: electroweak gauge boson rapidity distributions at NNLO*, Phys. Rev. D **69** (2004) 094008. 5.3.2

[182] S. Catani, L. Cieri, G. Ferrera, D. de Florian, and M. Grazzini, *Vector boson production at hadron colliders: a fully exclusive QCD calculation at NNLO*, Phys. Rev. Lett. **103** (2009) 082001, arXiv:0903.2120 [hep-ph]. 5.3.2

[183] J. Butterworth et al., *Single boson and diboson production cross sections in pp collisions at* $\sqrt{s} = 7$ *TeV*, ATL-COM-PHYS-2010-695, 2010. 5.3.2

[184] ATLAS Collaboration, *Data-quality requirements and event cleaning for jets and missing transverse energy reconstruction with the ATLAS detector in proton-proton collisions at a center-of-mass energy of* $\sqrt{s} = 7$ *TeV*, ATLAS-CONF-2010-038, 2010. 5.4.1

[185] M. Aharrouche et al., *Supporting document for egamma paper: Electron efficiency measurements using ATLAS 2010 data at* $\sqrt{s} = 7$ *TeV*, ATL-COM-PHYS-2011-322, 2011. 5.4.3

[186] ATLAS Collaboration, *Measurement of the mis-identification probability of* τ *leptons from QCD jets and from electrons*, ATLAS-CONF-2011-113, 2011. 5.4.4, 55

[187] Y. Coadou, S. Consonni, J. Griffiths, A. Kaczmarska, S. Kuehn, S. Lai, E. W. J. Moyse, R. Reece, and S. Tsuno, *Event display of* $Z \to \tau\tau \to \mu\tau_{\mathrm{h}}$ *in 7 TeV collisions*, ATL-COM-PHYS-2010-775, 2010. 5.22

[188] D. Cavalli, E. Coniavitis, S. Consonni, D. Evangelakou, S. Farrington, G. Fischer, F. Friedrich, J. Griffiths, A. Kaczmarska, S. Kuehn, S. Lai, A. Larner, E. Ptacek, R. Reece, T. Schwindt, T. Vickey, and S. Yacoob, *Observation of* $Z \to \tau\tau$ *decays with the ATLAS detector - support note for the* $\ell\tau_{\mathrm{h}}$ *channel*, ATL-COM-PHYS-2010-1033, 2010. Support note for ATLAS-CONF-2011-010. 5.5, 62

[189] A. Andreazza, L. Dell'Asta, J. Kraus, J. Kroseberg, P. Bechtle, C. Cuenca Almenar, N. Dawe, S. Johnert, J. Liebal, R. Mazini, Z. Meng, G. Nunes Hanninger, D. O'Neil, M. Uhlenbrock, E. von Toerne, M. Wolter, and S. Xella, *Measurement of the* $W \to \tau\nu$ *cross section in pp collisions at* $\sqrt{s} = 7$ *TeV with the ATLAS experiment*, ATL-PHYS-INT-2012-040, 2012. 59

[190] A. Sherstnev and R. S. Thorne, *Parton distributions for LO generators*, Eur.Phys.J.C **55** (2008) 553–575, arXiv:0711.2473 [hep-ph]. 5.8

[191] M. Aharrouche et al., $W \to e\nu$ *and* $Z \to ee$ *cross section measurements in proton-proton collisions at* $\sqrt{s} = 7$ *TeV with the ATLAS detector*, ATL-PHYS-INT-2010-130, 2010. 5.9.1

[192] ATLAS Collaboration, *A combined measurement of the top quark pair production cross-section using dilepton and single-lepton final states*, ATLAS-CONF-2011-040, 2011. 5.9.1

[193] ATLAS Collaboration, *Updated luminosity Determination in pp collisions at* $\sqrt{s} = 7$ *TeV using the ATLAS detector*, ATLAS-CONF-2011-011, 2011. 5.9.1

[194] L. Lyons, D. Gibaut, and P. Clifford, *How to combine correlated estimates of a single physical quantity*, Nucl.Instrum.Meth. A **270** (1988) 110–117. 5.10

[195] A. Valassi, *Combining correlated measurements of several different physical quantities*, Nucl.Instrum.Meth. A **500** (2003) 391–405. 5.10

[196] E. Barberio, M. Beckingham, C. Boddy, D. Capriotti, D. Cavalli, E. Coniavitis, S. Consonni, S. Dhaliwal, D. Evangelakou, S. Farrington, F. Friedrich, J. Griffiths, C. Gumpert, A. Kaczmarska, M. Kobel, J. Kretzschmar, J. Kroseberg, M. Schumacher, S. Kuehn, S. Lai, A. Larner, K. Leonhardt, Z. Liang, W. Mader, J. Novakova, X. Prudent, E. Ptacek, R. Reece, T. Shao, F. Seifert, T. Schwindt, M. Trottier-McDonald, N. Utecht, T. Vickey, C. Weiser, M. Wolter, and S. Yacoob, *Measurement of* $Z \to \tau\tau$ *production cross section in proton-proton collisions at* $\sqrt{s} = 7$ *TeV with the ATLAS detector - Combination of results*, ATL-COM-PHYS-2011-419, 2011. 5.10

[197] R. Reece, *Measurement of the W and Z boson production cross sections in pp collisions at 7 TeV with the ATLAS detector.*, ATL-PHYS-PROC-2011-240, 2011. 61

[198] CMS Collaboration, *Measurement of the inclusive Z cross section via decays to tau pairs in pp collisions at $\sqrt{s} = 7$ TeV*, JHEP **1108** (2011) 117, arXiv:1104.1617 [hep-ex]. 5.10

[199] P. Langacker, *The physics of heavy Z′ gauge bosons*, Rev.Mod.Phys. **81** (2009) 1199–1228, arXiv:0801.1345 [hep-ph]. 6.1

[200] M. Cvetic and S. Godfrey, *Discovery and identification of extra gauge bosons*, arXiv:hep-ph/9504216 [hep-ph]. 6.1

[201] M. Cvetic and P. Langacker, *Z′ physics and supersymmetry*, arXiv:hep-ph/9707451 [hep-ph]. 6.1

[202] A. Leike, *The Phenomenology of extra neutral gauge bosons*, Phys.Rept. **317** (1999) 143–250, arXiv:hep-ph/9805494 [hep-ph]. 6.1

[203] P. Langacker and M. Plumacher, *Flavor changing effects in theories with a heavy Z′ boson with family nonuniversal couplings*, Phys.Rev.D **62** (2000) 013006, arXiv:hep-ph/0001204 [hep-ph]. 6.1

[204] K. R. Lynch, E. H. Simmons, M. Narain, and S. Mrenna, *Finding Z′ bosons coupled preferentially to the third family at LEP and the Tevatron*, Phys.Rev. **D63** (2001) 035006, arXiv:0007286 [hep-ph]. 6.1

[205] P. Langacker, *TeV physics from the top down*, arXiv:hep-ph/0308033 [hep-ph]. 6.1

[206] T. G. Rizzo, *Z′ phenomenology and the LHC*, arXiv:hep-ph/0610104 [hep-ph]. 6.1

[207] T. G. Rizzo, *Indirect Searches for Z-prime-like Resonances at the LHC*, JHEP **0908** (2009) 082, arXiv:0904.2534 [hep-ph]. 6.1

[208] R. Diener, S. Godfrey, and T. A. Martin, *Unravelling an extra neutral gauge noson at the LHC using third generation fermions*, Phys.Rev.D **83** (2011) 115008, arXiv:1006.2845 [hep-ph]. 6.1

[209] CDF Collaboration, *Search for new physics using high mass tau pairs from 1.96 TeV $p\bar{p}$ collisions*, Phys.Rev.Lett. **95** (2005) 131801, arXiv:hep-ex/0506034 [hep-ex]. 6.1

[210] CMS Collaboration, *Search for new ditau resonances in pp collisions at $\sqrt{s} = 7$ TeV*, CMS-PAS-EXO-10-022, 2011. 6.1

[211] ATLAS Collaboration, *A search for high-mass resonances decaying to $\tau^+\tau^-$ in pp collisions at $\sqrt{s} = 7$ TeV with the ATLAS detector*, arXiv:1210.6604 [hep-ex]. 6.1, 6.14, 6.7, 6.10, 6.15, 86

[212] CMS Collaboration, *Search for high mass resonances decaying into τ lepton pairs in pp collisions at $\sqrt{s} = 7$ TeV*, Phys.Lett.B **716** (2012) 82–102, arXiv:1206.1725 [hep-ex]. 6.1, 6.7.3

[213] ATLAS Collaboration, *Search for high-mass resonances decaying to dilepton final states in pp collisions at $\sqrt{s} = 7$ TeV with the ATLAS detector*, JHEP **1211** (2012) 138, arXiv:1209.2535 [hep-ex]. 6.1

[214] CMS Collaboration, *Search for narrow resonances in dilepton mass spectra in pp collisions at $\sqrt{s} = 7$ TeV*, Phys.Lett.B **714** (2012) 158–179, arXiv:1206.1849 [hep-ex]. 6.1

[215] ATLAS Collaboration, *Search for high-mass dilepton resonances in 20 fb^{-1} of pp collisions at $\sqrt{s} = 8$ TeV with the ATLAS experiment*, ATLAS-CONF-2013-017, 2013. 6.1

[216] CMS Collaboration, *Search for resonances in the dilepton mass distribution in pp collisions at $\sqrt{s} = 8$ TeV*, CMS-PAS-EXO-12-061, 2013. 6.1

[217] R. S. Chivukula and E. H. Simmons, *Electroweak limits on nonuniversal Z' bosons*, Phys.Rev.D **D66** (2002) 015006, arXiv:hep-ph/0205064 [hep-ph]. 6.1

[218] ATLAS Muon Performance Group, *Muon performance twiki*, https://twiki.cern.ch/twiki/bin/view/AtlasProtected/MuonPerformance, 2012. 6.3.1

[219] *ATLAS*
Muon Combined Performance trigger recommendations for analyses of 2011 data in release 17, https://twiki.cern.ch/twiki/bin/viewauth/Atlas/MuonTriggerPhysicsTriggerRecommendations2011, 2011. 6.4.1

[220] ATLAS Egamma Performance Group, *ATLAS egamma efficiency measurements for 2011 data*, https://twiki.cern.ch/twiki/bin/viewauth/AtlasProtected/EfficiencyMeasurements, 2011. 6.4.1

[221] M. Hance, D. Olivito, and H. Williams, *Performance Studies for e/gamma Calorimeter Isolation*, ATL-COM-PHYS-2011-1186, 2011. 6.4.2

[222] ATLAS Collaboration, *Measurement of the WW cross section in $\sqrt{s} = 7$ TeV pp collisions with ATLAS*, Phys.Rev.Lett. **107** (2011) 041802, arXiv:1104.5225 [hep-ex]. 6.4.4

[223] ATLAS Collaboration, *Search for the Higgs boson in the $H \to WW^* \to \ell\nu\ell\nu$ decay channel in pp collisions at $\sqrt{s} = 7$ TeV with the ATLAS detector*, Phys.Rev.Lett. **108** (2012) 111802, arXiv:1112.2577 [hep-ex]. 6.4.4

[224] J. Alison, A. Arce, B. Cerio, A. Hawkins, S. Heim, A. Kotwal, E. Lytken, D. Olivito, and E. Thomson, *Search for anomalous production of like-sign dilepton events with at least one electron*, ATL-COM-PHYS-2011-1374, 2011. 6.4.4

[225] S. Banerjee, E. Barberio, M. Beckingham, J. Biesiada, C. Boddy, D. Cavalli, S. Consonni, E. Coniavitis, E. Costaneda-Miranda, S. Farrington, A. Goussiou, K. Hanawa, H. Hass, Y. Heng, D. Jennens, G.-Y. Jeng, J. Keller, J. Kraus, J. Kroseberg, R. Madar, K. Nakamura, G. Nunes Hanninger, D. O'Neil, E. Pianori, C. Pizio, A. Pranko, D. Rousseau, N. Ruthmann, Y. Sakurai, T. Schwindt, R. Simoniello, K. Tan, A. Tanasijczuk, M. Trottier-McDonald, D. Varouchas, T. Vickey, M. Volpi, and S.-L. Wu, *Re-optimized search for Standard Model $H \to \tau_\ell \tau_{\text{had}}$ with the ATLAS detector in 7 TeV proton-proton collisions*, ATL-COM-PHYS-2012-1087, 2012. 77

[226] K. Cranmer, G. Lewis, L. Moneta, A. Shibata, and W. Verkerke, *HistFactory: A tool for creating statistical models for use with RooFit and RooStats*, CERN-OPEN-2012-016, 2012. 81

[227] T. Junk, *Confidence level computation for combining searches with small statistics*, Nucl.Instrum.Meth. **A**434 (1999) 435–443, arXiv:hep-ex/9902006 [hep-ex]. 82

[228] A. L. Read, *Presentation of search results: the CL s technique*, Journal of Physics G: Nuclear and Particle Physics **28** (2002) no. 10, 2693.
http://stacks.iop.org/0954-3899/28/i=10/a=313. 82

[229] D. Casadei, *Reference analysis of the signal + background model in counting experiments*, Journal of Instrumentation **7** (2012) 1012, arXiv:1108.4270 [physics.data-an]. 83

[230] A. Caldwell, D. Kollár, and K. Kröninger, *BAT - The Bayesian analysis toolkit*, Computer Physics Communications **180** (2009) 2197–2209, arXiv:0808.2552 [physics.data-an]. 6.7.3

[231] S. Karlin and H. Taylor, *A First Course in Stochastic Processes*. Academic Press, 1975. 6.7.3

[232] E. W. R. Gilks, S. Richardson, and D. Spiegelhalter, *Markov Chain Monte Carlo in Practice*. Chapman and Hall, 1996. 6.7.3

[233] R. Reece, *Searches for charged Higgs bosons, supersymmetry, and exotica with tau leptons with the ATLAS and CMS detectors at the LHC*, ATL-PHYS-PROC-2012-302, 2012. 84

[234] ATLAS Collaboration, *Search for contact interactions in dilepton events from pp collisions at* $\sqrt{s} = 7$ *TeV with the ATLAS detector*, Phys.Lett.B **712** (2012) 40–58, arXiv:1112.4462 [hep-ex]. 85

[235] ALEPH Collaboration, DELPHI Collaboration, L3 Collaboration, OPAL Collaboration, SLD Collaboration, LEP Electroweak Working Group, SLD Electroweak Group, SLD Heavy Flavour Group Collaboration, S. Schael et al., *Precision electroweak measurements on the Z resonance*, Phys.Rept. **427** (2006) 257–454, arXiv:hep-ex/0509008 [hep-ex]. 6.7.4, A.2.7

[236] G. Burgess, C. Moore, *The Standard Model: A Primer*. Cambridge University Press, 2007. 6.7.4, 87

[237] ATLAS Collaboration, *A search for high-mass resonances decaying to* $\tau^+\tau^-$ *in the ATLAS detector*, ATLAS-CONF-2012-067, 2012. 86

[238] ATLAS Collaboration, *ATLAS combined summary plots*, https://twiki.cern.ch/twiki/bin/view/AtlasPublic/CombinedSummaryPlots, 2013. 7.1, 7.2

[239] M. Planck, *Where Is Science Going?* W.W. Norton & Company, 1932. 87

[240] F. Halzen and A. Martin, *Quarks and Leptons: An introductory course in modern particle physics*. John Wiley & Sons, 1984. 87

[241] T. Morii, C. Lim, and S. Mukherjee, *The Physics of the Standard Model and Beyond*. Cambridge University Press, 2004. 87

[242] Eds. Kane, G. and Pierce, A., *Persepectives on LHC Physics*. World Scientific, 2008. 87

[243] S. Martin, *Phenomenology of Particle Physics*, http://zippy.physics.niu.edu/phys686.html, 2011. Lecture notes for PHYS586, Northern Illinois University. 87, 104

[244] S. Weinberg, *V-A was the key*, Journal of Physics Conference Series **196** (2009) no. 1, 012002. 87

[245] J. Thomson, *Cathode rays*, Philosophical Magazine **44** (1897) 293. A.1.1

[246] M. Planck, *Entropie und temperatur strahlender wärme*, Annalen der Physik **306** (1900) 719–737. A.1.1

[247] M. Planck, *Über das gesetz der energieverteilung im normalspectrum*, Annalen der Physik **309** (1901) 553–563. A.1.1

[248] A. Einstein, *Über einen die erzeugung und verwandlung des lichtes betreffenden heuristischen gesichtspunkt*, Annalen der Physik **17** (1905) 132–148. A.1.1

[249] E. Rutherford, *The scattering of* α *and* β *particles by matter and the structure of the atom*, Philosophical Magazine **21** (1911) 669–688. A.1.1

[250] N. Bohr, *On the constitution of atoms and molecules, Part I*, Philosophical Magazine **26** (1913) 1–24. A.1.1

[251] N. Bohr, *On the constitution of atoms and molecules, Part II: systems conataining only a single nucleus*, Philosophical Magazine **26** (1913) 476–502. A.1.1

[252] N. Bohr, *On the constitution of atoms and molecules, Part III: systems conataining several neclei*, Philosophical Magazine **26** (1913) 857–875. A.1.1

[253] N. Bohr, *The spectra of helium and hydrogen*, Nature **92** (1913) 231–232. A.1.1

[254] L. de Broglie, *Recherches sur la théorie des quanta (Researches on the quantum theory), Thesis, Paris, 1924*, Ann. de Physique **10** (1925) . A.1.1

[255] W. Heisenberg, *Über quantentheoretische umdeutung kinematischer und mechanischer beziehungen.*, Zeitschrift für Physik **33** (1925) 879–893. A.1.1

[256] M. Born and P. Jordan, *Zur quantenmechanik*, Zeitschrift für Physik **34** (1925) 858–888. A.1.1

[257] M. Born, W. Heisenberg, and P. Jordan, *Zur quantenmechanik*, Zeitschrift für Physik **34** (1925) 858–888. A.1.1

[258] M. Born, *Zur quantenmechanik der stoβvorgänge*, Zeitschrift für Physik **37** (1926) 863–867. A.1.1

[259] W. Pauli, *On the hydrogen spectrum from the standpoint of the new quantum mechanics*, Zeitschrift für Physik **36** (1926) 336–363. A.1.1

[260] E. Schrödinger, *Quantisierung als eigenwertproblem*, Annalen der Physik **384** (1926) no. 4, 361–376. A.1.1

[261] E. Schrödinger, *An undulatory theory of the mechanics of atoms and molecules*, Phys. Rev. **2**8 (1926) 1049–1070. A.1.1

[262] E. Schrödinger, *Über das verhältnis der Heisenberg-Born-Jordanschen quantenmechanik zu der meinem*, Annalen der Physik **384** (1926) no. 8, 734–756. A.1.1

[263] W. Heisenberg, *Über den anschaulichen Inhalt der quantentheoretischen Kinematik und Mechanik*, Zeitschrift fur Physik **43** (1927) 172–198. A.1.1

[264] P. A. M. Dirac, *The quantum theory of the electron*, Proceedings of the Royal Society of London. Series A **117** (1928) no. 778, 610–624. A.1.1

[265] P. A. M. Dirac, *A theory of electrons and protons*, Proceedings of the Royal Society of London. Series A **126** (1930) no. 801, 360–365. A.1.1

[266] P. A. M. Dirac, *The Priciples of Quantum Mechanics*. Oxford University Press, 1930. A.1.1

[267] J. von Neumann, *The Mathematical Foundations of Quantum Mechanics*. Princeton University Press, 1932. A.1.1

[268] W. Pauli, *The connection between spin and statistics*, Phys. Rev. **58** (1940) 716–722. A.1.1

[269] A. Einstein, B. Podolsky, and N. Rosen, *Can Quantum-Mechanical Description of Physical Reality Be Considered Complete?*, Phys. Rev. **47** (1935) 777–780. A.1.2

[270] J. S. Bell, *On the Einstein Podolsky Rosen paradox*, Physics **1** (1964) 195. A.1.2

[271] S. J. Freedman and J. F. Clauser, *Experimental Test of Local Hidden-Variable Theories*, Physical Review Letters **28** (1972) 938–941. A.1.2

[272] A. Aspect, P. Grangier, and G. Roger, *Experimental realization of Einstein-Podolsky-Rosen-Bohm gedankenexperiment: A new violation of Bell's inequalities*, Phys. Rev. Lett. **49** (1982) 91–94. A.1.2

[273] A. Aspect, J. Dalibard, and G. Roger, *Experimental test of Bell's inequalities using time-varying analyzers*, Phys. Rev. Lett. **49** (1982) 1804–1807. A.1.2

[274] M. Tegmark, *The Interpretation of quantum mechanics: Many worlds or many words?*, Fortsch.Phys. **46** (1998) 855–862, arXiv:quant-ph/9709032 [quant-ph]. 91

[275] H. D. Zeh, *On the interpretation of measurement in quantum theory*, Foundations of Physics **1** (1970) 69–76. A.1.2

[276] W. H. Zurek, *Pointer basis of quantum apparatus: Into what mixture does the wave packet collapse?*, Phys. Rev. D **24** (1981) 1516–1525. A.1.2

[277] W. H. Zurek, *Environment-induced superselection rules*, Phys. Rev. D **26** (1982) 1862–1880. A.1.2

[278] E. Joos and H. D. Zeh, *The emergence of classical properties through interaction with the environment*, Zeitschrift fur Physik B Condensed Matter **59** (1985) 223–243. A.1.2

[279] D. Giulini, E. Joos, C. Kiefer, J. Kupsch, I. Stamatescu, and H. Zeh, *Decoherence and the appearance of a classical world in quantum theory*. Springer, 1996. A.1.2

[280] H. Everett, *"Relative State" Formulation of Quantum Mechanics*, Reviews of Modern Physics **29** (1957) 454–462. A.1.2

[281] B. S. DeWitt, *Quantum mechanics and reality*, Physics Today **23** (1970) 30. A.1.2

[282] M. F. Pusey, J. Barrett, and T. Rudolph, *On the reality of the quantum state*, Nature Phys. **8** (2012) 476, arXiv:1111.3328 [quant-ph]. 93

[283] *Field (mathematics)*, Wikipedia, http://en.wikipedia.org/wiki/Field_(mathematics), 2013. 94

[284] A. Einstein, *Zur elektrodynamik bewegter Körpe*, Annalen der Physik **17** (1905) 891. A.1.3

[285] A. Einstein, *Die Grundlage der allgemeinen Relativitätstheorie*, Annalen der Physik **354** (1916) 769–822. A.1.3

[286] W. Ehrenberg and R. E. Siday, *The Refractive Index in Electron Optics and the Principles of Dynamics*, Proceedings of the Physical Society. Section B **62** (1949) no. 1, 8. A.1.3

[287] Y. Aharonov and D. Bohm, *Significance of Electromagnetic Potentials in the Quantum Theory*, Phys. Rev. **115** (1959) 485–491. A.1.3

[288] R. G. Chambers, *Shift of an Electron Interference Pattern by Enclosed Magnetic Flux*, Phys. Rev. Lett. **5** (1960) 3–5. A.1.3

[289] M. Peshkin, I. Talmi, and L. J. Tassie, *The quantum mechanical effects of magnetic fields confined to inaccessible regions*, Annals of Physics **12** (1961) 426–435. A.1.3

[290] N. Osakabe, T. Matsuda, T. Kawasaki, J. Endo, A. Tonomura, S. Yano, and H. Yamada, *Experimental confirmation of Aharonov-Bohm effect using a toroidal magnetic field confined by a superconductor*, Phys. Rev. A **34** (1986) 815–822. A.1.3

[291] E. Noether, *Invariante variationsprobleme*, Nachr. d. König. Gesellsch. d. Wiss. zu Göttingen, Math-phys. Klasse (1918) 235–257, arXiv:physics/0503066. M. A. Tavel's English translation originally appeared in Transport Theory and Statistical Physics, 1 (3), 183–207 (1971). A.1.4

[292] F. C. Klein, *Vergleichende betrachtungen über neuere geometrische forschungen (A comparative review of recent researches in geometry)*, Mathematische Annalen **43** (1893) 63–100, arXiv:0807.3161 [math.HO]. originally published in 1872. 98

[293] E. Wigner, *On unitary representations of the inhomogeneous Lorentz group*, Annals of Mathematics **40** (1939) pp. 149–204. A.1.4

[294] S. Coleman and J. Mandula, *All possible symmetries of the S-matrix*, Physical Review **159** (1967) 1251–1256. A.1.4

[295] Wikimedia Commons, *Electron self energy loop*, http://commons.wikimedia.org/wiki/File:Electron_self_energy_loop.svg, 2013. CC BY-SA 3.0. A.1

[296] Wikimedia Commons, *Renormalized vertex*, http://en.wikipedia.org/wiki/File:Renormalized-vertex.png, 2013. CC BY-SA 3.0 (modified by the author). A.1

[297] J. Schwinger, *Quantum Electrodynamics. I. A covariant formulation*, Phys. Rev. **74** (1948) 1439–1461. A.1.5

[298] J. Schwinger, *Quantum Electrodynamics. II. Vacuum polarization and self-energy*, Phys. Rev. **75** (1949) 651–679. A.1.5

[299] J. Schwinger, *Quantum Electrodynamics. III. The electromagnetic properties of the electron radiative corrections to scattering*, Phys. Rev. **76** (1949) 790–817. A.1.5

[300] S. Tomonaga, *On a Relativistically Invariant Formulation of the Quantum Theory of Wave Fields*, Progress of Theoretical Physics **1** (1946) no. 2, 27–42. A.1.5

[301] Z. Koba, T. Tati, and S. Tomonaga, *On a Relativistically Invariant Formulation of the Quantum Theory of Wave Fields. II*, Progress of Theoretical Physics **2** (1947) no. 3, 101–116. A.1.5

[302] Z. Koba, T. Tati, and S. Tomonaga, *On a Relativistically Invariant Formulation of the Quantum Theory of Wave Fields. III*, Progress of Theoretical Physics **2** (1947) no. 4, 198–208. A.1.5

[303] S. Kanesawa and S. Tomonaga, *On a Relativistically Invariant Formulation of the Quantum Theory of Wave Fields. IV*, Progress of Theoretical Physics **3** (1948) no. 1, 1–13. A.1.5

[304] S. Kanesawa and S. Tomonaga, *On a Relativistically Invariant Formulation of the Quantum Theory of Wave Fields V*, Progress of Theoretical Physics **3** (1948) no. 2, 101–113. A.1.5

[305] R. P. Feynman, *Space-time approach to quantum electrodynamics*, Physical Review **76** (1949) 769–789. A.1.5

[306] R. P. Feynman, *Mathematical formulation of the quantum theory of electromagnetic interaction*, Phys. Rev. **80** (1950) 440–457. A.1.5

[307] R. P. Feynman, *Space-time approach to non-relativistic quantum mechanics*, Rev. Mod. Phys. **20** (1948) 367–387. A.1.5

[308] F. J. Dyson, *The radiation theories of Tomonaga, Schwinger, and Feynman*, Physical Review **75** (1949) 486–502. A.1.5

[309] F. J. Dyson, *The S matrix in quantum electrodynamics*, Phys. Rev. **75** (1949) 1736–1755. A.1.5

[310] K. G. Wilson, *Renormalization group and critical phenomena. 1. Renormalization group and the Kadanoff scaling picture*, Phys.Rev.B **4** 3174–3183. A.1.5

[311] K. G. Wilson, *Renormalization group and critical phenomena. 2. Phase space cell analysis of critical behavior*, Phys.Rev.B **4** (1971) 3184–3205. A.1.5

[312] K. G. Wilson and J. Kogut, *The renormalization group and the ε expansion*, Physics Reports **12** (1974) no. 2, 75–199. A.1.5

[313] M. Peskin and D. Schroeder, *An Introduction to Quantum Field Theory*. Westview Press, 1995. 100, 104

[314] Tong, D., *Lectures on Quantum Field Theory*, http://www.damtp.cam.ac.uk/user/tong/qft.html, 2011. Lecture notes for QFT at the University of Cambridge. 100

[315] E. H. Wichmann and J. H. Crichton, *Cluster decomposition properties of the S matrix*, Phys. Rev. **132** (1963) 2788–2799. A.1.5

[316] J. R. Taylor, *Cluster decomposition of S matrix elements*, Phys. Rev. **142** (1966) 1236–1245. A.1.5

[317] H. Lehmann, K. Symanzik, and W. Zimmermann, *Zur formulierung quantisierter feldtheorien*, Nuovo Cimento Serie **1** (1955) 205–225. A.1.5

[318] ATLAS Collaboration, *Luminosity determination in pp collisions at $\sqrt{s} = 7$ TeV using the ATLAS detector in 2011*, ATLAS-CONF-2011-116, 2011. A.1.5

[319] Wikimedia Commons, *Standard Model Feynman diagram vertices*, http://en.wikipedia.org/wiki/File:Standard_Model_Feynman_Diagram_Vertices.png, 2013. CC BY-SA 3.0. A.2

[320] Y. Nambu, *Quasi-particles and gauge invariance in the theory of superconductivity*, Phys. Rev. **117** (1960) 648–663. A.2.3

[321] J. Bardeen, L. N. Cooper, and J. R. Schrieffer, *Microscopic theory of superconductivity*, Phys. Rev. **106** (1957) 162–164. A.2.3

[322] J. Bardeen, L. N. Cooper, and J. R. Schrieffer, *Theory of superconductivity*, Phys. Rev. **108** (1957) 1175–1204. A.2.3

[323] Y. Nambu and G. Jona-Lasinio, *Dynamical model of elementary particles based on an analogy with superconductivity. I*, Physical Review **122** (1961) 345–358. A.2.3

[324] Y. Nambu and G. Jona-Lasinio, *Dynamical model of elementary particles based on an analogy with superconductivity. II*, Physical Review **124** (1961) 246–254. A.2.3

[325] J. Goldstone, *Field theories with superconductor solutions*, Il Nuovo Cimento (1955-1965) **19** (1961) 154–164. 10.1007/BF02812722. A.2.3

[326] J. Goldstone, A. Salam, and S. Weinberg, *Broken symmetries*, Physical Review **127** (1962) 965–970. A.2.3

[327] Wikimedia Commons, *Mexican hat potential polar*, https://en.wikipedia.org/wiki/File:Mexican_hat_potential_polar.svg, 2013. Public domain. A.3

[328] E. Fermi, *Versuch einer theorie der β-strahlen. I*, Zeitschrift fr Physik A Hadrons and Nuclei **88** (1934) 161–177. A.2.4

[329] C. L. Cowan, Jr., F. Reines, F. B. Harrison, H. W. Kruse, and A. D. McGuire, *Detection of the free neutrino: a confirmation*, Science **124** (1956) 103–104. A.2.4

[330] T. D. Lee and C. N. Yang, *Question of parity conservation in weak interactions*, Phys. Rev. **104** (1956) 254–258. A.2.4

[331] C. S. Wu, E. Ambler, R. W. Hayward, D. D. Hoppes, and R. P. Hudson, *Experimental test of parity conservation in beta decay*, Phys. Rev. **105** (1957) 1413–1415. A.2.4

[332] R. L. Garwin, L. M. Lederman, and M. Weinrich, *Observations of the Failure of Conservation of Parity and Charge Conjugation in Meson Decays: the Magnetic Moment of the Free Muon*, Phys. Rev. **105** (1957) 1415–1417. A.2.4

[333] E. C. G. Sudarshan and R. E. Marshak, *Chirality invariance and the universal Fermi interaction*, Phys. Rev. 109 (1958) 1860–1862. A.2.4

[334] R. P. Feynman and M. Gell-Mann, *Theory of the Fermi interaction*, Phys. Rev. **109** (1958) 193–198. A.2.4

[335] Y. Nambu, *Axial vector current conservation in weak interactions*, Physical Review Letters **4** (1960) 380–382. A.2.4

[336] B. W. Lee, *Renormalization of the σ-model*, Nuclear Physics B **9** (1969) 649–672. A.2.4

[337] G. 't Hooft, *Renormalization of massless Yang-Mills fields*, Nuclear Physics B **33** (1971) 173–199. A.2.4

[338] G. 't Hooft, *Renormalizable Lagrangians for massive Yang-Mills fields*, Nuclear Physics B **35** (1971) 167–188. A.2.4

[339] G. 't Hooft and M. Veltman, *Regularization and renormalization of gauge fields*, Nuclear Physics B **44** (1972) 189 – 213. A.2.4

[340] F. J. Hasert *et al.*, *Observation of neutrino-like interactions without muon or electron in the Gargamelle neutrino experiment*, Physics Letters B **46** (1973) 138–140. A.2.4

[341] F. J. Hasert *et al.*, *Observation of neutrino-like interactions without muon or electron in the Gargamelle neutrino experiment*, Nuclear Physics B **73** (1974) 1 – 22. A.2.4

[342] UA1 Collaboration, *Experimental observation of isolated large transverse energy electrons with associated missing energy at* $\sqrt{s} = 540$ *GeV*, Physics Letters B **122** (1983) 103–116. A.2.4

[343] UA1 Collaboration, *Further evidence for charged intermediate vector bosons at the SPS collider*, Physics Letters B **129** (1983) 273–282. A.2.4

[344] UA1 Collaboration, *Observation of the muonic decay of the charged intermediate vector boson*, Physics Letters B **134** (1984) 469–476. A.2.4

[345] UA1 Collaboration, *Experimental observation of lepton pairs of invariant mass around 95* GeV/c^2 *at the CERN SPS collider*, Physics Letters B **126** (1983) 398–410. A.2.4

[346] UA2 Collaboration, *Observation of single isolated electrons of high transverse momentum in events with missing transverse energy at the CERN pp collider*, Physics Letters B **122** (1983) 476–485. A.2.4

[347] UA2 Collaboration, *Evidence for $Z^0 \to e^+e^-$ at the CERN pp collider*, Physics Letters B **129** (1983) 130–140. A.2.4

[348] D. Haidt, *The Discovery of Weak Neutral Currents*, http://www.desy.de/~haidt/nc30_text.pdf, 2003. A.2.4

[349] M. Gell-Mann and A. H. Rosenfeld, *Hyperons and heavy mesons (systematics and decay)*, Annual Review of Nuclear Science **7** 407–478. A.2.5

[350] M. Gell-Mann, *A schematic model of baryons and mesons*, Physics Letters **8** (1964) 214–215. A.2.5

[351] G. Zweig, *An SU_3 model for strong interaction symmetry and its breaking; Part I*, . A.2.5

[352] G. Zweig, *An SU_3 model for strong interaction symmetry and its breaking; Part II*, . A.2.5

[353] E. D. Bloom, D. H. Coward, H. DeStaebler, J. Drees, G. Miller, L. W. Mo, R. E. Taylor, M. Breidenbach, J. I. Friedman, G. C. Hartmann, and H. W. Kendall, *High-energy inelastic $e-p$ scattering at 6° and 10°*, Phys. Rev. Lett. **23** (1969) 930–934. A.2.5

[354] M. Breidenbach, J. I. Friedman, H. W. Kendall, E. D. Bloom, D. H. Coward, H. DeStaebler, J. Drees, L. W. Mo, and R. E. Taylor, *Observed behavior of highly inelastic electron-proton scattering*, Phys. Rev. Lett. **23** (1969) 935–939. A.2.5

[355] H. Murayama, *Neutrino Physics*, http://hitoshi.berkeley.edu/neutrino/, 2011. A.4, A.9

[356] V. E. Barnes *et al.*, *Observation of a hyperon with strangeness minus three*, Phys. Rev. Lett. **12** (1964) 204–206. A.2.5

[357] Wikimedia Commons, *Eightfold Way (physics)*, http://en.wikipedia.org/wiki/Eightfold_Way_(physics), 2013. CC BY-SA 3.0. A.5, A.6

[358] O. W. Greenberg, *Spin and unitary-spin independence in a paraquark model of baryons and mesons*, Physical Review Letters **13** (1964) 598–602. A.2.5

[359] M. Y. Han and Y. Nambu, *Three-triplet model with double* SU(3) *symmetry*, Phys. Rev. **139** (1965) B1006–B1010. A.2.5

[360] S. L. Wu and G. Zobernig, *A method of three jet analysis in e^+e^- annihilation*, Z.Phys. **C2** (1979) 107. A.2.5

[361] TASSO Collaboration, *Evidence for planar events in e^+e^- annihilation at high-energies*, Physics Letters B **86** (1979) 243. A.2.5

[362] G. Sterman and S. Weinberg, *Jets from quantum chromodynamics*, Phys. Rev. Lett. **39** (1977) 1436–1439. A.2.5

[363] UA2 Collaboration, *Observation of very large transverse momentum jets at the CERN pp collider*, Physics Letters B **118** (1982) 203–210. A.2.5

[364] UA1 Collaboration, *Observation of jets in high transverse energy events at the CERN proton antiproton collider*, Physics Letters B **123** (1983) 115–122. A.2.5

[365] J. D. Bjorken, *Asymptotic sum rules at infinite momentum*, Phys. Rev. **179** (1969) 1547–1553. A.2.5

[366] R. P. Feynman, *Very High-Energy Collisions of Hadrons*, Phys. Rev. Lett. **23** (1969) 1415–1417. A.2.5

[367] J. C. Collins, D. E. Soper, and G. Sterman, *Factorization for short distance hadron-hadron scattering*, Nuclear Physics B **261** (1985) 104 – 142. A.2.5

[368] J. C. Collins, D. E. Soper, and G. F. Sterman, *Factorization of hard processes in QCD*, Adv.Ser.Direct.High Energy Phys. **5** (1988) 1–91, arXiv:hep-ph/0409313 [hep-ph]. A.2.5

[369] V. Gribov and L. Lipatov, *Deep inelastic e-p scattering in perturbation theory*, Sov.J.Nucl.Phys. **15** (1972) 438–450. A.2.5

[370] G. Altarelli and G. Parisi, *Asymptotic freedom in parton language*, Nucl.Phys.B **126** (1977) 298. A.2.5

[371] Y. L. Dokshitzer, *Calculation of the structure functions for deep inelastic scattering and e^+e^- annihilation by perturbation theory in quantum chromodynamics.*, Sov.Phys.JETP **46** (1977) 641–653. A.2.5

[372] E. Kuraev, L. Lipatov, and V. S. Fadin, *The Pomeranchuk singularity in nonabelian gauge theories*, Sov.Phys.JETP **45** (1977) 199–204. A.2.5

[373] I. Balitsky and L. Lipatov, *The Pomeranchuk singularity in quantum chromodynamics*, Sov.J.Nucl.Phys. **28** (1978) 822–829. A.2.5

[374] N. Cabibbo, *Unitary symmetry and leptonic decays*, Physical Review Letters **10** (1963) 531–533. A.2.6

[375] S. L. Glashow, J. Iliopoulos, and L. Maiani, *Weak interactions with lepton-hadron symmetry*, Phys. Rev. D **2** (1970) 1285–1292. A.2.6

[376] J. Augustin *et al.*, *Discovery of a narrow resonance in e^+e^- annihilation*, Phys. Rev. Lett. **33** (1974) 1406–1408. A.2.6

[377] J. Aubert *et al.*, *Experimental observation of a heavy particle J*, Phys. Rev. Lett. **33** (1974) 1404–1406. A.2.6

[378] W. S. Herb *et al.*, *Observation of a dimuon resonance at 9.5 GeV in 400 GeV proton-nucleus collisions*, Phys. Rev. Lett. **39** (1977) 252–255. A.2.6

[379] CDF Collaboration, *Observation of top quark production in $\overline{p}p$ collisions with the collider detector at fermilab*, Phys. Rev. Lett. **74** (1995) 2626–2631. A.2.6

[380] DØ Collaboration, *Observation of the top quark*, Phys. Rev. Lett. **74** (1995) 2632–2637. A.2.6

[381] M. Kobayashi and T. Maskawa, *CP-Violation in the renormalizable theory of weak interaction*, Progress of Theoretical Physics **49** (1973) 652–657. A.2.6

[382] CKMfitter Group Collaboration, *Predictions of selected flavour observables within the Standard Model*, Phys.Rev.D **84** (2011) 033005, arXiv:1106.4041 [hep-ph]. A.8, A.2.6

[383] L. Wolfenstein, *Parametrization of the Kobayashi-Maskawa Matrix*, Physical Review Letters **51** (1983) 1945–1947. A.2.6

[384] CKMfitter Group Collaboration, *CP violation and the CKM matrix: Assessing the impact of the asymmetric B factories*, Eur.Phys.J. **C**41 (2005) 1–131, arXiv:hep-ph/0406184 [hep-ph]. A.2.6

[385] G. Danby, J.-M. Gaillard, K. Goulianos, L. M. Lederman, N. Mistry, M. Schwartz, and J. Steinberger, *Observation of high-energy neutrino reactions and the existence of two kinds of neutrinos*, Phys. Rev. Lett. **9** (1962) 36–44. A.2.7

[386] M. L. Perl *et al.*, *Evidence for anomalous lepton production in e^+e^- annihilation*, Phys. Rev. Lett. **35** (1975) 1489–1492. A.2.7

[387] M. L. Perl *et al.*, *Properties of anomalous $e\mu$ events produced in e^+e^- annihilation*, Physics Letters B **63** (1976) 466–470. A.2.7

[388] M. L. Perl *et al.*, *Properties of the proposed tau charged lepton*, Physics Letters B **70** (1977) 487. A.2.7

[389] ALEPH Collaboration, *A precise determination of the number of families with light neutrinos and of the Z boson partial widths*, Physics Letters B **235** (1990) 399–411. A.2.7

[390] K. Kodama *et al.*, *Observation of tau neutrino interactions*, Physics Letters B **504** (2001) 218–224. A.2.7

[391] J. N. Bahcall, *Solar Neutrinos. I. Theoretical*, Physical Review Letters **12** (1964) 300–302. A.2.7

[392] J. N. Bahcall, *Solar Neutrinos*, Physical Review Letters **17** (1966) 398–401. A.2.7

[393] R. Davis, *Solar Neutrinos. II. Experimental*, Physical Review Letters **12** (1964) 303–305. A.2.7

[394] R. Davis, D. S. Harmer, and K. C. Hoffman, *Search for Neutrinos from the Sun*, Phys. Rev. Lett. **20** (1968) 1205–1209. A.2.7

[395] S. J. Freedman and B. Kayser, *The neutrino matrix*, ArXiv Physics e-prints (2004) , arXiv:physics/0411216. Joint study on the future of neutrino physics. A.2.7

[396] B. Pontecorvo, *Mesonium and anti-mesonium*, Sov.Phys.JETP **6** (1957) 429. A.2.7

[397] L. Wolfenstein, *Neutrino oscillations in matter*, Phys. Rev. D **17** (1978) 2369–2374. 112

[398] S. P. Mikheev and A. I. Smirnov, *Resonant amplification of neutrino oscillations in matter and solar-neutrino spectroscopy*, Nuovo Cimento C Geophysics Space Physics C **9** (1986) 17–26. 112

[399] P. Langacker, *Neutrino masses from the top down*, Ann.Rev.Nucl.Part.Sci. **62** (2012) 215–235, arXiv:1112.5992 [hep-ph]. A.2.7

[400] Z. Maki, M. Nakagawa, and S. Sakata, *Remarks on the unified model of elementary particles*, Progress of Theoretical Physics **28** (1962) 870–880. A.2.7

[401] B. Pontecorvo, *Neutrino experiments and the problem of conservation of leptonic charge*, Soviet Journal of Experimental and Theoretical Physics **26** (1968) 984. A.2.7

[402] SNO Collaboration, *Direct evidence for neutrino flavor transformation from neutral current interactions in the Sudbury Neutrino Observatory*, Phys.Rev.Lett. **89** (2002) 011301, arXiv:nucl-ex/0204008 [nucl-ex]. A.2.7

[403] KamLAND Collaboration, *Measurement of neutrino oscillation with KamLAND: Evidence of spectral distortion*, Phys.Rev.Lett. **94** (2005) 081801, arXiv:hep-ex/0406035 [hep-ex]. A.2.7

[404] Super-Kamiokande Collaboration, *Evidence for an oscillatory signature in atmospheric neutrino oscillation*, Phys.Rev.Lett. **93** (2004) 101801, arXiv:hep-ex/0404034 [hep-ex]. A.2.7

[405] T2K Collaboration, *Indication of electron neutrino appearance from an accelerator-produced off-axis muon neutrino beam*, Phys. Rev. Lett. **107** (2011) 041801. A.2.7

[406] F. P. An *et al.* (Daya Bay Reactor Neutrino Experiment), *Observation of electron-antineutrino disappearance at Daya Bay*, Phys. Rev. Lett. **108** (2012) 171803. A.2.7

[407] D. Forero, M. Tortola, and J. Valle, *Global status of neutrino oscillation parameters after Neutrino-2012*, Phys.Rev. **D**86 (2012) 073012, arXiv:1205.4018 [hep-ph]. A.2.7